Molecular-Based Single Crystal Surfaces as Functional Substrates for Directed Metal Binding

Christopher J. McGurk

A thesis submitted for the degree of
Doctor of Philosophy in Chemistry

School of Chemistry
Newcastle University
Newcastle upon Tyne, UK

December 2015

Abstract of the Dissertation

Molecular-Based Single Crystal Surfaces as Functional Substrates for Directed Metal binding

Molecular-based crystals provide faces offering specific chemical groups, ordered in a spatially well-defined array, dependent of the crystal space group. These surfaces therefore offer potential to be exploited as templates for directing material binding in order to construct regular arrays of technologically useful nanomaterials, *e.g.* preformed nanoparticles, metal clusters formed *in-situ*.

The dimensions typically associated with molecular crystalline materials (*i.e.* unit cell, spacing between repeating chemical groups in crystal structure) are typically on the angstrom scale. This offers potential for the construction of patterned arrays of materials with resolutions that may exceed the capabilities of current conventional lithographic techniques which can typically produce feature sizes down to 10 nm (for 2015, ITRS).

Towards this, a series bis-pyridyl derivatives containing metal binding sites, separated by a range of spacing groups (differing in length, rigidity and aromaticity), have been prepared and characterized. Single crystal X-ray diffraction has been used to determine the molecular orientation with respect to each crystal face, and hence assess the usefulness as a substrate for metal deposition.

A study into how to further influence the crystal structure, and therefore optimize the likelihood of producing surfaces with the desired binding site pattern, was conducted using a crystal engineering approach to generate polymorphs of previously synthesized compounds by varying the crystallization conditions of solvent and temperature.

Models for metal binding have been prepared in the form of ligand-metal complexes and have been studied by X-ray crystallography. Reactions involving silver or zinc salts with the prepared bis-pyridyl ligands afford complexes which identify the likely metal binding sites(s) of the organic compounds and also provide details of the effect of binding with respect to ligand conformation. This information is used to predict if there will be a strong interaction between metal ions and the organic single crystal surfaces, where

minimal changes in geometry are desired, so the pre-grown crystal substrates are left unaffected by metal deposition.

AFM (atomic force microscopy) and XPS (X-ray photoelectron spectroscopy) have been used to study a range of phosphine crystal surfaces before and after metal deposition. AFM provides topological analysis of surfaces and XPS provides chemical analysis. AFM experiments on the different bare crystal faces show a range of rough, smooth and stepped surfaces. It has also been shown here that XPS experiments can be performed on different faces of an organic single crystal, with potential to distinguish between faces based on peak intensity. Similar AFM and XPS experiments have also been performed on crystals after gold nanoparticle deposition and with deposition of gold ions in different oxidation states. These experiments show clear preferential binding to specific crystal faces in line with predictions made from viewing their crystal structures.

Acknowledgements

I would like to take this opportunity to thank all those who helped and contributed to the work in this thesis. Firstly, I would like to thank my supervisor, Professor Andrew Houlton, for giving me the opportunity to conduct my research within his group. I would also like to thank him for the valuable advice, knowledge and guidance given to me during my time here. I am particularly grateful to Dr Scott Watson, Dr David Smith, and of course, Dr Clare Mahon not only for their crucial guidance and support at the beginning and throughout my PhD (making me the scientist I am today) but also for their friendship, which I am sure will last a lifetime.

I have also been fortunate to have gained so many friends here during my studies. In particular, Sam Bhatt, Colette Whitfield, Michael Bracchi, Luke Dixon and Jonathan Pate, all of whom undoubtedly made Newcastle a great place to work.

I wish to acknowledge the contributions provided by the XPS service at Newcastle University for their help in the analysis of data as well as that of Dr Osama El Zubir for his guidance with AFM. I'd also like to thank my second supervisors Dr Ulrich Baisch and Dr Mike Probert for their helpful suggestions and guidance.

Finally, I wish to thank my family for their support throughout all stages of my education and especially during my PhD.

Table of Contents

Chapter 1

Strategies for the Continued Miniaturization of Electronic Devices

Table of Contents

1.1 Nanoscience, Nanotechnology and Chemistry

Nanoscience is a field of science, engineering and technology conducted on the nanoscale, approaching the size of atoms and molecules. It involves the manipulation of matter with dimensions in the region of 1-100 nm (1 nm = $1x10^{-9}$ m),[1] and connects areas of chemistry, biology, physics and engineering, making use of the combined knowledge and techniques acquired from many disciplines such as supramolecular chemistry, materials science, chemical and biological engineering and applied physics.

In chemistry, the nanoscale range is typically associated with aggregates of molecules or very large molecules such as polymers, micelles, dendrimers, vesicles, buckminsterfullerene, carbon nanotubes, and quantum dots, all of which provide interesting nanostructures and properties for investigation. The nanoscale range in the field of biology is typically associated with construction of cells, bacteria, viruses and organelles from building blocks and tools such as, proteins, DNA, ribosomes, antibodies and enzymes. In physics, the association with nanoscience lies in the study of quantum effects due to physical size limitation, as well as the change in electrical, mechanical, optical and magnetic properties of nanostructures where interfaces dominate over bulk properties.

Nanoscale structures may be further classed in terms of the dimensions they hold which are not restricted to the nanoscale. Two-dimensional nanomaterials exhibit two bulk dimensions (100 nm or above) and one nanoscale dimension (1-100 nm), these include nanofilms, nanosheets and quantum wells.[2-4] One dimensional nanomaterials exhibit one bulk dimension and two nanoscale dimensions such as nanowires, nanoropes,[5] nanoribbons,[6] nanorods, nanotubes[7, 8] and zero-dimensional nanomaterials have only nanoscale dimensions including nanoparticles[9] and quantum dots.[10] Many of these nanomaterials may be synthesized using knowledge and techniques that have their origins in chemistry. Supramolecular chemistry, and in particular, molecular self-assembly play an important role in the synthesis of nanostructures, the implementation of such techniques has lead to the emergence of the term ‘nanochemistry’.[11]

"In a sense, chemistry is (and always has been) the ultimate nanotechnology" are the words of one of the nanochemistry pioneers, George M. Whitesides.[12] Whitesides describes how operating on the sub-nanometre to nanometre scale, chemists routinely make new forms of matter by joining atoms and groups of atoms together with bonds through chemical synthesis. These synthetic processes and principles can be extended to the nanoscale, putting chemists at the forefront of nanotechnology. Nanochemistry utilizes chemical synthesis in the form of molecular self-assembly, a process in which molecules form ordered aggregates through spontaneous assembly, organization and growth. In this way, many possible routes to nanostructure fabrication exist, including the defining of shape, size and composition of nanostructures through their controlled growth.[13]

Fabricating, manipulating and controlling nanoscale structures are of particular interest to those in the nanoscale electronics field and semiconductor industry. The need for decreased feature size and controllable shape and composition is very important for the future of the industry. Self-assembly processes may offer routes to electronic systems via molecular-level control of material composition and structure not possible using conventional methods.[14]

1.2 The Ever-Smaller Future of Electronics

Computing performance over the past 55 years or so has improved dramatically in both processing power and efficiency.[15] This is largely due to the invention of the integrated circuit and continued improvement upon its performance, with many of the electronic devices in operation today incorporating the use of an integrated circuits in some way. An integrated circuit can consist of several electronic components such as transistors, diodes, resistors, capacitors and inductors, which are integrated into a single silicon semiconductor chip (monolith). The components are connected to each other by electrically conductive metal interconnections (wires), creating a circuit.

The semiconductor industry has improved productivity (power, efficiency and complexity) of integrated circuits by 25-30% annually[15] whilst maintaining (or even decreasing) overall product size. It does this by fitting more components

onto the same sized chips, increasing the density. The semiconductor industry can now manufacture over 7 billion transistors on a single 678 mm^2 wafer (IBM z13 storage controller), and over 5.5 billion transistors on a commercially available 611 mm^2 CPU (central processing unit) (Intel 18-core Xeon Haswell-E5). In 1965, Gordon E. Moore of Intel Corporation observed that since the integrated circuit was first introduced, the number of transistors per square inch on a circuit had doubled. He then went on to predict the downscaling of components within an integrated circuit, where the number of transistors would approximately double every two years. This trend is commonly referred to as 'Moore's law'[16] and implies that the complexity of the integrated circuit also doubles every two years. Fitting more transistors onto the same sized chip requires a reduction in transistor size[17] (defined by it's gate length, or feature size), Figure 1.1 shows the 'Moore's law' trend in terms of transistor size downscaling from its invention, to its projected future size. The reduction in transistor size also requires a reduction on interconnector (wires) width, with the two being of similar size currently and forecast to remain so.[18]

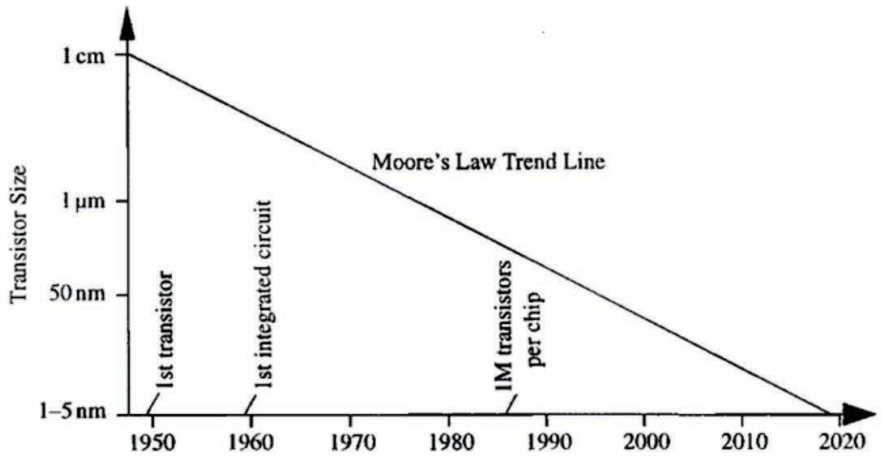

Figure 1.1 Illustration of the Moore's law trend, showing the projected decrease in transistor size with time.[1]

The Semiconductor Industry Association (SIA) frequently update the International Technology Roadmap for Semiconductors (ITRS),[19] outlining the advances in technology that will be required for the industry to continue the historical rate of improvement in productivity. 10 nm node process technologies are to be used this year (2015), producing a DRAM half pitch size of 24 nm, this is half the distance between two identical features of an array on

a dynamic random access memory chip, one of the main technology driver indicators for current memory intensive electronic devices. It is expected to reach 10 nm by 2025. However, the current industry consensus suggests that the use of conventional manufacturing methods will limit the downscaling of transistor, DRAM half pitch and interconnection size.[20]

These conventional methods utilize photolithography to pattern the desired network into a silicon semiconductor wafer, however, the resolution of such patterns is dictated by the wavelength of light used, which will soon reach a fundamental limit if the use of visible light to be continued.

Nanotechnology now plays an important role here as we move to operate on this scale. 'There's plenty of room at the bottom'[21] is the title of a 1959 popularized lecture given by Richard Feynman in which he invites the world of science and engineering to explore the nanoscale world. Feynman mainly discuses the potential for top-down fabrication of materials with nanoscale dimensions, but also alludes to the re-arrangement of atoms for the same purpose, an idea that is now known as a 'bottom-up' approach. There are many bottom-up approaches currently being pursued as viable alternatives to conventional top-down methods for producing nanoscale electronics.[14, 22, 23]

Whilst the principles of top-down and bottom-up approaches may oppose each other, they both offer solutions to the continuation of the Moore's law trend, with the ability to form nanomaterial constructs.

1.3 Top-Down Routes to Nanoscale Architectures

1.3.1 Photolithographic Methods

To date, the top-down approach to decreasing feature size of transistors and interconnections has fuelled their continued miniaturization, keeping the industry on-track with the Moore's law trend. The approach is analogous to the carving of a detailed sculpture from a larger block of the raw material.

The first monolithic integrated circuits were developed just after Feynman's talk 'There's plenty of room at the bottom' in the early 1960's, by Robert Noyce (Fairchild Semiconductor) and Jack Kilby (Texas Instruments) and employed the process of photolithography. Photolithography begins with the application

of a photoresist (light sensitive material) onto the oxide layer of a doped silicon substrate, a photomask is then applied either protecting or exposing the photoresist to a pattern of light. A positive photoresist becomes soluble in a developer solution with exposure to light whereas a negative photoresist becomes soluble in the developer solution when not exposed to light. The pattern is transferred to the surface by the removal of soluble photoresist, an etching solution is then used to remove the exposed oxide layer on the substrate before removal of the remaining photo resist material, leaving behind a pattern of doped silicon substrate (conductive) and oxide (non-conductive).

Current and future industry production of semi-conductor transistors is based on these well-established top-down photolithographic methods,[24] where high-energy light such as ultraviolet radiation (UV = 436-365 nm),[25] deep ultraviolet radiation (DUV = 248 nm),[26] extreme ultraviolet radiation (EUV = 13.5 nm)[27] and X-ray radiation (sub 10 nm)[28] are, and will be used to etch nano-scale patterns into a substrate. Particles[29] such as electrons[30] or ions[31] can also be used by similar lithographic methods showing potential for even greater resolutions.[24] The drawbacks and limitations of these techniques are the increasing implementation difficulty with miniaturization due to absorption of high-energy UV or damage to samples because of high-energy processes. These drawbacks lead to high costs and in the case of particle lithography, low throughput, leading to low-volume production of semiconductors.[32]

1.3.2 Scanning Probe Lithography

Scanning probe lithography can also be used for nanoscale patterning on surfaces where instruments originally intended to visualize molecules and atoms by microscopy, have since been used for the accurate placement of single atoms or molecules on a surface. A scanning tunnelling microscope (STM) was used by Eigler and Schweizer for the direct placement of xenon atoms on a nickel (110) surface to spell out 'IBM'[33] (Figure 1.2) This was also used by Heinrch et al. to move individual atoms on a copper surface in the IBM movie[34] 'A boy and his atom' where the atoms have been positioned to create 242 stop motion frames. A more practical application of the technique shows creation of a magnetic memory bit of just iron 12 atoms by Loth's team, the

STM can also be used here to electrically switch the magnetic information between 1 and 0.[35] The potential feature sizes created using this technique are only restricted to the size of the atoms used, however, the serial nature of this process means its very expensive and time consuming.

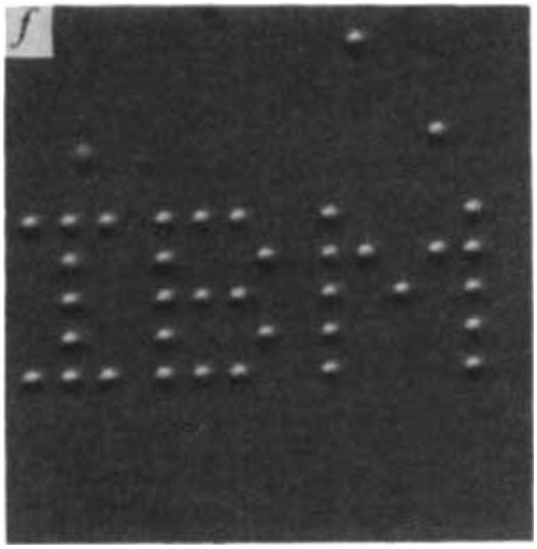

Figure 1.2 STM image of placed xenon atoms on a nickel (110) surface, each atom is 50 Å from top to bottom.[33] Reprinted by permission from Macmillan Publishers Ltd: *Nature* 1990, **344**, 524-526, copyright 1990.

Atomic force microscopes (AFM) have also been used as a tool for nanolithography, with Mirkin showing how an AFM can be used to transfer alkanethiols to a gold surface in a capillary transport process called 'dip-pen lithography' (DPN)[36] (Figure 1.3a). The AFM tip firstly dips into the writing material 'ink' before moving to the writing area and depositing the material through a water meniscus formed between the tip and the surface. The size of the water meniscus is controlled by the relative humidity and affects the material transport rate and contact area, ultimately controlling the DPN resolution, giving typical feature sizes of around 100-150 nm. The process has also been used to generate protein nanoarrays[37] and produce nanostructures of modified oligonucleotides,[38] Figure 1.3b, opening up possibilities for further modification of the oligomer once deposited.

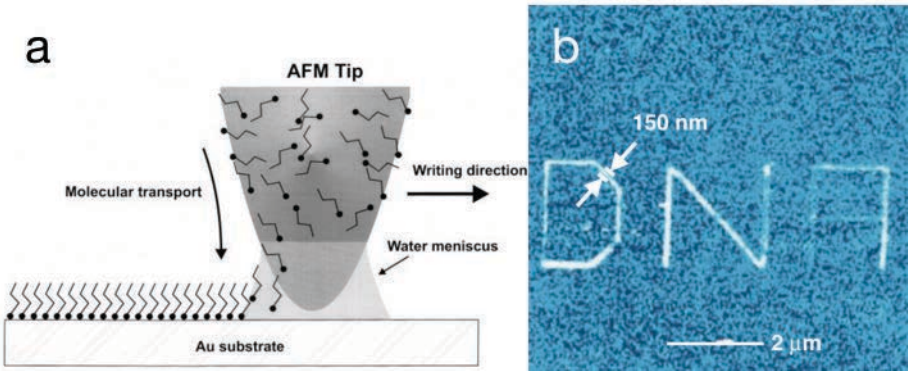

Figure 1.3 Dip-pen nanolithography, a schematic representation of the process, **a**,[36] From *Science*, 1999, **283**, 661-663. Reprinted with permission from AAAS. And an AFM image of direct transfer of hexanethiol-modified oligonucleotides patterned on a polycrystalline gold surface, **b**.[38] From *Science*, 2002, **296**, 1836-1838. Reprinted with permission from AAAS.

1.3.3 Physical Contact Printing

Physical contact printing such as nanoimprint lithography,[39] presents another top-down route to the formation of nanoscale structures on a surface. The method is performed by taking a mould of nanostructured material and placing it onto a thin resist cast on a substrate (Figure 1.4a), duplicating the nanostructured pattern. The process typically employs silicon or silicon oxide moulds and a poly(methyl methacrylate) (PMMA) resist and give potential resolutions below 10 nm. The PMMA template can then be used to transfer lift off metals to a surface in an ordered array. Figure 1.4b shows a scanning electron microscopy (SEM) image of such an array, where the deposited metal lines are 30 nm in width and exhibit a pitch (distance between two identical features) of 70 nm. This is a higher throughput method but is limited as to the starting resolution of the mould and the creation of defects due to imperfect transfer.

Scanning probe and nanoimprint lithographic techniques still have some issues regarding their serial nature and reproducibility giving them a low throughput. Further work is required in this field if viable, low-cost alternatives to conventional optical lithographic routes are to be pursued for the miniaturization of integrated circuits and transistors.

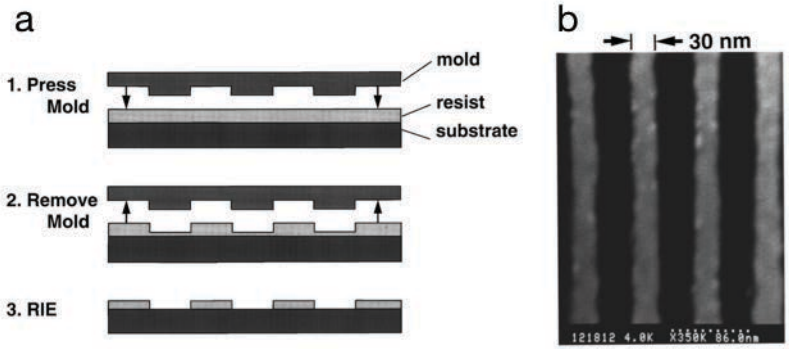

Figure 1.4 The nanoimprint lithographic technique. A schematic representation of the process, **a**, and an SEM image of patterned lift off metal created using the technique, **b**.[39] Reprinted with permission from *J. Vac. Sci. Technol., B*, 1996, **14**, 4129-4133. Copyright 1996, American Vacuum Society.

1.4 Bottom-Up Routes to Nanoscale Architectures

1.4.1 Self-Assembly of Building Blocks for Nanoscale Architectures

An alternative method to decreasing feature size is the 'bottom-up' approach. Bottom-up solutions involve building up the pattern from smaller components, i.e. atoms or molecules. In this manner, pattern information provided by molecules is on a smaller scale than that of the final architectures so does not limit them. These technologies rely on self-assembly processes, taking advantage of supramolecular forces.

In the world of supramolecular chemistry, self-assembly can be described as "the autonomous organization of components into patterns or structures without human intervention".[40] Systems of disordered components have the potential to form more organized patterns or structures through local interactions between them. In the case of molecular self-assembly, these interactions are supramolecular in nature, where molecules interact through ion-ion, ion-dipole and dipole-dipole interactions, as well as hydrogen bonding, cation-π, anion-π, π-π, van der Waals, crystal close packing and closed shell interactions.[41] These interactions have been shown to be very important in biological and chemical systems.[42] Possibly the most significant example of a self-assembled structure in biology is the structure of deoxyribonucleic acid (DNA). Its proposed and elucidated structure was arrived at by James Watson, Francis Crick,[43] Rosalind Franklin[44, 45] and Maurice Wilkins[46] in 1953, showing a double helical structure where nucleobases in each single strand pair-up

through hydrogen bonding interactions. The adenine (A) and thymine (T) bases both donate and accept one hydrogen bond each, whereas the guanine (G) base donates two hydrogen bonds, which are accepted by cytosine (C), and accepts one hydrogen bond donated by cytosine (Figure 1.5).

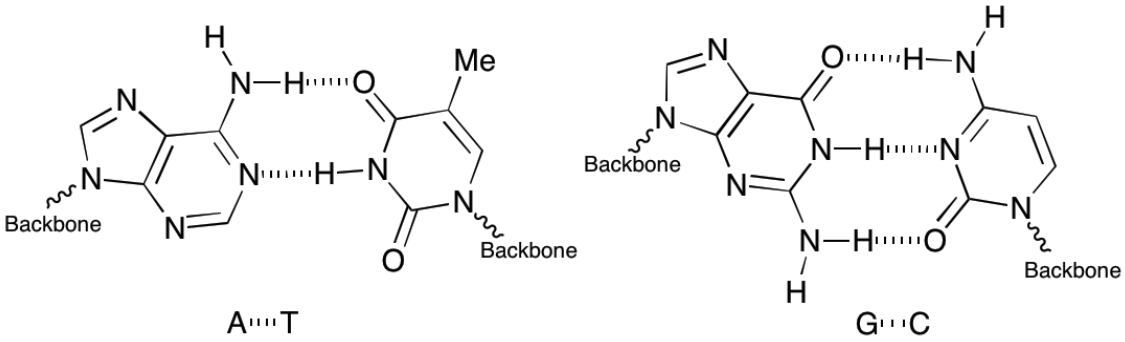

Figure 1.5 Hydrogen bonding interactions between adenine (A) and thymine (T), as well as between guanine (G) and cytosine (C).

In chemical systems, supramolecular interactions play an integral part in the assembly of supramolecular structures such as rotaxanes, pseudorotaxanes, polyrotaxanes and catenanes.[47] Their formation and stability utilize interactions such as hydrogen bonding and π-π stacking. Figure 1.6 shows the self assembly of a pseudorotaxane[48] stabilized by π-electron deficient bipyridinium units encircling an acyclic polyether derivative containing a π-electron rich hydroquinone ring. The exploitation and control of intermolecular interactions on this level and therefore control of these types of systems, forms the basis for molecular machines[49, 50] where larger, more complicated systems can be formed from a building block approach to form functional machines on a molecular level.

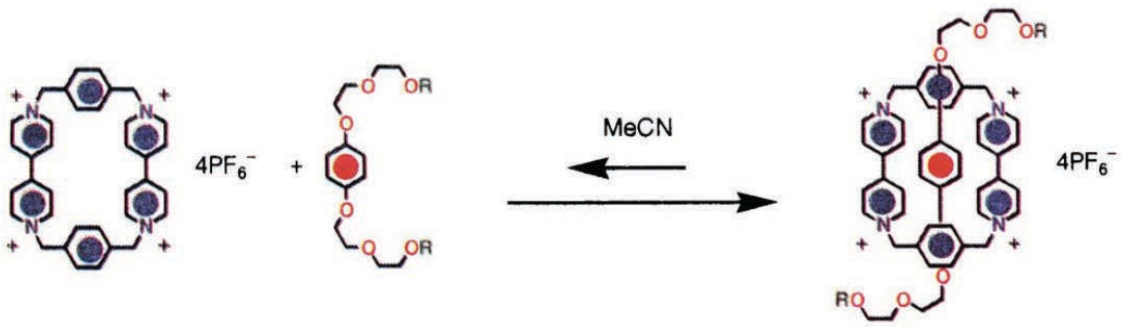

Figure 1.6 The self-assembly of a pseudorotaxane, stabilized by interactions between π-electron deficient and rich systems.[48] Reproduced (in part) from *Chem. Commun.*, 1996, 479-481 with permission of The Royal Society of Chemistry.

This utilization of supramolecular forces for self-assembly has also been identified for use in developing nanoscale architectures as integrated circuits and transistors.[11]

1.4.2 Self-Assembly of Surface Nanoarchitectures

The role of supramolecular chemistry is key in producing nanoscale architectures as they have the potential to be pre-programmed and low-cost due to self-assembly processes. For example, DNA origami[51, 52] utilizes hydrogen bond interactions and the sequencing of DNA strands to produce programmable patterns of nanostructures.[53] Figure 1.7 shows how smaller patterns of DNA can be assembled through choice of base sequencing (Figure 1.7a), how these smaller structures can be repeated and extended to create larger scale nanostructures (Figure 1.7b) and an AFM image of the final DNA origami grid produced using this method (Figure 1.7c). These systems can then also benefit from DNA's ability to act as a biosensor for pathogens and pollutants[54] and further functionality may be introduced for a designated purpose, such as addition of conductive metals[55] carbon nanotubes[56] or polymers[57] for use in nanocircuit fabrication.[58] The diameter of most forms of DNA (B-DNA) is 2.0 nm, meaning nanostructures created where DNA is a scaffold will have feature sizes of 2 nm and above.

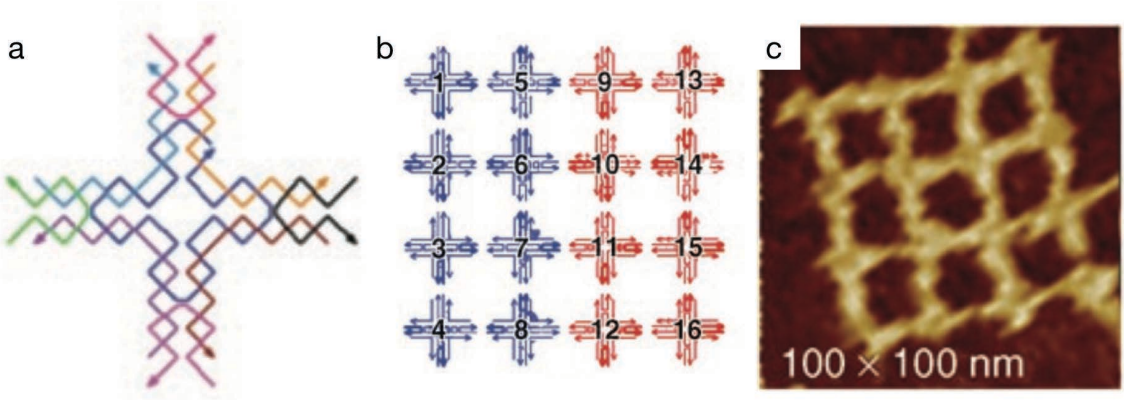

Figure 1.7 Nanostructures created through DNA origami, showing how different DNA sequences are programmed to self-assemble into small patterns, **a**, how these small patterns can then assemble into larger nanostructures, **b**, and an AFM image of such nanostructures formed by this technique, **c**.[53] Reproduced with permission from Wiley, S. H. Park, C. Pistol, S. J. Ahn, J. H. Reif, A. R. Lebeck, C. Dwyer and T. H. LaBean, *Angew. Chem. Int. Ed.*, 2006, **45**, 735-739.

Control over carbon nanotube dispersion (through use of surfactants)[59] and growth may also be achieved where peptide-wrapped carbon nanotubes interact with adjacent nanotubes through peptide-peptide interactions, forming macromolecular structures.[60]

Ordered arrays of nanostructures directly patterned onto surfaces more closely resemble the electronic circuitry seen on current integrated circuits. The feature size and spacing is more controllable in these systems, meaning the pitch size measurement is more easily designed and measured. Self-assembled nanoscale architectures created in patterns directly on surfaces have been shown, with many examples of structure formation using intermolecular interactions. Champness has shown the formation of single molecule chains[61] on a silver terminated silicon (111) surface, imaged by STM (Figure 1.8). The chains are made up of the diimide derivative of naphthalene tetracarboxilic dianhydride (NTCDI) molecules (Figure 1.8a), which interact with adjacent molecules through hydrogen bonding (Figure 1.8b). Planar molecules such as NTCDI used here, tend to lie flat to the substrate surface, allowing the hydrogen bonding functional groups to extend from the molecules edge and interact with other molecules. The chains produced were imaged by STM (Figure 1.8c) showing chains of individual molecules.

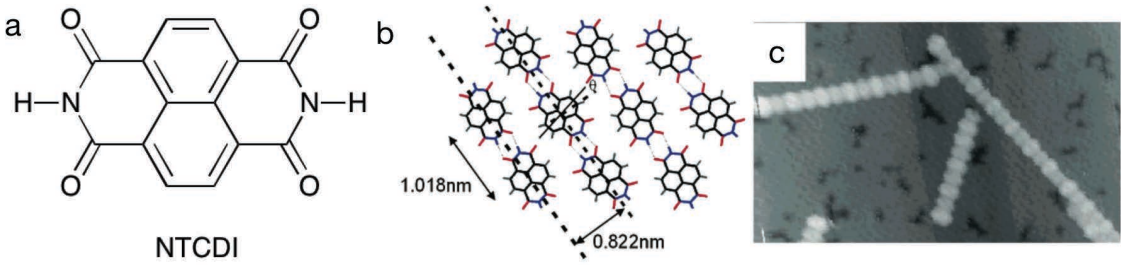

Figure 1.8 Nanostructure chains of NTCDI, schematic diagrams showing the structure of NTCDI, **a**, and its crystal structure, **b**, and a 16 x 26 nm^2 STM image of the nanostructure chains formed by this technique, **c**.[61] Reprinted (adapted) with permission from *Nano Lett.*, 2003, **3**, 9-12. Copyright 2003 American Chemical Society.

In the Champness group, networks of honeycomb motifs have also been created with similar molecules. In these structures hydrogen-bonding interactions are still exploited, however, corners have been added to the structure in the form of melamine, leading to honeycomb motifs. One example of these structures was created through the triple hydrogen-bonding interactions between melamine and perylene tetra-carboxilic di-imide,[62] and was again imaged on a silver terminated silicon (111) surface by STM. Figure 1.9 shows the honeycomb motif nanostructures created between melamine and perylene tetra-carboxilic di-imide by STM, both scale bars here are 3 nm in width. Smaller honeycomb networks[63] were also created using melamine and cyanuric acid on a silver terminated silicon (111) surface, as well as honeycombs with functionalized pores,[64] where melamine forms hexagonal hydrogen bonded structures with di(propylthio) functionalized perylene tetra-carboxilic di-imide (Figure 1.10). This kind of functionalization means these structures can now be used as templates, which may give them additional properties such as electrical conductivity.

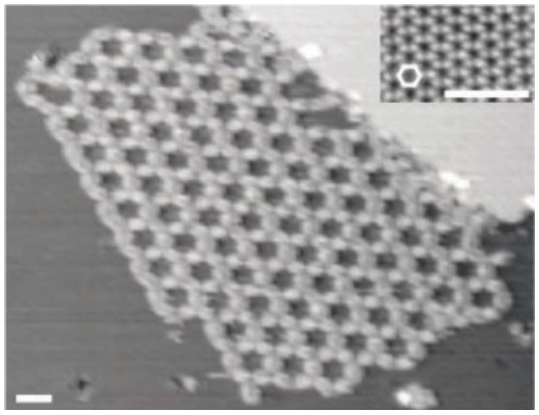

Figure 1.9 Honeycomb motif nanostructures created between melamine and perylene tetra-carboxilic di-imide imaged by STM. Scale bars = 3 nm.[62] Reprinted by permission from Macmillan Publishers Ltd: *Nature*, 2003, **424**, 1029-1031, copyright 2003.

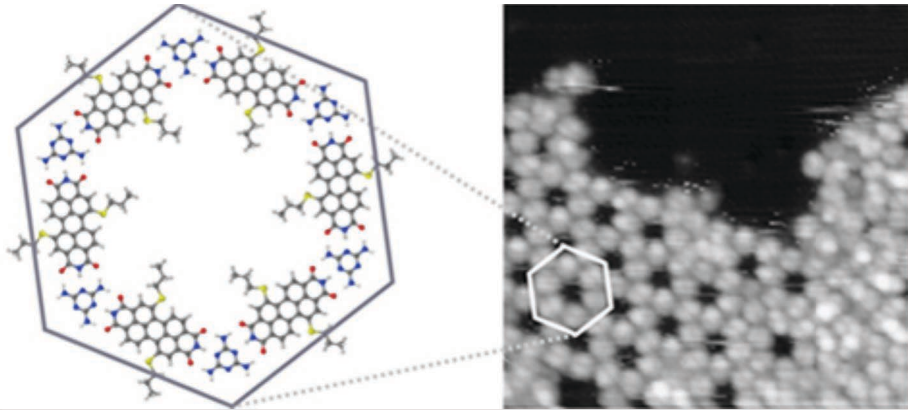

Figure 1.10 Functionalized honeycomb motif nanostructures created between melamine and di(propylthio) perylene tetra-carboxilic di-imide imaged by STM.[64] Reproduced with permission from Wiley, L. M. A. Perdigão, A. Saywell, G. N. Fontes, P. A. Staniec, G. Goretzki, A. G. Phillips, N. R. Champness and P. H. Beton, *Chem. Eur. J.*, 2008, **14**, 7600-7607.

Barth and Kern have produced nanostructure chains of organic material on surfaces. 4-[trans-2-(pyrid-4-yl-vinyl)]benzoic acid (PVBA) molecules consisting of molecular twin chains, stabilized by intermolecular hydrogen bonds have been shown to form nanostructures on a Ag (111) surface[65]. Figure 1.11 shows an STM image of the one-dimensional nanostructure chains with ~1 nm width for the two chains of PVBA. Separation between the nanostructures is in the range of 3-6 nm.

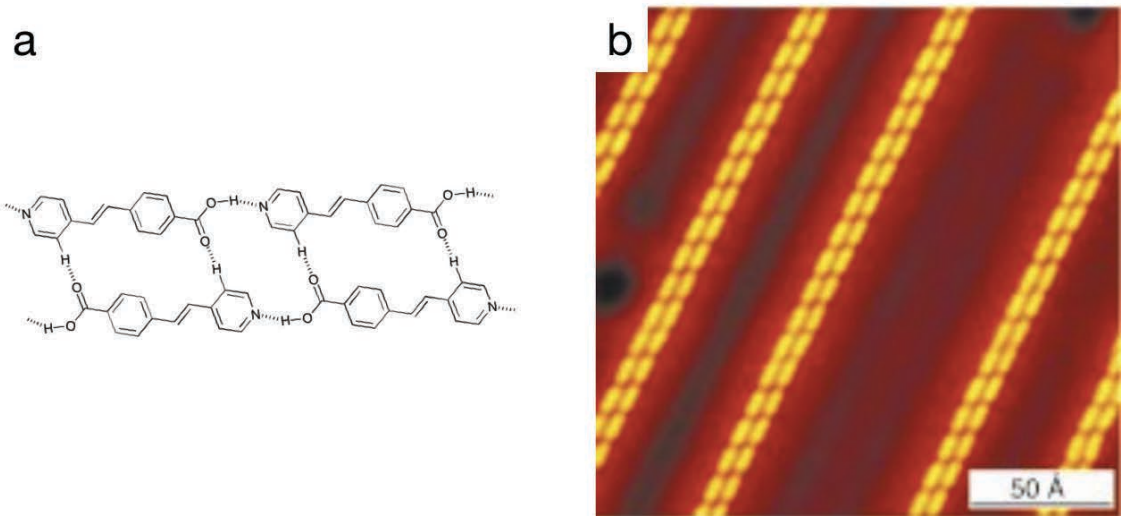

Figure 1.11 Nanostructure twin-chains of PVBA, schematic diagram showing the hydrogen-bonded structure twin-chains of PVBA, **a**, and an STM image of the chains formed on a Ag (111) surface, **b**.[65] Reproduced with permission from Wiley, J. V. Barth, J. Weckesser, C. Cai, P. Günter, L. Bürgi, O. Jeandupeux and K. Kern, *Angew. Chem. Int. Ed.*, 2000, **39**, 1230-1234.

The utilization of hydrogen bonding is undoubtedly a very useful technique for creating nanostructures of molecular organic materials, but structures have been formed by self-assembly using other supramolecular forces. Yokohama has shown the formation of one-dimensional chains of cyanophenyl modified porphyrin molecules.[66] The technique utilizes the asymmetric charge distribution of the cyano group of the phenylcyano substituent to induce dipole-dipole interactions between neighbouring cyanophenyl substituents, forming nanostructured chains of molecules. These nanostructures have feature heights of ~4.4 nm, chain spacing of ~6-12 nm and total lengths of over 100 nm. Figure 1.12 shows the formation of cyanophenyl modified porphyrin molecules (Figure 1.12a) into nanostructures chains on a gold (111) surface (Figure 1.12b), and how each molecule interacts to the next at the 'elbow' position (Figure 1.12c and d) through the cyanophenyl groups. The final formation of long one-dimensional nanostructures can be seen in Figure 1.13.

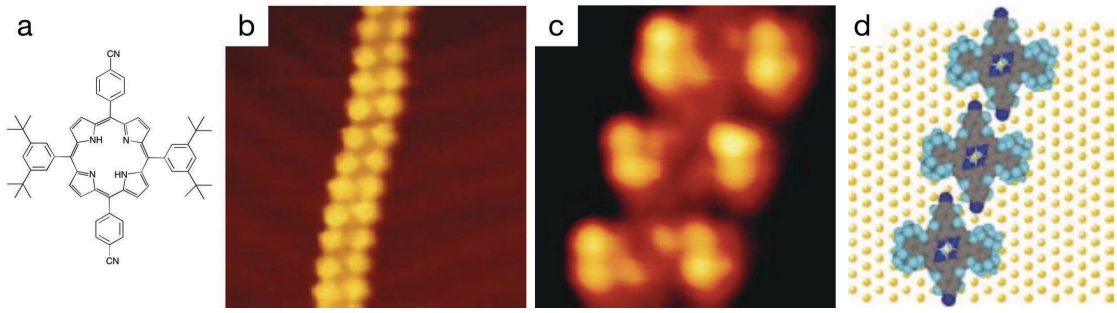

Figure 1.12 Nanostructure chain formation of cyanophenyl modified porphyrin molecules. Molecular diagram, **a**, a 20 x 20 nm STM image of the nanostructure chains, **b**, a close-up 5.3 x 5.3 nm STM image showing alignment of molecules, **c**, and a diagram of molecular alignment, **d**.[66] Reprinted by permission from Macmillan Publishers Ltd: *Nature*, 2001, **413**, 619-621, copyright (2001).

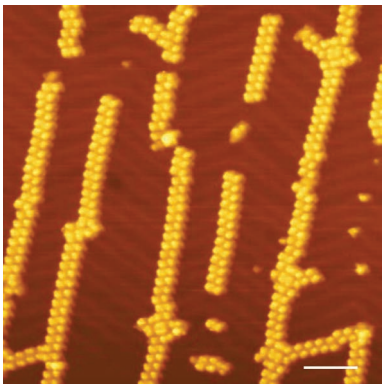

Figure 1.13 STM image (70 x 70 nm) of nanostructure chains of cyanophenyl modified porphyrin molecules formed by cyanophenyl to cyanophenyl dipole-dipole interactions. Scale bar = 10 nm.[66] Reprinted by permission from Macmillan Publishers Ltd: *Nature*, 2001, **413**, 619-621, copyright (2001).

1.4.3 Functional Surfaces for Material Deposition

Whilst the surfaces in the previous examples may provide some role in stabilizing the formed nanostructures, they have also been shown to have a more direct impact on their structure. By influencing the order or growth of nanostructures, surfaces are said to be functional, offering pre-organized sites to program the self-assembly of material. The concept of pre-organized surface binding sites is most well studied in the area of self-assembled monolayers (SAMs).[67] These are highly ordered molecular assemblies formed through adsorption on a substrate by molecules bearing end-groups of a high binding affinity to the substrate.[68] SAMs typically consist of organic material attached to metal single crystal substrates, these systems have been extensively studied for their surface engineering capabilities, most notably alkanethiolates, which when formed on a Au (111) surface produce an ordered array as a result of directed growth.[69]

Ultrathin block co-polymer films have been studied because of their potential to act as pre-programmed substrates for self-assembly.[70] Di-block poly(styrene)-*b*-poly(methyl methacrylate) (PS-*b*-PMMA) can be grown from a surface in a monolayer type growth[71, 72] where controllably sized pores may be used for nanowire formation.[73] The stripe-like layers formed by this approach offer a pre-programmed surface for ordered metal deposition, where gold, silver, indium, tin, lead and bismuth have been shown to selectively bind to the polystyrene layers, forming nanowire structures.[74] Figure 1.14, imaged by transmission electron microscopy (TEM) shows the stripe-like layers formed by the PS-*b*-PMMA ultrathin films (Figure 1.14a) followed by aggregation of gold metal at the polystyrene sites through vapour deposition (Figure 1.14b).

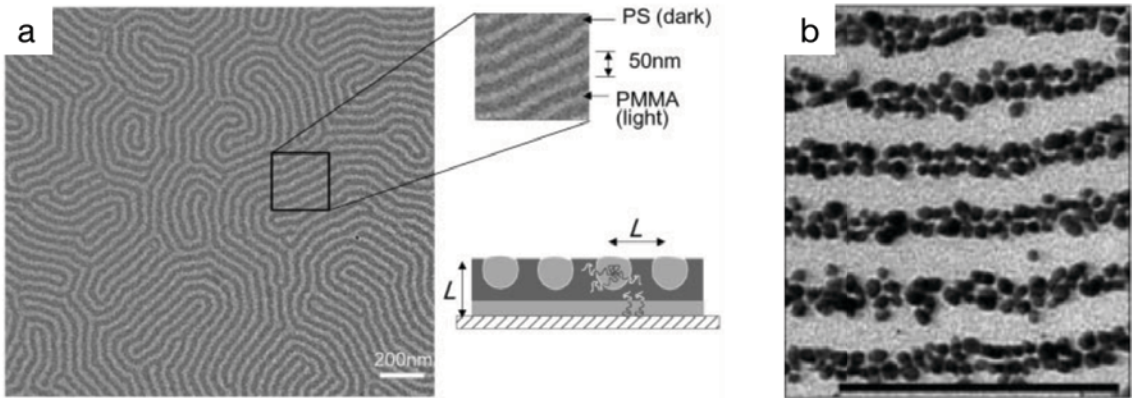

Figure 1.14 TEM images of PS-*b*-PMMA thin film surfaces before, **a**, and after gold vapour deposition, **b**. Scale bars on both images = 200 nm.[74] Reprinted by permission from Macmillan Publishers Ltd: *Nature*, 2001, **414**, 735-738, copyright (2001).

Copper nanostructures have been shown to grow on palladium (110) surfaces through diffusion controlled aggregation,[75] one-dimensional copper aggregates form due to directional anisotropy, where preferential growth in the [1-10] direction occurs because of lower migration barrier energy in that direction. The feature size here is potentially as small as one copper atom across (~2.5 Å), with spacing shown by STM to be about 3 nm between chains. Figure 1.15 shows the pre-organized palladium (110) surface, where the face-centered cubic structure exhibits alternating layers of protruding and recessed atoms (Figure 1.15a) and STM showing the preferential growth of copper nanostructures in the [1-10] direction (Figure 1.15b).

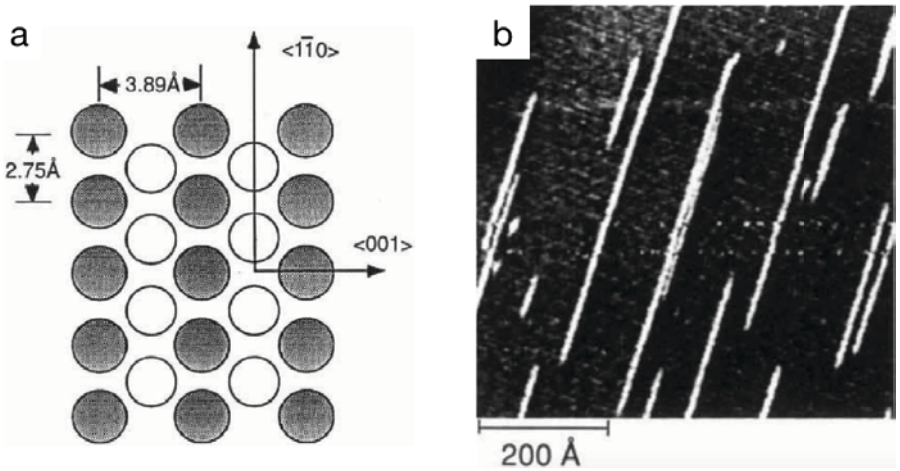

Figure 1.15 Schematic representation of pre-organized palladium (110) surface, **a**, and STM image of copper nanostructures, **b**.[75] Reprinted by permission from Macmillan Publishers Ltd: *Nature*, 1993, **366**, 141-143, copyright (1993).

1.5 A Crystal Engineering Approach to Tuneable Functional Surfaces

Another potential bottom-up route to the organization of material at the low nm scale on a surface is outlined here. This route involves using molecular single crystal surfaces as 'pre-programmed' functional substrates on which metal binding may occur, displaying the programmed spatial information through guided assembly, in a process where one level of self-assembly guides the next. Surface-bound material can then be reduced to form aggregates with spatial resolution that may exceed that of current top-down lithographical techniques (Figure 1.16). The self-assembly nature of the substrate formation (crystallization) and of the material deposition stages, suggest this could be a low-cost route to nanostructure formation on this scale.

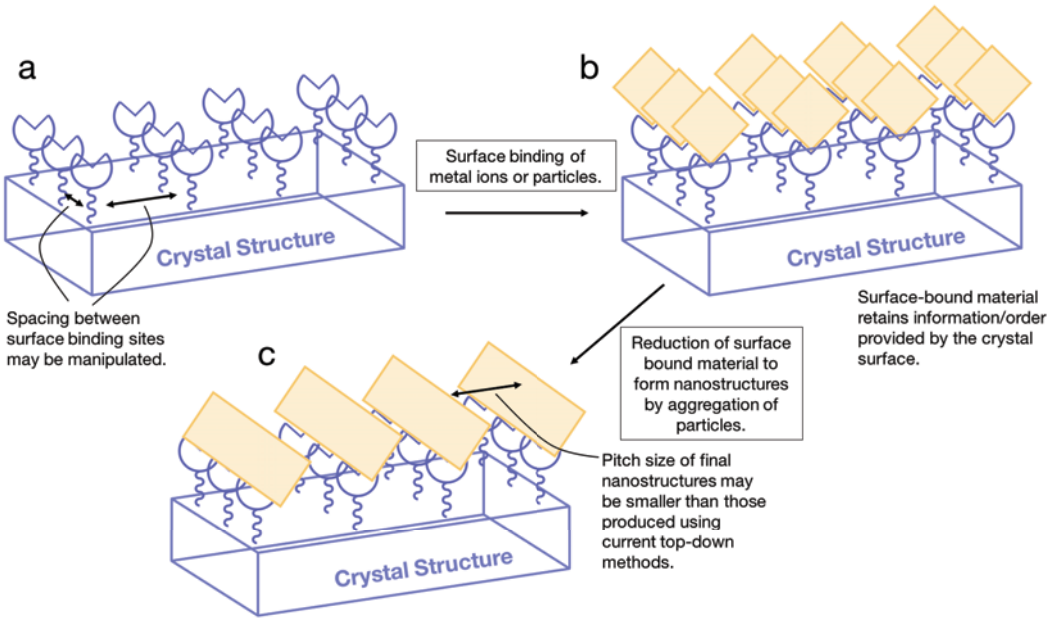

Figure 1.16 Schematic representation of pre-organized crystal surface, **a**, spatially controlled metal particle deposition, **b**, and reduction to metal nanostructures, **c**.

The inherent order and repeating pattern of molecules in crystals is carried through to their surfaces giving the potential for material to bind to these surfaces with the same degree of order. Figure 1.17 shows the crystal structure of anti-D-arabinose-oxime[76] within a predicted BFDH (Bravias, Friedel, Donnay and Harker) morphology where the same OH groups are presented across the (001) surface in an ordered array. The spacing between these (001) surface oxygen atoms is 5.16 Å in the b-axis and 4.90 Å in the a-axis.

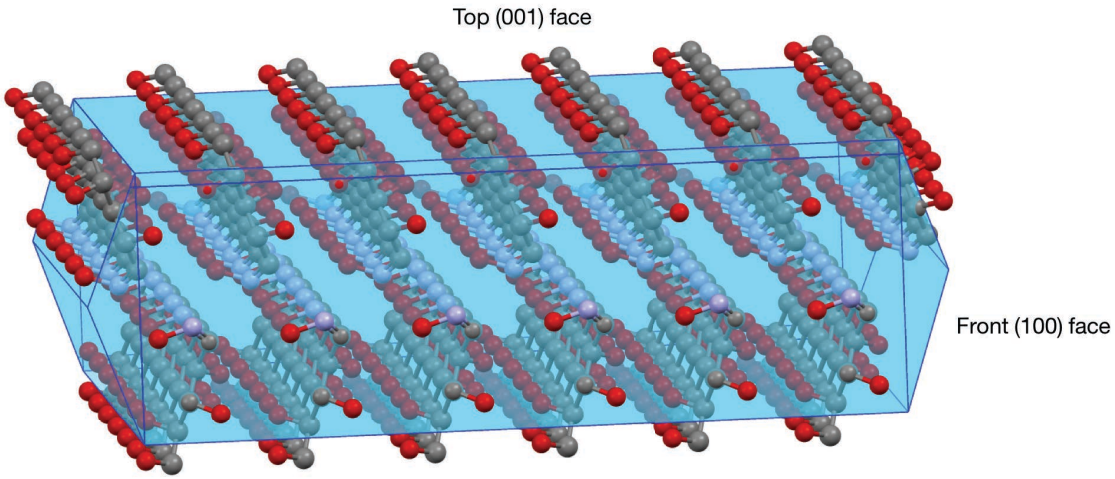

Figure 1.17 Crystal structure and BFDH morphology for anti-D-Arabinose-oxime,[76] hydrogen atoms removed for clarity.

Crystals of organic compounds typically possess intermolecular spacing in the angstrom to twenty-nanometre range, meaning any surface nanostructures formed on this scale could exceed current lithographic resolutions (~20 nm). Atomic force microscopy (AFM) of molecular crystal faces has shown these resolutions with molecular contrast being achieved.[77] Figure 1.18 shows an example where the unit cell dimensions of a crystal structure (Figure 1.18a) can be related to the surface topology of specific crystal faces obtained by AFM (Figure 1.18b), the (010) plane and surface of glycine. Further examples include Ward's studies on nucleation and growth of (tetrathiafulvalene)$Br_{0.76}$ crystals[78] and studies by Ichikawa of NaCl[79] and KBr[80] crystal surfaces.

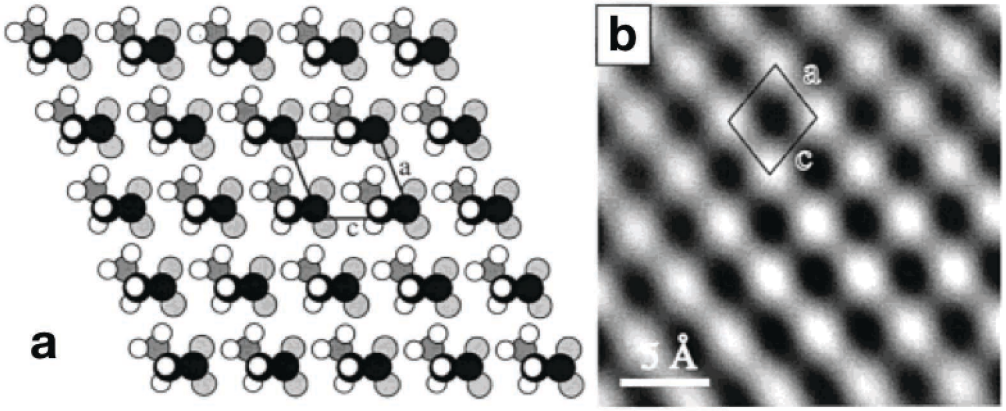

Figure 1.18 a, model of the (010) plane of glycine, **b**, AFM image of the (010) indexed face of a glycine crystal.[77] Reprinted (adapted) with permission from *Chem. Rev.*, 2001, **101**, 1697-1726. Copyright 2001 American Chemical Society.

Attempts to bind metals to molecular crystals surfaces have been made previously, with studies by Sada showing crystal face selectivity with respect to gold nanoparticle binding to L-cystine[81] and crystallized palladium complexes binding to charge-transfer complexes of naphthalene diimide and pyrene.[82] Studies to show the transfer of information (ordered arrangement) from crystal surfaces to bound material have also been performed. Barrientos binds gold nanoparticles on crystal surfaces of a cyclodextrin inclusion complex,[83] claiming the ordered arrangement of bound nanoparticles (Figure 1.19), however the evidence seems weak, with microscopy of surfaces open to interpretation. Studies by Ichikawa however, do show binding in an ordered array, where macrotricyclic ammonium cage hosts act as chloride receptors, binding to NaCl crystal surfaces.[84]

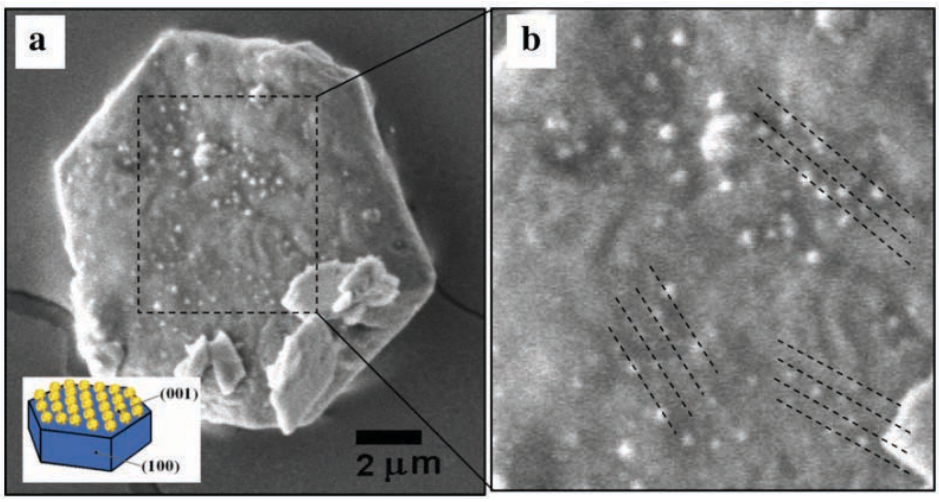

Figure 1.19 SEM image of selective deposition of metal nanoparticles onto (001) crystal plane of α-CD/$C_8H_{17}NH_2$ (a). Magnification of the previous image showing the arrangements of metal nanoparticles (b). Reprinted from Inorganica Chimica Acta, Vol 380, L. Barrientos, P. Allende, C. Orellana and P. Jara. Ordered arrangements of metal nanoparticles on alpha-cyclodextrin inclusion complexes by magnetron sputtering, 372-377, Copyright (2012), with permission from Elsevier.

Another reason for using molecular crystals as binding substrates is the ability to spatially manipulate any surface bound material by simply using different crystal structures, therefore making programmable functional substrates. As the molecule or arrangement of molecules in a crystal varies, so does the arrangement of possible binding sites present at their surfaces, giving a potentially limitless range of possible surface architectures. The Cambridge Structural Database (CSD)[85] provides a huge number of already determined crystal structures, containing over 750,000 deposited known crystal structures with over 40,000 new structures added each year (as of 16th February 2015). These structures may be used to assess the potential surface binding site spacing, and in some cases surfaces can be identified where face-indexing analysis has already been performed on the crystal.

The number of crystal structures is potentially limitless, but the use of crystal engineering offers a route to both predict and create structures with the desired surface features. The growth of molecular crystals is inherently a bottom-up, building block process, creating self-assembled structures with possible dimensions on the nanometre scale and above. However, this process typically involves the use of many different intermolecular interactions

simultaneously, which can compete or complement each other, making this process, and their final packing structures very difficult to predict.[86] Despite this, the self-assembly nature of crystal growth has been harnessed to some extent. Crystal engineering utilizes strong, highly directional intermolecular forces such as hydrogen bonding, as well as metal atom centres with predicable geometries to design and create framework style crystal structures.[87-89] These frameworks can be designed with controllable pore sizes with uses in gas capture and storage.[90, 91]

When crystal structures aren't so predictable, polymorph structures may be found by employing screening methods.[92] These are structures of the same compound but found in different molecular and packing conformations, leading to a different crystal structure, with sometimes-different physical properties such as bioactive uptake of pharmaceutical drugs.[93] A range of structures may be created using screening methods, where crystal growth conditions and solvent are varied.

The crystal habit is the morphology of a crystal with respect to its exterior faces. The molecular packing arrangement within a crystal structure may also be used to help predict this crystal habit, where the area of a crystal face depends inversely on the surface energy, low-energy functional groups, having little intermolecular interaction tend to form larger crystal faces, as they are more stable as termination sites. A BFDH (Bravias,[94] Friedel,[95] Donnay and Harker[96]) morphology may also be used in an attempt to predict the habit, this is calculated using an algorithm based on unit cell and symmetry operations of crystal structure. However, these techniques are not infallible, so the choice to use centrosymmetric molecules for the crystal substrate may provide a higher chance for binding sites to be presented at surfaces. Figure 1.20 shows how molecules not containing an inversion centre, may align more often with the binding sites (nitrogen in this case) facing away from the crystal surface (Figure 1.20a), but molecules containing an inversion centre and dual binding sites, show a higher chance to align binding sites at the crystal surface (Figure 1.20b). These dual binding site molecules can be made to contain a variety of different spacer-units, which separate the binding sites within a molecule (Figure 1.20c). This capability allows for the potential engineering, or tuning of

crystal structures to give a range of surface templates with controllable spatial arrangement of binding sites, and therefore a controllable range of nanoarchitectures after material binding. This tuneability of spacing within a crystal structure is something that has been pursued by Sada et al., where crystal structures show tunable interlayer distances of 1-naphthylmethylammonium n-alkanoates.[97]

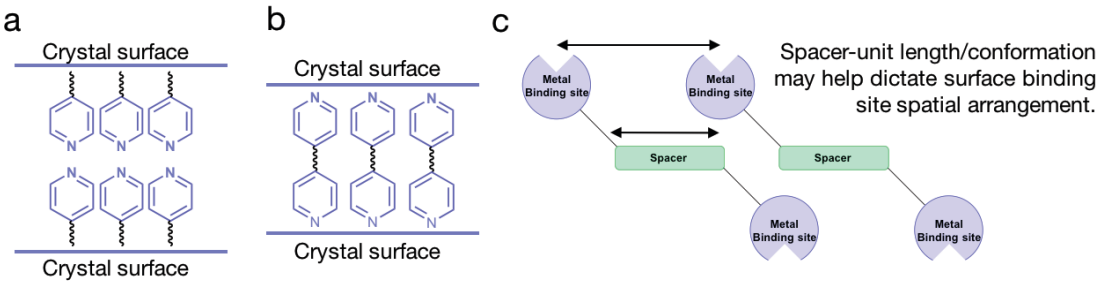

Figure 1.20 Schematic representation of binding sites potentially facing away from the crystal surface, **a**, towards the crystal surface, **b**, and variation in binding site spacing by placing spacer-units within the molecule, **c**.

1.6 Conclusions

In the pursuit of continued miniaturization of electronic devices, the reduction in pitch size is a major objective. Bottom-up approaches to this reduction in pitch size are now seen to be the preferred routes, this is due to their potential to form nanostructures with size and spacing which may exceed current resolutions whilst maintaining a low production cost.

We have identified a new bottom-up approach to creating potentially conductive nanostructures with possibility for spatial control. This approach is based on the inherent order of molecular crystal structures, offering ordered surface binding sites with potentially controllable spacing that may exceed the resolution of current top-down methods employed in industry. The self-assembly nature of crystal growth and low cost of materials potentially affords this technique very low production costs when compared to that of current, and future top-down approaches.

1.7 Aims

Our aims in this project are to see if molecular crystals of organic compounds can be used as directed metal binding substrates with the potential to be pre-

programmed. This will be done by firstly crystallizing a range of dual binding site molecules with varying spacer units separating the binding sites, and looking at the potential to manipulate these existing structures to further expand the range of suitable binding substrates using a crystal engineering approach. Metal binding models using these molecules will then be studied using X-ray crystallography looking at their ability and disposition to bind metals. Specific crystal faces of molecular crystals will then be characterized by AFM and XPS giving information on their suitability for metal binding. Finally, surface characterization of these substrates will be performed after metal binding has taken place, indicating whether or not ordered nanostructures have formed.

1.8 References

1. G. Cao, *Nanostructures and Nanomaterials - Synthesis, Properties and Applications*, Imperial College Press, 2004.
2. Q. Wang and D. O'Hare, *Chem. Rev.*, 2012, **112**, 4124-4155.
3. C. N. R. Rao, A. K. Sood, K. S. Subrahmanyam and A. Govindaraj, *Angew. Chem. Int. Ed.*, 2009, **48**, 7752-7777.
4. O. Ambacher, J. Majewski, C. Miskys, A. Link, M. Hermann, M. Eickhoff, M. Stutzmann, F. Bernardini, V. Fiorentini, V. Tilak, B. Schaff and L. F. Eastman, *J. Phys.: Condens. Matter*, 2002, **14**, 3399.
5. J. P. Lu, *Phys. Rev. Lett.*, 1997, **79**, 1297-1300.
6. X. Li, X. Wang, L. Zhang, S. Lee and H. Dai, *Science*, 2008, **319**, 1229-1232.
7. Y. Xia, P. Yang, Y. Sun, Y. Wu, B. Mayers, B. Gates, Y. Yin, F. Kim and H. Yan, *Adv. Mater.*, 2003, **15**, 353-389.
8. C. M. Lieber, *Solid State Commun.*, 1998, **107**, 607-616.
9. D. Astruc, F. Lu and J. R. Aranzaes, *Angew. Chem. Int. Ed.*, 2005, **44**, 7852-7872.
10. M. V. Wolkin, J. Jorne, P. M. Fauchet, G. Allan and C. Delerue, *Phys. Rev. Lett.*, 1999, **82**, 197-200.
11. G. M. Whitesides, J. P. Mathias and C. T. Seto, *Science*, 1991, **254**, 1312-1319.
12. G. M. Whitesides, *Small*, 2005, **1**, 172-179.
13. G. A. Ozin, *Adv. Mater.*, 1992, **4**, 612-649.
14. W. Lu and C. M. Lieber, *Nat. Mater.*, 2007, **6**, 841-850.
15. P. S. Peercy, *Nature*, 2000, **406**, 1023-1026.
16. R. R. Schaller, *Spectrum, IEEE*, 1997, **34**, 52-59.
17. G. E. Moore, *Proc. IEEE*, 1998, **86**, 82-85.
18. G. Schindler, G. Steinlesberger, M. Engelhardt and W. Steinhogl, *Solid-State Electron.*, 2003, **47**, 1233-1236.

19. ITRS Roadmap, http://www.itrs.net/).
20. R. W. Keyes, *Proc. IEEE*, 2001, **89**, 227-239.
21. R. P. Feynman, *Eng. Sci.*, 1960, 22-36.
22. Y. Cui and C. M. Lieber, *Science*, 2001, **291**, 851-853.
23. C. M. Lieber, *MRS Bull.*, 2003, **28**, 486-491.
24. G. M. Wallraff and W. D. Hinsberg, *Chem. Rev.*, 1999, **99**, 1801-1822.
25. B. Fay, *Microelectron. Eng.*, 2002, **61–62**, 11-24.
26. B. J. Lin, *J. Vac. Sci. Technol.*, 1975, **12**, 1317-1320.
27. J. Roberts, T. Bacuita, R. L. Bristol, H. Cao, M. Chandhok, S. H. Lee, M. Leeson, T. Liang, E. Panning, B. J. Rice, U. Shah, M. Shell, W. Yueh and G. Zhang, *Microelectron. Eng.*, 2006, **83**, 672-675.
28. I. S. Henry, *Phys. Scr.*, 1996, **1996**, 26.
29. K. Vutova and G. Mladenov, *Microelectron. Eng.*, 2001, **57–58**, 349-353.
30. S. D. Berger and J. M. Gibson, *Appl. Phys. Lett.*, 1990, **57**, 153-155.
31. J. Melngailis, A. A. Mondelli, I. L. Berry and R. Mohondro, *J. Vac. Sci. Technol., B*, 1998, **16**, 927-957.
32. Y. Xia, J. A. Rogers, K. E. Paul and G. M. Whitesides, *Chem. Rev.*, 1999, **99**, 1823-1848.
33. D. M. Eigler and E. K. Schweizer, *Nature*, 1990, **344**, 524-526.
34. IBM Research - A Boy And His Atom:The World's Smallest Movie, http://www.research.ibm.com/articles/madewithatoms).
35. S. Loth, S. Baumann, C. P. Lutz, D. M. Eigler and A. J. Heinrich, *Science*, 2012, **335**, 196-199.
36. R. D. Piner, J. Zhu, F. Xu, S. Hong and C. A. Mirkin, *Science*, 1999, **283**, 661-663.
37. K.-B. Lee, S.-J. Park, C. A. Mirkin, J. C. Smith and M. Mrksich, *Science*, 2002, **295**, 1702-1705.
38. L. M. Demers, D. S. Ginger, S.-J. Park, Z. Li, S.-W. Chung and C. A. Mirkin, *Science*, 2002, **296**, 1836-1838.
39. S. Y. Chou, P. R. Krauss and P. J. Renstrom, *J. Vac. Sci. Technol., B*, 1996, **14**, 4129-4133.
40. G. M. Whitesides and B. Grzybowski, *Science*, 2002, **295**, 2418-2421.
41. J. W. Steed and J. L. Atwood, *Supramolecular Chemistry*, John Wiley & Sons, Ltd., 2009.
42. D. Philp and J. F. Stoddart, *Angew. Chem. Int. Ed.*, 1996, **35**, 1154-1196.
43. J. D. Watson and F. H. C. Crick, *Nature*, 1953, **171**, 737-738.
44. R. Franklin and R. G. Gosling, *Nature*, 1953, **171**, 740-741.
45. R. Franklin and R. G. Gosling, *Nature*, 1953, **172**, 156-157.
46. M. H. F. Wilkins, A. R. Stokes and H. R. Wilson, *Nature*, 1953, **171**, 738-740.
47. S. A. Nepogodiev and J. F. Stoddart, *Chem. Rev.*, 1998, **98**, 1959-1976.
48. P. R. Ashton, S. Iqbal, J. F. Stoddart and N. D. Tinker, *Chem. Commun.*, 1996, 479-481.
49. V. Balzani, A. Credi, F. M. Raymo and J. F. Stoddart, *Angew. Chem. Int. Ed.*, 2000, **39**, 3348-3391.
50. E. R. Kay, D. A. Leigh and F. Zerbetto, *Angew. Chem. Int. Ed.*, 2007, **46**, 72-191.
51. P. W. K. Rothemund, *Nature*, 2006, **440**, 297-302.
52. N. C. Seeman, *Nature*, 2003, **421**, 427-431.

53. S. H. Park, C. Pistol, S. J. Ahn, J. H. Reif, A. R. Lebeck, C. Dwyer and T. H. LaBean, *Angew. Chem. Int. Ed.*, 2006, **45**, 735-739.
54. J. Wang, G. Rivas, X. Cai, E. Palecek, P. Nielsen, H. Shiraishi, N. Dontha, D. Luo, C. Parrado, M. Chicharro, P. A. M. Farias, F. S. Valera, D. H. Grant, M. Ozsoz and M. N. Flair, *Anal. Chim. Acta*, 1997, **347**, 1-8.
55. C. F. Monson and A. T. Woolley, *Nano Lett.*, 2003, **3**, 359-363.
56. K. Keren, R. S. Berman, E. Buchstab, U. Sivan and E. Braun, *Science*, 2003, **302**, 1380-1382.
57. L. Dong, T. Hollis, S. Fishwick, B. A. Connolly, N. G. Wright, B. R. Horrocks and A. Houlton, *Chem. Eur. J.*, 2007, **13**, 822-828.
58. J. Liu, Y. Geng, E. Pound, S. Gyawali, J. R. Ashton, J. Hickey, A. T. Woolley and J. N. Harb, *ACS Nano*, 2011, **5**, 2240-2247.
59. L. Vaisman, H. D. Wagner and G. Marom, *Adv. Colloid Interface Sci.*, 2006, **128–130**, 37-46.
60. G. R. Dieckmann, A. B. Dalton, P. A. Johnson, J. Razal, J. Chen, G. M. Giordano, E. Muñoz, I. H. Musselman, R. H. Baughman and R. K. Draper, *J. Am. Chem. Soc.*, 2003, **125**, 1770-1777.
61. D. L. Keeling, N. S. Oxtoby, C. Wilson, M. J. Humphry, N. R. Champness and P. H. Beton, *Nano Lett.*, 2003, **3**, 9-12.
62. J. A. Theobald, N. S. Oxtoby, M. A. Phillips, N. R. Champness and P. H. Beton, *Nature*, 2003, **424**, 1029-1031.
63. L. M. A. Perdigao, N. R. Champness and P. H. Beton, *Chem. Commun.*, 2006, 538-540.
64. L. M. A. Perdigão, A. Saywell, G. N. Fontes, P. A. Staniec, G. Goretzki, A. G. Phillips, N. R. Champness and P. H. Beton, *Chem. Eur. J.*, 2008, **14**, 7600-7607.
65. J. V. Barth, J. Weckesser, C. Cai, P. Günter, L. Bürgi, O. Jeandupeux and K. Kern, *Angew. Chem. Int. Ed.*, 2000, **39**, 1230-1234.
66. T. Yokoyama, S. Yokoyama, T. Kamikado, Y. Okuno and S. Mashiko, *Nature*, 2001, **413**, 619-621.
67. J. C. Love, L. A. Estroff, J. K. Kriebel, R. G. Nuzzo and G. M. Whitesides, *Chem. Rev.*, 2005, **105**, 1103-1170.
68. A. Ulman, *Chem. Rev.*, 1996, **96**, 1533-1554.
69. C. A. Alves, E. L. Smith and M. D. Porter, *J. Am. Chem. Soc.*, 1992, **114**, 1222-1227.
70. M. J. Fasolka and A. M. Mayes, *Anuu. Rev. Mater. Res.*, 2001, **31**, 323-355.
71. J. Bang, U. Jeong, D. Y. Ryu, T. P. Russell and C. J. Hawker, *Adv. Mater.*, 2009, **21**, 4769-4792.
72. C. Tang, E. M. Lennon, G. H. Fredrickson, E. J. Kramer and C. J. Hawker, *Science*, 2008, **322**, 429-432.
73. T. Thurn-Albrecht, J. Schotter, G. A. Kästle, N. Emley, T. Shibauchi, L. Krusin-Elbaum, K. Guarini, C. T. Black, M. T. Tuominen and T. P. Russell, *Science*, 2000, **290**, 2126-2129.
74. W. A. Lopes and H. M. Jaeger, *Nature*, 2001, **414**, 735-738.
75. H. Roder, E. Hahn, H. Brune, J.-P. Bucher and K. Kern, *Nature*, 1993, **366**, 141-143.
76. A. Mostad, *Acta Chem. Scand.*, 1978, **32b**, 733-742.
77. M. D. Ward, *Chem. Rev.*, 2001, **101**, 1697-1726.
78. A. C. Hillier and M. D. Ward, *Science*, 1994, **263**, 1261-1264.

79. I. Kazuhiko and Y. Masanori, *J. Phys.: Condens. Matter*, 1996, **8**, 4889.
80. I. Kazuhiko, S. Sato and N. Shimomura, *Pure Appl. Chem.*, 2004, **76**, 115-122.
81. Y. Fujiki, N. Tokunaga, S. Shinkai and K. Sada, *Angew. Chem. Int. Ed.*, 2006, **45**, 4764-4767.
82. Y. Fujiki, S. Shinkai and K. Sada, *Cryst. Growth Des.*, 2009, **9**, 2751-2755.
83. L. Barrientos, P. Allende, C. Orellana and P. Jara, *Inorg. Chim. Acta*, 2012, **380**, 372-377.
84. K. Ichikawa, M. Yamada and N. Ito, *Chem. Eur. J.*, 1998, **4**, 914-918.
85. Cambridge Structural Database, http://www.ccdc.cam.ac.uk/).
86. A. Gavezzotti, *Acc. Chem. Res.*, 1994, **27**, 309-314.
87. G. R. Desiraju, *Crystal engineering: the design of organic solids*, Elsevier, 1989.
88. G. R. Desiraju, *Angew. Chem. Int. Ed.*, 1995, **34**, 2311-2327.
89. D. Braga, F. Grepioni and G. R. Desiraju, *Chem. Rev.*, 1998, **98**, 1375-1406.
90. K. Sumida, D. L. Rogow, J. A. Mason, T. M. McDonald, E. D. Bloch, Z. R. Herm, T.-H. Bae and J. R. Long, *Chem. Rev.*, 2012, **112**, 724-781.
91. N. L. Rosi, J. Eckert, M. Eddaoudi, D. T. Vodak, J. Kim, M. O'Keeffe and O. M. Yaghi, *Science*, 2003, **300**, 1127-1129.
92. C.-H. Gu, V. Young and D. J. W. Grant, *J. Pharm. Sci.*, 2001, **90**, 1878-1890.
93. P. Vishweshwar, J. A. McMahon, J. A. Bis and M. J. Zaworotko, *J. Pharm. Sci.*, 2006, **95**, 499-516.
94. A. Bravais, *Etudes Cristallographiques* Gauthier-Villars, 1866.
95. G. Friedel, *Bull. Soc. Franc. Mineral.*, 1907, **30**, 326.
96. J. D. H. Donnay and D. Harker, *Am. Mineral.*, 1937, **22**, 446.
97. K. Sada, K. Inoue, T. Tanaka, A. Tanaka, A. Epergyes, S. Nagahama, A. Matsumoto and M. Miyata, *J. Am. Chem. Soc.*, 2004, **126**, 1764-1771.

Chapter 2

Design, Synthesis and Characterization of Dual Binding Site Molecules with Varying Spacer Units

Table of Contents

2.1 Introduction

After reviewing the possible routes to continued miniaturization of electronic devices and integrated circuits (chapter 1), we became interested in the concept of using an ordered array of organic molecules as a template for material deposition in a "bottom-up" approach. Previous research has shown the order of molecules in a crystal structure is translated to the crystal surface and may be imaged by atomic force microscopy (AFM) so long as the crystal morphology exhibits defined faces.[1]

Testing our hypothesis firstly requires us to select the molecules, and therefore crystals to be used as templates for material binding. The molecular arrangement in a crystal structure can be very unpredictable,[2] so it is sensible to begin with a known crystal structure or a family of structures expected to be similar, using the Cambridge Structural Database (CSD) as a reference. The CSD contains a huge library of deposited crystal structures obtained by experiment with over 750,000 known crystal structures and more than 40,000 new structures added each year (as of 16th February 2015).[3]

Crystal structure can be determined by single crystal X-ray diffraction.[4, 5] This analytical technique is used to determine the structure of molecular and non-molecular materials. The technique, developed in 1913 by William H. Bragg[6] and William L. Bragg,[7] utilizes the diffraction of X-rays by the similarly sized atoms in a crystal sample to reveal atomic positions relative to one another. The data obtained is transformed into positions of electron density and then interpreted using chemical sense to give geometrical information about the molecule(s) under investigation, such as bond lengths, bond angles, dihedral (torsion) angles and non-bonded distances (intermolecular).

The technique is primarily used as a means of characterizing the intramolecular structure of single molecules, however, due to the nature of the technique, looking at a sample of multiple molecules in a repeating pattern, information regarding the intermolecular structure of the material is also obtained. The packing arrangement of molecules in a crystal is governed by the intermolecular forces present during crystallization, this includes directional forces such as π-π stacking or hydrogen-bonding, as well as the weaker

attractive Van der Waals forces and short-range electron-cloud repulsions (close crystal packing).[8]

Both the intramolecular and intermolecular structures of a crystal are important to the pharmaceutical industry, as polymorphs of a compound can alter its bioavailability[9] and be liable to independent patent protection due to the slight differences in the synthesis or structure from the original.[10]

The extended structures of crystalline materials are also of interest in making advanced materials for use in high pressure environments such as deep underwater telecommunication lines or for shock absorbing materials such as body armour.[11] These materials can exhibit mechanical anisotropy when put under high pressures of isotropic compression, and occasionally show negative linear compressibility (the expansion along a specific direction when under these conditions). These materials make use of the framework style extended structure present in certain crystals, such as the $[NH_4][Zn(HCOO)_3]$ structure, which expands in the c-axis when under isotropic compression (Figure 2.1). The porous structure of these framework style materials mean they can also be used for environmental benefits such as CO_2 capture,[12] or in fuel cells for hydrogen storage[13] and methane storage.[14]

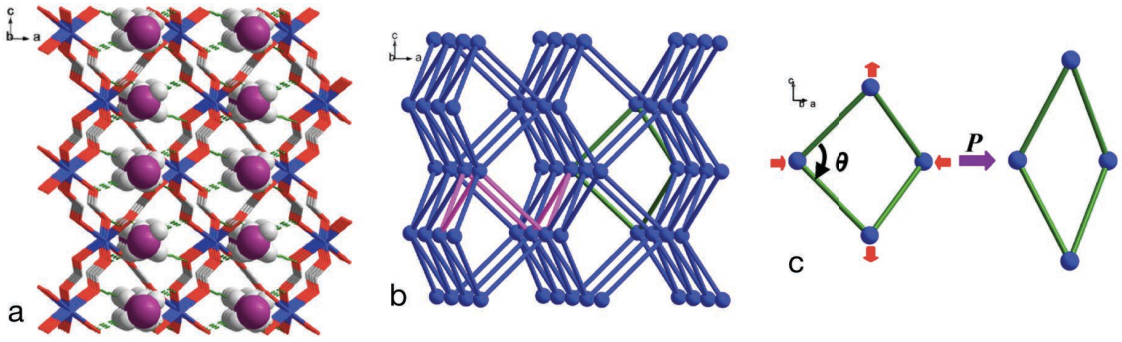

Figure 2.1[11] **a**, crystal structure and **b**, schematic representation of $[NH_4][Zn(HCOO)_3]$ framework structure. **c**, compression behaviour in response to an increase in pressure. Reprinted (adapted) with permission from *J. Am. Chem. Soc.*, 2012, **134**, 11940-11943. Copyright 2012 American Chemical Society.

The intermolecular packing of molecules in our crystals will also play an important role as it may influence the binding site positions in the extended structure. Our system aims to utilize this characteristic in the hope that it is possible to tune the surface binding site spacing by subtly changing the crystal structure beneath.

2.2 Results and Discussion

2.2.1 Dual Binding Site Molecules with Varying Spacer Units

Previously determined crystal structures provide us with a solid starting point in choosing molecules that may crystallize in a certain way. If a family of molecules crystallize in an expected manner, fine-tuning the desired crystal properties (binding site spacing at surface) becomes more achievable.

A search through the Cambridge Structural Database (CSD) was conducted in order to find suitable crystal structures to use as guides for our system of directed metal binding at crystal surfaces. Two structures were chosen because of their dual binding sites and the presence of an easily variable linker unit. These qualities are important as a centrosymmetric molecule (containing an inversion centre) may give a higher chance of the binding sites being present at the crystal surface (Figure 2.2), as well as having the opportunity to compounds with different spacer units.

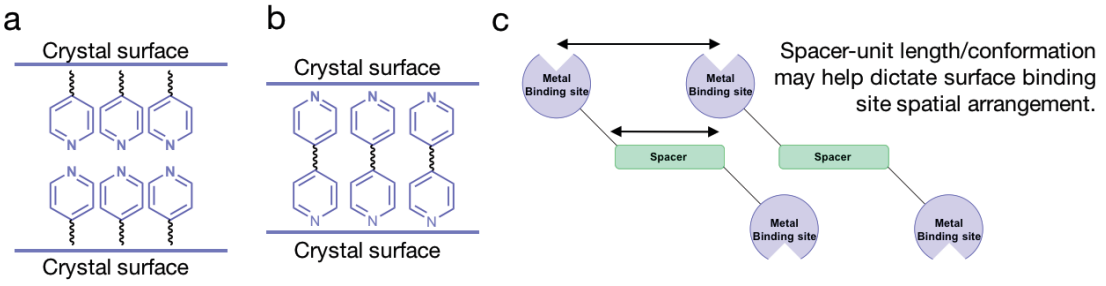

Figure 2.2 Schematic representation of binding sites potentially facing away from the crystal surface, **a**, towards the crystal surface, **b**, and variation in binding site spacing by placing spacer-units within the molecule, **c**.

These types of molecules also offer the potential to bind metal atoms at a crystal surface through the pyridine nitrogen atoms. The chosen molecules are an ethylene-linked pyridine-pyrazole compound[15] (Figure 2.3a) and a phenylene linked pyridine-imine compound[16] (Fig 2.3b). Both structures contain bridge linkers between potential metal binding groups, ethylene in Figure 2.3a and phenylene in Figure 2.3b. In our system numerous linking (or spacing) groups would replace these bridge linkers in an attempt to subtly change the crystal structure, increasing or decreasing the binding site spacing. Even subtle differences in molecule length may lead to very different crystal structures. This is because of a change in the packing arrangement of the molecules and may

create very different surface patterns of binding sites, increasing or decreasing the spacing in any direction. This means the resulting structures may be unpredictable, but a library of structures with varying surface patterns will be created.

The pyrazole functionality is not well known for metal binding when attached to a pyridyl group, only a few examples of metal binding at this point and no examples of the same metal atom binding to both sites exist in the CSD. The presence of both pyridyl and imine groups in the phenylene-linked pyridine-imine molecule (Figure 2.3b) does provide the molecule with two potential binding sites (lone pairs on two nitrogen atoms) of which there are many examples in the CSD. Also, because of extra atoms it is also longer than the pyridine-imine metal binding group (Figure 2.3b), where the intramolecular pyridyl(N)···(N)pyridyl distances are 14.77 Å for the ethylene-linked pyridine-pyrazole compound, and 14.16 Å. However, the imine bond in this molecule may produce more rigid structures because of electron delocalization through the pyridyl ring and imine group, potentially keeping the entire molecule in the same plane, maximizing the molecule's length, and possibly the distance between the pyridyl binding sites.

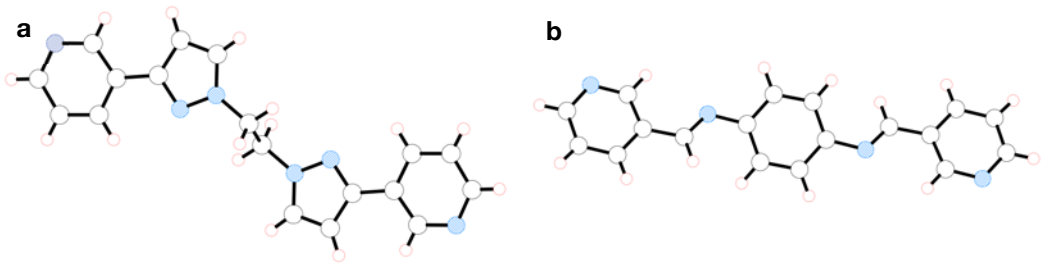

Figure 2.3 Crystal structures of ethylene-linked pyridine-pyrazole,[15] **a**, and phenylene-linked pyridine-imine,[16] **b**, taken from the Cambridge Structural Database.

2.2.2 Bis(3-(pyridin-3-yl)-1*H*-pyrazol-1-yl) Binding Site Molecules

A range of dual binding site pyridine-pyrazole molecules with various spacer units were prepared by firstly synthesizing the metal binding pyridine-pyrazole groups, 3-(1H-pyrazol-3-yl)pyridine (**2**)[17] (scheme 2.1) through conversion of the acetyl group to a pyrazole group via a 3-dimethylamino-prop-2-ene-1-one intermediate (**1**).

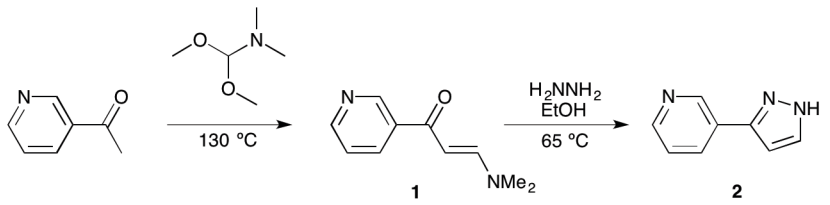

Scheme 2.1 Formation of 3-(3-pyridyl)pyrazole binding site molecule (**2**) via intermediate **1**.

Alkylation of **2** at the pyrazole ring with the appropriate dibrominated spacer unit (X) produces the linked compounds to be investigated[15] (scheme 2.2).

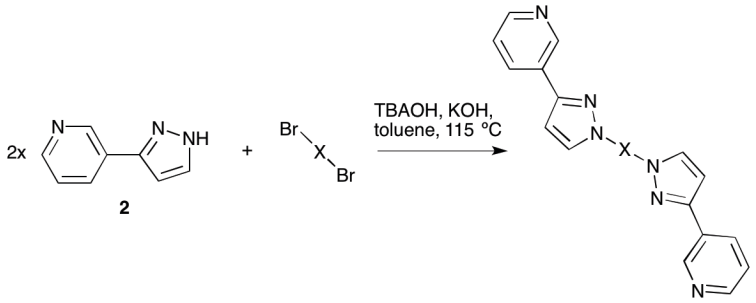

Scheme 2.2 Formation of linked pyridine-pyrazole compounds (**3**-**7**) by reacting two equivalents of **2** with the appropriate dibromonated spacer unit. TBAOH = tetrabutylammonium hydroxide.

The pyridine-pyrazole molecules chosen to be studied (Figure 2.4, **3**-**7**) consist of spacer units of a butylene chain (**3**), as a base molecule, a butenylene chain (**4**), to compare extra rigidity when a double bond is introduced, a hexylene chain (**5**) and an octylene chain (**6**), to compare extra length and bis methylene biphenyl spacing unit (**7**), to compare extra rigidity and the possibility of more intermolecular interactions with the ring groups.

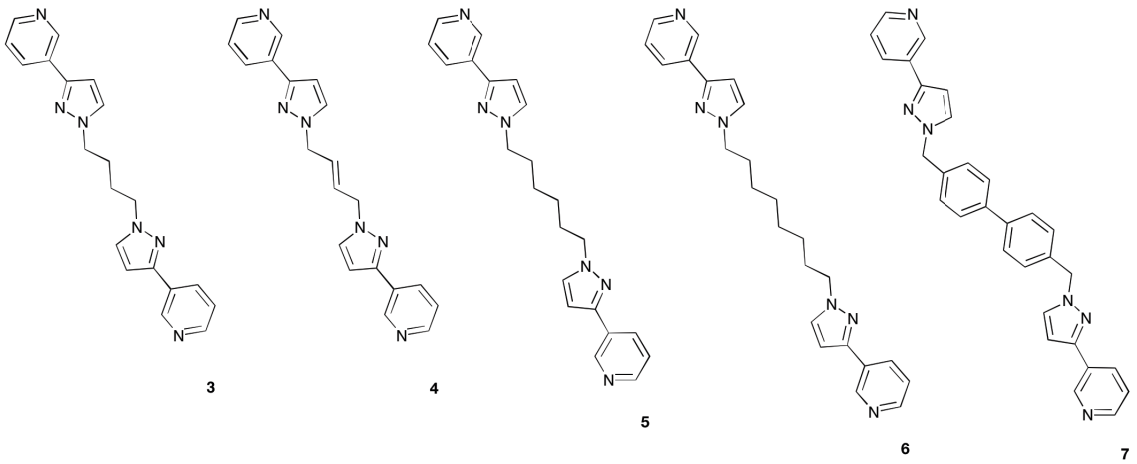

Figure 2.4 The five pyridine-pyrazole linked molecules chosen to be studied, containing butylene (**3**), butenylene (**4**), hexylene (**5**), octylene (**6**) and bis methylene biphenyl (**7**) spacing units.

1,4-bis(3-(pyridin-3-yl)-1*H*-pyrazol-1-yl)butane (Pypy-Bu) (3)

Compound **3** (Pypy-Bu) was produced through the alkylation of 3-(1H-pyrazol-3-yl)pyridine (**2**) with 1,4-dibromobutane, giving an orange solid in 38% yield. Crystals were grown from acetonitrile and analysed by X-ray diffraction. This molecule is centrosymmetric with the asymmetric unit comprising of exactly half of the molecule. The centrosymmetry puts the inversion centre midway along the butylene spacer which in this case gives the pyridyl binding groups a transoid geometry with respect to one another (Figure 2.5). The pyridyl nitrogen atom and pyrazole nitrogen atoms face towards the same side in each half of the molecule and are co-planar (with a C2-C3-C7-C8 torsion angle of 170.9° i.e. 9.1° removed from being fully co-planar). The torsion angle at the linkage of the pyrazole to the butyl spacer (N3-N2-C12-C13) was measured to be 68.1°, this is smaller than for most of the other molecules of this type, possibly as the spacer group is small so its rotation is restricted in favour of more stabilizing effects of between the ring systems of adjacent molecules in the packing structure. Due to the distortion of the butylene spacer, the two ends of the molecule are brought closer together giving an internal pyridyl nitrogen atom (binding site) spacing of 13.90 Å.

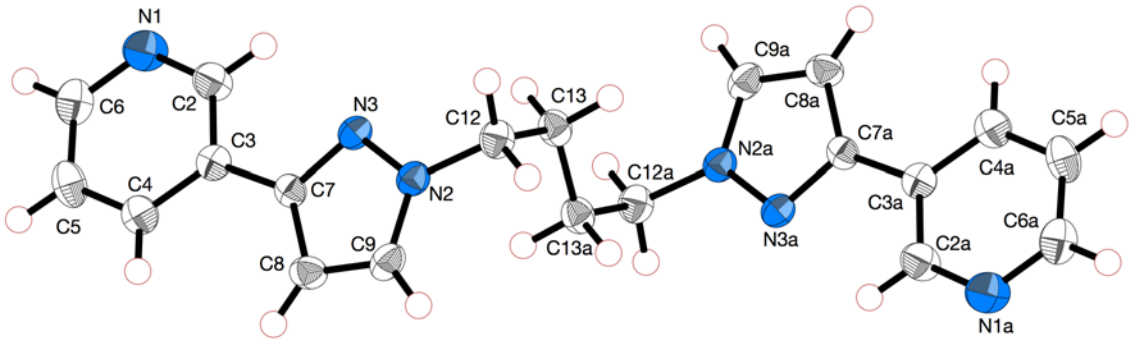

Figure 2.5 Molecular structure of **3** obtained by X-ray diffraction. All non-hydrogen atoms labelled, showing both the asymmetric unit and symmetry generated atoms (denoted by 'a').

The packing arrangement of the molecule is dominated by parallel displaced face to face π interactions of adjacent molecules in the b- and c-axes between the pyridyl rings and the pyrazole rings, where the parallel displaced inter-planar distance (centroid to edge) is 3.52 Å. This gives the packing arrangement its distinctive herringbone motif (Figure 2.6). Possible edge to face π interactions seen here are too weak to be classed as interacting, with C-

H···centroid distances above 3.5 Å. However, C-H···N interactions can be seen, these are classed as weak hydrogen-bonds with distances of up to ~3.70 Å.[18-20] Packing in the a-axis may be influenced by these weak N-H hydrogen-bonds between the pyridyl N1 and the pyridyl H4 of adjacent molecules where the C5-H5···N1 distance is 3.54 Å (H5···N1 = 2.99 Å). Further weak N-H hydrogen-bonding can be seen between the pyrazole N3 to the pyrazole H8 of the adjacent molecule, C8-H8···N3 = 3.62 Å (H8···N1 = 2.94 Å).

One of our objectives was to create a large N···N binding site distance between molecules for the purpose of imaging metal containing species bound to these sites. Any distance smaller than ~ 1 nm (~ 10 Å) would be very difficult to resolve by atomic force microscopy (AFM) as the tip radius is generally between 10-40 nm, giving poor lateral resolution. Sharper tips may be used when higher resolution is needed, however, they are much more expensive. The intermolecular N1···N1 distances for this molecule are 5.72 Å, 10.91 Å and 9.46 Å for the a-, b- and c- axes respectively, meaning spacing in the b- and c-axes may just be resolved by AFM.

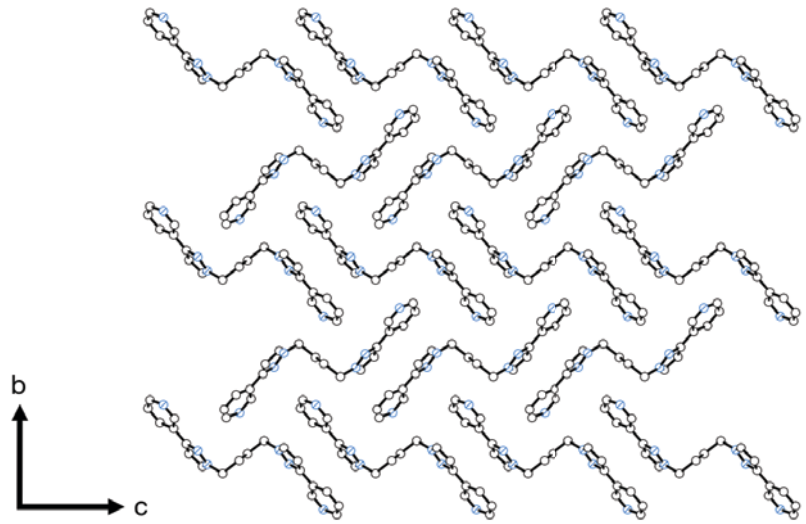

Figure 2.6 Packing arrangement in crystal of **3** viewed down the a-axis. Hydrogen atoms removed for clarity.

1,4-bis(3-(pyridin-3-yl)-1*H*-pyrazol-1-yl)but-2-ene (Pypy-Bt) (4)

Compound **4** (Pypy-Bt) was produced through the alkylation of 3-(1H-pyrazol-3-yl)pyridine (**2**) with 1,4-dibromobutene, giving an orange solid in 11% yield. Crystals were grown from acetonitrile and analysed by X-ray diffraction. The centrosymmetry of this molecule again gives the pyridyl nitrogen binding sites

a transoid geometry with the inversion centre midway along the butenylene double bond (Figure 2.7). The C2-C3-C7-N3 torsion angle was measured at 160.0° meaning the rings are 20.0° removed from being co-planar. The pyridyl nitrogen atom is facing towards the opposite side of the molecule to the pyrazole nitrogen atoms with the C2-C3-C7-C8 torsion angle being 17.0° compared to the equivalent torsion angle in **3** of 170.9°, this shows that the rings have rotated 153.8° about the C3-C7 bond relative to each other. As this bond (C3-C7) is free to rotate, any intermolecular interaction between the nitrogen or hydrogen atoms and the adjacent molecules can affect its rotation. The N3-N2-C12-C13 torsion angle this time is 84.9°, this is slightly larger than for **3**, possibly because the lack of rotation about the butenyl double bond may reduce the free rotation of the spacer as a whole. This rotation has also increased the overall length of the molecule, with the intramolecular pyridyl nitrogen atom spacing now at 15.5 Å.

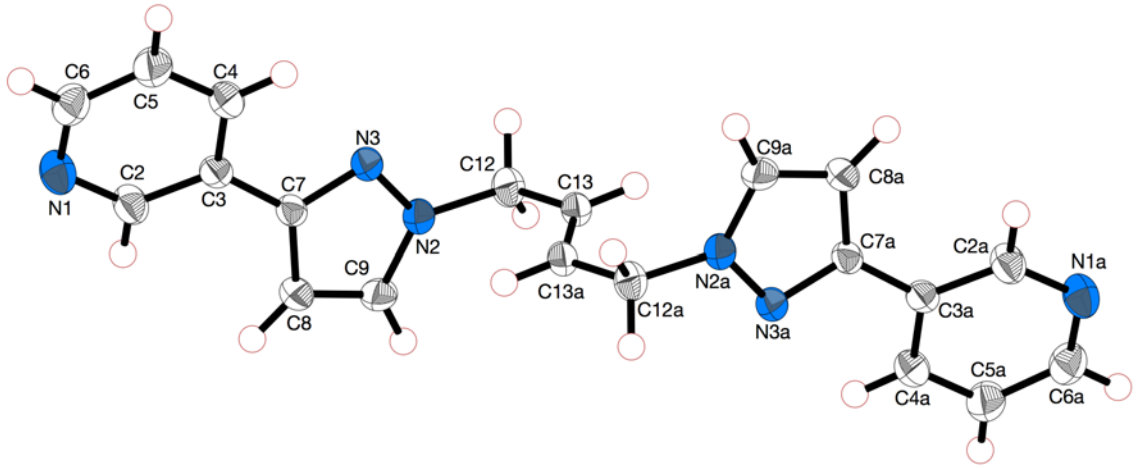

Figure 2.7. Molecular structure of **4** obtained by X-ray diffraction. All non-hydrogen atoms labelled, showing both the asymmetric unit and symmetry generated atoms (denoted by 'a').

The packing arrangement again shows parallel displaced face to face π interactions between pyridyl rings and pyrazole rings where the inter-planar distance was measured at 3.45 Å. Very weak hydrogen-bonding interactions can also be seen between the N1 of one molecule and the H12 of another, C12-H12···N1 = 3.77 Å (H12···N1 = 3.15 Å), as well as between the N3 of one molecule and the H8 of another, C8-H8···N3 = 3.54 Å (H8···N3 = 2.59 Å). These hydrogen-bonding interactions have resulted in a layered packing arrangement (Figure 2.8) where molecules are stacked in alternating directions in each layer. The N1···N1 distance between these molecules are now 5.15 Å, 14.68 Å and

11.21 Å for the a-, b- and c-axes respectively.

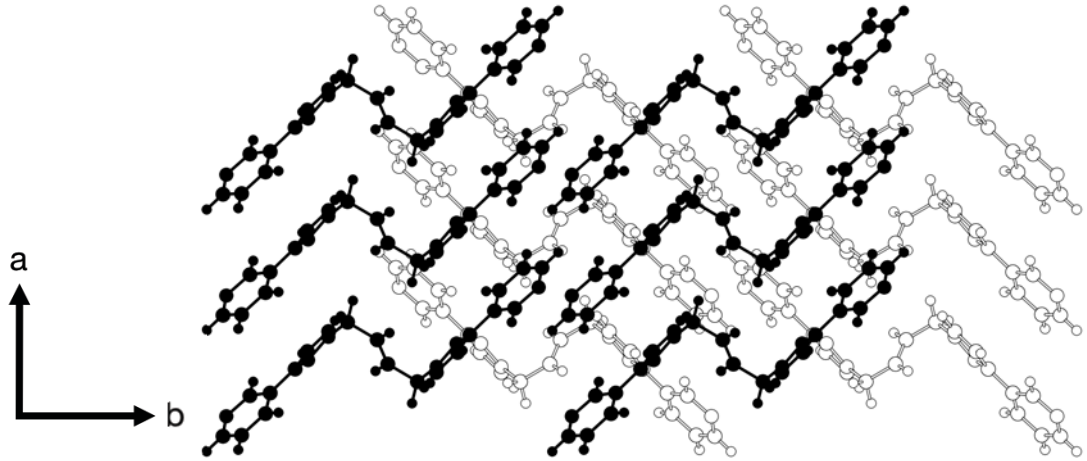

Figure 2.8. Packing arrangement in crystal of **4** viewed down the c-axis, showing molecules of alternating direction in each layer, black on top.

1,6-bis(3-(pyridin-3-yl)-1*H*-pyrazol-1-yl)hexane (Pypy-Hx) (5)

Compound **5** (Pypy-Hx) was produced through the alkylation of 3-(1H-pyrazol-3-yl)pyridine (**2**) with 1,6-dibromohexane, giving an orange solid in 28% yield. Crystals were grown from acetonitrile and analysed by X-ray diffraction. The centrosymmetry of this molecule gives it a transoid geometry with respect to the pyridyl nitrogen atom binding sites and the inversion centre falls midway along the hexylene spacer (Figure 2.9). This time the pyridyl nitrogen atom and pyrazole nitrogen atoms face towards the same side of the molecule with a torsion angle (C2-C3-C7-C8) of 154.8° i.e. 25.2° removed from being co-planar. The linkage from the pyrazole to the spacer (N3-N2-C12-C13) gives a torsion angle of 76.1° and all six carbon atoms in the spacer are in the same plane giving the intramolecular pyridyl nitrogen atoms a 16.43 Å spacing.

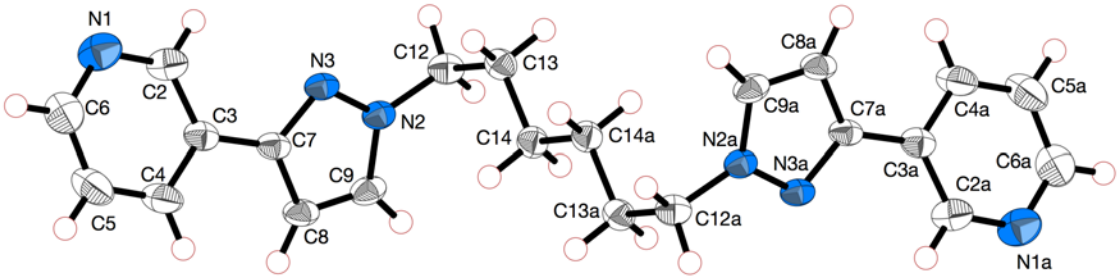

Figure 2.9. Molecular structure of **5** obtained by X-ray diffraction. All non-hydrogen atoms labelled, showing both the asymmetric unit and symmetry generated atoms (denoted by 'a').

The packing arrangement shows weak hydrogen-bonding from N3-H4 in adjacent molecules of 3.54 Å for C4-H4···N3 (H4···N3 = 2.74 Å), as well as from N3-H8 in adjacent molecules where C8-H8···N3 = 3.65 Å (H8···N3 = 2.74 Å). Viewed down the c-axis, the pyridyl binding site groups come together as a pyramid of three molecules, with another three offset beneath. This arrangement can be seen in Figure 2.10, where six blue dots (nitrogen) come together. The N1···N1 distances in the a- and b- plane were measured at 5.12 Å.

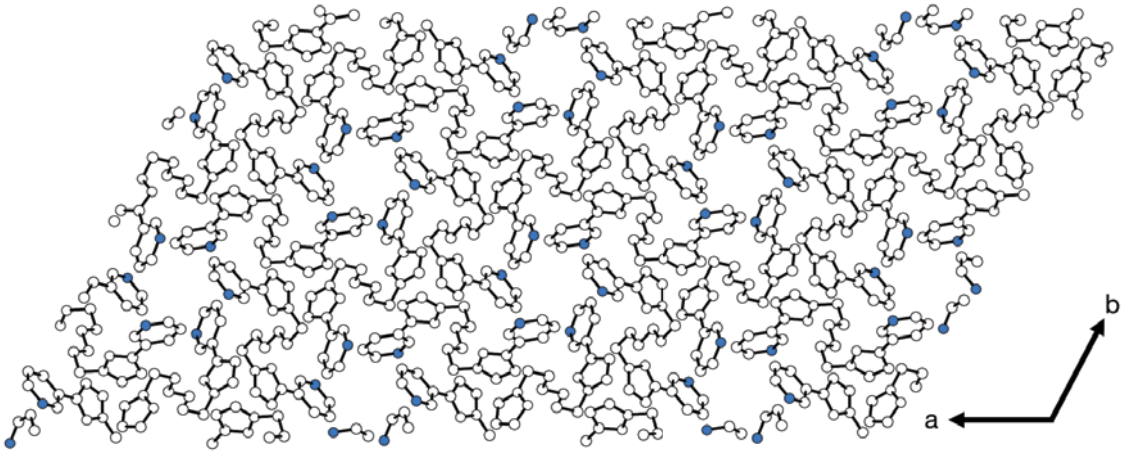

Figure 2.10 Packing arrangement in crystal of **5** viewed down the c-axis, showing pyridyl groups clustered together. Hydrogen atoms removed for clarity.

1,8-bis(3-(pyridin-3-yl)-1*H*-pyrazol-1-yl)octane (Pypy-Oc) (6)

Compound **6** (Pypy-Oc) was produced through the alkylation of 3-(1H-pyrazol-3-yl)pyridine (**2**) with 1,8-dibromooctane, giving an orange solid in 28% yield. Colourless crystals were grown from toluene and analysed by X-ray diffraction. This molecule is again centrosymmetric giving the pyridyl nitrogen atom binding sites a transoid geometry with an inversion centre midway along the octylene spacer unit (Figure 2.11). The pyridyl and pyrazole rings are co-planar here, where the C2-C3-C7-N3 torsion angle is now 177.8º meaning the rings are only 2.2º removed from being fully co-planar, this is much smaller than for the previous molecules. The pyridyl nitrogen atom is facing towards the opposite side of the molecule to the pyrazole nitrogen atoms with the C2-C3-C7-C8 torsion angle being 4.3º compared to the equivalent torsion angle in **5** of 154.8º, this shows that the rings have rotated 150.5º about the C3-C7 bond relative to each other. The torsion angle between the pyrazole and the octyl

spacer unit (N3-N2-C12-C13) was measured at 71.9° putting it in a similar range to the equivalent angle in **5**, however, the C12-C13-C14-C15 torsion angle was measured at 68.0° meaning only the central six carbon atoms are in the same plane as each other. The deformation of the spacer group due to the torsion angles make the intramolecular pyridyl nitrogen atom distance 17.02 Å, only just longer than for **5** (16.43 Å).

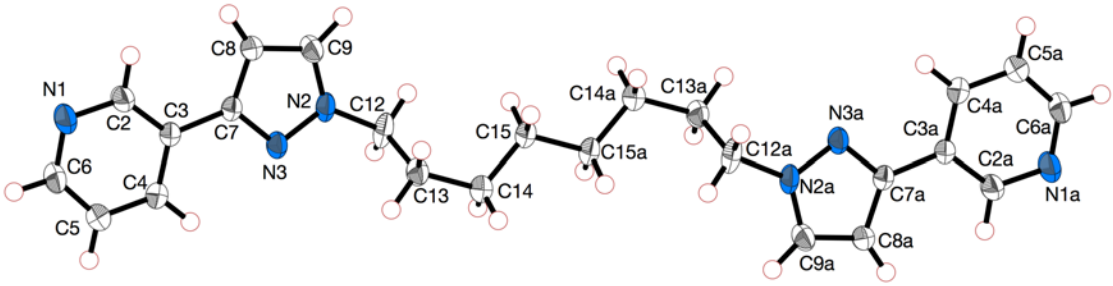

Figure 2.11 Molecular structure of (**6**) obtained by X-ray diffraction. All non-hydrogen atoms labelled, showing both the asymmetric unit and symmetry generated atoms (denoted by 'a').

There are two examples of edge to face π interactions between a pyridyl centroid of one molecule and the H2 of another, C2-H2···centroid = 3.90 Å (H2···centroid = 3.18 Å) (Figure 2.12a), as well as the pyrazole centroid and H8 interaction of adjacent molecules, C8-H8···centroid = 3.68 Å (H8···centroid = 2.84 Å) (Figure 2.12b). These edge to face interactions are seen as very weak, but may still play some part in directing the crystal packing.[21]

The intermolecular N1···N1 distances from this packing arrangement are, 9.09 Å and 15.26 Å in the a- and b- axes and 4.33 Å and 14.37 Å for the c-axis.

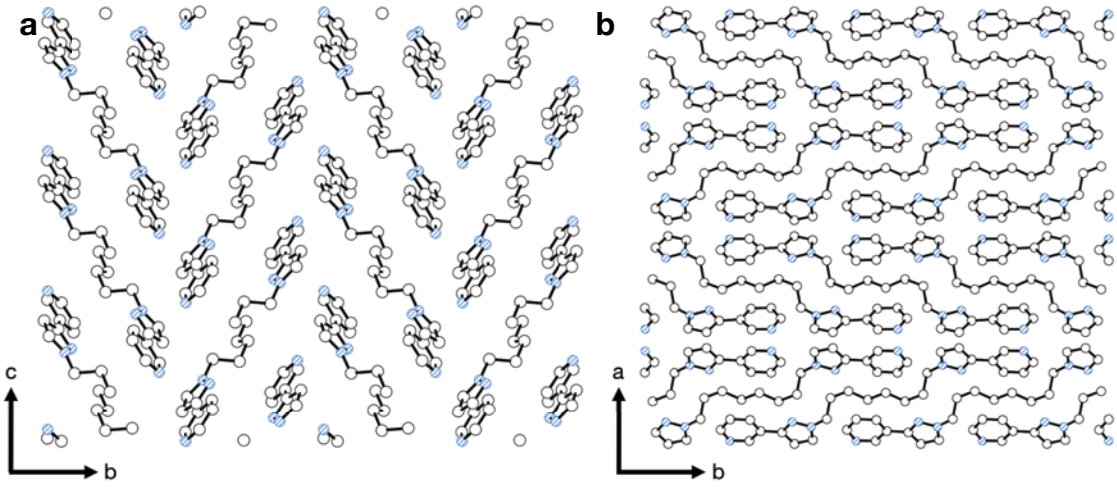

Figure 2.12 Packing arrangement in crystal of **6** viewed down the a-axis (**a**) and c-axis (**b**). Hydrogen atoms removed for clarity.

4,4'-bis((3-(pyridin-3-yl)-1*H*-pyrazol-1-yl)methyl)-1,1'-biphenyl (Pypy-Me-BiPh) (7)

Compound **7** (Pypy-Me-BiPh) was produced through the alkylation of 3-(1H-pyrazol-3-yl)pyridine (**2**) with 4,4-bis(bromomethyl)biphenyl, giving an orange solid in 31% yield. Colourless crystals were grown from methanol and analysed by X-ray diffraction. The centrosymmetry of the molecule gives a transoid geometry with respect to the pyridyl binding groups and an inversion centre between the two phenyl rings of the bis methylene biphenyl spacer (Figure 2.13). The pyridyl nitrogen atom and pyrazole nitrogen lie on the same side of the molecule with a torsion angle C2-C3-C7-C8 of 167.7º between the rings i.e. 12.3º removed from being fully co-planar. The pyrazole-spacer linkage (N3-N2-C12-C13) was measured at 67.2º, this biphenyl spacer unit is very rigid but the C12-C13 bond gives it some rotational freedom putting the plane twist angle between the pyridyl ring and the phenyl rings at 31.7º. This rigid linker also helps to generate the large spacing between the intramolecular pyridyl nitrogen atoms, 16.98 Å.

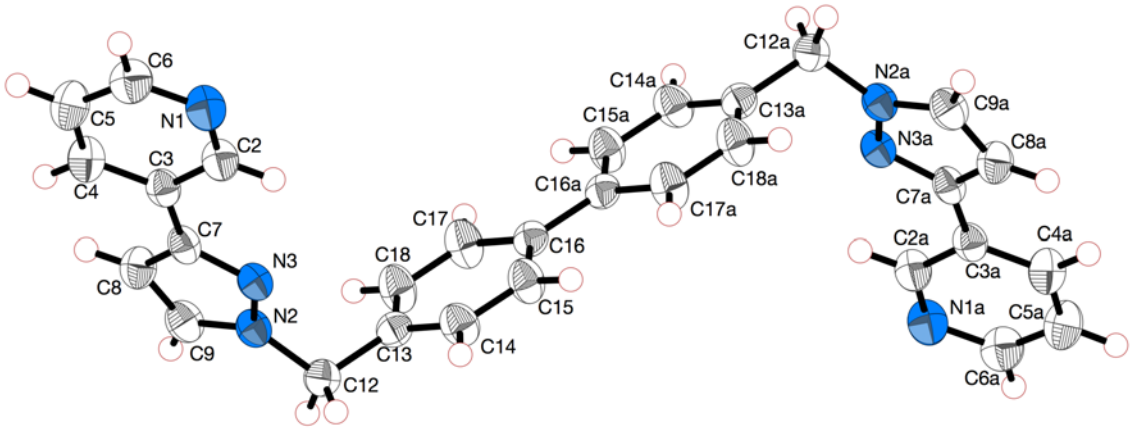

Figure 2.13 Molecular structure of (**7**) obtained by X-ray diffraction. All non-hydrogen atoms labelled, showing both the asymmetric unit and symmetry generated atoms (denoted by 'a').

The packing structure in this crystal shows many possible parallel displaced face to face π interactions between molecules, with the pyridyl to pyridyl inter-planar distance measured at 3.52 Å (centroid to edge) and the pyrazole to pyrazole inter-planar distance measured at 3.44 Å (centroid to edge), and a pyridyl to pyarzole interaction, 3.41 Å (centroid to edge). Parallel displaced face to face π interactions between the phenyl rings of adjacent molecules are also present, 3.56 Å (centroid to edge). The structure shows very weak hydrogen-

bonding between C18-H18···N of 3.01 Å (H18···N1 = 3.80 Å), and C9-H9···N3 of 2.89 Å (H9···N3 = 3.62 Å) (Figure 2.14).

The intermolecular N1···N1 distances this time are 4.51 Å in the a-axis, 22.28 Å in the b-axis and 7.96 Å and 17.79 Å in the c-axis.

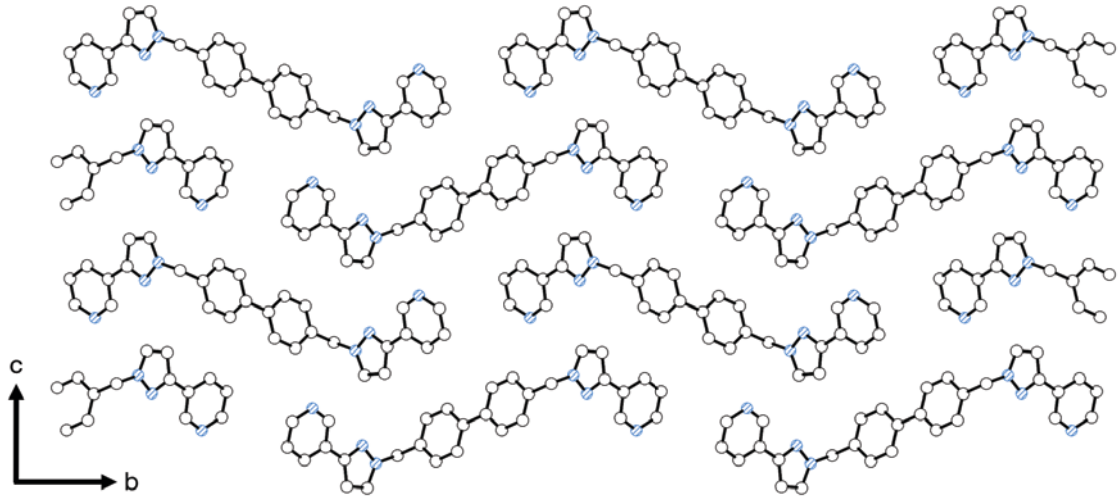

Figure 2.14 Packing arrangement in crystal of **7** viewed down the a-axis. Hydrogen atoms removed for clarity.

In general, the torsion angles between the pyrazole rings and their adjoining spacer units seem to favour an 'out of plane' conformation (all close to 90º), meaning the maximum internal N1-N1 spacing can not be reached, as they would in an anti-periplanar arrangement.

In the absence of a major deformation of the molecules during crystallization, it can be assumed that a longer spacer unit would provide an increased intramolecular N1-N1 binding site spacing. These molecules show this trend and interestingly there also seems to be a trend towards larger intermolecular binding site spacing when using a spacer unit with increased length. However, given that the packing arrangements vary so much, binding site spacing within the crystal structure is still unpredictable.

2.2.3 Bis(1-(pyridin-3-yl)methanimine) Binding Site Molecules

The pyridine-imine binding site molecules were prepared via imine formation through dehydration reactions between pyridine-3-carboxaldehyde and both ends of the appropriate diamine spacer unit[22] (X) (scheme 2.3).

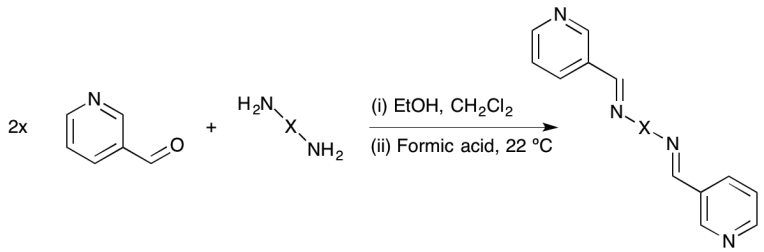

Scheme 2.3 Formation of linked pyridine-imine compounds (**8**-**12**) by reacting two equivalents of 3-pyridinecarboxaldehyde with the appropriate diamine spacer unit.

The pyridine-imine linked molecules chosen to be studied (Figure 2.15, **8**-**12**) consist of spacer units of an ethylene chain (**8**), as a base molecule, a phenylene ring (**9**), to compare extra rigidity and increased intermolecular interactions, a cyclohexylene ring (**10**), to see what changes when the six membered ring loses its rigidity, a hexylene chain (**11**), to compare extra length and napthylene spacing unit (**12**), to compare extra rigidity and the possibility of increased intermolecular interactions involving the ring groups.

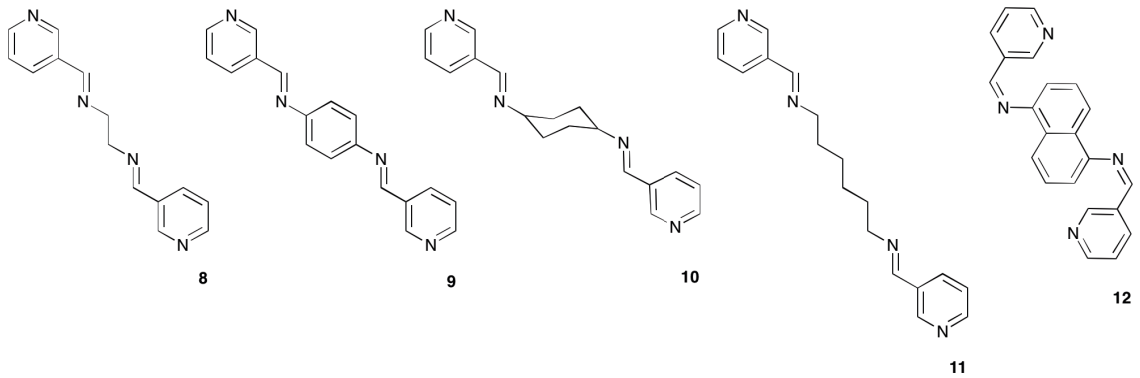

Figure 2.15 The five pyridine-imine linked molecules chosen to be studied, containing ethylene (**8**), phenylene (**9**), cyclohexylene (**10**), hexylene (**11**) and napthylene (**12**) spacing units.

N,*N*'-(ethane-1,2-diyl)bis(1-(pyridin-3-yl)methanimine) (Py-Im-Et) (8)

Compound **8** (Py-Im-Et), originally produced by Sun et al.[23] was synthesized through a dehydration reaction of pyridine-3-carboxaldehyde with 1,2-diaminoethane, giving a yellow solid in a 90% yield. Crystals were grown from ethyl acetate and analysed by X-ray diffraction. This molecule is also centrosymmetric, having the asymmetric unit comprised of exactly half of the molecule. The inversion centre is midway along the ethylene bridge spacer giving the molecule a transoid geometry with respect to the two pyridyl nitrogen atoms (Figure 2.16). The pyridyl nitrogen atom is facing towards the opposite side of the molecule to the imine nitrogen atom, with the C2-C3-C7-N2 torsion angle at 172.9º. The link between the imine bond and the ethyl

spacer unit (C7-N2-C9-C9a) has a torsion angle of 134.9°, twisting the molecule slightly and contributing to a 13.10 Å intramolecular pyridyl nitrogen atom spacing despite the small spacer molecule.

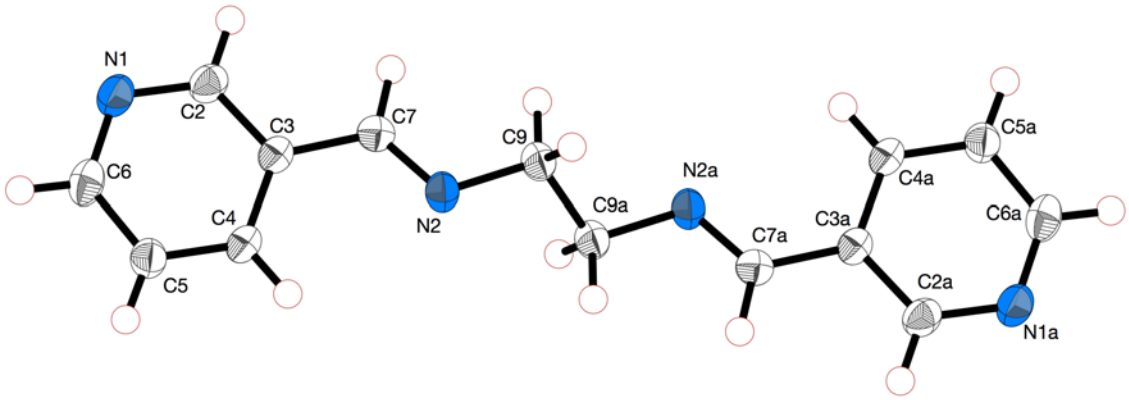

Figure 2.16 Molecular structure of (**8**) obtained by X-ray diffraction. All non-hydrogen atoms labelled, showing both the asymmetric unit and symmetry generated atoms (denoted by 'a').

The packing structure of these crystals show weak hydrogen-bonding between molecules in the c-axis where C5-H5···N1 = 3.54 Å (H5···N1 = 2.89 Å) as well as between adjacent molecules in the a-axis, where C6-H6···N1 = 3.60 Å (H6···N1 = 2.65 Å) (Figure 2.17). In the c-axis, molecules pack in alternating layers of direction, possibly due to hydrogen-bonding of N2-H2, C2-H2···N2 = 3.76 Å (H2···N2 = 2.86 Å) as well as close crystal packing (Figure 2.18).
The intermolecular N1···N1 distances are 4.14 Å, 13.46 Å, and 5.91 Å in the a-, b- and c-axes respectively.

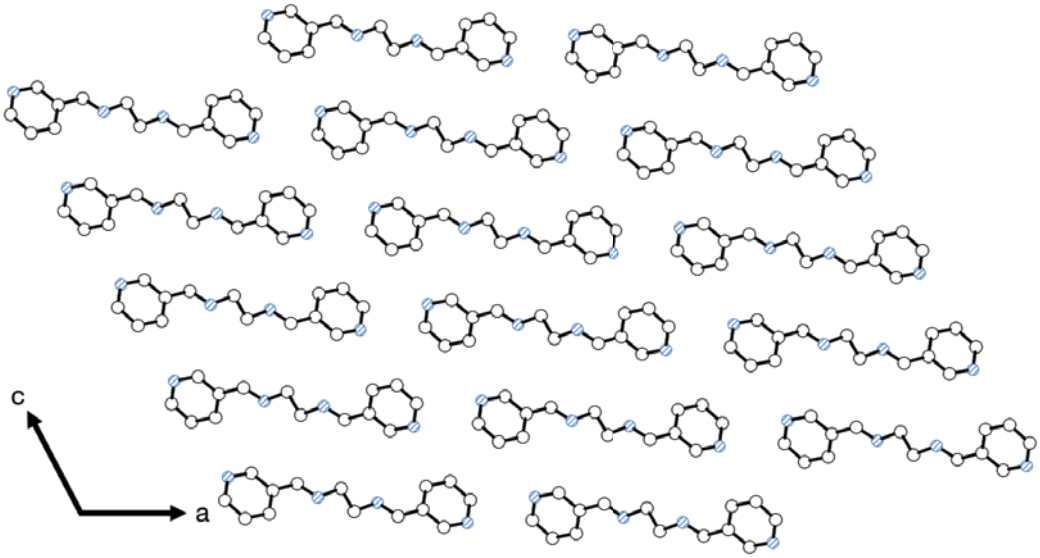

Figure 2.17 Packing arrangement in crystal of **8** viewed down the b-axis. Hydrogen atoms removed for clarity.

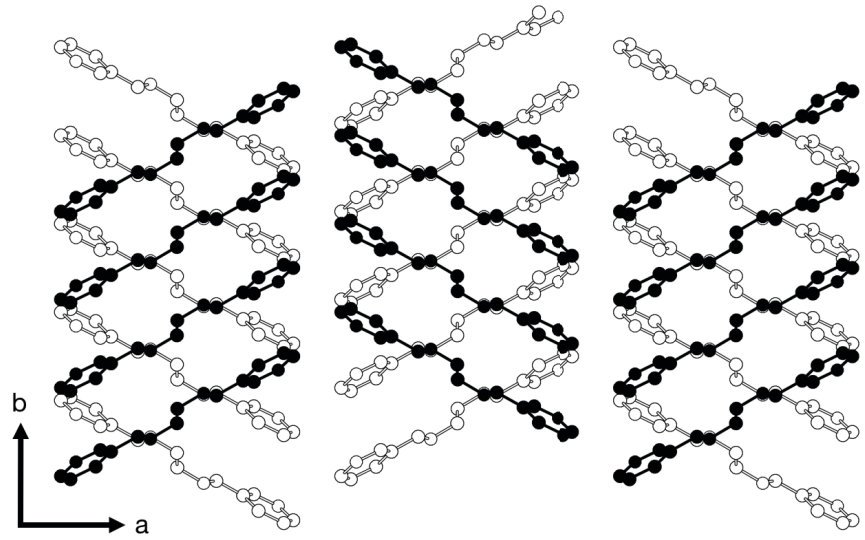

Figure 2.18 Packing arrangement in crystal of **8** viewed down the c-axis, showing molecules of alternating direction in each layer. Hydrogen atoms removed for clarity.

N,*N*'-(1,4-phenylene)bis(1-(pyridin-3-yl)methanimine) (Py-Im-Ph) (9)

Compound **9** (Py-Im-Ph), originally produced by Ha et al.[16] was synthesized through a dehydration reaction of pyridine-3-carboxaldehyde with 1,4-diaminobenzene, giving a yellow solid in 43% yield. Crystals were grown from an ethanol/hexane mixture and analysed by X-ray diffraction. The centrosymmetry of this molecule again gives the pyridyl nitrogen atoms a transoid geometry relationship with the inversion centre located in the centre of the phenylene spacer ring (Figure 2.19). The pyridyl nitrogen atom and imine nitrogen atom in the asymmetric unit lie on the same side in each half of the molecule, and the pyridyl ring and imine group are essentially co-planar with a torsion angle (C2-C3-C7-N2) of 4.8º where a rotation about the C3-C7 bond has occurred when compared with **8**. The (C7-N2-C9-C10) linkage between the imine group and the phenyl spacer group has a torsion angle of 145.6º and another (C7-N2-C9-C11) of 36.8º. This rotation about the N2-C9 bond accounts for the plane twist angle between the pyridyl ring and the phenyl ring of 31.3º as the rest of the molecule is almost planar. The rigid phenyl linker also means an intramolecular pyridyl nitrogen atom spacing of 14.0 Å can be seen despite the small size of the spacer unit.

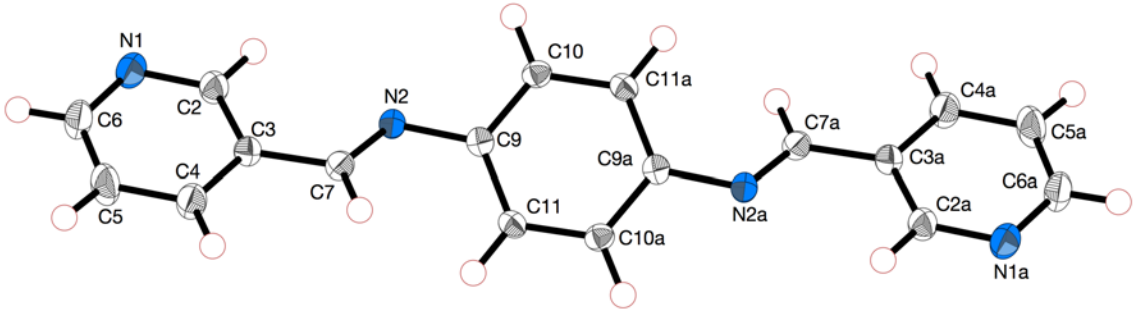

Figure 2.19 Molecular structure of (**9**) obtained by X-ray diffraction. All non-hydrogen atoms labelled, showing both the asymmetric unit and symmetry generated atoms (denoted by 'a').

The packing arrangement shows weak hydrogen-bonding between molecules in the a- direction where C6-H6···N1 = 3.53 Å (H6···N1 = 2.64 Å) (Figure 2.20b). The packing also shows edge to face π interactions in c- direction between the phenyl centroid of one molecule and H11 of another, where C11-H11···centroid = 3.39 Å (H11···centroid = 2.54 Å) (Figure 2.20b).

Intermolecular N1···N1 distances in this packing arrangement are, 16.50 Å, 6.12 Å and 3.56 Å for the a-, b- and c-axes respectively.

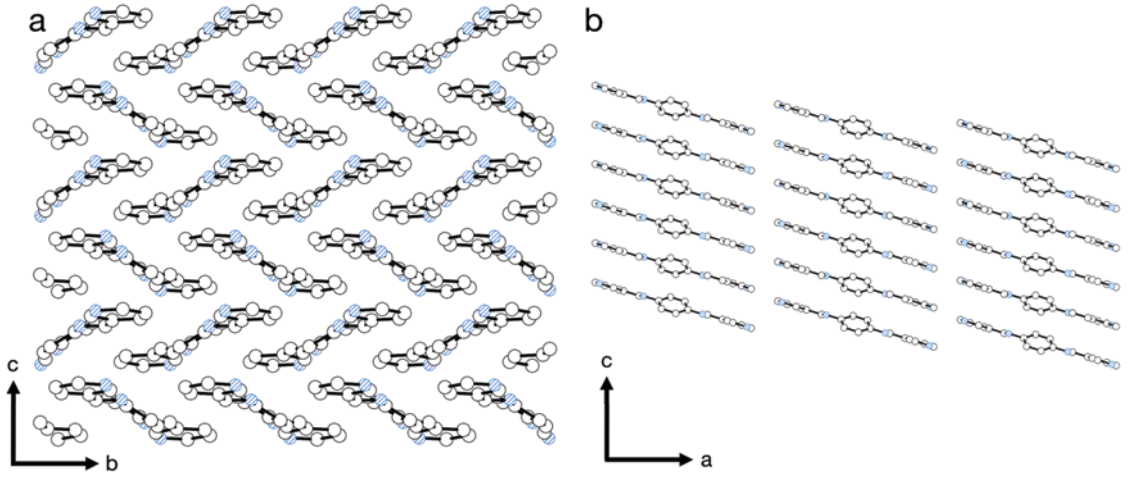

Figure 2.20 Packing arrangement in crystal of **9** viewed down the a-axis (**a**) and the b-axis (**b**). Hydrogen atoms removed for clarity.

N,*N*'-(cyclohexane-1,4-diyl)bis(1-(pyridin-3-yl)methanimine) (Py-Im-Cy) (10)

Compound **10** (Py-Im-Cy) was produced through a dehydration reaction of pyridine-3-carboxaldehyde with 1,4-transdiaminocyclohexane, giving a white solid in 54% yield. Crystals were grown from ethyl acetate and analysed by X-ray diffraction. This molecule also has a transoid geometry with respect to the two pyridyl nitrogen atoms, with an inversion centre in the centre of the

cyclohexylene ring spacer (Figure 2.21). The asymmetric unit shows the pyridyl nitrogen atom is facing towards the opposite side of the molecule to the imine nitrogen atom with the C2-C3-C7-N2 torsion angle at 168.9º. The imine to spacer linkage has torsion angles of 135.0º (C7-N2-C9-C10) and 99.8º (C7-N2-C9-C11). Plane twist angle between the pyridyl ring and the averaged plane of the cyclohexyl ring is 121.8º and the intramolecular pyridyl nitrogen atom distance again makes use of the full length of the spacing unit, 15.04 Å.

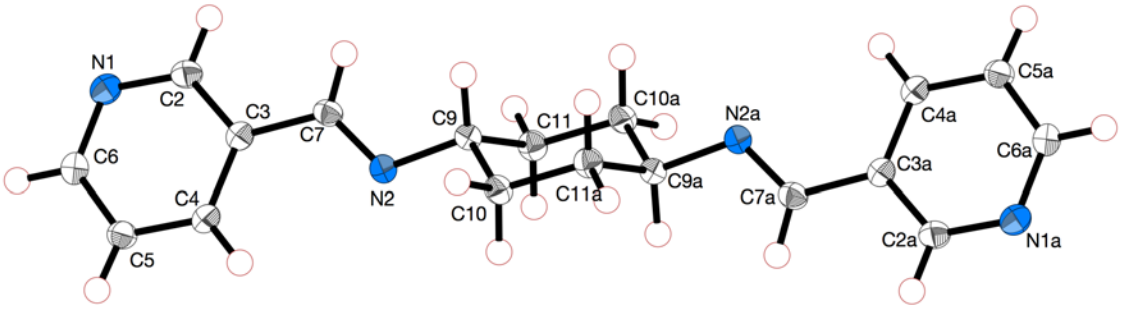

Figure 2.21 Molecular structure of (**10**) obtained by X-ray diffraction. All non-hydrogen atoms labelled, showing both the asymmetric unit and symmetry generated atoms (denoted by 'a').

The arrangement of molecules in this crystal show edge to face π interactions between the pyridyl centroid and H5, where C5-H5···centroid = 3.60 Å (H5···centroid = 2.83 Å) (Figure 2.22). Weak hydrogen-bonding can also be seen between N1-H4 atoms, where C4-H4···N1 = 3.46 Å (H4···N1 = 2.67 Å), in the a-axis.

The N1···N1 distances between molecules are now 6.06 Å, 5.56 Å and 11.81 Å in the a-, b- and c-axes respectively.

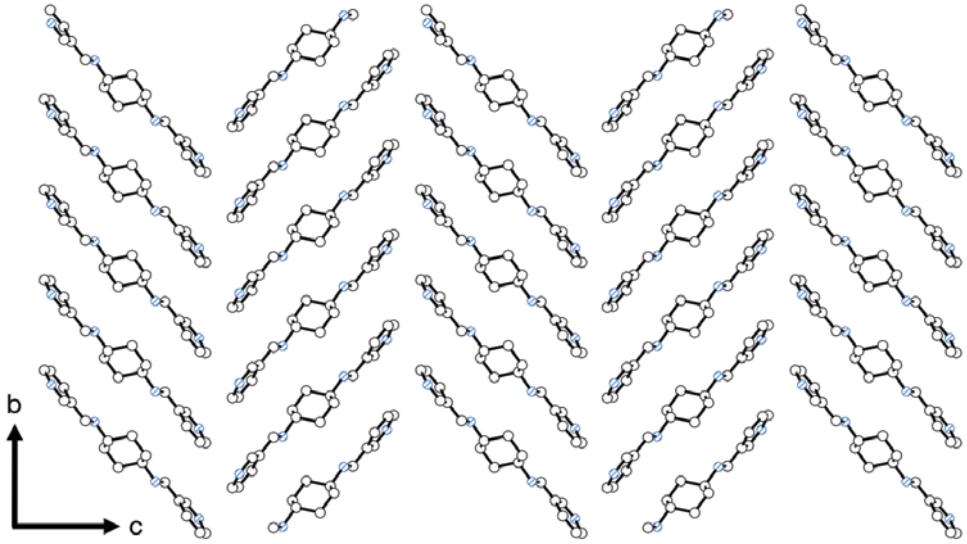

Figure 2.22 Packing arrangement in crystal of **10** viewed down the a-axis. Hydrogen atoms removed for clarity.

N,*N*'-(hexane-1,6-diyl)bis(1-(pyridin-3-yl)methanimine) (Py-Im-Hx) (11)

Compound **11** (Py-Im-Hx) was produced through a dehydration reaction of pyridine-3-carboxaldehyde with 1,6-diaminohexane, giving an orange solid in 72% yield. Crystals were grown from an ethanol/dichloromethane mixture and analysed by X-ray diffraction. The centrosymmetry of this molecule also gives the pyridyl nitrogen atoms a transoid geometry to each other with the inversion centre midway along the hexylene spacer unit (Figure 2.23). The asymmetric unit contains a pyridyl nitrogen atom facing towards the opposite side of the molecule to the imine nitrogen atom with the C2-C3-C7-N2 torsion angle at 179.5°, nearly exactly in the same plane. The torsion angle between the imine group and the hexyl spacer unit (C7-N2-C9-C10) is also nearly 180° (179.2°), putting every non-hydrogen atom in the molecule in the same plane. Being planar maximizes the length of this molecule, giving the largest intramolecular pyridyl nitrogen atom binding site spacing of the molecules synthesized and crystallized here (18.27 Å) by using the full length of the already long hexyl spacing unit.

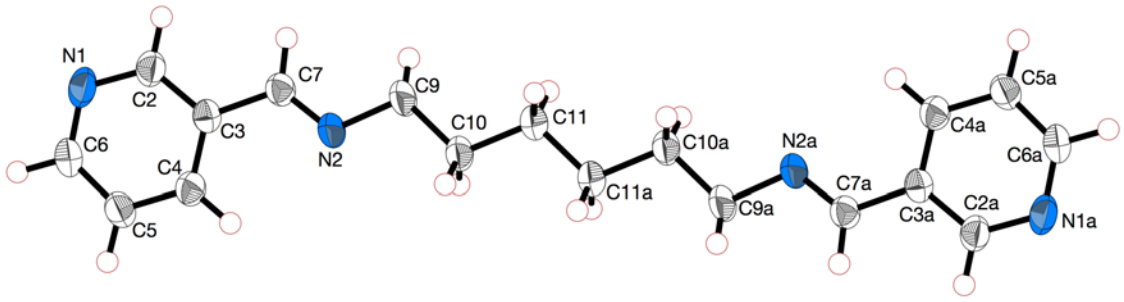

Figure 2.23 Molecular structure of (**11**) obtained by X-ray diffraction. All non-hydrogen atoms labelled, showing both the asymmetric unit and symmetry generated atoms (denoted by 'a').

Molecular packing in the crystal shows some parallel displaced face to face π interactions between pyridyl rings of adjacent molecules, the inter-planar distance was measured at 3.60 Å (centroid to edge). Weak hydrogen-bonding can also be seen between the N2-H5 atoms, C5-H5···N2 = 3.65 Å (H5···N2 = 2.69 Å) in the b-axis. These forces coupled with crystal close packing help to keep the molecule in its linear conformation resulting in an efficient closely packed arrangement (Figure 2.24).

The intermolecular N1···N1 distances were measured at, 10.10 Å, 9.67 Å and 8.58 Å in the a-, b- and c-axes respectively.

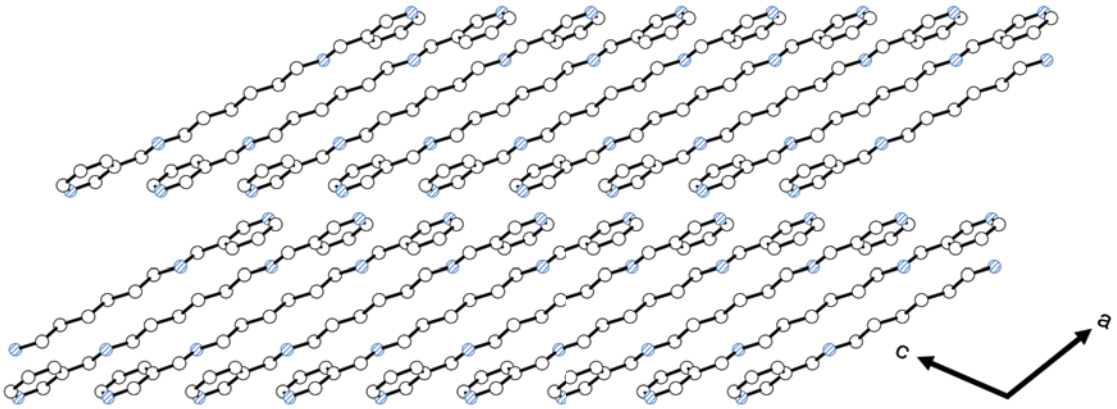

Figure 2.24 Packing arrangement in crystal of **11** viewed down the b-axis. Hydrogen atoms removed for clarity.

N,*N*'-(naphthalene-1,5-diyl)bis(1-(pyridin-3-yl)methanimine) (Py-Im-Np) (12)

Compound **12** (Py-Im-Np) was produced through a dehydration reaction of pyridine-3-carboxaldehyde with 1,5-diaminonapthalene, giving an orange solid in a 65% yield. Crystals were grown from dichloromethane and analysed by X-ray diffraction. The centrosymmetry of the molecule gives a transoid geometry

between the two pyridyl nitrogen atoms and the inversion centre sits midway along the bond which fuses the napthylene rings together (C9-C9a). The pyridyl nitrogen atom and imine nitrogen atoms in the asymmetric unit face towards the same side of the molecule (Figure 2.25) with a torsion angle (C2-C3-C7-N2) of 5.1° where a rotation about the C3-C7 bond has occurred. The torsion angles between the imine and napthyl groups C7-N2-C8-C9 and C7-N2-C8-C12 are 142.1° and 40.3° respectively putting the plane twist angle between the pyridyl ring and the napthyl rings at 33.0°. The spacing unit here is essentially a butyl unit that is locked in place and provides an intramolecular pyridyl nitrogen atom spacing of 14.23 Å.

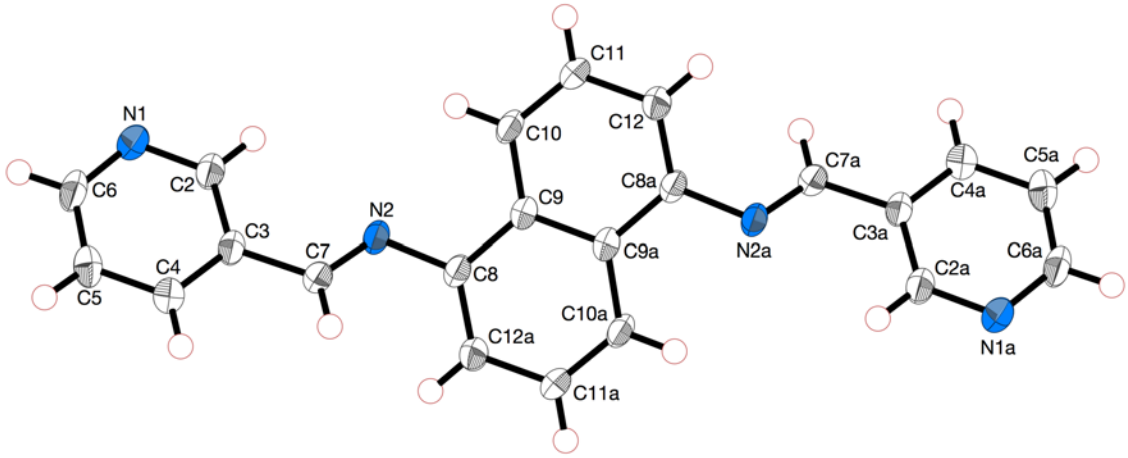

Figure 2.25 Molecular structure of (**12**) obtained by X-ray diffraction. All non-hydrogen atoms labelled, showing both the asymmetric unit and symmetry generated atoms (denoted by 'a').

The molecular packing arrangement in these crystals show parallel displaced face to face π stacking interactions between the pyridyl groups (centroid-edge distance is 3.59 Å). Very weak edge to face π interactions can be seen between the napthyl centroid of one molecule and the H2 atom of an adjacent molecule, where C2—H2···centroid = 3.51 Å (H2···centroid = 3.34 Å) (Figure 2.26).

In the a-axis, weak hydrogen-bonding can be seen between adjacent molecules, C7-H7···N1 = 3.70 Å (H7···N1 = 2.80 Å).

The intermolecular N1···N1 distances this time are 6.67 Å, 7.59 Å and 9.31 Å for the a-, b- and c-axes respectively.

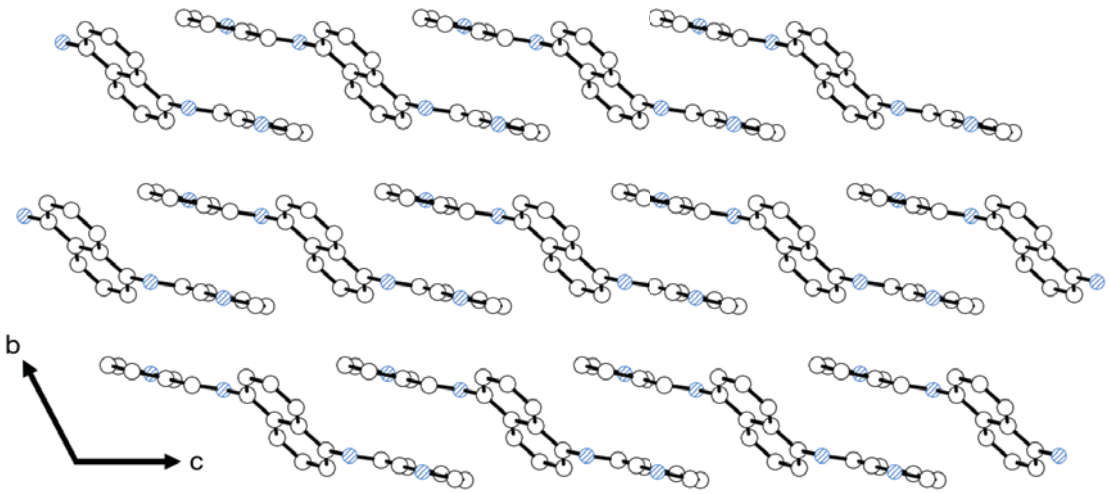

Figure 2.26 Packing arrangement in crystal of **12** viewed down the a-axis. Hydrogen atoms removed for clarity.

For the pyridine-imine binding site set of molecules, there is a tendency for the binding site to spacer unit torsion angle to favour a planar conformation (most of which are approaching 180°), this is in contrast to what is seen for the pyridine-pyrazole set of molecules, and gives the molecule an increased probability to reach the maximum internal N1-N1 spacing, potentially giving surface binding site spacing that is easier to resolve by AFM.

These molecules also show the expected trend of increased internal N1-N1 distance with increasing spacer unit length, however, they do not show the same correlation regarding the intermolecular N1-N1 binding site spacing, meaning, for this set of molecules the crystal packing arrangements are more important in determining this spacing.

2.3 Conclusions

We have shown the synthesis of dual metal-binding site molecules possessing changeable spacer units using simple substitution and dehydration reactions and produced single crystal X-ray diffraction quality crystals of all molecules studied. Diffraction studies of these crystals revealed the molecular structure and intermolecular packing arrangements of these molecules are mostly influenced by parallel displaced face to face π interactions, weak C-H···N hydrogen-bonding and weak edge to face π interactions.

It also seems noteworthy that the imine containing molecules, **8**-**12,** give generally higher yields (42.9% and upwards), which will be important to consider as additional studies of the molecules will require more material.

The resulting binding site spacing provided by a crystal may not be predictable by simply choosing a different spacing unit and relying on the molecules length or rigidity, however, a broad range of spacing distances were shown by our various molecules. The binding site spacing distances generated here all fall between 2.2 nm (for **7**) and 0.4 nm (for **9**), this is much smaller than the spacing currently provided by conventional lithographic methods used in the semiconductor industry, i.e. 10 nm, suggesting that any structures formed across the crystal surface may show higher resolution. The binding site spacing in each axis of a crystal is also largely different, indicating that any deposited material would likely form a nanowire structure upon aggregation as opposed to an array of equally spaced nanostructures.

With respect to the small binding site spacing and potential to tune this spacing in different axes, organic crystals of this type could provide the ideal template substrate on which to produce nanoscale circuitry for the continued miniaturization of electronic devices.

2.4 Experimental Details

All chemicals were purchased from Sigma-Aldrich, Alfa Aesar or Fisher Scientific and were used as received without further purification. Melting points were obtained using a Stuart melting point apparatus SMP11. Infra-red data was collected on a Varian 800 FT-IR spectrometer and interpreted using the Varian Resolutions software. Accurate mass electrospray mass spectrometry using leucine as a reference was carried out using a Waters Micromass MS Technologies LCT Premier mass spectrometer and interpreted using the Waters Laboratory Infomatics Mass Lynx software. ^{1}H NMR and ^{13}C NMR measurements were all carried out on a Jeol 400MHz spectrometer and interpreted using MestReNova. Crystal structures were determined by single crystal X-ray diffraction at 150 K using Cu or Mo radiation on an Oxford Diffraction Gemini A Ultra diffractometer. Crystal structures were solved by direct methods and resolved using least squares analysis using the ShelXS and ShelXL packages respectively and Olex 2 (OlexSys Ltd.) as an interface.

Graphics of the structures were produced in CrystalMaker (CrystalMaker Software Ltd.).

NMR numbering from crystal structure atom labels.

Synthesis of 3-(dimethylamino)-1-(pyridine-3-yl)prop-2-en-1-one (1)

3-acetylpyridine (24.20 g, 0.20 mol) and *N,N*-dimethylformamide-dimethyl acetate (40 mL) were heated to reflux (~130 °C) for 2 hours. Any methanol created and excess DMFDA were then removed in vacuo. to give a viscous brown liquid which was recrystallized by trituration in chloroform and hexane. The product of orange crystals was obtained, 28.02 g, 80% yield. ^{1}H NMR ($CDCl_3$): δ 9.05 (1H, s; pyridyl H^2), 8.60 (1H, d, *J* = 4.8 Hz; pyridyl H^6), 8.20 (1H, d, *J* = 7.6 Hz; pyridyl H^4), 7.60 (1H, d, J = 12.3 Hz; alkene CH), 7.25 (1H, dd, *J* = 7.9, 4.7 Hz; pyridyl H^5), 5.60 (1H, d, *J* = 12.3 Hz; alkene CH), 3.15 (3H, s; Me), 2.85 (3H,s; Me). $^{13}C\{^{1}H\}$ NMR ($CDCl_3$): δ 186.29, 154.69, 151.40, 148.85, 135.67, 135.12, 123.31, 91.76, 45.20, 37.38. HRMS (ESI): m/z: calc for $C_{10}H_{12}N_2O_1$ $[M+H]^+$: 177.1028; found: 177.1025. M.P. 112-113 °C.

Synthesis of 3-(1H-pyrazol-3-yl)pyridine (2)

3-(dimethylamino)-1-(pyridine-3-yl)prop-2-en-1-one (28.00 g, 0.16 mol) was dissolved in ethanol (50 mL) before hydrazine hydrate (50 mL) was added and set to reflux with stirring at 65 °C for 40 minutes. Solvent was removed in vacuo. to give a dark orange oil. This was heated under vacuum over night before being washed twice with dichloromethane and water to remove any residual hydrazine. The organic layer was collected and a recrystallization was attempted using dichloromethane/hexane, however, the product separated as an oil. The solvent was removed and the oil was dissolved in chloroform and washed once more with water. The organic layer was collected and the solvent removed. The product was a dark orange oil. Final yield was 20.6 g, 90% yield. ^{1}H NMR ($CDCl_3$): δ 9.05 (1H, s; pyridyl H^2), 8.50 (1H, d, *J* = 4.8 Hz; pyridyl H^6), 8.20 (1H, d, *J* = 8.0 Hz; pyridyl H^4), 7.60 (1H, d, *J* = 1.8 Hz; pyazolyl H^9), 7.25 (1H, dd, *J* = 7.7, 4.9 Hz; pyridyl H^5), 5.50 (1H, d, *J* = 1.8 Hz; pyrazolyl H^8). $^{13}C\{^{1}H\}$ NMR ($CDCl_3$): δ 148.78, 148.63, 147.22, 132.75, 130.90, 129.42,

123.60, 102.09. HRMS (ESI): m/z: calc for $C_{10}H_{12}N_2O_1$ $[M+H]^+$: 146.0718; found: 146.0719. B.P. 144-150 °C.

General procedure for the alkylation of 3-(1H-pyrazol-3-yl)pyridine (3-7)

3-(1H-pyrazol-3-yl)pyridine (1.00 g, 6.89 mmol) was dissolved in toluene (30 mL). To this solution potassium hydroxide (5M, 13 mL) and tetrabutylammonium hydroxide (0.259 mL) were added before addition of the appropriate dibromide linker (4.13 mmol, 0.6 equivalents). The reaction was stirred vigorously and refluxed under nitrogen for 48 hours. A brown precipitate formed and was filtered off, the organic layer from the reaction was separated and the aqueous layer was washed twice with diethyl ether. The organic layers were combined and dried over anhydrous magnesium sulfate. The solvent was reduced to around 10 mL. The remaining mixture was placed in the fridge overnight and precipitation of a solid occurred which was filtered off to yield the pure product.

1,4-bis(3-(pyridin-3-yl)-1*H*-pyrazol-1-yl)butane (3)

Using 1,4-dibromobutane, yield: 38% as a solid. ^{1}H NMR ($CDCl_3$): δ = 9.00 (2H, s; pyridyl H^2), 8.50 (2H, d, *J* = 4.8 Hz; pyridyl H^6), 8.10 (2H, d, *J* = 7.9 Hz; pyridyl H^4), 7.40 (2H, d, *J* = 2.3 Hz; pyrazolyl H^9), 6.50 (2H, dd, *J* = 7.7, 4.8 Hz; pyridyl H^5), 4.20 (4H, m; butyl H^a), 1.90 (4H, m; butyl H^b). $^{13}C\{^1H\}$ NMR ($CDCl_3$): δ = 148.73, 148.64, 147.23, 132.76, 130.92, 129.50, 123.59, 103.02, 51.86, 27.58. FT-IR (wavenumber, cm^{-1}): 2950 (C-H alkyl), 1575 (C=C, aromatic), 820, 790, 750, 710 (C-H, aromatic). HRMS (ESI): m/z: calc for $C_{20}H_{20}N_6$ $[M+H]^+$: 345.1828; found: 345.1837. M.P. 94-95 °C.

50 mg was dissolved acetonitrile (2 mL), giving crystals of X-ray diffraction quality by using solvent evaporation techniques.

Molecular formula	$C_{20}H_{20}N_6$
Formula weight	344.42
Temperature	150.01(10) K
Radiation, wavelength	MoKα, λ = 0.71073 Å
Crystal system, space group	Monoclinic, $P2_1/n$
Unit cell parameters	a = 5.7247(5) Å α = 90°
	b = 10.9096(11) Å β = 93.665(9)°
	c = 13.8441(11) Å γ = 90°

Cell volume	862.86(14) $Å^3$
Z	2
Crystal colour and size	Orange, 0.05 × 0.27 × 0.42 mm^3
Final *R* indices [$F^2>2\sigma$]	R_1 = 0.0525
R indices (all data)	wR_2 = 0.1209
Large diff. peak and hole	0.17/-0.22 e $Å^{-3}$

1,4-bis(3-(pyridin-3-yl)-1*H*-pyrazol-1-yl)but-2-ene (4)

Using 1,4-dibromobutene, yield: 11% as a solid. ^{1}H NMR ($CDCl_3$): δ = 9.00 (2H, s; pyridyl H^2), 8.50 (2H, d, *J* = 4.7 Hz; pyridyl H^6), 8.10 (2H, d, *J* = 7.8 Hz; pyridyl H^4), 7.40 (2H, d, *J* = 2.3 Hz; pyrazolyl H^9), 6.60 (2H, m; pyridyl H^5), 5.80 (4H, m; butenyl H^a), 4.70 (2H, m; butenyl H^b). $^{13}C\{^1H\}$ NMR ($CDCl_3$): δ = 148.90, 148.85, 147.28, 132.84, 130.89, 129.37, 128.99, 23.60, 103.56, 53.56. FT-IR (wavenumber, cm^{-1}): 1660, (C=C, alkenyl) 750, 710, 610 (C-H, aromatic). HRMS (ESI): m/z: calc for $C_{20}H_{18}N_6$ $[M+H]^+$: 343.1671; found: 343.1678. M.P. 134-136 °C.

100 mg was dissolved in acetonitrile (5 mL), giving crystals suitable for x-ray diffraction by solvent evaporation.

Molecular formula	$C_{20}H_{18}N_6$
Formula weight	342.40
Temperature	150.01(10) K
Radiation, wavelength	MoKα, λ = 0.71073 Å
Crystal system, space group	Monoclinic, $P2_1/c$
Unit cell parameters	a = 5.1521(4) Å α = 90°
	b = 14.6833(10) Å β = 94.886(7)°
	c = 11.2126(7) Å γ = 90°
Cell volume	845.14(10) $Å^3$
Z	2
Crystal colour and size	Orange, 0.06 × 0.10 × 0.02 mm^3
Final *R* indices [$F^2>2\sigma$]	R_1 = 0.0536
R indices (all data)	wR_2 = 0.1210
Large diff. peak and hole	0.20/-0.21 e $Å^{-3}$

1,6-bis(3-(pyridin-3-yl)-1*H*-pyrazol-1-yl)hexane (5)

Using 1,6-dibromohexane, yield: 28% as a solid. ^{1}H NMR ($CDCl_3$): δ = 9.00 (2H, s; pyridyl H^2), 8.50 (2H, d, *J* = 4.8 Hz; pyridyl H^6), 8.06 (2H, d, *J* = 8.0 Hz; pyridyl H^4), 7.39 (2H, d, *J* = 2.3 Hz; pyrazolyl H^9), 6.50 (2H, dd, *J* = 7.9, 4.9 Hz; pyridyl H^5), 4.13 (4H, d, *J* = 7.2 Hz; hexyl H^a), 1.90 (4H, m; hexyl H^b), 1.36 (4H, m; hexyl H^c). $^{13}C\{^1H\}$ NMR ($CDCl_3$): δ = 148.66, 148.42, 147.25, 132.76, 130.74, 129.60, 123.60, 102.87, 52.39, 30.33, 26.21. FT-IR (wavenumber, cm^{-1}): 2950 (C-H,

alkyl), 1575 (C=C, aromatic), 800, 780, 600 (C-H, aromatic). HRMS (ESI): m/z: calc for $C_{22}H_{24}N_6$ $[M+H]^+$: 373.2141; found: 373.2146. M.P. 97-99 °C.

10 mg was dissolved in acetonitrile (5 mL), giving crystals suitable for x-ray diffraction using solvent evaporation.

Molecular formula	$C_{22}H_{24}N_6$
Formula weight	327.47
Temperature	150.01(10) K
Radiation, wavelength	MoKα, λ = 0.71073 Å
Crystal system, space group	Trigonal, *R* -3
Unit cell parameters	a = 21.5811(13) Å α = 90°
	b = 21.5811(13) Å β = 90°
	c = 11.0451(7) Å γ = 120°
Cell volume	4455.0(6) Å^3
Z	9
Crystal colour and size	Orange, 0.07 × 0.25× 0.88 mm^3
Final *R* indices [$F^2>2\sigma$]	R_1 = 0.0463
R indices (all data)	wR_2 = 0.1119
Large diff. peak and hole	0.20/-0.24 e Å^{-3}

1,8-bis(3-(pyridin-3-yl)-1*H*-pyrazol-1-yl)octane (6)

Using 1,8-dibromooctane, yield: 28% as a solid. ^{1}H NMR ($CDCl_3$): δ 9.00 (2H, s; pyridyl H^2), 8.50 (2H, d; *J* = 4.91 Hz; pyridyl H^6), 8.07 (2H, d; *J* = 7.9 Hz; pyridyl H^4), 7.40 (2H, d; *J* = 2.3 Hz; pyrazolyl H^9), 7.29 (2H, dd; *J* = 7.9, 4.8 Hz; pyridyl H^5), 6.55 (2H, d; *J* = 2.3 Hz; pyrazolyl H^8), 4.13 (4H, d; *J* = 7.1 Hz; octyl H^a), 1.83 (4H, m; octyl H^b) 1.32 (8H, m; octyl H^c). $^{13}C\{^1H\}$ NMR ($CDCl_3$): δ 148.54, 148.28, 147.16, 132.79, 130.68, 129.65, 123.58, 102.80, 52.53, 30.45, 29.01, 26.56. FT-IR (wavenumber, cm^{-1}): 2950 (C-H,alkyl), 1575 (C=C, aromatic), 810, 780, 610 (C-H, aromatic). HRMS (ESI): m/z: calc for $C_{24}H_{28}N_6$ $[M+H]^+$: 401.2454; found: 401.2455. M.P. 60-65°C.

50 mg was dissolved in toluene (5 mL), giving crystals suitable for x-ray diffraction by solvent evaporation.

Molecular formula	$C_{24}H_{28}N_6$
Formula weight	400.52
Temperature	150(2) K
Radiation, wavelength	MoKα, λ = 0.71073 Å
Crystal system, space group	Monoclinic, $P2_1/c$
Unit cell parameters	a = 9.0925(9) Å α = 90°
	b = 15.2647(15) Å β = 108.924(12)°
	c = 8.1260(10) Å γ = 90°
Cell volume	1066.9(2) Å^3

Z	2
Crystal colour and size	Colourless, 0.05 × 0.09 × 0.17 mm^3
Final *R* indices [$F^2>2\sigma$]	R_1 = 0.0645
R indices (all data)	wR_2 = 0.1340
Large diff. peak and hole	0.19/-0.22 e $Å^{-3}$

4,4'-bis((3-(pyridin-3-yl)-1*H*-pyrazol-1-yl)methyl)-1,1'-biphenyl (7)

Using 4,4-bis(bromomethyl)biphenyl, yield: 31% as a solid. ^{1}H NMR ($CDCl_3$): δ 9.05 (2H, s; pyridyl H^2), 8.54 (2H, d, *J* = 4.9 Hz, pyridyl H^6), 8.12 (2H, d; *J* = 7.7 Hz, pyridyl H^4), 7.55 (2H, dd, *J* = 8.0 Hz; pyridyl H^5), 7.45 (2H, d, *J* = 2.3 Hz; pyrazolyl H^9), 7.33 (4H, d, *J* = 8.3 Hz; phenyl H^8), 7.30 (4H, d, *J* = 5.0 Hz; phenyl $H^{12,13}$), 6.64 (2H, d, *J* = 2.3 Hz; pyrazolyl $H^{14,15}$), 5.40 (4H, s; CH_2), $^{13}C\{^1H\}$ NMR ($CDCl_3$): δ 148.83, 147.32, 140.50, 135.65, 132.87, 131.08, 129.45, 128.30, 127.64, 123.59, 103.69, 55.98. FT-IR (wavenumber, cm^{-1}): 2920 (C-H, alkyl), 1565 (C=C, aromatic), 1550 (C=C, aromatic), 800, 770, (C-H, aromatic). HRMS (ESI): m/z: calc for $C_{30}H_{24}N_6$ $[M+H]^+$: 469.2141; found: 469.2143. M.P. 53-55°C

50 mg was dissolved in methanol (10 mL), giving crystals suitable for x-ray diffraction after solvent evaporation.

Molecular formula	$C_{30}H_{24}N_6$	
Formula weight	468.55	
Temperature	150.15 K	
Radiation, wavelength	CuKα, λ = 1.54184 Å	
Crystal system, space group	Monoclinic, $P2_1/c$	
Unit cell parameters	a = 4.5083(4) Å	α = 90°
	b = 22.2817(14) Å	β = 93.297(6)°
	c = 11.5798(7) Å	γ = 90°
Cell volume	1161.30(14) $Å^3$	
Z	2	
Crystal colour and size	Colourless, 0.04 × 0.14 × 0.29 mm^3	
Final *R* indices [$F^2>2\sigma$]	R_1 = 0.0506	
R indices (all data)	wR_2 = 0.1400	
Large diff. peak and hole	0.15/-0.24 e $Å^{-3}$	

General procedure for dehydration reactions of pyridine-3-carboxaldehyde (8-12)

Pyridine-3-carboxaldehyde (5.00 mL, 53.26 mmol) was mixed with ethanol (50 mL), dichloromethane (50 mL) and the appropriate diamine linker (26.63 mmol, 0.5 equivalents) before formic acid (two drops) was added. The mixture was

stirred at room temperature overnight. The solvent was reduced to dryness and the solid was washed with hexane and dried.

***N,N'*-(ethane-1,2-diyl)bis(1-(pyridin-3-yl)methanimine) (8)**

Using 1,2-diaminoethane, yield: 90% as a solid. ^{1}H NMR ($CDCl_3$): δ = 9.09 (2H, s; pyridyl H^{2}), 8.68 (2H, d, *J* = 4.8 Hz; pyridyl H^{6}), 8.24 (2H, s; imine H^{7}), 8.05 (2H, d, *J* = 8.0 Hz; pyridyl H^{4}), 7.43 (2H, dd, *J* = 7.7, 4.8 Hz; pyridyl H^{5}), 1.40 (4H, s; CH_2). ^{13}C{^{1}H} NMR ($CDCl_3$): δ = 158.28, 151.60, 150.32, 134.55, 132.06, 124.40, 61.89. FT-IR (wavenumber, cm^{-1}): 2940, (C-H, alkyl), 1670 (C=N, imine), 1540 (C=C, aromatic), 710, (aromatic C-H). HRMS (ESI): m/z: calc for $C_{14}H_{14}N_4$ $[M+H]^+$: 239.1297; found: 239.1301. M.P. 84-86 °C.

100 mg was dissolved in ethyl acetate (3 mL), giving crystals suitable for x-ray diffraction by solvent evaporation.

Molecular formula	$C_{14}H_{14}N_4$
Formula weight	238.29
Temperature	150.1 K
Radiation, wavelength	MoKα, λ = 0.71073 Å
Crystal system, space group	Monoclinic, $P2_1/c$
Unit cell parameters	a = 13.4568(19) Å α = 90°
	b = 4.1390(6) Å β = 102.282(14)°
	c = 11.1975(18) Å γ = 90°
Cell volume	609.40(16) Å^3
Z	2
Crystal colour and size	Yellow, 0.20 × 0.24 × 0.80 mm^3
Final *R* indices [$F^2>2\sigma$]	R_1 = 0.0529
R indices (all data)	wR_2 = 0.1458
Large diff. peak and hole	0.17/-0.26 e Å^{-3}

***N,N'*-(1,4-phenylene)bis(1-(pyridin-3-yl)methanimine) (9)**

Using 1,4-diaminobenzene, yield: 43% as a solid. ^{1}H NMR ($CDCl_3$): δ = 9.02 (2H, s; pyridyl H^{2}), 8.71 (2H, d, *J* = 4.7 Hz; pyridyl H^{6}), 8.55 (2H, s; imine H^{7}), 8.30 (2H, d, *J* = 8.0 Hz; pyridyl H^{4}), 7.42 (2H, dd, *J* = 7.8, 4.7 Hz; pyridyl H^{5}), 7.31 (4H, s; phenyl H^{9,10}). ^{13}C{^{1}H} NMR ($CDCl_3$): δ = 158.14, 150.87, 150.04, 141.22, 133.20, 129.93, 123.99, 123.22. FT-IR (wavenumber, cm^{-1}): 2930, (C-H, alkyl), 1660 (C=N, imine), 1540 (C=C, aromatic), 710, 620 (aromatic C-H). HRMS (ESI): m/z: calc for $C_{18}H_{14}N_4$ $[M+H]^+$: 287.1297; found: 287.1297. M.P. 148-149 °C.

50 mg was dissolved in ethanol/hexane (4 mL, 50:50, v:v), giving crystals suitable for x-ray diffraction by solvent evaporation.

Molecular formula	$C_{18}H_{14}N_4$
Formula weight	286.33
Temperature	150.15 K
Radiation, wavelength	CuKα, λ = 1.54184 Å
Crystal system, space group	Monoclinic, $P2_1/c$
Unit cell parameters	a = 16.4979(9) Å α = 90°
	b = 6.1170(3) Å β = 95.868(5)°
	c = 7.0645(4) Å γ = 90°
Cell volume	709.19(7) Å^3
Z	2
Crystal colour and size	Yellow, 0.17 × 0.14 × 0.25 mm^3
Final *R* indices [$F^2>2\sigma$]	R_1 = 0.0355
R indices (all data)	wR_2 = 0.0953
Large diff. peak and hole	0.14/-0.21 e Å^{-3}

_N,N_'-(cyclohexane-1,4-diyl)bis(1-(pyridin-3-yl)methanimine) (10)

Using 1,4-transdiaminocyclohexane, yield: 54% as a solid. ^{1}H NMR ($CDCl_3$): δ = 8.85 (2H, s; pyridyl H^2), 8.63 (2H, d, *J* = 4.8 Hz; pyridyl H^6), 8.40 (2H, s; imine H^7), 8.11 (2H, d, *J* = 8.0 Hz; pyridyl H^4), 7.33 (2H, dd, *J* = 7.9, 4.8 Hz; pyridyl H^5), 3.33 (2H, m; cyclohexyl H^8), 1.83 (8H, m; cyclohexyl H^{9,10}). ^{13}C{^{1}H} NMR ($CDCl_3$): δ = 156.90, 151.27, 150.22, 133.99, 131.98, 124.48, 69.37, 32.35. FT-IR (wavenumber, cm^{-1}): 2940, (C-H, alkyl), 1670 (C=N, imine), 1530 (C=C, aromatic), 710, 610 (aromatic C-H). HRMS (ESI): m/z: calc for $C_{18}H_{20}N_4$ $[M+H]^+$: 293.1766; found: 293.1760. M.P. 160-161 °C.

100 mg was dissolved in ethyl acetate (5 mL), giving crystals suitable for x-ray diffraction by solvent evaporation.

Molecular formula	$C_{18}H_{20}N_4$
Formula weight	292.38
Temperature	120.0 K
Radiation, wavelength	MoKα, λ = 0.71073 Å
Crystal system, space group	Monoclinic, $P2_1/n$
Unit cell parameters	a = 6.0581(4) Å α = 90°
	b = 5.5638(4) Å β = 93.8144(19)°
	c = 23.2277(14) Å γ = 90°
Cell volume	781.18(9) Å^3
Z	2
Crystal colour and size	Colourless, 0.20 × 0.25 × 0.44 mm^3
Final *R* indices [$F^2>2\sigma$]	R_1 = 0.0395
R indices (all data)	wR_2 = 0.1066
Large diff. peak and hole	0.30/-0.24 e Å^{-3}

***N*,*N*'-(hexane-1,6-diyl)bis(1-(pyridin-3-yl)methanimine) (11)**

Using 1,6-diaminohexane, yield: 72% as a solid. ^{1}H NMR ($CDCl_3$): δ = 9.10 (2H, s; pyridyl H^2), 8.73 (2H, d, *J* = 4.8 Hz; pyridyl H^6), 8.26 (2H, s; imine H^7), 8.04 (2H, d, *J* = 8.0 Hz; pyridyl H^4), 7.45 (2H, dd, *J* = 7.8, 4.8 Hz; pyridyl H^5), 1.47 (4H, m; hexyl H^8). 1.33 (8H, m; hexyl $H^{9,10}$). $^{13}C\{^{1}H\}$ NMR ($CDCl_3$): δ = 157.20, 151.90, 150.19, 135.04, 132.11, 124.42, 61.17, 33.14, 28.03. FT-IR (wavenumber, cm^{-1}): 2930, 2920 (C-H, alkyl), 1670 (C=N, imine), 1550 (C=C, aromatic), 710, 700 (aromatic C-H). HRMS (ESI): m/z: calc for $C_{18}H_{22}N_4$ $[M+H]^+$: 295.1923; found: 295.1919. M.P. 108-110 °C.

100 mg was dissolved in ethanol/CH_2Cl_2 (5 mL, 50:50, v:v), giving crystals suitable for x-ray diffraction after solvent evaporation.

Molecular formula	$C_{18}H_{20}N_4$
Formula weight	292.38
Temperature	150.01(10) K
Radiation, wavelength	CuKα, λ = 1.54184 Å
Crystal system, space group	Monoclinic, $P2_1/c$
Unit cell parameters	a = 10.1006(5) Å α = 90°
	b = 9.6729(4) Å β = 104.181(5)°
	c = 8.5768(4) Å γ = 90°
Cell volume	812.44(7) $Å^3$
Z	2
Crystal colour and size	Orange, 0.10 × 0.28 × 0.63 mm^3
Final *R* indices [$F^2>2\sigma$]	R_1 = 0.0622
R indices (all data)	wR_2 = 0.1746
Large diff. peak and hole	0.43/-0.35 e $Å^{-3}$

***N*,*N*'-(naphthalene-1,5-diyl)bis(1-(pyridin-3-yl)methanimine) (12)**

Using 1,5-diaminonapthalene, yield: 65% as a solid. ^{1}H NMR ($CDCl_3$): δ = 9.13 (2H, s; pyridyl H^2), 8.75 (2H, d, *J* = 3.6 Hz; pyridyl H^6), 8.62 (2H, s; imine H^7), 8.43 (2H, d, *J* = 7.0 Hz; pyridyl H^4), 8.26 (2H, d, *J* = 8.2 Hz; napthyl H^{12}), 7.50 (4H, m; napthyl $H^{10,11}$), 7.14 (2H, dd, *J* = 9.1, 5.0 Hz; pyridyl H^5). $^{13}C\{^{1}H\}$ NMR ($CDCl_3$): δ = 157.48, 151.55, 150.16, 147.68, 133.41, 130.01, 128.90, 128.12, 127.04, 123.76, 114.58. FT-IR (wavenumber, cm^{-1}): 3010 (aromatic C-H). 2930, (C-H, alkyl), 1670 (C=N, imine), 1550 (C=C, aromatic), 1520 (C=C, aromatic) 710, 670, 610 (aromatic C-H). HRMS (ESI): m/z: calc for $C_{22}H_{16}N_4$ $[M+H]^+$: 337.1453; found: 337.1459. M.P. 133-135 °C.

100 mg was dissolved in CH_2Cl_2 (7 mL), giving crystals suitable for x-ray diffraction after solvent evaporation.

Molecular formula	$C_{22}H_{16}N_4$
Formula weight	336.39
Temperature	150.0(2) K
Radiation, wavelength	MoKα, λ = 0.71073 Å
Crystal system, space group	Triclinic, *P*-1
Unit cell parameters	a = 6.6653(11) Å α = 74.820(14)°
	b = 7.5932(13) Å β = 80.358(13)°
	c = 9.3116(14) Å γ = 65.075(16)°
Cell volume	411.58(13) Å^3
Z	1
Crystal colour and size	Orange, 0.19 × 0.14 × 0.08 mm^3
Final *R* indices [$F^2>2\sigma$]	R_1 = 0.0527
R indices (all data)	wR_2 = 0.1578
Large diff. peak and hole	0.30/-0.25 e Å^{-3}

2.5 References

1. M. D. Ward, *Science*, 2005, **308**, 1566-1567.
2. A. Gavezzotti, *Acc. Chem. Res.*, 1994, **27**, 309-314.
3. Cambridge Structural Database, http://www.ccdc.cam.ac.uk/).
4. J. P. Glusker and K. N. Trueblood, *Crystal Structure Analysis; A Primer*, Oxford University Press, 1985.
5. W. Clegg, *Crystal Structure Determination; Oxford Chemistry Primer*, Oxford University Press, 1998.
6. W. H. Bragg, *Nature*, 1913, 572.
7. W. L. Bragg, *Proc. Camb. Phil. Soc.*, 1913, **17**, 43-57.
8. A. Kitaigorodskii, *Acta Crystallogr.*, 1965, **18**, 585-590.
9. P. Vishweshwar, J. A. McMahon, J. A. Bis and M. J. Zaworotko, *J. Pharm. Sci.*, 2006, **95**, 499-516.
10. J. Haleblian and W. McCrone, *J. Pharm. Sci.*, 1969, **58**, 911-929.
11. W. Li, M. R. Probert, M. Kosa, T. D. Bennett, A. Thirumurugan, R. P. Burwood, M. Parinello, J. A. K. Howard and A. K. Cheetham, *J. Am. Chem. Soc.*, 2012, **134**, 11940-11943.
12. K. Sumida, D. L. Rogow, J. A. Mason, T. M. McDonald, E. D. Bloch, Z. R. Herm, T.-H. Bae and J. R. Long, *Chem. Rev.*, 2012, **112**, 724-781.
13. N. L. Rosi, J. Eckert, M. Eddaoudi, D. T. Vodak, J. Kim, M. O'Keeffe and O. M. Yaghi, *Science*, 2003, **300**, 1127-1129.
14. M. Eddaoudi, J. Kim, N. Rosi, D. Vodak, J. Wachter, M. O'Keeffe and O. M. Yaghi, *Science*, 2002, **295**, 469-472.
15. Y. P. Prananto, D. R. Turner, J. Lu and S. R. Batten, *Aust. J. Chem.*, 2009, **62**, 108-114.
16. K. Ha, *Acta Crystallogr. Sect. E: Struct. Rep. Online*, 2011, **67**, o2250.
17. H. Adams, S. R. Batten, G. M. Davies, M. B. Duriska, J. C. Jeffery, P. Jensen, J. Lu, G. R. Motson, S. J. Coles, M. B. Hursthouse and M. D. Ward, *J. Chem. Soc., Dalton Trans.*, 2005, 1910-1923.
18. R. Taylor and O. Kennard, *J. Am. Chem. Soc.*, 1982, **104**, 5063-5070.
19. C. Foces-Foces, N. Jagerovic and J. Elguero, *Acta Crystallogr. Sect. C: Cryst. Struct. Commun.*, 2000, **56**, 215-218.
20. A. N. M. M. Rahman, R. Bishop, Donald C. Craig and Marcia L. Scudder, *Eur. J. Org. Chem.*, 2003, **2003**, 72-81.

21. W. B. Jennings, B. M. Farrell and J. F. Malone, *Acc. Chem. Res.*, 2001, **34**, 885-894.
22. H. N. Kim, H. K. Lee and S. W. Lee, *Bull. Korean Chem. Soc.*, 2005, **26**, 892-898.
23. Y.-h. Sun, K.-q. Ye, J.-f. Kong, D.-x. Zhu and Y. Wang, *Chin. J. Mol. Sci.*, 2006, **7**, 22.

Chapter 3

Influencing Potential Crystal Surface Binding Sites by Crystal Engineering

Table of Contents

3.1 Introduction

One of the attractive prospects of using molecular single crystals as template substrates for material binding, is the ability to manipulate the binding site spacing by simply using a different crystal structure as the template. As shown in Chapter 2, manipulation of the potential binding site spacing can be achieved by using a range of similar molecules, having the same binding site but with varying 'spacer unit' between them. It is now proposed that this binding site spacing can be further manipulated by creating a range of crystal structures from the same molecule, i.e. polymorphs. Using the same molecule should provide structures with binding site spacing on a very similar scale to each other, potentially offering 'fine-tuning' of their positions.

Probably the most widely used and accepted definition of polymorphism is given by McCrone,[1] "a solid crystalline phase of a given compound resulting from the possibility of at least two crystalline arrangements of the molecules of that compound in the solid state". As each polymorph has a different structure, it is effectively a unique material with its own physical and chemical properties[2] with consequences ranging from the bioavailability of a drug[3] to independent patent protection.[4] Polymorphism in crystals comes in the form of molecular conformational changes and changes in the packing arrangement of molecules (Scheme 3.1).[5]

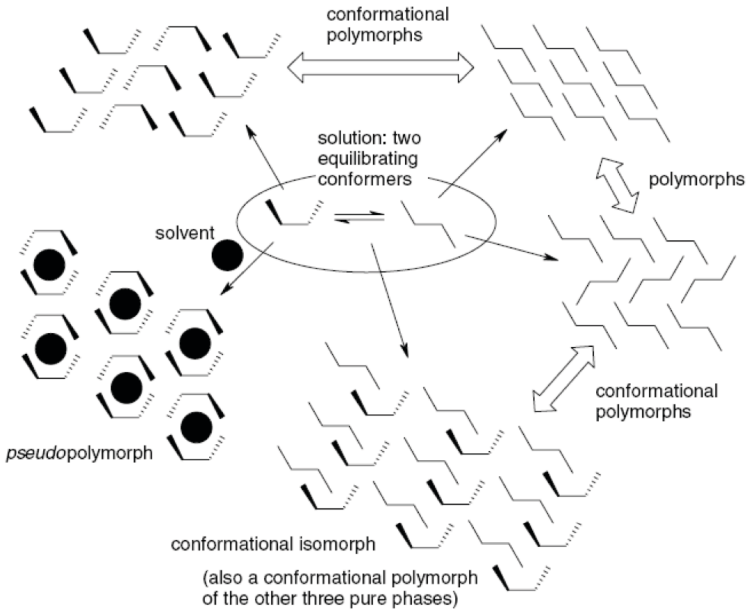

Scheme 3.1.[5] Illustration of the various types of polymorph and their relationship to one another. Reprinted with permission from J. W. Steed and J. L. Atwood, *Supramolecular Chemistry*, John Wiley & Sons, Ltd., Copyright 2009.

Here, we produce a library of crystals using a crystal engineering based screening approach to induce polymorphism, with the intent of expanding the range of possible binding site architectures present at our crystal surfaces.

As described by Desiraju,[6] crystal engineering is "the understanding of intermolecular interactions in the context of crystal packing and the utilization of such understanding in the design of new solids with desired physical and chemical properties". Mostly based on highly directional hydrogen bonding and coordination complexation,[7] the design of such structures makes use of supramolecular synthons and secondary building units[8] with hydrogen bonding interactions being of particular interest in crystals of small, discrete molecules because of their influence on molecular packing.[9, 10] The field encompasses both the analysis and synthesis of crystalline materials where the ability to predict crystal structures to precisely control a material's properties, is of great interest.[11] The enormous number of variables to account for in crystal growth, and multiple possible outcomes (polymorphs) mean it is no easy feat,[12] with no complete system yet proposed. Current techniques involve calculations by empirical methods such as atom-atom potentials,[13] ab initio methods such as tonto,[14] and combinations of the two such as PIXEL or DFT-D.[15]

To gain some insight into the formation of the Bis(3-(pyridin-3-yl)-1*H*-pyrazol-1-yl) and Bis(1-(pyridin-3-yl)methanimine) type crystals formed in Chapter 2, and the potential for polymorphism, a study of the empirical atom-atom intermolecular potentials was performed in Mercury (CCDC).[12, 13] This included looking at the strongest three intermolecular interactions in seven crystal structures of molecules from chapter 2. These values were then compared with the total energies calculated by density functional theory (DFT) for each interacting pair, using the Spartan software (WAVEFUNCTION INC).

Currently the most accurate predictions for crystal structure packing arrangements come from hybrid calculations (semi-empirical) where experimentally obtained data is used to aid ab initio methods.[15] Any data obtained here experimentally (polymorph structures created) and by calculation may provide a good foundation on which future structure predictions of which molecules may be performed.

3.2 Results and Discussion

3.2.1 Energy Calculations for Pypy-Hx (5)

Energy calculations were performed in order to gain insight into the molecular conformation and packing arrangement in crystals from chapter 2. Equilibrium geometry and single point energies for molecules in these crystals were calculated using density functional theory (DFT) with a B3LYP functional and using the 6-31G* basis set. These energies were then compared to the intermolecular potentials and crystal packing energy which were calculated using unified pair-potential parameters (UNI).

These energy calculations were performed on the molecules and crystal structures of the Bis(3-(pyridin-3-yl)-1*H*-pyrazol-1-yl) Pypy-Hx (**5**) and Pypy-Me-BiPh (**7**) as well as the Bis(1-(pyridin-3-yl)methanimine) molecules Py-Im-Et (**8**), Py-Im-Ph (**9**) and Py-Im-Cy (**10**) from chapter 2. Whilst structurally quite similar, these molecules show variation in the crystal packing arrangement, giving us a wide range of interactions to study.

Firstly, looking at Pypy-Hx (**5**), the equilibrium geometry energy for one molecule was calculated to be -3101455.65471 $kJmol^{-1}$, this is the energy of the molecule when it has no external constraints, such as in the gas phase. The crystal structure single point energy is higher, at -3100664.69658 $kJmol^{-1}$. A lower energy equates to a more stable conformation, so these values show what is expected, which is a lower energy in the gas phase as the molecule has more conformational freedom than in the crystal phase, where it is hindered by the surrounding lattice.

Intermolecular interaction (ordered by UNI strength)	UNI intermolecular potential ($kJmol^{-1}$)	Single point total energy per molecule ($kJmol^{-1}$)	Symmetry operation for interacting pair
1st	-43.84560	-3100673.57077	screw (3-fold)
2nd	-26.73770	-3100666.60006	screw (3-fold)
3rd	-21.30070	-3100674.55533	translation

Table 3.1 Intermolecular potential energies, single point crystals structure energies and symmetry operations for Pypy-Hx (**5**), ranked by intermolecular interaction strength (UNI).

The strongest three interacting pairs were calculated using UNI (Figure 3.1a) and the comparison of the intermolecular potential energies, single point crystal structure energies and symmetry operations for these molecular pairs is shown in Table 3.1. The strongest interaction is related by a screw (3-fold) symmetry operation in which the molecules' centre points are separated by 9.65 Å (Figure 3.1b).

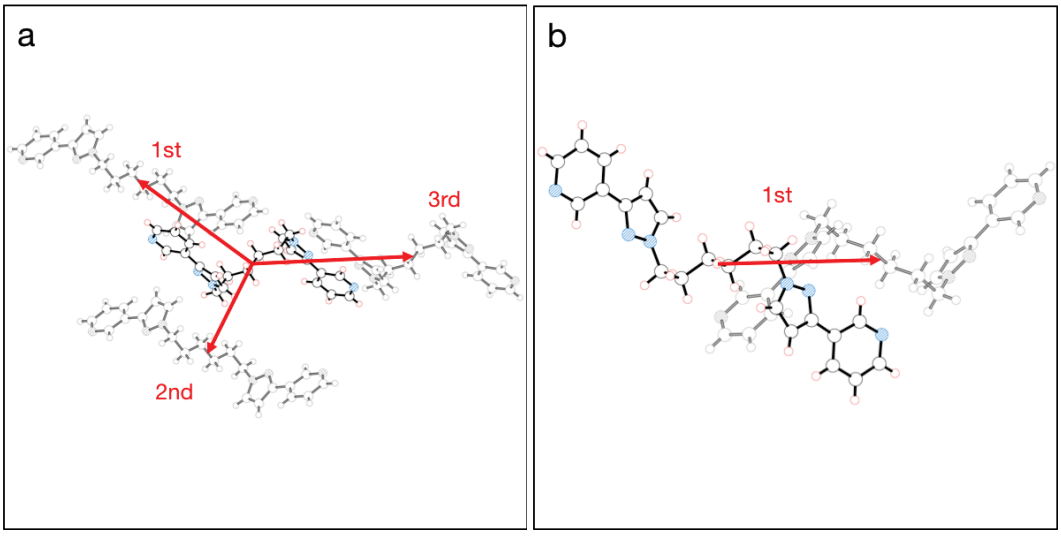

Figure 3.1 View of the strongest three intermolecular interactions in **5** as calculated by UNI, **a**, and a closer view of the 3-fold screw in the first interacting pair of molecules in **5**, **b**, viewed down b-axis. Red lines connect the molecules' central points from an origin molecule (in colour).

The second strongest interacting pair are also related to each other by a screw (3-fold) symmetry operation, with the molecules' centre points separated by 7.24 Å (Figure 3.2a). And the third strongest interacting pair are related to each other by a translation of 11.05 Å in the c-axis (Figure 3.2b).

The second strongest interaction here (by UNI) gives the highest energy pair of molecules (single point total energy), with the other pairs having a lower energy (shown by single point total energy) as the interactions are supposedly less stable (UNI). These observations may be due to the use of atom-atom potentials being a simplistic approach, with empirical parameters and atomic charges needing to be assigned individually from a library of experimental statistical data such as atom-atom close contact distances, vaporization enthalpies and sublimation enthalpies.[11] Another factor which may reduce the accuracy of these values is that the standard DFT calculations do not take into

account the van der Waals interactions between molecules, as they use an independent electron approximation.[16]

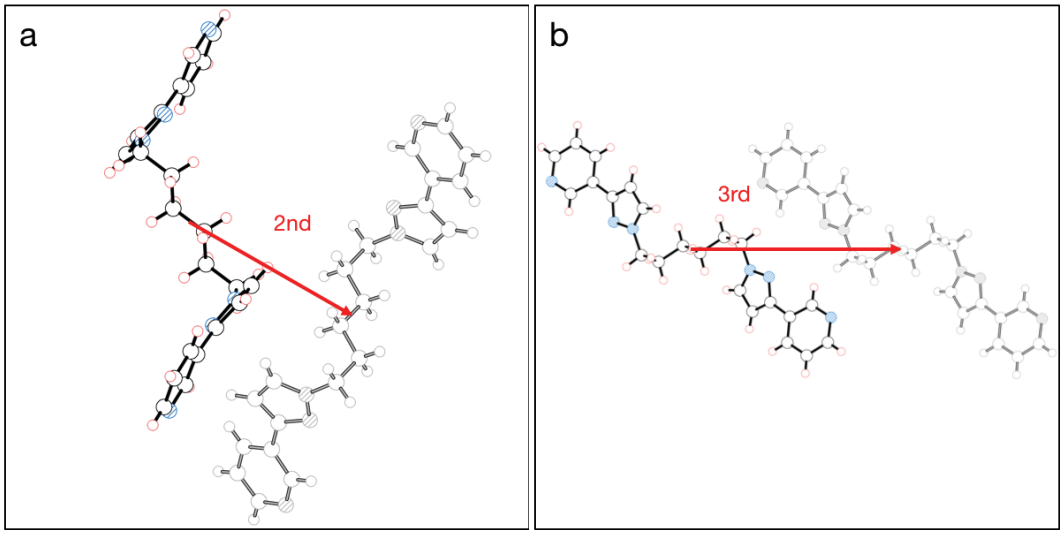

Figure 3.2 a, View down a-axis of the second interacting pair '3-fold screw' in **5**, and **b**, View down b-axis of the third interacting pair 'translation' in **5**. Red lines connect the molecules' central points from an origin molecule (in colour).

3.2.2 Energy Calculations for Pypy-Me-BiPh (7)

The gas phase equilibrium geometry for one molecule of **7** has a calculated energy of -3901837.88568 $kJmol^{-1}$, and from the crystal structure, a single point energy of -3900928.70129 $kJmol^{-1}$ which is again, higher than for the gas phase.

The strongest three interacting pairs were calculated from the crystal structure of **7** (Figure 3.3a) with their intermolecular potential energy, single point crystal structure energy and symmetry operations shown in Table 3.2. The strongest interacting pair are related to each other by a translation of 4.51 Å in the a-axis (Figure 3.3b), and show a much lower intermolecular potential energy than for all the other pairs, making it a very stabilizing interaction.

Intermolecular interaction (ordered by UNI strength)	UNI intermolecular potential ($kJmol^{-1}$)	Single point total energy per molecule ($kJmol^{-1}$)	Symmetry operation for interacting pair
1st	-134.83200	-3900925.03871	translation
2nd	-31.96470	-3900934.83183	screw (2-fold)
3rd	-16.28130	-3900937.96930	screw (2-fold)

Table 3.2 Intermolecular potential energies, single point crystals structure energies and symmetry operations for Pypy-Me-BiPh (**7**), ranked by intermolecular interaction strength (UNI).

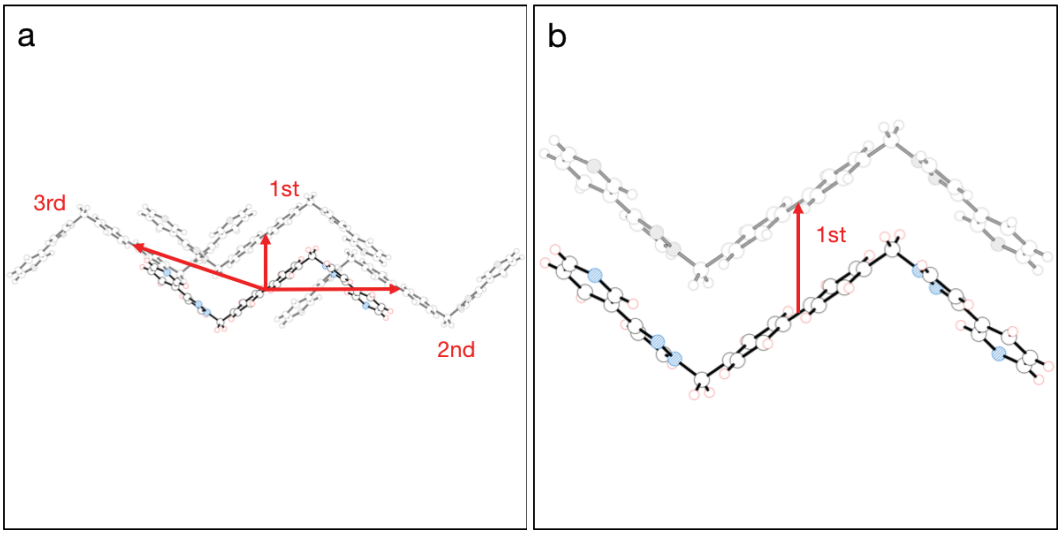

Figure 3.3 View of the strongest three intermolecular interactions in **7** as calculated by UNI, **a**, and a closer view of the translation of the first interacting pair of molecules in **7**, **b**, viewed down c-axis. Red lines connect the molecules' central points from an origin molecule (in colour).

The pair showing the second strongest interaction (by UNI) are related to each other by a screw (2-fold) symmetry operation, with the molecules' centre points separated by 12.56 Å (Figure 3.4a) and the third strongest interacting pair in this crystal structure are also related by a screw (2-fold) symmetry operation, with the centre points separated by 13.45 Å (Figure 3.4b).

The single point total energies for each pair here seem to increase as the intermolecular potential (UNI) suggests stabilizing interactions, again showing the opposite trend to what is expected, highlighting the shortcomings of empirical and ab initio calculations when used separately.

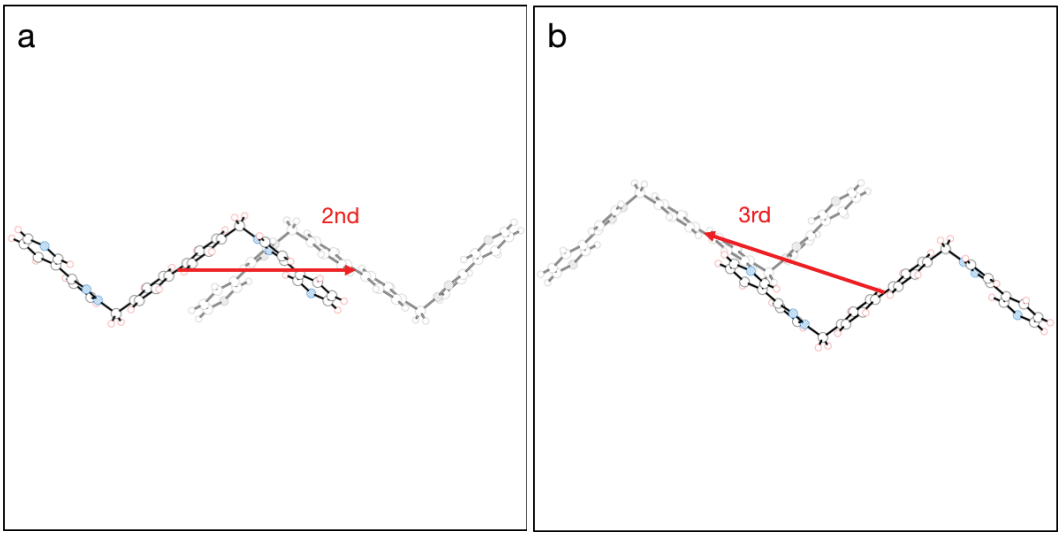

Figure 3.4 a, View down c-axis of the second interacting pair '2-fold screw' in **7**, and **b**, View down c-axis of the third interacting pair '2-fold screw' in **7**. Red lines connect the molecules' central points from an origin molecule (in colour).

3.2.3 Energy Calculations for Py-Im-Et (8)

Now looking at Py-Im-Et (**8**) first produced by Sun et al.[17] the energy of a single molecule in the gas phase (equilibrium geometry) was calculated to be -1997721.29488 kJmol^{-1}, lower than for a single molecule in the crystal structure (single point energy taken from the crystal structure of **8**), which was calculated to be -1997386.68540 kJmol^{-1}.

The energies for the strongest three interacting molecular pairs (as calculated by UNI) (Figure 3.5a) were then compared through intermolecular potential energy, single point crystal structure energy and symmetry operations (Table 3.3). The first (strongest) interacting pair has a 'translation' symmetry operation and is separated by its partner molecule by 4.14 Å in the b-axis (Figure 3.5b).

Intermolecular interaction (ordered by UNI strength)	UNI intermolecular potential (kJmol^{-1})	Single point total energy per molecule (kJmol^{-1})	Symmetry operation for interacting pair
1st	-60.51800	-1997387.75923	translation
2nd	-19.20490	-1997387.99553	screw (2-fold)
3rd	-9.82198	-1997390.96234	screw (2-fold)

Table 3.3 Intermolecular potential energies, single point crystals structure energies and symmetry operations for Py-Im-Et (**8**), ranked by intermolecular interaction strength (UNI).

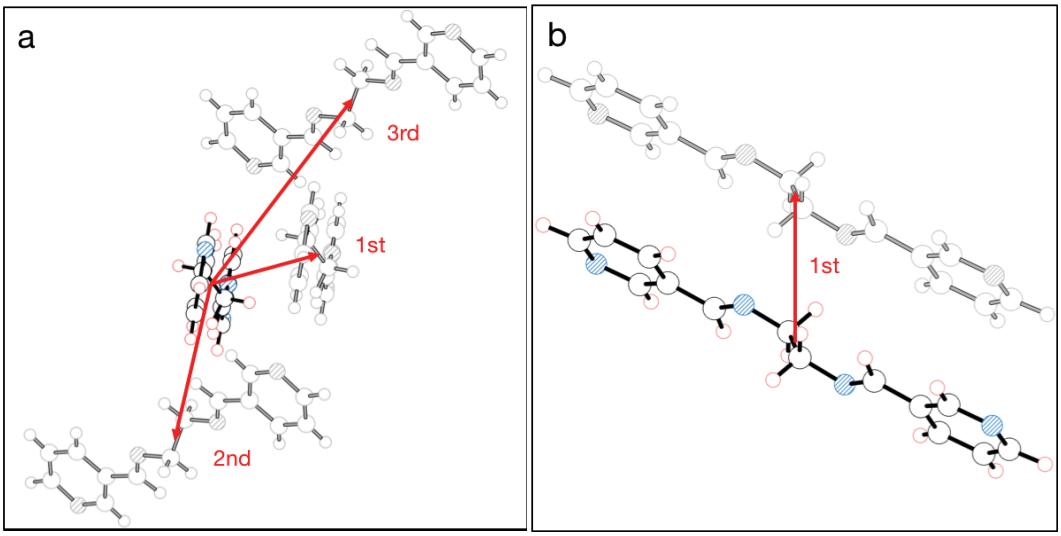

Figure 3.5 View of the strongest three intermolecular interactions in **8** as calculated by UNI, **a**, and a closer view of the translation of the first interacting pair of molecules in **8**, **b**, viewed down c-axis. Red lines connect the molecules' central points from an origin molecule (in colour).

The second strongest interacting pair have a screw (2-fold) symmetry operation, with the molecules' centre points separated by 6.00 Å (Figure 3.6a), with the third strongest interacting pair also having a screw (2-fold) symmetry relationship with the centre points separated by 8.36 Å (Figure 3.6b). The energies calculated here for each pair seem to increase as the intermolecular potential suggests more stabilizing interactions, showing the opposite trend to what is expected as a stronger interaction should lower the overall energy. These values again show the opposite trend to what is expected, highlighting the shortcomings of empirical and ab initio calculations when used separately.

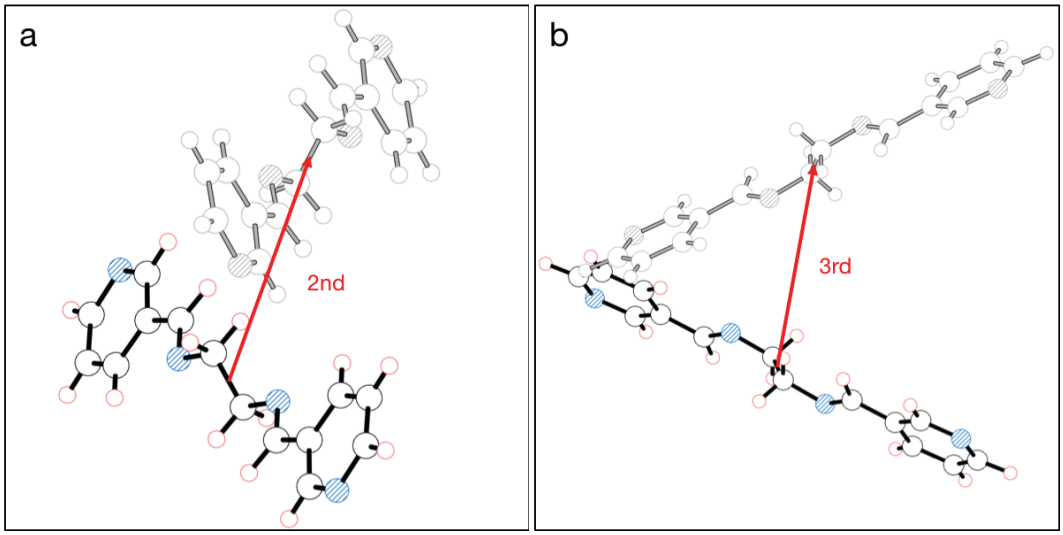

Figure 3.6 a, View down a-axis of the second interacting pair '2-fold screw' in **8**, and **b**, View down c-axis of the third interacting pair '2-fold screw' in **8**. Red lines connect the molecules' central points from an origin molecule (in colour).

3.2.4 Energy Calculations for Py-Im-Ph (9)

Molecule **9**, first produced by Ha et al.[18] has a calculated equilibrium geometry energy of -2397936.59122 kJmol^{-1} and a higher single point energy (taken from the **9** crystal structure) of -2397594.44656 kJmol^{-1}. From the crystal structure of **9**, the strongest three interacting pairs of molecules were calculated using UNI (Figure 3.7a) and their intermolecular potential energy, single point crystal structure energy and symmetry operations are shown in Table 3.4. The strongest interacting pair are related by a screw (2-fold) symmetry operation, with the molecules' centre points separated by 4.67 Å (Figure 3.7b).

Intermolecular interaction (ordered by UNI strength)	UNI intermolecular potential (kJmol^{-1})	Single point total energy per molecule (kJmol^{-1})	Symmetry operation for interacting pair
1st	-49.98320	-2397594.87714	screw (2-fold)
2nd	-20.57650	-2397604.11890	translation
3rd	-7.85060	-2397596.39993	translation

Table 3.4 Intermolecular potential energies, single point crystals structure energies and symmetry operations for Py-Im-Ph (**9**), ranked by intermolecular interaction strength (UNI).

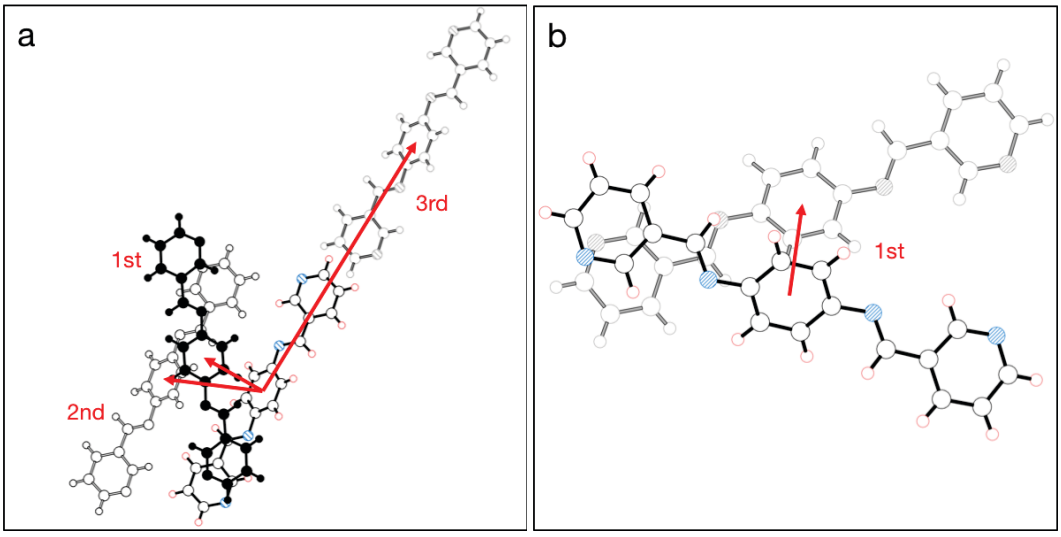

Figure 3.7 View of the strongest three intermolecular interactions in **9** as calculated by UNI, **a**, and a closer view of the 2-fold screw in the first interacting pair of molecules in **9**, **b**, viewed down c-axis. Red lines connect the molecules' central points from an origin molecule (in colour).

The next strongest interacting pair (2nd) is related by a translation of 6.12 Å in the b-axis (Figure 3.8a) and the third strongest interacting pairs of molecules in

this crystal structure are also related by a translation, this time of 17.60 Å in the a-axis (Figure 3.8b).

The energy of the interacting pairs here increases as the intermolecular potentials also show an increase in energy, with the exception of the strongest interacting pair (lowest intermolecular potential), which has the highest energy.

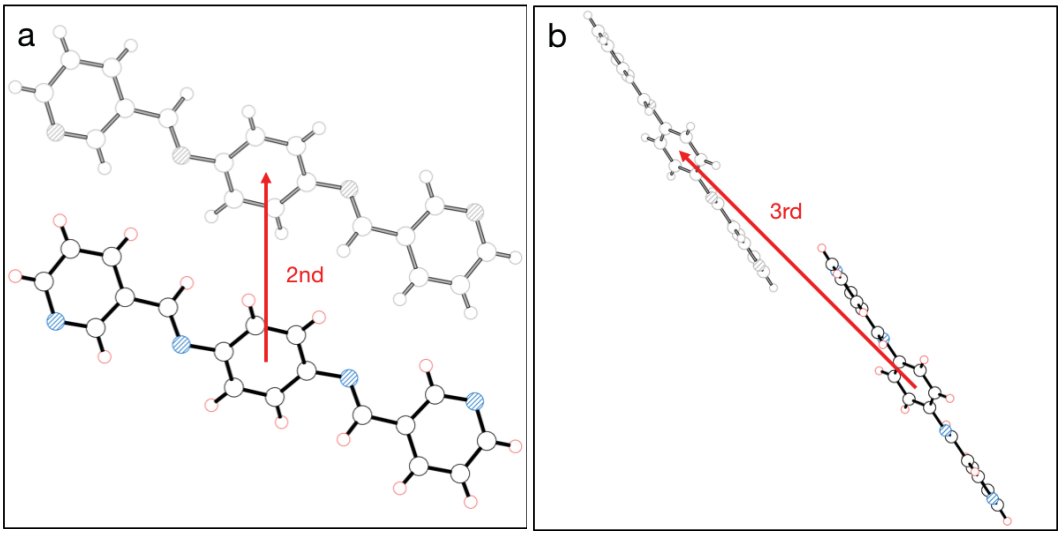

Figure 3.8 a, View down c-axis of the second interacting pair 'translation' in **9**, and **b**, View down b-axis of the third interacting pair 'translation' in **9**. Red lines connect the molecules' central points from an origin molecule (in colour).

3.2.5 Energy Calculations for Py-Im-Cy (10)

Now looking at the cyclohexyl linked imine molecule (**10**), the equilibrium geometry energy for one molecule was calculated to be -2407452.74485 kJmol^{-1} and the single point energy for one molecule from the crystal structure of **10** was calculated to be -2406775.51813 kJmol^{-1} which is again higher than for the gas phase. The strongest three interacting pairs of molecules in the **10** crystal structure were calculated using UNI (Figure 3.9a) with their intermolecular potential energy, single point crystal structure energy and symmetry operations shown in Table 3.5. The strongest interacting pair have a 'translation' symmetry relationship and are separated by 8.23 Å in the b-axis (Figure 3.9b).

Intermolecular interaction (ordered by UNI strength)	UNI intermolecular potential ($kJmol^{-1}$)	Single point total energy per molecule ($kJmol^{-1}$)	Symmetry operation for interacting pair
1st	-53.23270	-2406780.01824	translation
2nd	-33.75720	-2406783.53641	translation
3rd	-26.48410	-2406778.60047	translation

Table 3.5 Intermolecular potential energies, single point crystals structure energies and symmetry operations for Py-Im-Cy (**10**), ranked by intermolecular interaction strength (UNI).

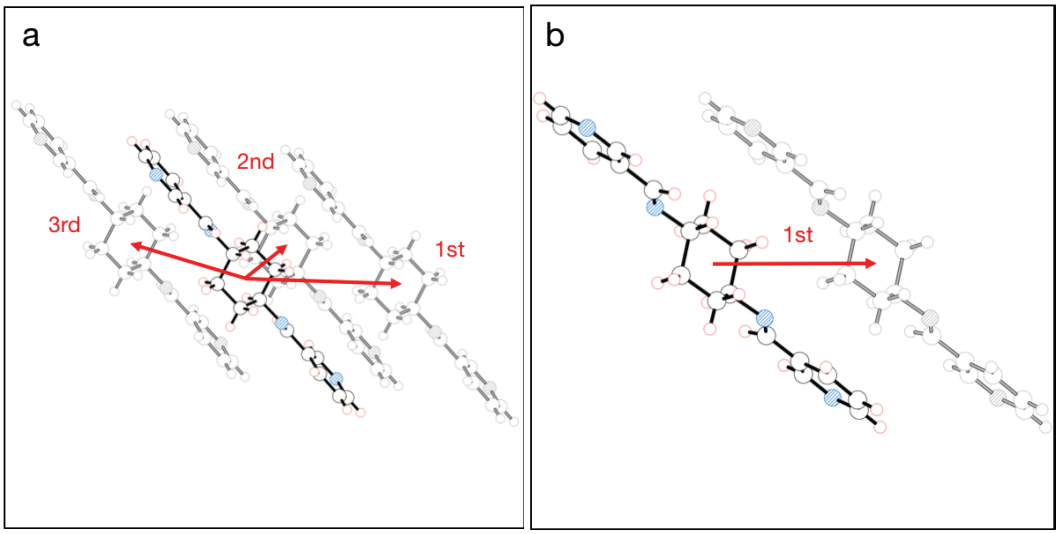

Figure 3.9 View of the strongest three intermolecular interactions in **10** as calculated by UNI, **a**, and a closer view of the translation of the first interacting pair of molecules in **10**, **b**, viewed down a-axis. Red lines connect the molecules' central points from an origin molecule (in colour).

The second strongest interacting pair also show a translation symmetry relationship separated by 6.06 Å in the a-axis (Figure 3.10a) and the third strongest interacting pair again show a translation symmetry relationship, separated by 5.56 Å in the b-axis (Figure 3.10b).

The lowest energy pair here (calculated by single point total energy) show the second strongest interaction potential (by UNI) with the highest energy pair (single point total energy) being the third strongest by UNI, these values show more of an agreement with each other than for **8**.

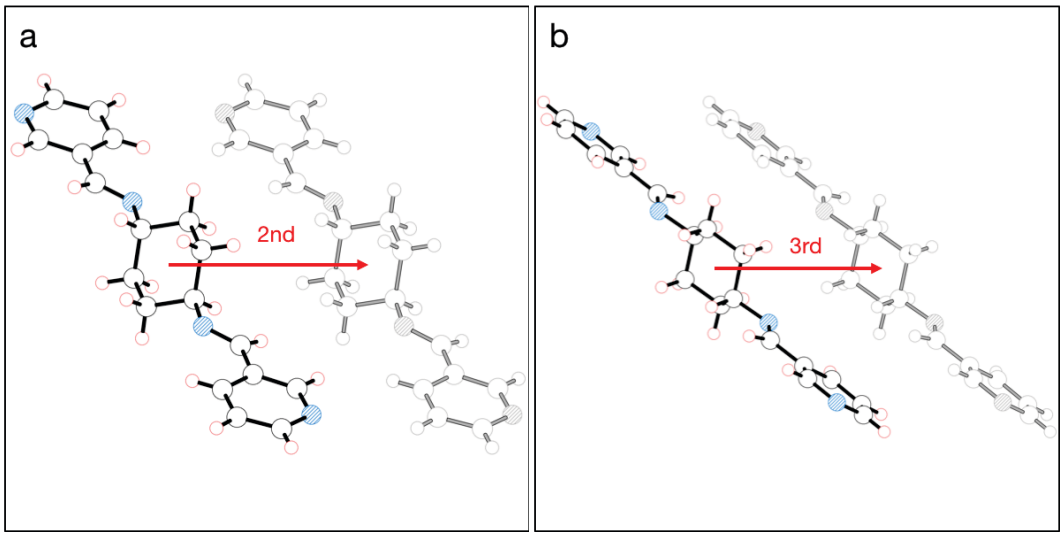

Figure 3.10. a, View down b-axis of the second interacting pair 'translation' in **10**, and **b**, View down a-axis of the third interacting pair 'translation' in **10**. Red lines connect the molecules' central points from an origin molecule (in colour).

3.2.6 Crystal Engineering of 8, 9 and 10

A library-based crystal engineering approach was used in an attempt to induce crystal polymorphism. Manipulation of the crystal structure in this way may expand the potential for spatial fine-tuning of potential surface binding sites of our crystals. The library is made up of three compounds, crystallized using a range of solvents and crystallization conditions.

The molecules looked at here were Py-Im-Et (**8**), Py-Im-Ph (**9**) and Py-Im-Cy (**10**). These molecule were chosen because they can be produced in the higher yields necessary for multiple crystallizations under different conditions and using various solvents. These molecules have also previously shown to crystallize easily, producing large crystals with defined edges.

The range of solvents was chosen to include varying solvent properties, including polar protic solvents such as ethanol, methanol and water, polar aprotic solvents such as, acetone, acetonitrile and ethyl acetate, and non-polar solvents, such as toluene. The changes in solvent property may alter the crystal growth of our molecules.

Crystallization typically occurs in a sample when the concentration of the solute increases past the solution's saturation point, it is no longer soluble. Different methods of crystallization can also affect the final crystal structure, so different methods applied here are, such as solvent evaporation, where the solute concentration slowly increases as the solvent evaporates, cooling, where the solubility decreases as the solution cools and the addition of an anti-

solvent, which decreases the solubility as it diffuses through the solution. The final method of crystallization used was to cool slowly from a melt of the compound.

50 mg of each compound was used per sample in the library. Saturated solutions of each compound were made up in either hot solvent (10ºC below the boiling point of the solvent) or at room temperature (~22ºC) and left to crystallize. In the cases where anti-solvents were used to trigger crystallization, a few drops were added to a saturated cold solution of the compound until the solution turned cloudy which then disappeared after stirring. An appropriate anti-solvent was chosen for each to be miscible with the solvent. The solvents, anti-solvents, crystallization conditions and temperatures used can be found in Table 3.6, as well as the results indicating whether single crystals, powder or an oil was formed.

Molecule and condition ↓	Solvent 1	Solvent 2	Solvent 3	Solvent 4	Solvent 5	Melt
(8) Dissolved hot (slow cooling)	Acetone (46.2°C), single crystals obtained	Acetonitrile (71.6°C), single crystals obtained	Toluene (100.6°C), single crystals obtained	Ethanol (68.5°C), single crystals obtained	Water (90.0°C), single crystals obtained	Meting point = 84-86°C, single crystals obtained
(8) Dissolved cold (evaporation)	Acetone (~22°C), powder diffraction obtained	Acetonitrile (~22°C), powder diffraction obtained	Toluene (~22°C), single crystals obtained, new polymorph	Ethanol (~22°C), powder diffraction obtained	Water (~22°C), powder diffraction obtained	
(8) Anti-solvent added	Acetone/ diethyl ether, powder diffraction obtained	Acetonitrile/ diethyl ether, powder diffraction obtained	Toluene/ diethyl ether, powder diffraction obtained	Ethanol/diethyl ether, powder diffraction obtained	Water/THF, powder diffraction obtained	
(10) Dissolved hot (slow cooling)	Acetone (46.2°C), oil formed	Acetonitrile (71.6°C), single crystals obtained	Toluene (100.6°C), single crystals obtained	Ethyl acetate (77°C), single crystals obtained	Methanol (54.6°C), single crystals obtained	Meting point = 160-161°C, single crystals obtained
(10) Dissolved cold (evaporation)	Acetone (~22°C), single crystals obtained	Acetonitrile (~22°C), powder diffraction obtained	Toluene (~22°C), single crystals obtained	Ethyl acetate (~22°C), single crystals obtained	Methanol (~22°C), single crystals obtained	
(10) Anti-solvent added	Acetone/ water, powder diffraction obtained	Acetonitrile/ water, powder diffraction obtained	Toluene/THF, powder diffraction obtained	Ethyl acetate/THF, powder diffraction obtained	Methanol/ water, single crystals obtained	
(9) Dissolved hot (slow cooling)	Acetone (46.2°C), single crystals obtained literature polymorph	Acetonitrile (71.6°C), single crystals obtained	Toluene (100.6°C), single crystals obtained	Ethanol, single crystals obtained	Ethyl acetate (77°C), single crystals obtained	Meting point = 148-149°C, single crystals obtained
(9) Dissolved cold (evaporation)	Acetone (~22°C), single crystals obtained literature polymorph	Acetonitrile (~22°C), powder diffraction obtained	Toluene (~22°C), single crystals obtained literature polymorph	Ethanol (~22°C), Oil formed	Ethyl acetate (~22°C), single crystals obtained	
(9) Anti-solvent added	Acetone/ water, powder diffraction obtained	Acetonitrile/ water, powder diffraction obtained	Toluene/THF, powder diffraction obtained	Ethanol/water, powder diffraction obtained	Ethyl acetate/THF, powder diffraction obtained	

Table 3.6 Screening library for **8**, **9** and **10** showing different solvents and crystallization methods used. Polymorphs indicated in red boxes.

For the samples obtained as single crystals, optical images were also taken, showing the different crystal habits produced as well as the crystal quality. These features are also important if the crystals are to be used as substrates for metal binding, crystals with well defined edges are necessary for face indexing analysis, which underpins the concept of using crystals as substrates for binding, enabling molecular orientation with respect to the surface to be determined. The most easily analysed crystals by microscopy and surface

chemical identification are large and plate-like, as the faces can easily be identified and accessed. Block crystals can also be easily accessed however, faces are not easily identified by optical microscopy alone. Needle shaped and undefined crystal faces cannot be used for our metal binding studies.

The crystals formed of **8** tend to form in plate-like morphologies (Figure 3.11) with the exception of the crystals grown by cooling of toluene (Figure 3.11c) which form in more of a block shape. Crystals formed by cooling of water, evaporation of toluene and from a melt (Figure 3.11e, f and g) are very thin and fragile, as can be seen from the slight rainbow effect in their colour, which indicates this. Even on a larger scale, very thin crystals will be difficult to handle as substrates.

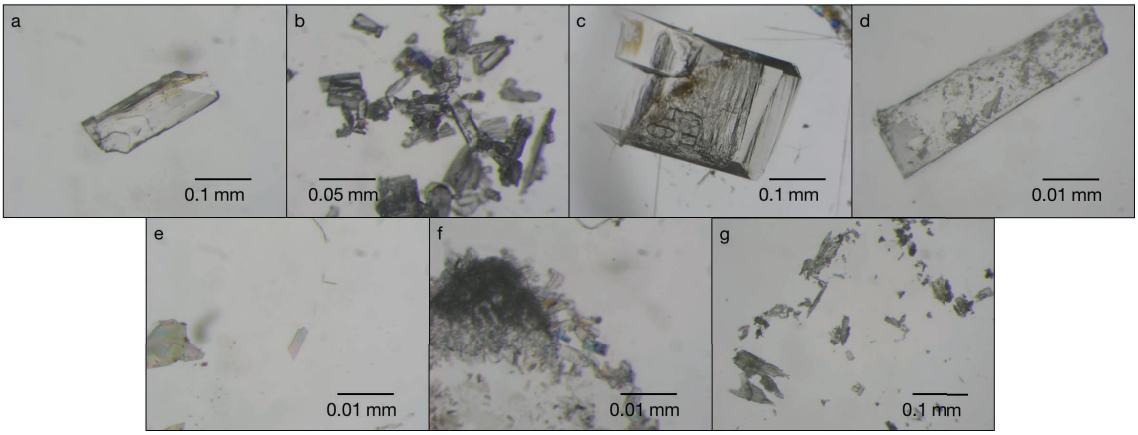

Figure 3.11 Optical images taken of crystals of **8** grown from cooling in acetone (**a**), acetonitrile (**b**), toluene (**c**), ethanol (**d**) and water (**e**), evaporation of toluene (**f**) and from a melt (**g**).

Crystals produced of **9** seem to mostly form as very thin plates, with the exception of the crystals formed from cooling and evaporation of acetone, evaporation of toluene and from a melt, which give thicker plates (Figure 3.12a and f), blocks (Figure 3.12g) and undefined clumps (Figure 3.12i) respectively. The yellow colour of the phenyl linked pyridyl imine can be also seen in these thicker crystals.

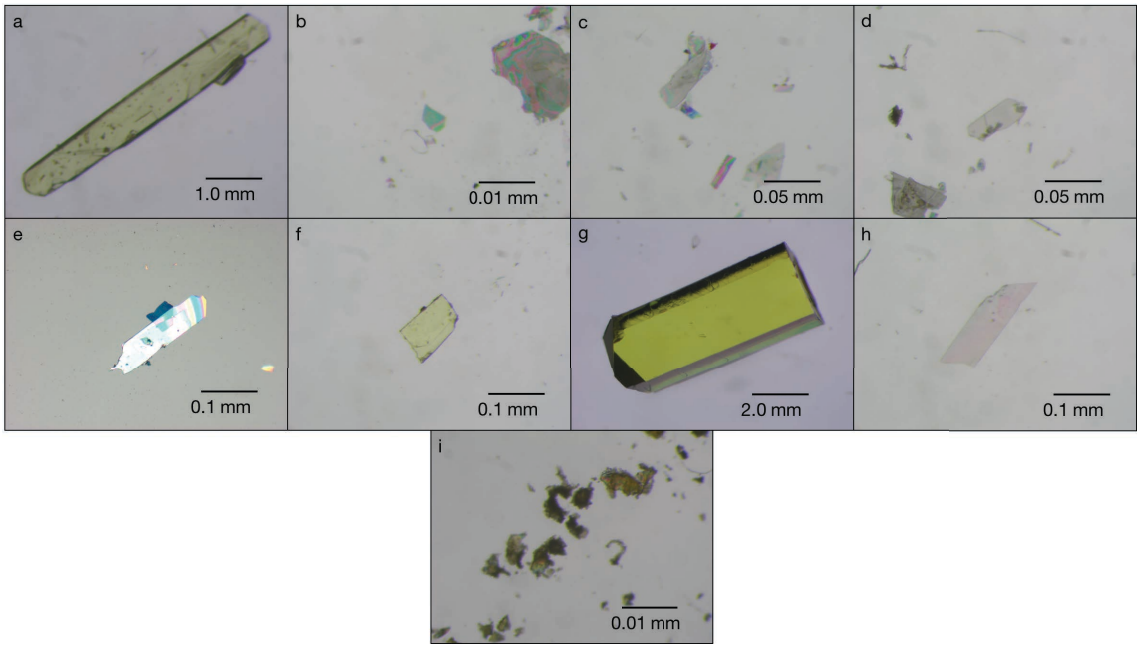

Figure 3.12 Optical images taken of crystals of **9** grown from cooling in acetone (**a**), acetonitrile (**b**), toluene (**c**) ethanol (**d**) and ethyl acetate (**e**), evaporation of acetone (**f**) toluene (**g**) and ethyl acetate (**h**), and from a melt (**i**).

The crystals of **10** obtained, all form with plate-like morphologies, however, the edges of the crystals formed by evaporation of toluene and ethyl acetate (Figure 3.13f and g) seem to be very rough and undefined, making them unsuitable for face identification. Crystals formed by cooling in ethyl acetate or methanol, evaporation of acetone and by the addition of a water anti-solvent in methanol (Figure 3.13c, d, e and i) are also very thin, as seen by the rainbow colour.

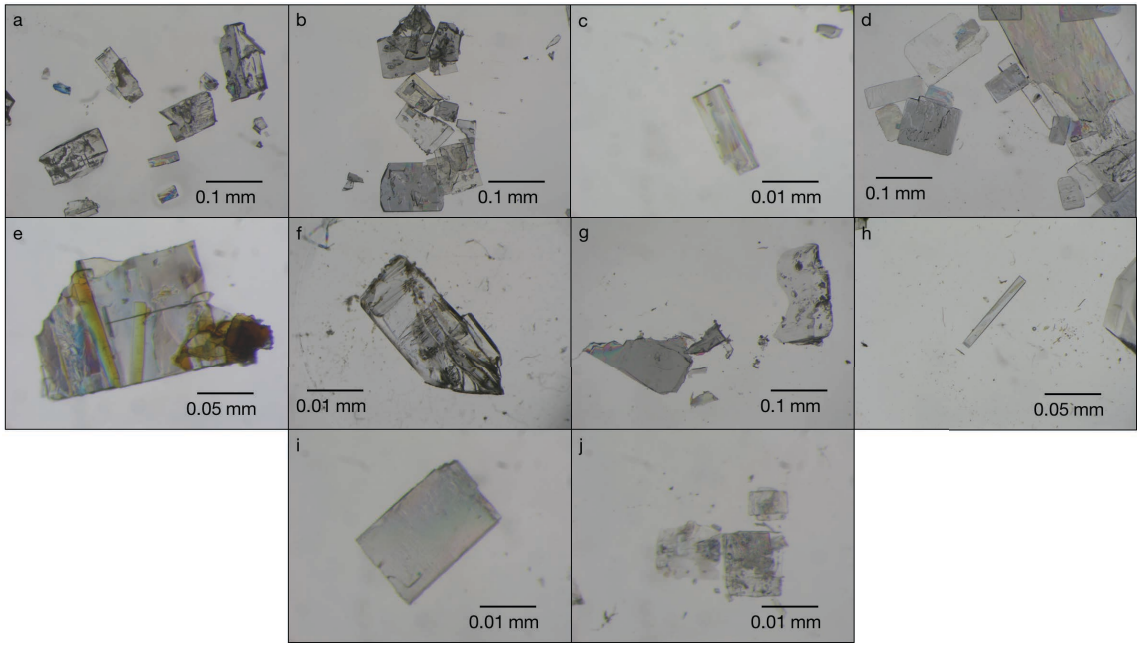

Figure 3.13 Optical images taken of crystals of **10** grown from cooling in acetonitrile (**a**), toluene (**b**), ethyl acetate (**c**) and methanol (**d**), evaporation of acetone (**e**), toluene (**f**) ethyl acetate (**g**) and methanol (**h**), addition of water anti-solvent in methanol (**i**), and from a melt (**j**).

Single crystals could not be produced for all of the samples in the library, however X-ray powder diffraction data was obtained for most of the remaining samples, with only two samples forming oils. X-ray powder diffraction patterns can be compared to one another and to predicted patterns, where discrepancies between patterns is an indication of different unit cell parameters and therefore a different crystals structure. Here, this means forming polymorphs of our original crystal structures. Example powder diffraction patterns for the samples are shown here (Figures 3.14, 3.15 and 3.16) and are compared to the predicted powder diffraction patterns (obtained from the original crystal structures of **8**, **9** and **10**). The examples shown here were all obtained by evaporation of an acetonitrile solvent.

The remaining powder diffraction patterns obtained in the library can be found in the appendix.

X-ray powder diffraction patterns for the material obtained when trying to form single crystals of **8** all show a very similar diffractograms, indicating no differences in unit cell parameters. Comparison of the diffractograms to the calculated pattern for the original crystal structure shows a good agreement (Figure 3.14), with all significant peaks present and generally with the correct intensity, with the exception of the peaks at 13-13.5 2-Theta and 20-20.5 2-Theta, where the intensities are higher than predicted. The experimental peaks are much broader than the predicted peaks, encompassing smaller shoulder peaks and shifting their position slightly. The agreement of the experimental and predicted patterns suggests the microcrystals within the powders are all of the same crystal form as the original structure of **8**.

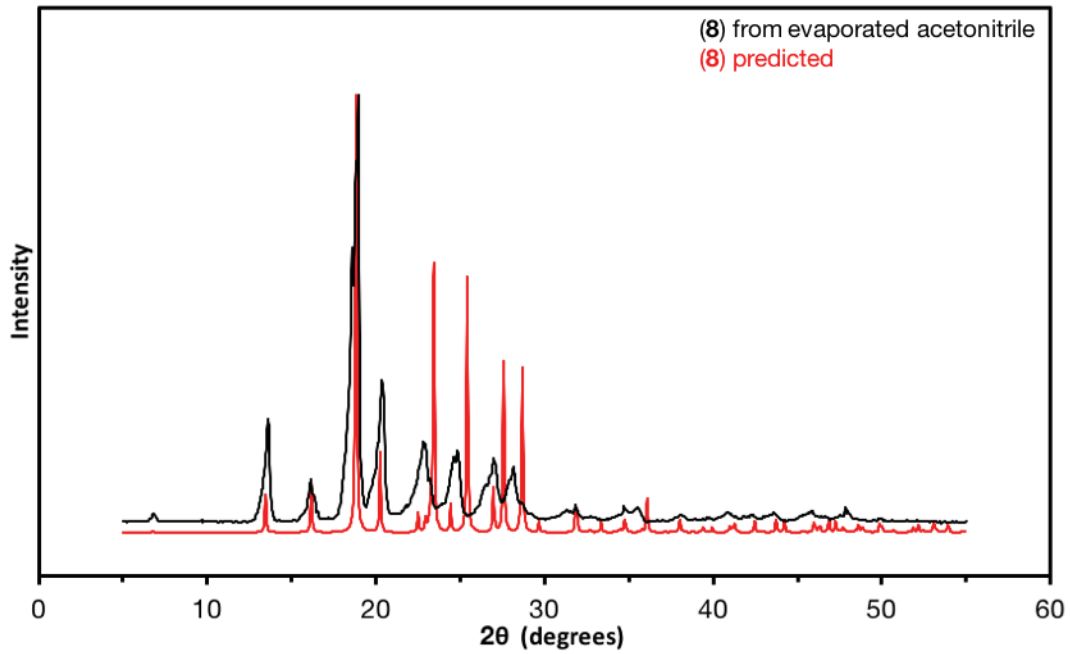

Figure 3.14 Predicted X-ray diffraction pattern of **8** taken from original crystal structure (in red) and X-ray diffraction pattern for powder obtained from **8** grown by evaporation of acetonitrile (in black).

Powder diffraction data obtained for samples of **9** once again all show good agreement with each other but less so with the predicted diffractogram (Figure 3.15). All of the significant peaks seem to be present but are shifted to a lower 2-Theta value than predicted, indicating that the calculation for the predicted pattern here is of a lower accuracy than seen for **8** and **10**. The peak intensities generally follow the same trend as for the predicted pattern, with the exception of the peaks at 15-16 2-Theta, where the intensities are higher than predicted. As before, the agreement of experimental and predicted patterns suggests all samples are of the same crystal form as the original structure for **9**.

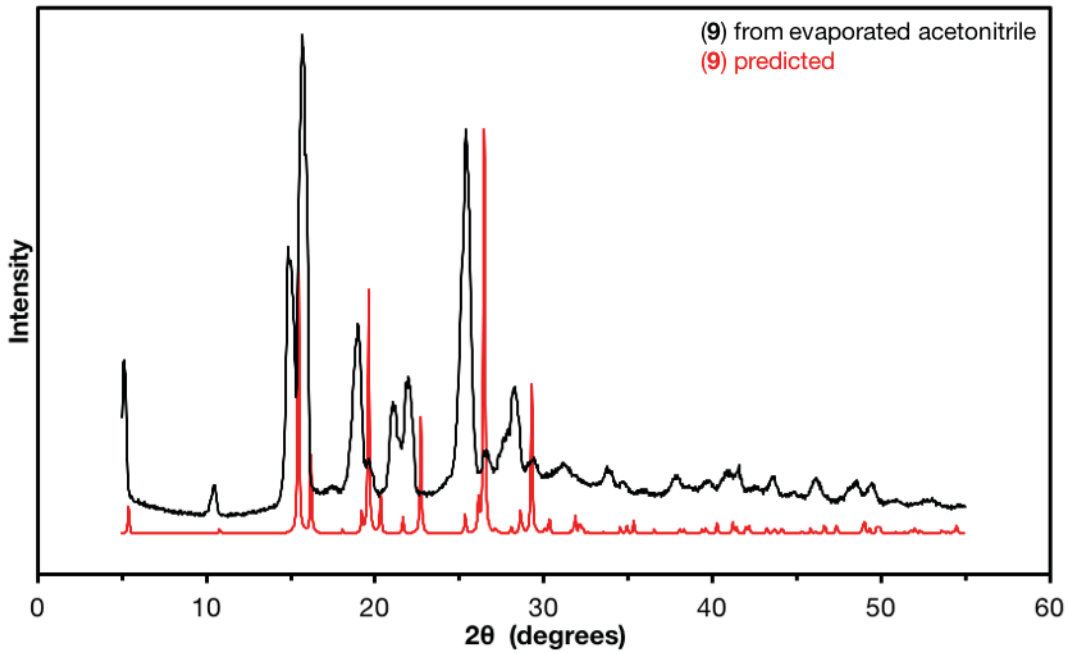

Figure 3.15 Predicted X-ray diffraction pattern of **9** taken from original crystal structure (in red) and X-ray diffraction pattern for powder obtained from **9** grown by evaporation of acetonitrile (in black).

X-ray powder diffraction patterns of material obtained of **10** also all show very similar patterns to each other, and to that of the predicted pattern (Figure 3.16), where all the major peaks are broader but present with the correct intensities. This again suggests that all of the powder samples here are of the same crystal form as the original structure for **10**, forming no polymorphs.

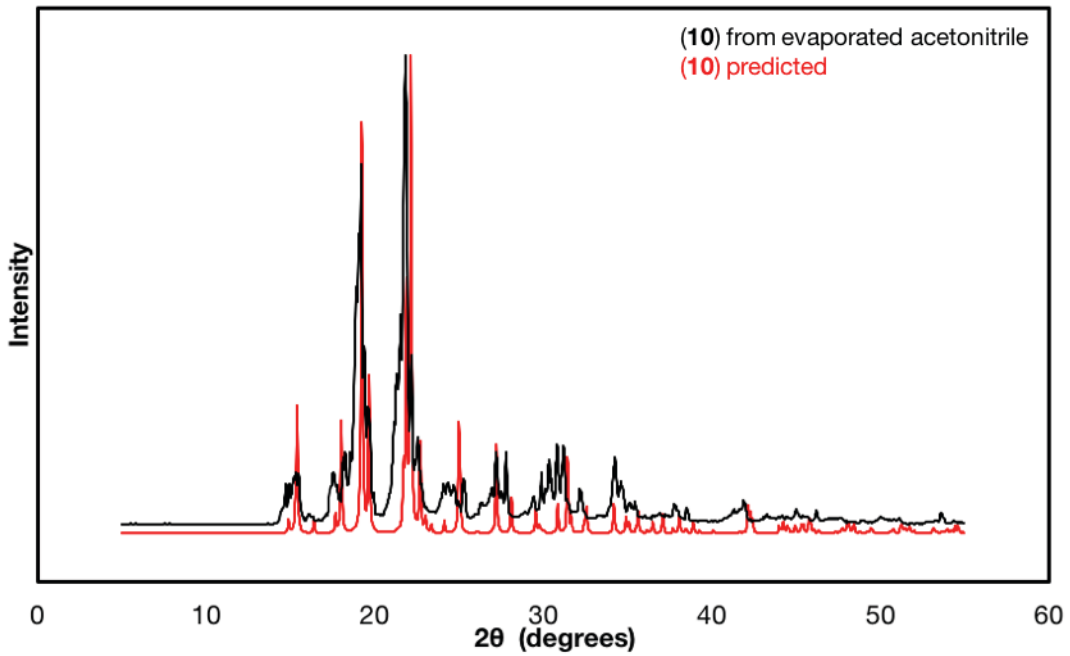

Figure 3.16 Predicted X-ray diffraction pattern of **10** taken from original crystal structure (in red) and X-ray diffraction pattern for powder obtained from **10** grown by evaporation of acetonitrile (in black).

Unit cell determination of all single crystal samples was obtained (see appendix), most gave the same unit cell dimensions as for their original crystal structure, with the exception of one Py-Im-Et (**8**) sample which formed an unknown polymorph, and three Py-Im-Ph (**9**) samples, which form a different literature polymorph. [19]

The sample of **8** grown from evaporation of toluene gave unit cell measurements that indicated the formation of a polymorph, so a full structural analysis was performed by X-ray diffraction. This allowed for a structural conformation and energy comparison of the two polymorphs to be completed. The samples of **9** grown by cooling in acetone, evaporation of acetone and evaporation of toluene gave the unit cell dimensions of a known literature polymorph, so a conformational comparison and energy comparison of the two polymorphs was performed.

3.2.7 Py-Im-Et Polymorph (8P1)

Comparing this new polymorph structure to the original crystal structure for (**8**), there is also an inversion centre mid-way along the ethyl bridge, with the molecule exhibiting a trans geometry with respect to the pyridyl nitrogen atoms (Figure 3.17). The pyridyl and imine nitrogen atoms this time face the same side of the molecule in a near co-planar arrangement with a C2-C3-C7-N2 torsion angle of only 12.6º, meaning there has been a rotation about the C3-C7 bond of 160.3º from the structure of (**8**). The torsion angle between the imine bond and the ethyl spacer unit (C7-N2-C9-C9a) has decreased by 18.4º to 116.5º putting the ethyl spacer unit further out of plane from the phenyl ring and imine bond than in the original structure. These changes in torsion angles mean the internal pyridyl nitrogen atom spacing is now 12.04 Å, 1.06 Å shorter than before.

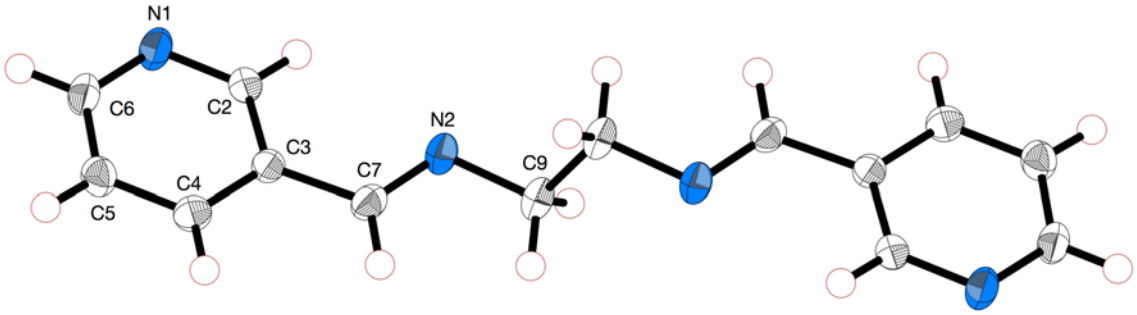

Figure 3.17 Molecular structure of **8P1** obtained by X-ray diffraction. All unique non-hydrogen atoms labelled (asymmetric unit).

The molecular packing arrangement in this crystal structure shows parallel displaced face to face π stacking interactions, where the parallel displaced inter-planar distance (centroid to edge) is 3.30 Å in b-axis (Figure 3.18a and b). Weak hydrogen-bonding between pyridyl rings of adjacent molecules can also be seen with C6-H6···N1 = 3.45 Å (H6···N1 = 2.61 Å) in the c-axis as well as to a different molecule where C5-H5···N1 = 3.70 Å (H5···N1 = 2.95 Å) in the a-axis, both can be seen in Figure 3.18b. Unlike in the original structure of **8**, all molecules here align in the same direction, possibly due to the stronger π-π interactions present here. Intermolecular N1···N1 distances here are 5.82 Å, 8.46 Å and 12.18 Å in the a-, b- and c-axes respectively. These distances are larger than for **8** in the a- and c-axes but smaller in the b-axis, showing that these potential surface binding sites can be spatially manipulated by polymorphism.

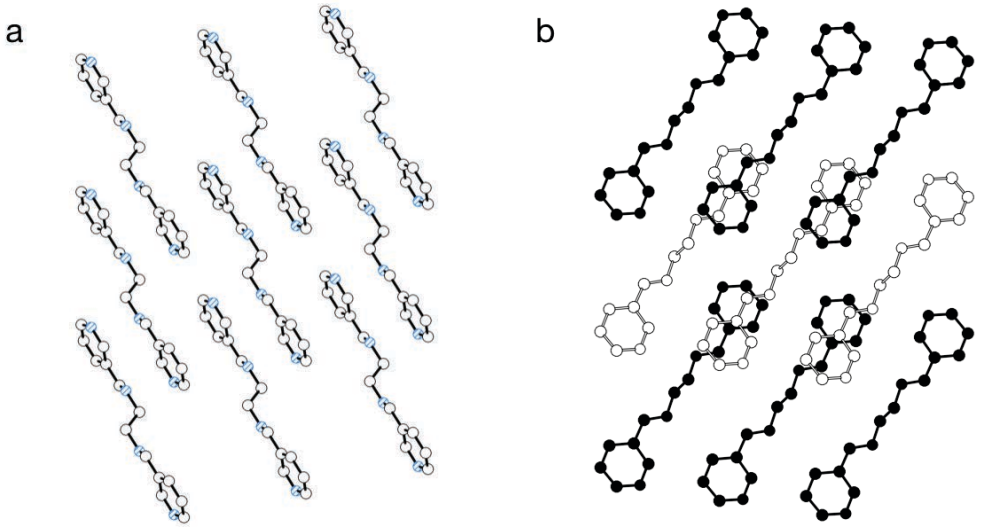

Figure 3.18 Packing arrangement in crystal of **8P1** viewed down the a-axis **a**, and the b-axis **b**. Hydrogen atoms removed for clarity.

3.2.8 Energy Calculations for 8P1

As with the original structures, energy calculations for **8P1** were performed to give energies for the molecule in the gas phase, the crystal phase and for the strongest three interacting pairs.

The equilibrium geometry, and therefore its energy, is the same as the original (-1997721.29488 kJmol^{-1}) as this looks at the gas phase where the molecular conformation is free to change. The single point energy when in this conformation however, does change, and is now -1997169.04983 kJmol^{-1}, this is 217.63557 kJmol^{-1} higher than for the original conformation, making it less stable. The strongest three interacting pairs of molecules in this polymorph structure were calculated using UNI (Figure 3.19a) and their intermolecular potential energy, single point crystal structure energy and symmetry operations are shown in Table 3.7.

Intermolecular interaction (ordered by UNI strength)	UNI intermolecular potential (kJmol^{-1})	Single point total energy per molecule (kJmol^{-1})	Symmetry operation for interacting pair
1st	-36.12420	-1997167.16472	translation
2nd	-33.61580	-1997168.66126	translation
3rd	-25.35270	-1997177.39105	translation

Table 3.7 Intermolecular potential energies, single point crystals structure energies and symmetry operations for Py-Im-Et (**8P1**), ranked by intermolecular interaction strength (UNI).

The single point energy for each of the molecules in the strongest interacting pair was calculated to be -1997167.16472 kJmol^{-1} and the intermolecular potential was calculated to be -36.12420 kJmol^{-1}. This is nearly half as stabilizing as the strongest pair for the original structure of **8** (-60.51800 kJmol^{-1}). This pair show a translation relationship, separated by 9.11 Å close to the c-axis in direction (Figure 3.19b).

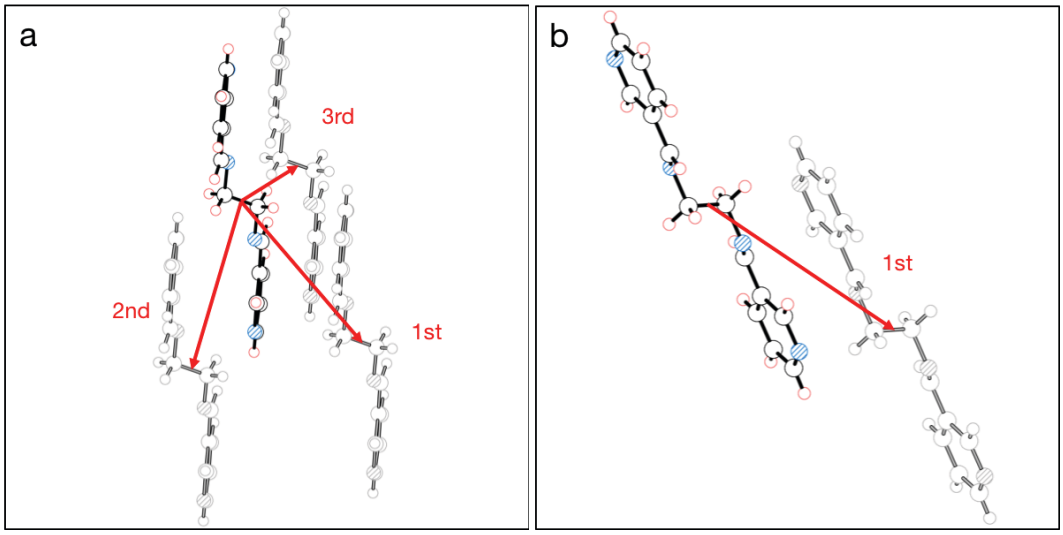

Figure 3.19 View of the strongest three intermolecular interactions in **8P1** as calculated by UNI, **a**, and a closer view of the translation of the first interacting pair of molecules in **8P1**, **b**, viewed down a-axis. Red lines connect the molecules' central points from an origin molecule (in colour).

The second strongest interacting pair also show a translation, this time of 10.09 Å (Figure 3.20a), and the third strongest interacting pair are again related to each other by a translation, this time of 5.82 Å in the a-axis (Figure 3.20b). The intermolecular potentials for the second and third strongest interactions here are more stabilizing (lower energy) than in the original structure for **8**, but the strongest interaction is much more stabilizing for the original structure. Perhaps this is one reason why the original structure is more frequently grown, the first interaction when growing is stronger for the original crystal structure, leading to this structure being more likely produced.

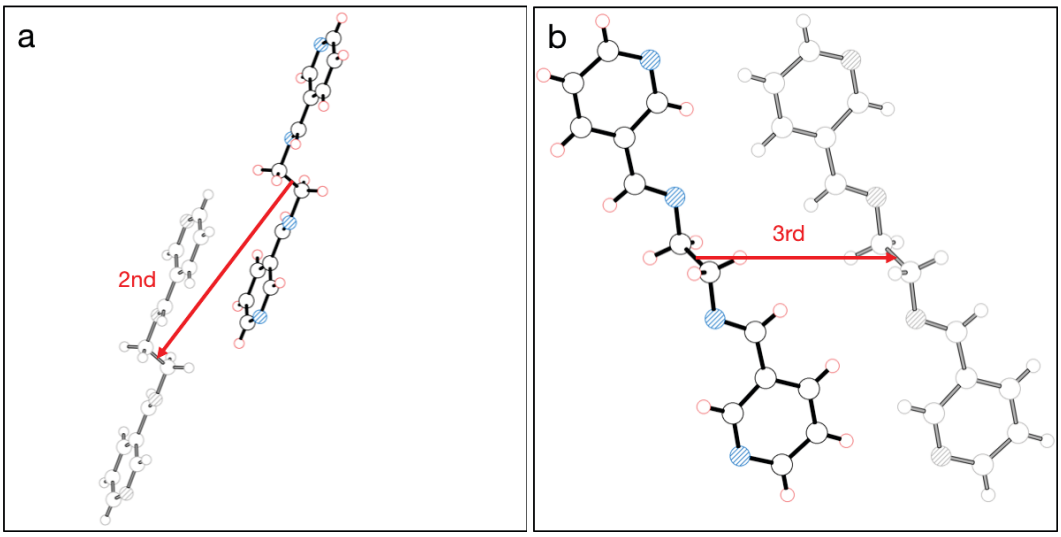

Figure 3.20 a, View down a-axis of the second interacting pair 'translation' in **8P1**, and **b**, View down b-axis of the third interacting pair 'translation' in **8P1**. Red lines connect the molecules' central points from an origin molecule (in colour).

3.2.9 Phenyl linked Pyridyl-Imine Polymorph (9P1)

Looking at this second form of the phenyl linked pyridyl-imine crystal (**9P1**) taken from the literature[19] and comparing to the original structure **9**, it can be seen that there is an inversion centre in the middle of the phenyl ring spacer unit, and the molecule exhibits a trans geometry with respect to the pyridyl nitrogen atoms (Figure 3.21). As in the original crystal structure, the pyridyl nitrogen atoms face towards the same side of the molecule as the imine nitrogen atoms, however, these two groups are now fully co-planar with a C2-C3-C7-N2 torsion angle of 1.0º, this is 3.8º lower than in **9**. The rest of the molecule also seems highly planar, with the C7-N2-C9-C10 and C7-N2-C9-C11 torsion angles at 178.6º and 2.8º respectively.

The rigid phenyl linker, with a lack of conformational freedom means the internal pyridyl nitrogen atom spacing is still 14.0 Å, despite the changes in torsion angles.

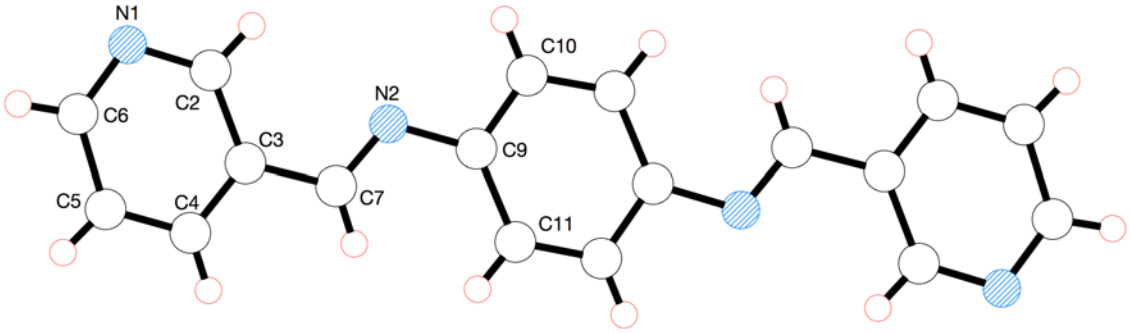

Figure 3.21 Molecular structure of **9P1** taken from the CSD.[19] All unique non-hydrogen atoms labelled (asymmetric unit).

The packing arrangement of this polymorph shows molecules aligned in the a-axis (Figure 3.22a), and shows molecules which are encouraged to stack together in the b-axis (Figure 3.22b) by parallel displaced face to face π stacking interactions. These are between all three rings in one molecule to all three rings of another molecule in the b-axis, where the parallel displaced inter-planar distances (centroid to edge) are all 3.23 Å. The molecules stack in alternating layers of direction (Figure 3.22b) influenced by edge to face π interactions between pyridyl rings in each layer. This C6-H6···pyridyl centroid distance is 3.78 Å (H6···pyridyl centroid = 3.00 Å). The intermolecular N1···N1 distances for this polymorph are 11.60 Å, 4.77 Å and 6.83 Å in the a-, b- and c-axes respectively. These distances are shorter than for the first polymorph (**9**) in the a- and b- axes but longer in the c-axis, which again shows the potential surface binding site spacing of these molecules can be manipulated by polymorphism.

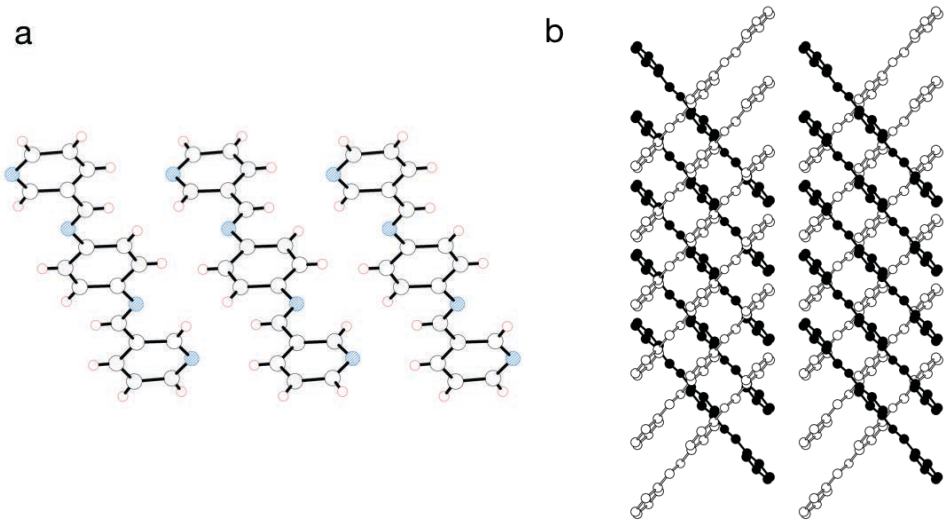

Figure 3.22 Packing arrangement in crystal of **9P1** viewed down the b-axis **a**, and the c-axis **b**. Hydrogen atoms removed for clarity.

3.2.10 Energy Calculations for 9P1

Total energy and intermolecular potentials were also calculated for the **9P1** literature polymorph, where the equilibrium geometry of the molecule is -2397936.59122 kJmol^{-1}. The single point energy of the molecule in the conformation present in **9P1** is -2396755.22912 kJmol^{-1}, 839.21745 kJmol^{-1} higher than for the conformation present in **9**. These values show that this conformation is less stable, suggesting one reason why this polymorph is less often seen in our studies.

Single point energies for the strongest three interacting pairs (Figure 3.23a) were calculated, with their intermolecular potential energy, single point crystal structure energy and symmetry operations shown in Table 3.8. The strongest pair symmetry operation is classed as a translation of 4.77 Å in the b-axis (Figure 3.23b).

Intermolecular interaction (ordered by UNI strength)	UNI intermolecular potential (kJmol^{-1})	Single point total energy per molecule (kJmol^{-1})	Symmetry operation for interacting pair
1st	-78.1333	-2396738.38653	translation
2nd	-12.9278	-2396758.05153	screw (2-fold)
3rd	-12.751	-2396758.07778	screw (2-fold)

Table 3.8 Intermolecular potential energies, single point crystals structure energies and symmetry operations for Py-Im-Ph (**9P1**), ranked by intermolecular interaction strength (UNI).

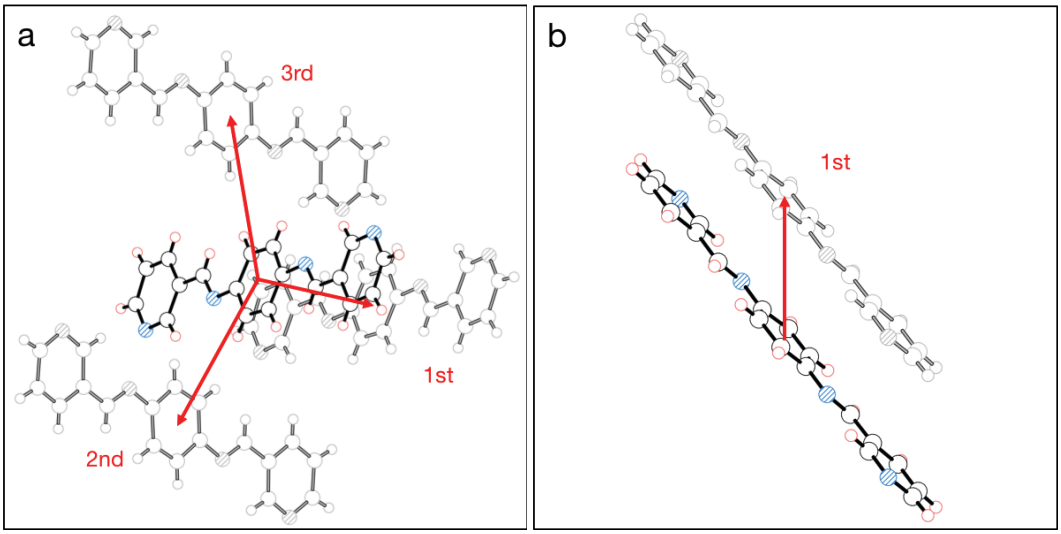

Figure 3.23. View of the strongest three intermolecular interactions in **9P1** as calculated by UNI, **a**, and a closer view of the translation of the first interacting pair of molecules in **9P1**, **b**, viewed down c-axis. Red lines connect the molecules' central points from an origin molecule (in colour).

The next strongest interacting pair is in the form of a screw (2-fold) with the centre points of the molecules separated by 6.86 Å (Figure 3.24a) and the third strongest interacting pair seems to be the same as the second strongest pair (a 2-fold screw separated by 6.86Å as seen in Figure 3.24b), where the paired molecule is a translation of the previous one (12.86 Å in c-axis). Changes in energy from the second pair are very small, with the total energy for each molecule calculated to be -2396758.07778 $kJmol^{-1}$ and an intermolecular potential of -12.751 $kJmol^{-1}$.

The total energy calculations for this set of interacting pairs again shows the opposite trend to that of the intermolecular potentials, once again highlighting the differences between DFT and empirical calculations.

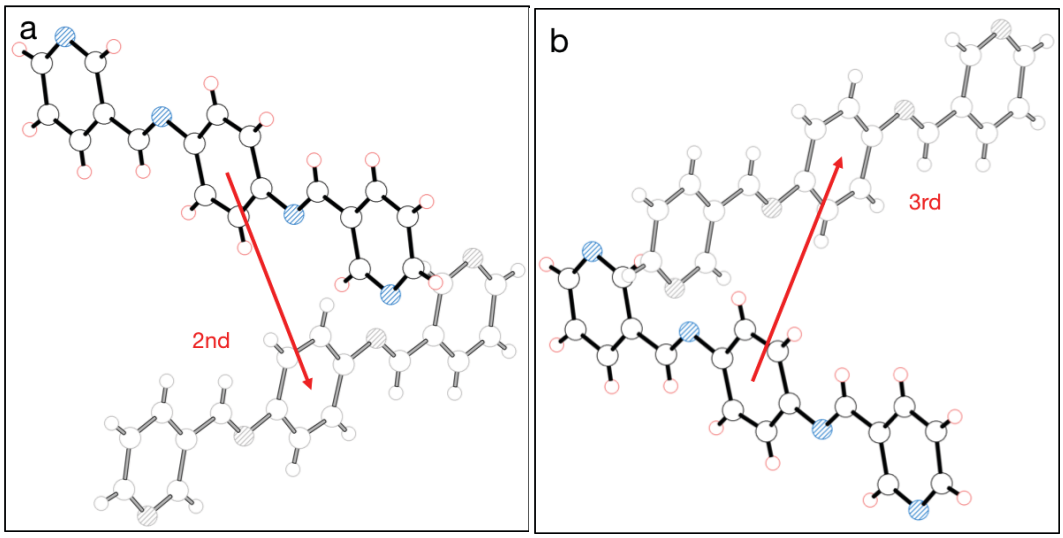

Figure 3.24. a, View down a-axis of the second interacting pair '2-fold screw' in **9P1**, and **b**, View down a-axis of the third interacting pair '2-fold screw' in **9P1**. Red lines connect the molecules' central points from an origin molecule (in colour).

3.3 Conclusions

By creating both a new polymorph of the Py-Im-Et compound, and identifying the conditions which facilitate the growth of each literature polymorph of the Py-Im-Ph compound (making it controllable), we have shown that it is possible to change the spatial arrangement of potential crystal surface binding sites of the same compound by using a crystal engineering approach. The pyridyl binding site spacing of **8** was altered in **8P1** to be larger in the a- and c-axes, and smaller in the b-axis. Similarly, the binding site spacing of **9** was changed in **9P1** to be longer in the c-axis and shorter in the a- and b-axes.

Results here show that the strongest intermolecular interactions (as calculated by UNI) seem to never give the lowest energy pair of molecules, and in fact the trend is mostly highest energy to lowest energy for strongest to weakest interactions. These opposing trends show that total energy calculation and intermolecular potential can give very different answers to which interactions are most stabilizing in our crystal structures and may just show a poor agreement due to the different types of calculations used. Atom-atom potentials are empirical and heavily reliant on database values for structures which are likely to be different, giving inaccurate energy values. The DFT calculations used are ab initio and don't account for intermolecular van der Waals forces. A different approach for the future, possibly a combination of the two techniques (such as PIXEL or DFT-D[15]) is required if our crystal structures

are to be accurately predicted and manipulated for the spatial control of surface functional groups. The experimental and calculated data obtained here may help any future calculations/predictions made of crystal structures using these types of molecules.

Single point total energies calculated for the less commonly seen polymorph structures **8P1** and **9P1** were significantly higher than for their counterpart original form structures **8** and **9**, with changes in energy in the order of hundreds of $kJmol^{-1}$.

This observation suggests this is why the original crystal forms are more frequently produced in our crystal engineering studies.

In general, specific symmetry operations do not seem to give lower or higher energy interactions, however, the 'translation' symmetry operation between interacting pairs seems to be the most frequent for our molecules, with 12 out of 21. Screw (2-fold) and screw (3-fold) operators are far less frequent for our crystals, being observed 7 and 2 times respectively.

Also seen here was the variation of crystal habits produced when changing the crystallization conditions, enabling the choice of the optimal external crystal morphology on which to study surface binding by microscopy or surface chemical analysis. Large, plate-like crystals with well defined edges are most easily studied (such as when **8** is grown by slow cooling in ethanol), followed by block shaped crystals (such as when **9** is grow by evaporation from toluene). The surfaces of needle shaped crystals, or crystals with undefined edges (such as when **9** is grown from a melt), cannot easily be studied due to the lack of face identification and small surface size.

3.4 Experimental Details

All solvent chemicals were purchased from Sigma-Aldrich, Alfa Aesar or Fisher Scientific and were used as received without further purification. Molecules **5**, **7**, **8**, **9** and **10** were synthesized in chapter 2. Unit cell parameters of crystals were determined by single crystal X-ray diffraction at 150 K using Cu or Mo radiation on an Oxford Diffraction Gemini A Ultra diffractometer and crystal structures were visualized in CrystalMaker (CrystalMaker Software Ltd.). X-ray powder diffraction patterns were obtained on a Bruker D2 Phaser desktop

powder diffractometer.

Energy calculations

Total energy calculations were performed using DFT calculations with a B3LYP functional and a 6-31G* basis set on the Spartan '14 program (WAVEFUNCTION INC). Intermolecular potentials were calculated using the crystal structures of **5**, **7**, **8**, **9** and **10** obtained in chapter 2 and the unified pair-potential parameters calculation function (UNI) of Mercury (CCDC).

Crystal growth

The library of crystal structures and powder patterns produced for crystal engineering of **8**, **9** and **10** was created by using 50 mg of each compound per sample, where saturated solutions of each compound were made up in either hot solvent (10°C below the boiling point of the solvent) or at room temperature (~22°C) and left to crystallize. In the cases where anti-solvents were used to trigger crystallization, a few drops were added to a saturated room temperature solution of the compound until the solution turned cloudy which then disappeared after stirring. Concentrations can be found below.

For **8**, 50 mg dissolved in hot acetone (1 mL), in room temperature acetone (1 mL), in hot acetonitrile (1 mL), in room temperature acetonitrile (3 mL), in hot toluene (2 mL), in room temperature toluene (3 mL), in hot ethanol (1 mL), in room temperature ethanol (1 mL) and in hot water (1 mL), in room temperature water (2 mL).

For **9**, 50 mg dissolved in hot acetone (3 mL), in room temperature acetone (6 mL), in hot acetonitrile (2 mL), in room temperature acetonitrile (4 mL), in hot toluene (1 mL), in room temperature toluene (6 mL), in hot ethanol (2 mL), in room temperature ethanol (4mL) and in hot ethyl acetate (2 mL), in room temperature ethyl acetate (6 mL)

For **10**, 50 mg dissolved in hot acetone (3 mL), in room temperature acetone (7 mL), in hot acetonitrile (2 mL), in room temperature acetonitrile (14 mL), in hot toluene (1 mL), in room temperature toluene (4 mL), in hot ethyl acetate (2 mL), in room temperature ethyl acetate (6 mL) and in hot methanol (0.5 mL), in room

temperature methanol (1 mL).

Polymorph 8P1 Crystal Data

Molecular formula	$C_{14}H_{14}N_4$	
Formula weight	238.29	
Temperature	150.0 K	
Radiation, wavelength	MoKα, λ = 0.71073 Å	
Crystal system, space group	Triclinic, *P*-1	
Unit cell parameters	a = 5.8191(4) Å	α = 99.915(5)°
	b = 7.2333(5) Å	β = 95.918(6)°
	c = 7.6349(5) Å	γ = 99.943(6)°
Cell volume	308.87(4) Å^3	
Z	1	
Crystal colour and size	Colourless, 0.25 × 0.28 × 0.38 mm^3	
Final *R* indices [$F^2>2\sigma$]	R_1 = 0.0423	
R indices (all data)	wR_2 = 0.1189	
Large diff. peak and hole	0.17/-0.20 e Å^{-3}	

Additional X-ray powder diffraction and single crystal diffraction unit cell data can be found in the appendix.

3.5 References

1. D. Fox, M. M. Labes and A. Weissberger, *Physics and Chemistry of the Organic Solid State, Vol 2*, Interscience, New York, 1965.
2. J. Bernstein, R. J. Davey and J.-O. Henck, *Angew. Chem. Int. Ed.*, 1999, **38**, 3440-3461.
3. P. Vishweshwar, J. A. McMahon, J. A. Bis and M. J. Zaworotko, *J. Pharm. Sci.*, 2006, **95**, 499-516.
4. J. Haleblian and W. McCrone, *J. Pharm. Sci.*, 1969, **58**, 911-929.
5. J. W. Steed and J. L. Atwood, *Supramolecular Chemistry*, John Wiley & Sons, Ltd., 2009.
6. G. R. Desiraju, *Crystal engineering: the design of organic solids*, Elsevier, 1989.
7. D. Braga, F. Grepioni and G. R. Desiraju, *Chem. Rev.*, 1998, **98**, 1375-1406.
8. G. R. Desiraju, *Angew. Chem. Int. Ed.*, 1995, **34**, 2311-2327.
9. M. C. Etter, *Acc. Chem. Res.*, 1990, **23**, 120-126.
10. A. D. Burrows, C.-W. Chan, M. M. Chowdhry, J. E. McGrady and D. M. P. Mingos, *Chem. Soc. Rev.*, 1995, **24**, 329-339.
11. J. D. Dunitz and A. Gavezzotti, *Chem. Soc. Rev.*, 2009, **38**, 2622-2633.
12. A. Gavezzotti, *Acc. Chem. Res.*, 1994, **27**, 309-314.
13. A. Gavezzotti and G. Filippini, *J. Phys. Chem.*, 1994, **98**, 4831-4837.

14. D. Jayatilaka and D. Grimwood, in *Computational Science — ICCS 2003*, eds. P. A. Sloot, D. Abramson, A. Bogdanov, Y. Gorbachev, J. Dongarra and A. Zomaya, Springer Berlin Heidelberg, 2003, vol. 2660, ch. 15, pp. 142-151.
15. L. Maschio, B. Civalleri, P. Ugliengo and A. Gavezzotti, *J. Phys. Chem. A*, 2011, **115**, 11179-11186.
16. M. A. Neumann and M.-A. Perrin, *J. Phys. Chem. B*, 2005, **109**, 15531-15541.
17. Y.-h. Sun, K.-q. Ye, J.-f. Kong, D.-x. Zhu and Y. Wang, *Chin. J. Mol. Sci.*, 2006, **7**, 22.
18. K. Ha, *Acta Crystallographica Section E*, 2011, **67**, o2250.
19. H. N. Kim, H. K. Lee and S. W. Lee, *Bull. Korean Chem. Soc.*, 2005, **26**, 892-898.

Chapter 4

Metal Complexes as Models for Crystal Surface Binding of Metal Particles

Table of Contents

4.1 Introduction

An important part of our proposed system for directed metal binding on organic single crystal surfaces is the ability of the crystal to bind the desired metal. Our binding site groups contain pyridine nitrogen atoms as the intended binding site, chosen because of this group's proven ability to bind a wide range of metal ions[1-3] and nanoparticles.[4, 5] However, even with this reputation for metal binding, it is useful to establish the binding of our chosen molecules with metal ions by preparing metal complexes as models for analysis by X-ray crystallography. This structural analysis of model complexes can provide valuable information regarding the disposition to metal binding, the angle of binding and changes in the ligand structure when bound. Only small deviations from an ideal trigonal planar geometry around the pyridyl nitrogen atom are expected, as the sp^2 nitrogen atom is locked in the planar pyridyl ring, forcing the internal ring angle to be as close to 120° as possible. Minimal structural changes to the ligand are also desired so that any surface bound metal retains the pre-characterized order of the crystal structure. These models can be achieved by reactions with metal salts to produce high quality single crystals of metal complexes for X-ray diffraction measurements.[6]

The use of bridging ligands with large binding site separation in these metal co-ordination experiments tends to form extended structures through the ligand-metal interactions, giving co-ordination polymers.[7] These structures are not expected to form on the surfaces of our large crystals, as there shouldn't be any free ligand in solution to contribute to the extension. These structural features aren't the focus in our model studies, however, they are noteworthy and interesting, with the potential to form discrete, one-, two- and three-dimensional architectures (Scheme 4.1).[8]

In the presence of an excess of metal ion, it is generally found that co-ordination polymers and other extended structures are formed, with three-dimensional metal-organic frameworks (MOFs) being of great interest.[9]

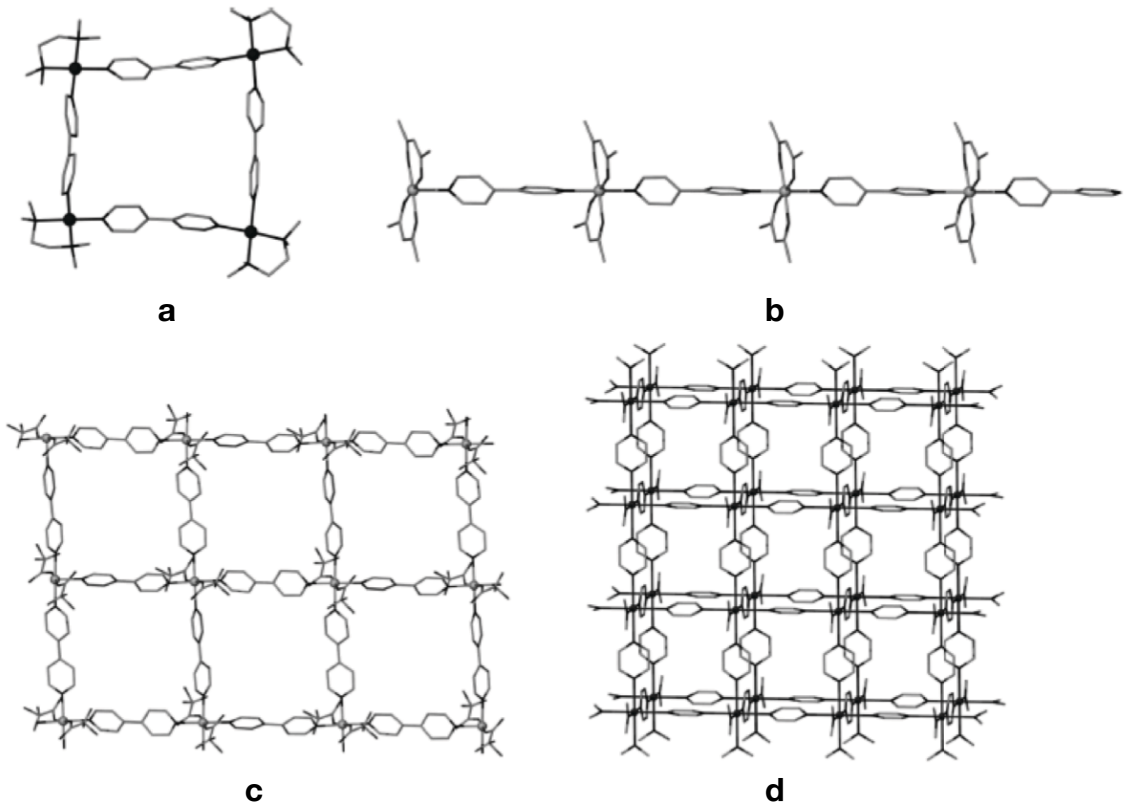

Scheme 4.1.[8] **a**, discrete 0-D self-assembled complex $[\{Pd(en)(\mu\text{-bpy})\}_4]^{8+}$,[10] **b**, 1-D architecture $[Zn(acac)_2(\mu\text{-bpy})]_n$,[11] **c**, 2-D architecture $[Co(bpy)_2(CF_3CO_2)_2]_n$[12] and **d**, 3-D architecture $\{[Ag(pyrazene)_3](SbF_6)\}_n$.[13] Reprinted with permission from J. W. Steed and J. L. Atwood, *Supramolecular Chemistry*, John Wiley & Sons, Ltd., Copyright 2009.

Built up from nodes (generally metal ions) and linkers (ligand molecules) the most significant property of these architectures is the open framework structure, creating large pores that are highly tuneable in size and surface functionality because of the building block approach used in creating them.[14] These pores enable the structures to have interesting properties such as CO_2 capture,[15] as well as hydrogen[16] and methane storage,[17] where the channels created by the framework have the capability for gases to be absorbed into them. Tuneable electrical conductivity in MOFs has also been achieved in which pores can be infiltrated with redox-active molecules,[18] and the tuneable surface functionalities of MOF pores mean they have uses in catalysis[19] and chemical sensing.[20]

The results obtained in this chapter show a range of metal-ligand complexes for compounds **8**, **9**, and **10** with copper, zinc and silver. The assessment of conformational changes to each ligand with metal binding was performed, as well as an assessment of crystal surface binding accessibility for these types of metals.

4.2 Results and Discussion

4.2.1 Metals and Ligands to be used

For our study we have chosen to look at model binding systems with metals of copper, zinc, and silver, and use the bis(1-(pyridin-3-yl)methanimine) binding site molecules **8** (Py-Im-Et), **9** (Py-Im-Ph) and **10** (Py-Im-Cy) as ligands.

Once formed on a crystal surface, an important attribute of our nanostructures is to exhibit very low electrical resistivity, i.e. high electrical conductance, if they are to be employed in the electrical semiconductor industry. As the second most electrically conductive element in the periodic table (5.96×10^7 Sm^{-1} at 20°C),[21] copper is currently widely used in the semiconductor industry for interconnections because of its high electrical conduction properties,[22] and has potential to show similar properties at the nanoscale.[23] The most common oxidation states for copper to exist in are +1 and +2, examples include 2 co-ordinate Cu(I), such as $[CuCl_2]^-$, 3 co-ordinate Cu(I) such as $[Cu(CN)_3]^{2-}$, 4 co-ordinate Cu(II), such as $[CuCl_4]^{2-}$, 5 co-ordinate Cu(II), such as $[CuCl_5]^{3-}$ and 6 co-ordinate Cu(II), such as $[Cu(NO_2)_6]^{4-}$. These complexes exhibit linear, trigonal planar, tetrahedral, trigonal bipyramidal and octahedral co-ordination geometries respectively, giving a wide range of potential binding geometries in our models.

Zinc(II) has chemical behaviour in common with copper(II) and is the 14th most electrically conductive element in its bulk form,[21] 1.69×10^7 Sm^{-1} at 20°C, with examples of zinc oxide nanowires also in the literature.[24] Zinc displays a lower range of common oxidation states than the other first row d-block metals, where chemistry is limited to that of Zn(II).

No particular geometry is preferred for Zn(II), showing similarities to Mg(II) with many compounds being isomorphous with their Mg analogues.[25] Common examples of co-ordination complexes include 4 co-ordinate Zn(II), such as $[ZnCl_4]^{2-}$, 5 co-ordinate Zn(II), such as $[Zn(acac)_2(H_2O)]$ (acac = acetylacetone) and 6 co-ordinate Zn(II), such as $[Zn(H_2O)_6]^{2+}$. These complexes exhibit tetrahedral, square-based pyramidal and octahedral co-ordination geometries respectively.

As well as being the most electrically conductive element in bulk form,[21] 6.30 x 10^7 Sm^{-1} at 20°C, silver also shows potential for conductive nanostructures.[26] Silver generally holds the common oxidation state of +1, with examples of co-ordination complexes including 2 co-ordinate Ag(I), such as $[Ag(NH_3)_2]^+$ and 3 co-ordinate Ag(I), such as $[Ag(PPh_3)_3]^+$. These complexes display linear and trigonal planar co-ordination geometries respectively.

The conductive properties of copper, zinc and silver mean they are ideal metals for forming potentially conductive nanostructures on surfaces, and between them, these complexes have the ability to adopt many different geometries, giving us a potentially wide range of metal binding systems to study.

The pyridyl-imine spacer molecules, **8**, **9** and **10** were used as ligands here, as they can easily be prepared in the large amounts needed for multiple ligand-metal crystallization attempts.

4.2.2 $[Cu(en)_2(NO_3)_2]$ (M1)

Plate-shaped greenish-blue crystals of trans bis(ethylenediamine)Cu(II) nitrate were produced by the reaction of **8** (Py-Im-Et) and copper(II) nitrate hemi(pentahydrate) in a 2:1 ratio in water, where an excess of ligand is used to try and form discrete molecules 0-D which tend to be easier to work with than co-ordination polymers. X-ray crystal structure determination shows the product as a six co-ordinate copper(II) complex with two ethylenediamine (en) bi-dentate ligands in the equatorial plane and two monodentate nitrate ions binding in the apical positions (Figure 4.1a and b).

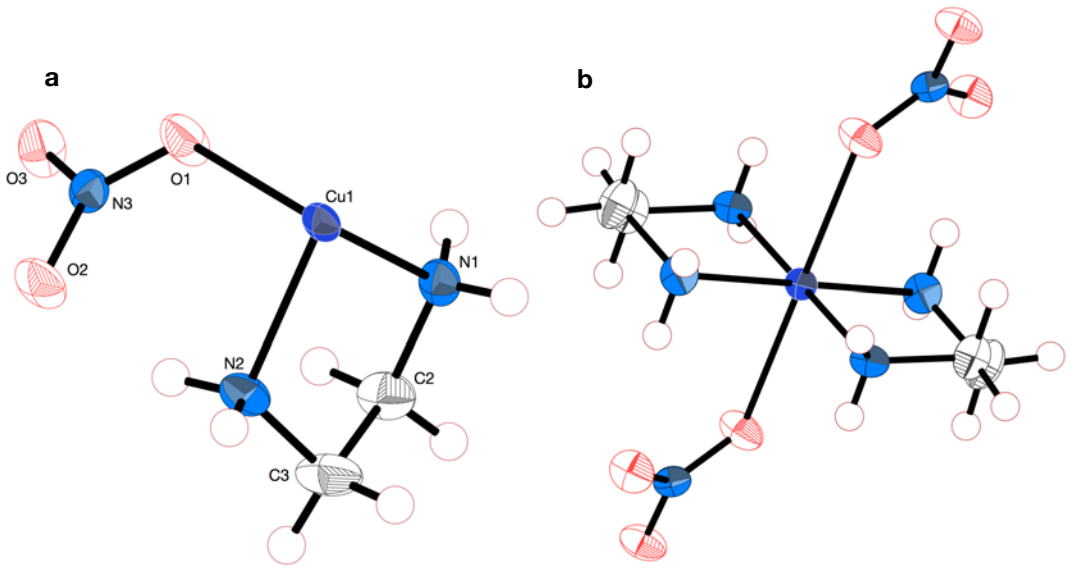

Figure 4.1 Crystal structure of $[Cu(en)_2(NO_3)_2]$ (M1), showing the labelled asymmetric unit, **a** and metal co-ordination geometry, **b**.

The N1-Cu1 and N2-Cu1 bond lengths are 2.00 Å and 2.01 Å respectively, with the O1-Cu1 distance at 2.55 Å. Trans angles around the metal centre are all 180.0° as half of the atoms are symmetry generated. Cis angles around the metal centre are N1-Cu1-O1, 93.3°, N2-Cu1-O1, 88.6°, N1-Cu1-N2 (within one ligand), 84.8° and N1-Cu1-N1(between ligands), 95.2°, giving a very distorted octahedral co-ordination geometry around the central copper atom.

Hydrogen bonding between the nitrogen donor for the ethylenediamine and the oxygen acceptor of the nitrate ion (N1-H···O3 = 2.98 Å, H···O3 = 2.17 Å and N2-H···O2 = 2.98 Å, H···O2 = 2.12 Å) are present in the b- and c-axes between molecules.

There are 340 six co-ordinate copper structures with bis(ethylenediamine) ligands reported in the CSD, none of which have nitrates also attached, making this crystal structure unique.[27] However, our intention here was to establish details of the effect of metal ion binding on the ligand conformation of **8** (Py-Im-Et), which has decomposed to give diaminoethane co-ordinated to copper. Despite the stability of ligand **8** in water (due to delocalization of the imine double bond) this aqueous copper nitrate solution seems to have catalysed this degradation of **8** by increasing the acidity of the mixture enough to facilitate hydrolysis. Attempts to produce crystals with Cu(II) trifluoromethane sulfonate under dry conditions (using MeCN as the solvent) were unsuccessful, as too were attempts using Cu(I) trifluoromethane sulfonate toluene complex.

Degradation of the ligand means this complex cannot be used as a model for our surface binding studies. The sp^3 hybridized amine binding sites in this crystal structure posses a different geometry and electron configuration to our pyridine binding sites where N is sp^2 hybridized. The ethylenediamine ligand here is also bi-dentate with a tendency to bind in a cis arrangement due to it's length, our ligands are expected to be mono-dentate with respect to one metal atom and can freely bind at any position.

4.2.3 $[Zn(8)(H_2O)_4]2NO_3 \cdot 2H_2O$ (M2)

The reaction between **8** (Py-Im-Et) and zinc(II) nitrate hexahydrate in a 2:1 ratio in water, produced blue needle-shaped crystals. X-ray diffraction revealed the structure to be a one-dimensional co-ordination polymer where two molecules of **8** are bound to one zinc(II) atom by a pyridyl nitrogen atom (Zn1-N1 = 2.12 Å) (Figure 4.2), and form an extended chain molecule by binding to another zinc atom through the other pyridyl nitrogen atom (Figure 4.3). These chains form even when using an excess of ligand, giving a preferred 1:1 binding ratio. The zinc atom shows a regular six co-ordinate octahedral geometry with the ligands (**8**) in a trans arrangement to each other (N1-Zn1-N1 = 178.2°). The other four ligands are water molecules with bond lengths of 2.12 Å for both Zn1-O1 and Zn1-O2 in an equatorial arrangement around the zinc atom, with cis bond angles of 89.9°, 88.7°, 91.9° for N1-Zn1-O1, N1-Zn1-O2 and O1-Zn1-O2 respectively.

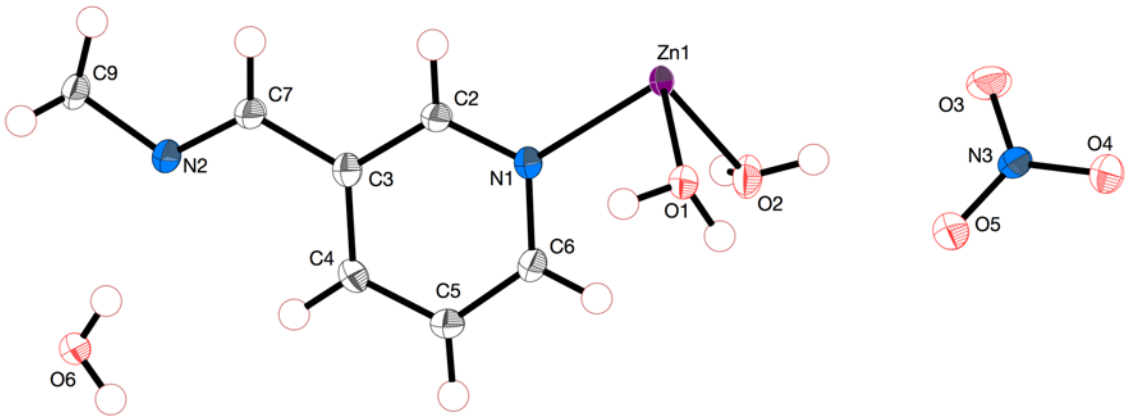

Figure 4.2 The asymmetric unit of $[Zn(\mathbf{8})(H_2O)_4]2NO_3 \cdot 2H_2O$ (**M2**) as determined by X-ray diffraction.

This seems to be quite a common co-ordination number for zinc, with 7491 examples of six co-ordinate zinc complexes reported in the CSD (2015),[27] 2643 of which contain at least two pyridyl groups as co-ordinating ligands. The structure also contains unbound solvent molecules of water, which exhibit hydrogen bonding interactions as a donor to the unbound imine nitrogen atoms (O6-H···N2 = 2.85 Å, H···N2 = 2.09 Å) as well as an acceptor to the zinc bound water molecules (O2-H···O6 = 2.76 Å, H···O6 = 1.91 Å). Nitrate anions are also present and interact with the bound water molecules by hydrogen bonding (O2-H···O5 = 2.75 Å, H···O5 = 2.03 Å and O1-H···O4 = 2.73 Å, H···O4 = 1.85 Å). These unbound water and nitrate molecules fill the gaps between the polymer chains for efficient packing whilst also possibly directing this packing through hydrogen bonding.

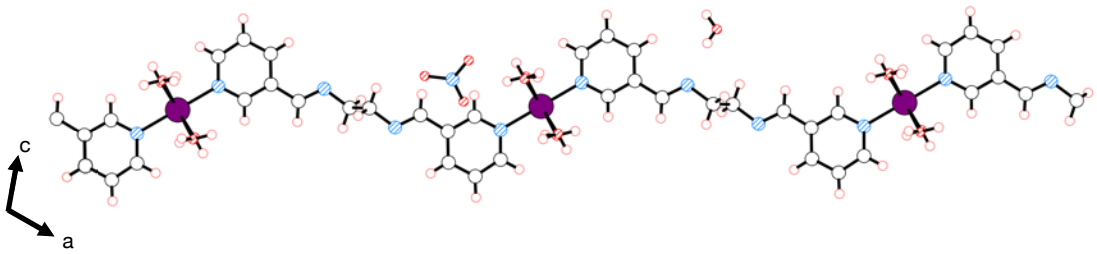

Figure 4.3 One-dimensional chain of $[Zn(\mathbf{8})(H_2O)_4]2NO_3{\cdot}2H_2O$ (**M2**) viewed down the b-axis.

These metal binding experiments serve as a model for metal binding to crystal surfaces. Surface binding sites are easily accessible to metal species when presented perpendicular to the crystal surface. However, these binding sites may still be accessible to metal species even when not presented perpendicular to the crystal surface (Figure 4.4). Metal species may not require to (and may prefer not to) bind in a perfect trigonal planar geometry, allowing both larger and smaller binding angles. The metal to pyridyl binding site angles in these metal complexes provide us with a preferred range of access for the metal. If the binding sites are presented at the crystal surface in such a way as to meet this range, metal binding is more likely to occur.

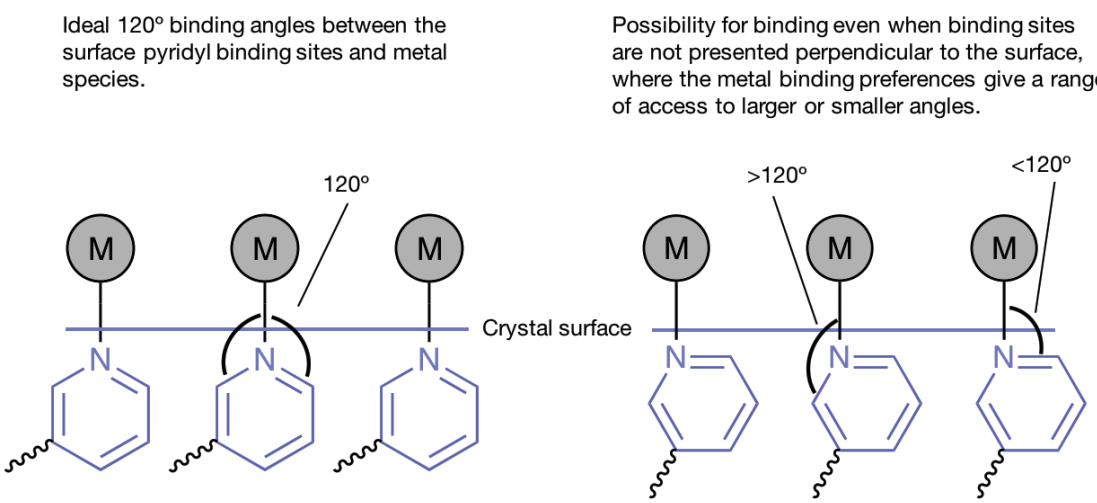

Figure 4.4 Schematic representation of surface binding sites presented perpendicular to the surface (left) and not presented perpendicular to the surface (right) indicating that metal binding may still occur because of the range of angles they can adopt.

As a model for surface metal binding, the pyridyl group to metal binding angles deviate from a perfect trigonal planar geometry (with respect to the nitrogen atom) by only 2.0° and 0.0° in the plane of the ring and 3.2° perpendicular to the plane of the ring (C2-N1-Zn1 and C6-N1-Zn1 are 122.0° and 120.0° respectively with the C4-N1-Zn1 at 176.8°). This shows that surface binding may still occur up to the point where these angles cannot be met (118.0°-122.0° in the plane of the ring and 176.8°-183.2° perpendicular to the ring plane), hindered by the surface and the size of the metal atom.

A comparison of the ligand structure before and after binding was made, allowing us to evaluate how likely changes to ligand conformation would be when metal is bound to the surface of these crystals. Minimal conformational changes are desired so that the underlying crystal structure is not disturbed. The pyridyl rings still exhibit a trans geometry with respect to one another, and the pyridyl and imine nitrogen atoms are still on the same side of the molecule with only a small rotation of the pyridyl group. The torsion angle (C2-C3-C7-N2) is 176.5°, 3.6° rotated away from its original position. The link between the imine bond and the ethyl spacer unit (C7-N2-C9-C9a) now has a torsion angle of 114.2°, 20.7° rotated away from the original angle, putting the atoms more ‘out of plane’ and decreasing the internal N1-N1 distance by 0.25 Å to 12.85 Å. The only significant structural change to **8** through co-ordinating to zinc is the C7-N2-C9-C9a torsion angle, however, we suspect that this change in

conformation is due to the zinc atoms being included in the crystal structure with the ligand conformation adjusting to the packing arrangement, therefore metal binding to the surface of a pre-formed crystal would not have this same effect, leaving the ligands in the crystal unchanged.

4.2.4 [Ag(10)(tos)] (M3)

The reaction between **10** (Py-Im-Cy) in dichloromethane and silver(I) tosylate in acetonitrile a 1:1 ratio gave small colourless crystals. X-ray diffraction showed the crystal structure where a three co-ordinate silver(I) atom binds to two different binding sites in the ligand molecule (Figure 4.5) and extends in a two-dimensional sheet arrangement (Figure 4.6). The silver binds to one pyridyl nitrogen atom (Ag1-N1 = 2.19 Å) and one imine nitrogen atom from another molecule (Ag1-N2, also 2.19 Å) as well as one tosylate anion (tos) (Ag1-O1 = 2.52 Å). The angles around the central silver atom are 154.6° (N1-Ag1-N2), 99.2° (N1-Ag1-O1) and 103.1° (N2-Ag1-O1), giving it a distorted trigonal planar geometry (possibly due to the crystal packing).

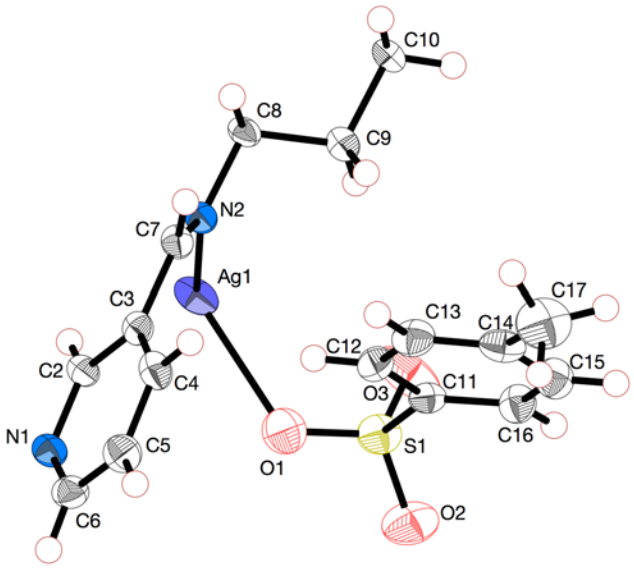

Figure 4.5 The asymmetric unit of [Ag(**10**)(tos)] (**M3**) as determined by X-ray diffraction.

This is a reasonably common co-ordination number for silver complexes, with 4226 examples of three co-ordinate silver complexes reported in the CSD (2015), of which 501 contain two or more pyridyl groups as co-ordinating sites. As both nitrogen atoms are involved in metal binding, there are no typical heteroatom hydrogen bonds in the packing arrangement. It is also unlikely that edge to face π interactions play any role in the crystal packing as they are very

weak, with distances above 4 Å. Crystal packing in this structure must be mostly governed by close crystal packing interactions (van der Waals or short-range electron-cloud repulsions).

Used as a model for metal binding, the structure shows that the pyridyl-metal binding angles in the plane of the pyridyl ring are 123.4° (C6-N1-Ag1) and 127.7° (C2-N1-Ag1), and orthogonal to the ring plane is 176.8° (C4-N1-Ag1). These values deviate from an ideal trigonal planar geometry by 3.4°, 7.7° and 3.2° respectively, meaning surface-metal binding may still occur to the point where these angles cannot be met (112.3°-127.7° in the plane of the ring and 176.8°-183.2° perpendicular to the ring plane), due to hindrance by the surface and size of metal atom.

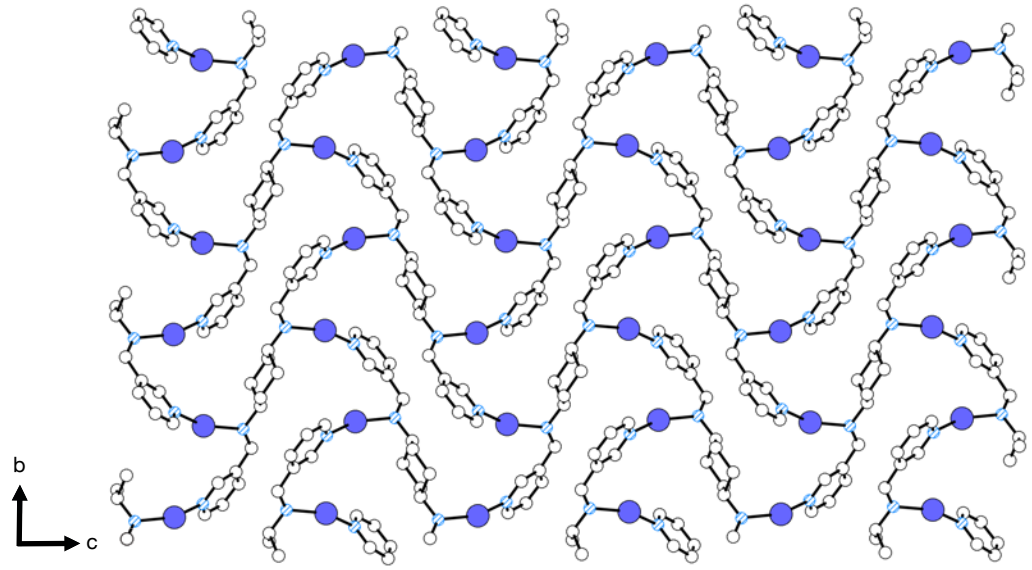

Figure 4.6 Two-dimensional sheet of [Ag(**10**)(tos)] (**M3**), viewed down the a-axis. Hydrogen atoms and tosylate anion molecules removed for clarity.

This structure shows how the imine nitrogen atom can act as a second binding site, influencing the 2-D sheet structure (Figure 4.6). The imine-metal binding angles were measured at 126.9° (C7-N2-Ag1) and 115.3 (C8-N2-Ag1). These angles are 6.9° and 4.7° away from an ideal trigonal planar geometry meaning surface-metal binding could occur at this site if they are displayed at the surface with a 113.1°-126.9° range of access.

Comparison of the structure of this co-ordinated ligand to the uncoordinated ligand (**10**) show the pyridyl groups still have a trans relationship to each other,

however, the pyridine nitrogen atom is now on the same side of the molecule as the imine nitrogen atom due to a large rotation of the pyridyl group. This rotation is seen in a torsion angle (C2-C3-C7-N2) of 33.6º, which is a 135.3º rotation about the C3-C7 bond (relative to the conformation of **10** in the just ligand crystal structure) and likely occurs so that the silver atom can bind to the imine nitrogen atom as well as the more common binding site of the pyridyl nitrogen atom. The torsion angles between the imine and spacer unit show very little change, with only a 1.8º and 1.7º difference for C7-N2-C8-C9, 101.6º and C7-N2-C8-C10, 136.7º, respectively. These conformational changes to the ligand give an internal N1-N1 distance of 14.23 Å, 0.81 Å shorter than for the uncoordinated ligand.

The large rotation of the pyridyl groups seen here is attributed to the silver atom being able to bind to both nitrogen atoms of the ligand molecule (**10**), this lack of selectivity means that on a pre-formed crystal surface, deposited metal atoms could bind to either of the binding sites depending on which is present at that surface, but probably not both, as the structure of **10** would have to change and possibly destroy the crystal.

4.2.5 $[Ag(10)_3]NO_3$ (M4)

M4 was produced by the reaction between **10** (Py-Im-Cy) and silver(I) nitrate (3:1 ratio) in dichloromethane/acetonitrile mixtue and gave small colourless crystals. An excess of ligand was again used in order to obtain a discrete metal complex, however, X-ray diffraction shows the structure as a three-dimensional MOF, where one silver(I) atom binds to six Py-Im-Cy ligands by their pyridyl nitrogen atom binding sites, forming an octahedral geometry (Figure 4.7). All Ag1-N1 bond lengths are 2.53 Å, significantly longer than in the 3 co-ordinate structure, **M3** (2.19 Å). The trans bond angles around the silver centre (N1-Ag1-N1(trans)) all measured at 180.0º, the cis bond angles however, deviate from a perfect octahedral geometry and come in two forms, N1-Ag1-N1(cis1), 83.9º and N1-Ag1-N1(cis2), 96.1º.

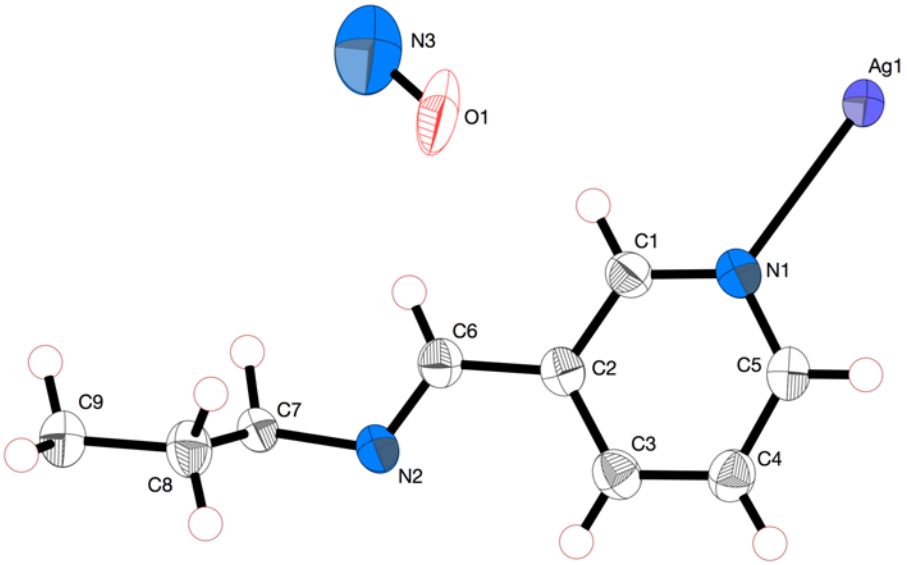

Figure 4.7 The asymmetric unit of [Ag(**10**)$_3$]NO$_3$ (**M4**) as determined by X-ray diffraction.

Each of the six ligands bind to another silver atom via the nitrogen atom at the opposite end of the molecule (Figure 4.8), creating a three-dimensional metal-organic framework with a wine-rack architecture (Figure 4.9). The structure also contains some disordered nitrate anions which balance the +1 charge of the silver centres. Each of the six pyridyl groups bound to the silver centre give and receive weak edge to face π interactions from each other, (C5-H5···centroid = 3.92 Å, H5···centroid = 3.19 Å). Six co-ordinate silver complexes are far less common than the three co-ordinate structure seen in compound **M3**, with only 1381 examples of six co-ordinate silver complexes reported in the CSD (2015) (compared to 4226 three co-ordinate), of which just 9 contain pyridyl groups as the only ligand type.

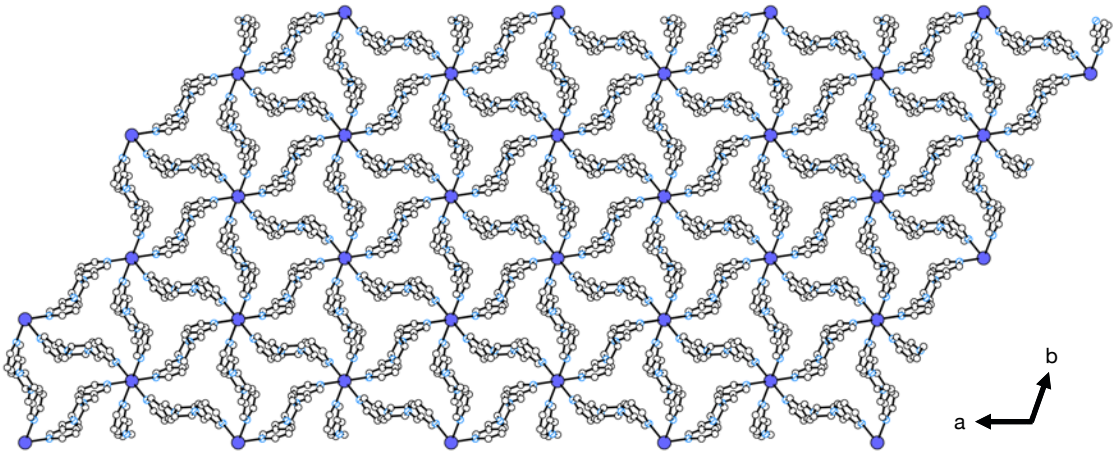

Figure 4.8 Structure of [Ag(**10**)$_3$]NO$_3$ (**M4**) viewed down the c-axis, showing the connectivity between metal atoms through the ligands. Hydrogen atoms and anion molecules removed for clarity.

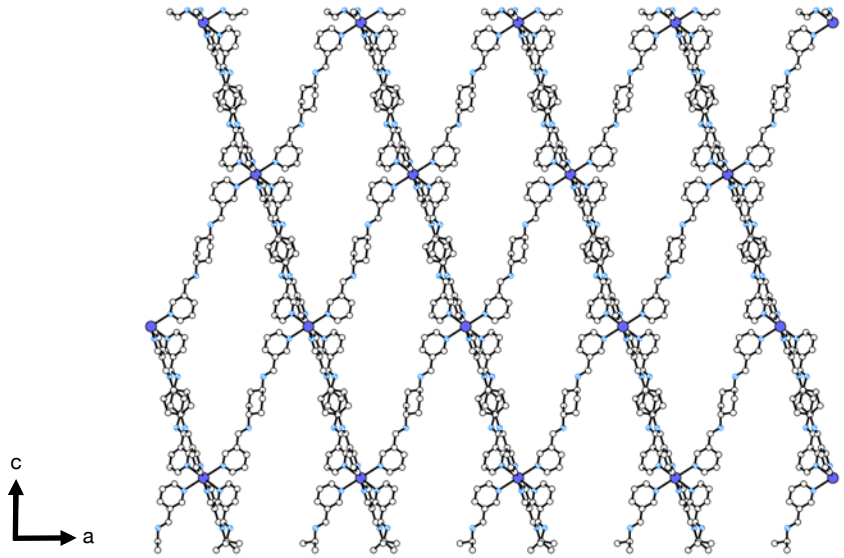

Figure 4.9 Three-dimensional wine-rack structure of [Ag(**10**)$_3$]NO_3 (**M4)** viewed down the b-axis. Hydrogen atoms and anion molecules removed for clarity.

Looking at the details of the metal binding in **10,** the pyridyl-metal binding angles differ from an ideal trigonal planar geometry by 4.2º and 2.1º in the plane of the ring and 11.4º perpendicular to the plane of the ring (all 124.2º for C1-N1-Ag1 and all 117.9º for C5-N1-Ag1, as well as 168.6º for C3-N1-Ag1). These angles show that surface-metal binding may still occur if the binding sites are displayed with a range of access of 115.8º-124.2º in the plane of the ring and 168.6º-191.4º perpendicular to the ring plane.

Comparing the metal-bound ligand in this structure to the unbound (**10**), the pyridyl nitrogen groups are still trans to each other, and the pyridine and imine nitrogen atoms are on opposite sides of the molecule as in the crystal structure of **10**, with a torsion angle (C1-C2-C6-N2) of 177.7º. This is a rotation of only an 8.8º from the unbound ligand which may be due to edge to face π interactions between two adjacent pyridyl rings, N1-C1-C2-C3-C4-C5 centroid to H5, 3.19 Å.

Torsion angles between the imine group and the cyclohexyl spacer unit were measured at 109.7º for C6-N2-C7-C8 and 129.6º for C6-N2-C7-C9, rotations of 9.9º and 5.4º respectively. The small torsion angle changes to the ligand (**10**) in this crystal mean the internal N1-N1 distance only decreases by 0.01 Å to 15.03 Å. The small conformational changes to **10** suggest that any metal binding to the surface of a pre-formed crystal of this molecule would exert minimal influence, possibly leaving the crystal structure unaffected.

4.2.6 [Ag(9)(NO_3)] (M5)

Reaction of **9** (Py-Im-Ph) with silver(I) nitrate (1:1 ratio) in a dichloromethane/acetonitrile mixture, gave small yellow crystals. The compound was identified by X-ray crystallography, having a structure of a one-dimensional metal co-ordination polymer where the full molecule of **9** is in the asymmetric unit (Figure 4.10), giving two independent pyridyl groups. Two Py-Im-Ph ligand molecules (**9**) are bound to one silver(I) atom by a pyridyl nitrogen atoms N1 and N4, and form an extended chain by binding to another silver atom through the other pyridyl nitrogen (Figure 4.11).

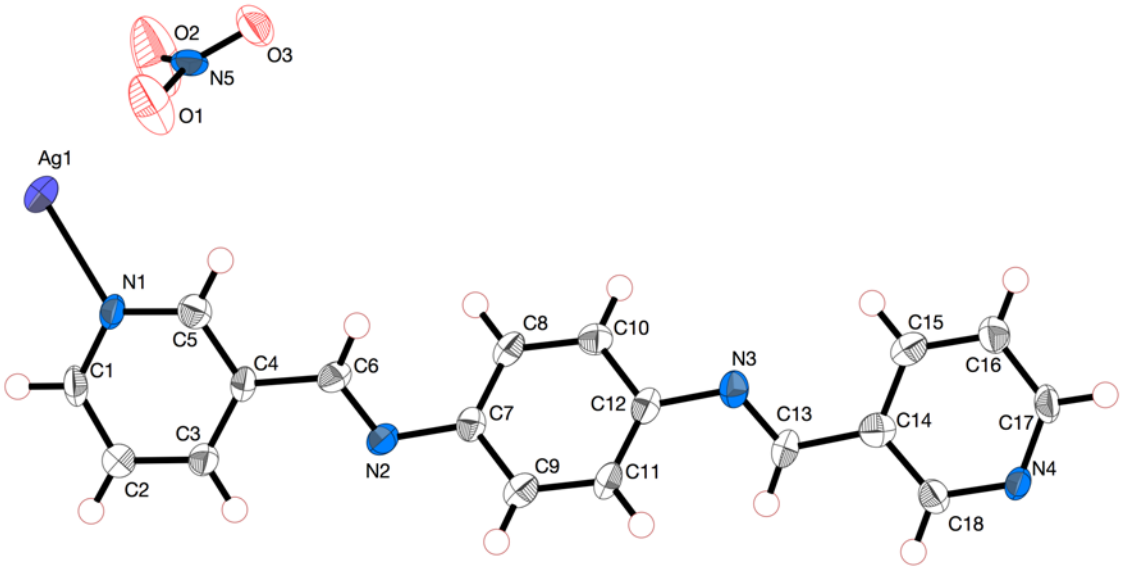

Figure 4.10 The asymmetric unit of [Ag(**9**)(NO_3)] (**M5**) as determined by X-ray diffraction.

This structure is a polymorph of a previously reported crystal structure found in the CSD.[28] The silver atom shows a three co-ordinate bent trigonal geometry with the pyridyl groups (N1-Ag1-N4) 155.5° in relation to each other with bond lengths of 2.16 Å for Ag1-N1 and for Ag1-N4. The nitrate ion is in the third position with the Ag1-O1 distance measured at 2.53 Å and N1-Ag1-O1 angle measured at 96.2° and the N4-Ag1-O1 angle measured at 106.8°. Hydrogen bonding is observed between nitrate ions and the pyridyl rings of the ligand molecule possibly assisting the β-structure packing seen in Figure 4.10 (C1-H1···O3 = 2.26 Å, H1···O3 = 3.35 Å and C17-H17···O3 = 3.29 Å, H17···O3 = 2.37 Å). Cation-π interactions were also identified between the silver atoms and pyridyl centroids between chains in the a-axis (Ag1···N1-C1-C2-C3-C5 centroid = 3.36 Å and Ag1···N4-C18-C14-C15-C16-C17 centroid = 3.40 Å) and

seem to offset the chains when compared to the literature form which is aligned by silver-silver interactions.

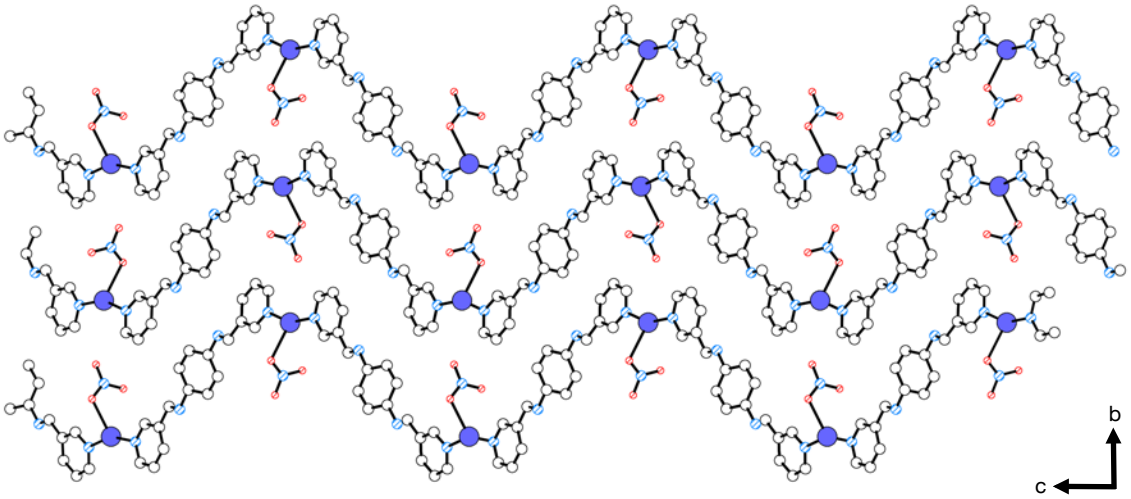

Figure 4.11 One dimensional chain of [Ag(**9**)(NO_3)] (**M5**), viewed down the a-axis. Hydrogen atoms removed for clarity.

In this crystal structure, the whole of the ligand molecule is in the asymmetric unit, meaning the two pyridyl binding sites are not the same due to symmetry. The pyridyl-metal binding angles for the first binding site (involving N1) are now 121.1° (C1-N1-Ag1) and 120.8° (C5-N1-Ag1) in the plane of the ring, and 175.7° (C3-N1-Ag1) perpendicular to the plane of the ring, only 1.1°, 0.8° and 4.3° away from the ideal trigonal planar geometry, meaning, if this binding site was present at the crystal surface, it could be accessible to binding up to the point where these angles cannot be met when bound (118.9°-121.1° in the plane of the ring and 175.7°-184.3° perpendicular to the ring plane).

The second pyridyl-metal binding site (involving N4) shows angles of 119.5° for C17-N4-Ag1 and 121.3° for C18-N4-Ag1 in the plane of the ring, and 176.1° (C15-N4-Ag1) perpendicular to the plane of the ring, these are only 0.5°, 1.3° and 3.9° away from the ideal trigonal planar geometry, meaning, if this binding site is present at the surface, binding would occur providing suitable access to the site, i.e. the range of access is 118.7°-121.3° in the plane of the pyridyl ring and 176.1°-183.9° perpendicular to the ring plane.

Structural comparison of the bound ligand to the unbound ligand **9** shows that the pyridyl groups remain trans to one another but now the pyridyl and imine nitrogen atoms face opposite sides of the molecule after a large rotation of the pyridyl group. The C5-C4-C6-N2 torsion angle is 171.2°, a 166.4° rotation from

the equivalent angle in **9**. The imine to phenyl spacer torsion angles were measured at 34.4º for C6-N2-C7-C8 and 149.5º for C6-N2-C7-C9; these are relatively small rotations of 2.4º and 3.9º respectively. The conformational changes to **9** in this crystal structure increase the length of the molecule by 0.52 Å to give an internal N1-N1 distance of 14.56 Å.

The large rotation of the pyridyl groups is attributed to the need to satisfy both the binding site co-ordination to silver and the overall packing arrangement of the chains. It is expected that this packing arrangement would not need to be satisfied when the metal is bound only to the surface of a pre-formed crystal of **9** as the co-ordination polymer chains would not be formed. This would leave crystals of **9** unaffected by surface-metal binding.

4.2.7 2D/3D Interpenetrated $[Ag(9)_3]NO_3$ Framework and $[Ag(9)_3]NO_3$ MOF (M6)

Small pale yellow crystals of **M6** were produced in the reaction of **9** (Py-Im-Ph) and silver(I) nitrate in a dichloromethane/dimethylformamide/acetonitrile mixture, a 3:1 ratio was again used in an attempt to obtain a discrete metal complex but instead affords the formation of a material consisting of two separate MOFs (metal-organic frameworks) (Figure 4.12), a two-dimensional framework and a three-dimensional framework (Figure 4.13). The two form no chemical bonds between one another and are said to be interpenetrated.[29] This involves three arms (ligands) of the 3-D component passing through a triangular hole in the 2-D framework created by three arms bridging three silver atoms (Figure 4.14). Interpenetrated structures can be considered the polymeric analogue of rotaxanes and catenanes.[30] Few examples of interpenetrated structures exist where the separate frameworks are of the same molecules and not self-penetrating, with only a handful reported in the CSD being 2D/3D interpenetrated. Furthermore, our structure seems to be the only example where both the 2-D and 3-D components consist of the same node and linker, six co-ordinate silver with ligands of **9**.

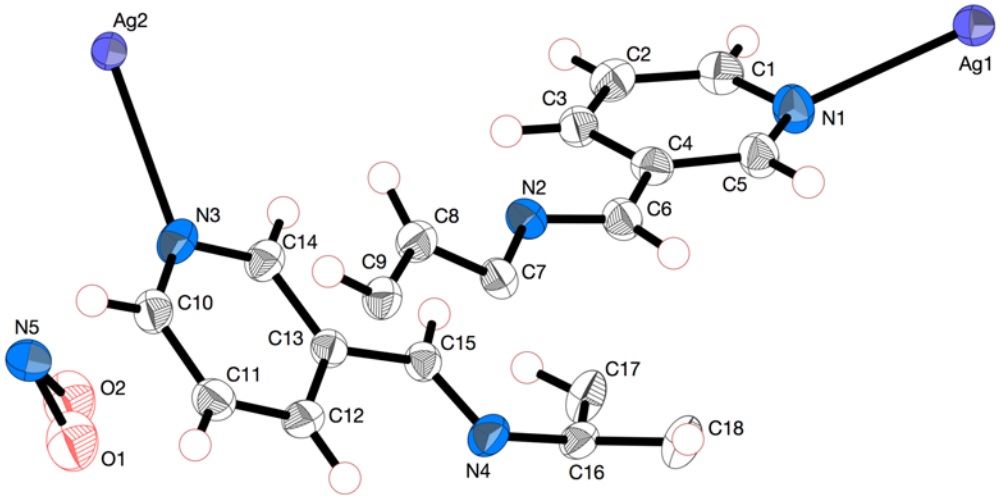

Figure 4.12 The asymmetric unit of (**M6**), showing both the two-dimensional and three-dimensional components, as determined by X-ray diffraction.

The asymmetric unit (Figure 4.12) consists of two unique silver(I) atoms (Ag1 and Ag 2) each co-ordinated to a crystallographically unique ligand molecule (**9**) only half of which is in the asymmetric unit. Also present is a nitrate anion molecule. When the structures are completed, they extend to form a 3-D component, bound to Ag1, and a 2-D component, bound to Ag2. Both of these structures are further examples of the rarely seen six co-ordinate silver. The structures both show an octahedral geometry, where each of the six co-ordinating ligands (**9**) connect to another silver atom via the second pyridyl nitrogen atom, extending to form either the 2-D or 3-D structures.

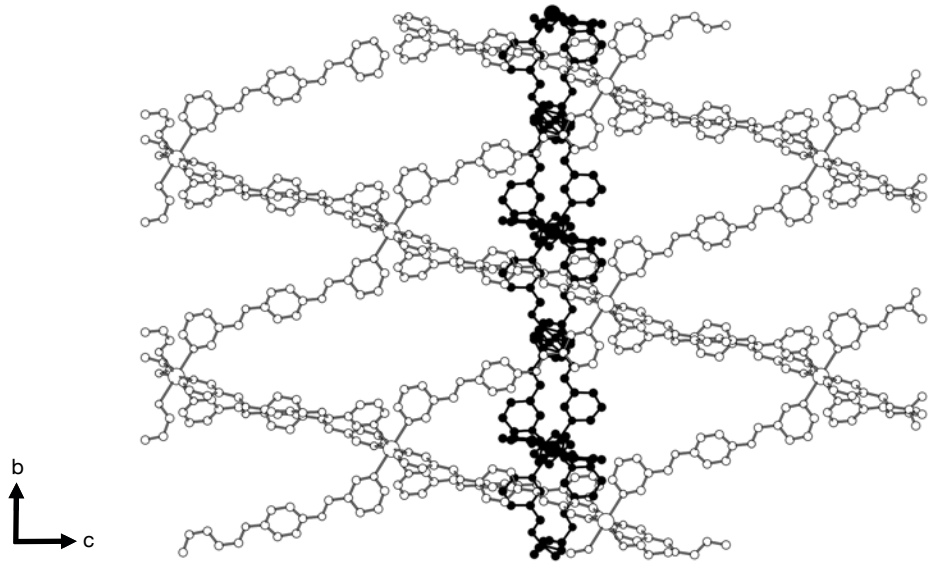

Figure 4.13 M6 viewed down the a-axis showing the 3-D wine-rack structure (white) interpenetrating with the 2-D sheet (black). Hydrogen atoms removed for clarity.

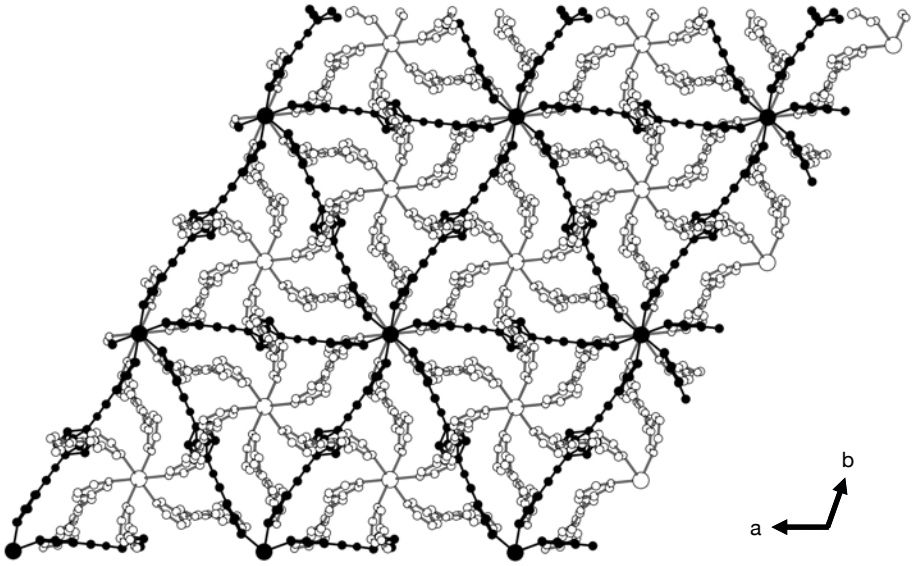

Figure 4.14 M6 viewed down the c-axis showing the 3-D component (white) extending through triangular shaped pores created by the 2-D component (black). Hydrogen atoms removed for clarity.

2-D $[Ag(9)_3]NO_3$ Framework in M6

The 2-D framework contains a six co-ordinate silver atom bound to six molecules of (**9**) via the pyridyl nitrogen atom. The Ag2-N3 distance is 2.56 Å, again, this six co-ordinate complex shows significantly longer Ag-N distances than for the 3 co-ordinate compound **M5** (2.16 Å). This framework has an octahedral geometry (Figure 4.15) with the trans substituents all being 180.0° from each other and the cis related substituents being either 90.9° or 89.1° from each other (six of each angle).

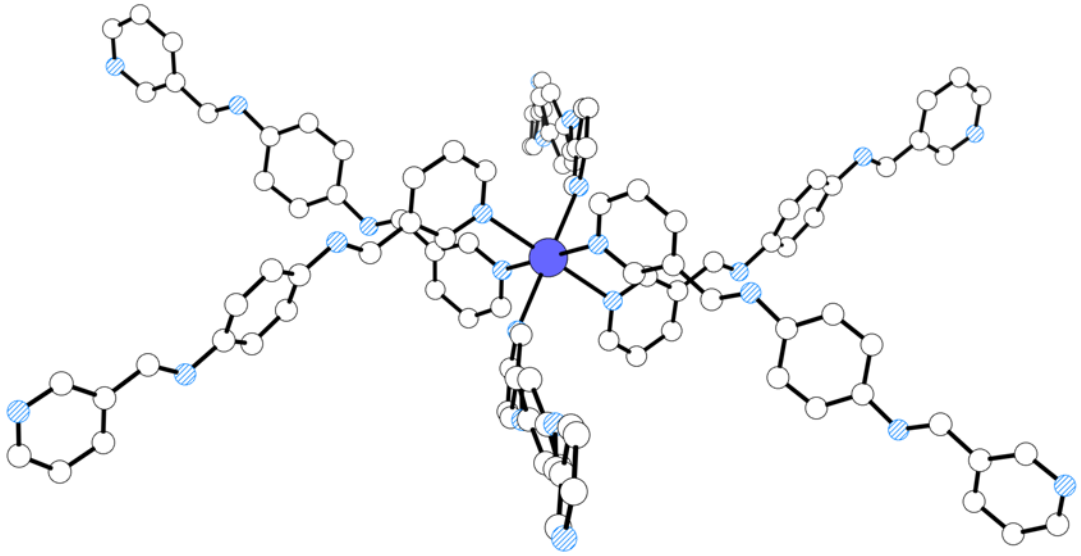

Figure 4.15 Co-ordination centre of the 2-D component in **M6**, showing how the ligands extend in one plane.

There is a lack of face to face π interactions between the pyridyl groups around the metal centre compared to the other six co-ordinate silver centres studied

here, **M4** and the **M6** 3-D component. These ligands contort in a way to give a 2-D sheet where the ligand arms extend in the a/b plane (Figure 4.16 and Figures 4.13 and 4.14 in black).

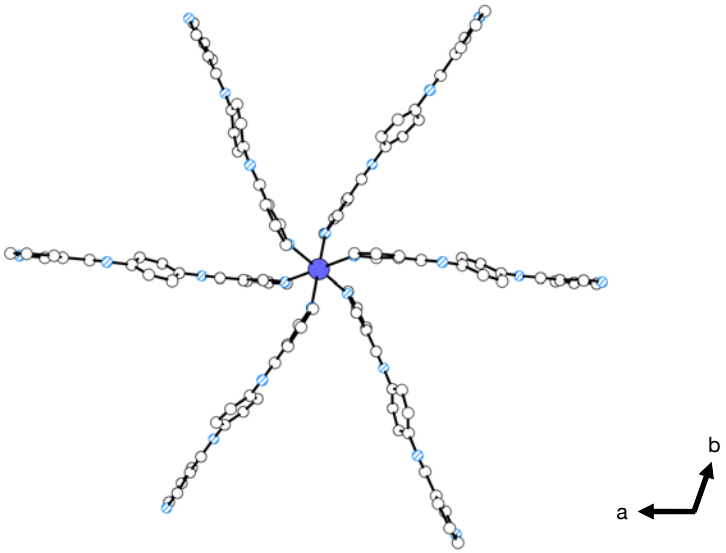

Figure 4.16 The 2-D component of **M6** viewed down the c-axis, showing the fully extended ligand arms.

The pyridyl-metal binding angles found in this 2-D framework were measured at 124.5° (C10-N3-Ag2) and 115.8° (C14-N3-Ag2) in the plane of the pyridyl ring, and 162.5° (C12-N3-Ag2) perpendicular to the ring plane. These angles are 4.5°, 4.2° and 17.5° away from the expected trigonal planar geometry, implying that surface binding may occur if these sites were present at a crystal surface so long as the access angles can be met, these are 115.5°-124.5° in the plane of the pyridyl ring and 162.5°-197.5° perpendicular to this plane.

Comparison of the unbound **9** to the bound molecule in this 2-D framework reveals that the pyridyl groups are still trans to each other, however, the pyridyl and imine nitrogen atoms are now on opposite sides of the molecule (C14-C13-C15-N4 torsion angle is 174.8°), meaning the pyridyl groups have rotated by 170.0° about the C13-C15 bond. The linkage between the imine group and the phenyl spacer unit now has a torsion angles of 24.9° for C15-N4-C16-C17, and 158.7° for C15-N4-C16-C18, meaning rotations of 11.9° and 13.1° are observed respectively. These conformational changes increase the internal N1-N1 distance by 0.66 Å to 14.66 Å.

3-D $[Ag(9)_3]NO_3$ MOF in M6

The 3-D component of the structure also consists of a six co-ordinate silver atom with all ligands of **9** co-ordinating through the pyridyl nitrogen atom (Ag1-

N1 distance is 2.53 Å). It has an octahedral geometry (Figure 4.17) with one of the trans N1-Ag1-N1 angles at 180.0º and the other two at 179.9º, the ligands with a cis relationship are 82.4º and 97.6º from each other (six of each angle).

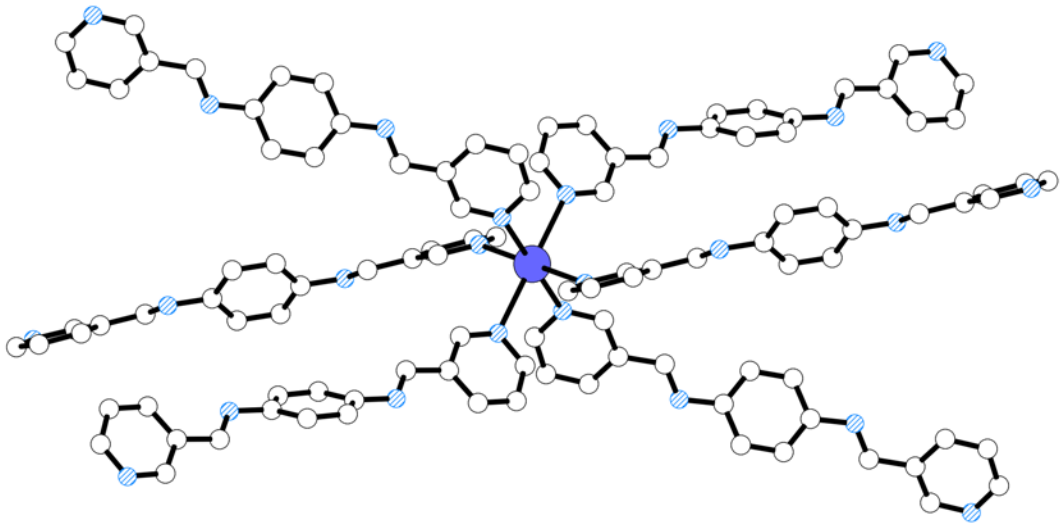

Figure 4.17 Co-ordination centre of the 3-D component in **M6**, showing how the ligands extend in multiple planes.

Edge to face π interactions around the metal centre are observed between the pyridyl groups (C10-H10···centroid = 3.80 Å, C10···centroid = 3.12 Å. These interactions are not observed in the 2-D component and may contribute to the change in framework structure, favouring the 3-D architecture over 2-D, as seen in **M4**. The ligands this time extend in three planes of direction giving the 3-D framework resembling a wine-rack motif which has been stretched in the c-axis (Figure 4.18 and Figures 4.13 and 4.14 in white).

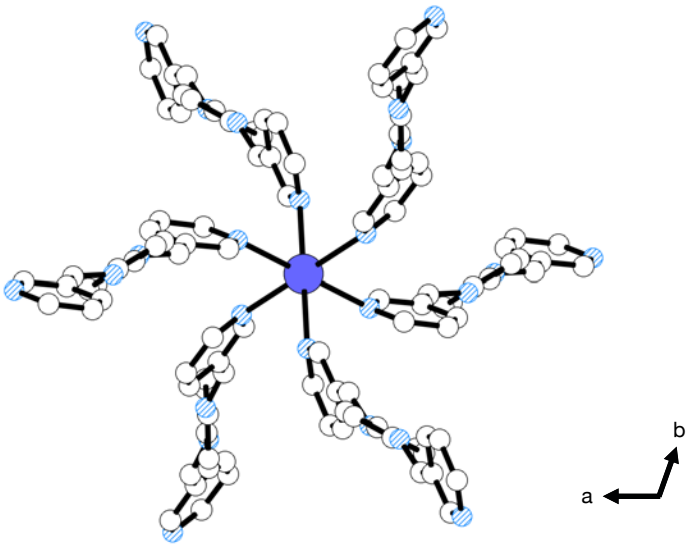

Figure 4.18 The 3-D component of **M6** viewed down the c-axis, showing the less extended ligand arms in this plane.

The binding angles for pyridyl-metal in this 3-D component are 115.1°, 124.6° and 159.7° for the in plane angles (C1-N1-Ag1 and C5-N1-Ag1), and out of plane angle (C3-N1-Ag1) respectively. These angles are 4.9°, 4.6° and a huge 20.3° away from the ideal trigonal planar geometry, meaning surface-metal binding could occur at this site if they are displayed at the surface with a 115.1°-124.9° range of access in the plane of the pyridyl ring and a 159.7°-200.3° range of access perpendicular to the pyridyl ring plane.

A structural comparison of the metal-bound molecule of **9** in this 3-D component to its unbound form shows the pyridyl groups still trans to each other. The pyridyl rings have again twisted so that the pyridyl and nitrogen atoms face opposite sides of the molecule, with a torsion angle of 171.4° for C5-C4-C6-N2, a 166.8° rotation. The imine to phenyl spacer linkage shows much smaller rotations of 0.2° and 4.2° for the C6-N2-C7-C9, 36.6° and C6-N2-C7-C8, 149.8°, torsion angles respectively. The internal N1-N1 distance has increased by 0.75 Å to 14.75 Å due to these conformational changes.

As with **M5**, the rotation of the pyridyl groups when bound to silver is accredited to the packing arrangement in the crystal structure, and not purely due to silver binding. Metal bound molecules of **9** are unlikely to be restricted to this conformation, so metal-binding to a pre-formed crystal of **9** in its original configuration is unlikely to induce this rotation, leaving the crystal structure intact.

4.3 Conclusions

A series of metal complexes with ligands of **8** (Py-Im-Et), **9** (Py-Im-Ph), and **10** (Py-Im-Cy) were prepared as models for crystal surface binding experiments.

Firstly, these compounds show that the molecules intended to be used as crystal substrate surfaces, do indeed bind to metal atoms such as zinc and silver, and do so through the primary binding site of the pyridyl groups. Though less frequently observed, the imine nitrogen can also bind.

The models all show a near trigonal planar geometry (with respect to the pyridyl nitrogen atom), meaning surface-metal binding would be favoured if the nitrogen atom was present at the crystal surface such that the pyridyl ring plane was orthogonal to the surface, easily providing metal atoms with the potential to bind in this favoured trigonal planar geometry. The 3-D component

in the **M6** structure showed the widest binding range of access, 115.1°-124.9° in the plane of the pyridyl ring, and 159.7°-200.3° perpendicular to the ring plane, where binding outside this range may be hindered by the crystal surface and the size of atom/particle.

The range of surface binding angles deduced here, represent favoured binding conformations for these metals and ligands, acting only as a guide for known, stable binding interactions. The possibility for metal binding beyond this range of angles at our crystal surfaces has not been ruled out.

Conformational changes in the ligand from its unbound crystalline state (determined in chapter 2) were also studied. It is desirable to change the ligand conformation as little as possible, as this would lead to destruction of the crystal if metal species were to bind to a crystal surface. Four of the six model structures show a significant rotation of the pyridyl ring, however, they are all close to 180° rotations, with the remaining structures making only minimal rotations. This shows the preferred conformations are syn-periplanar and anti-periplanar with respect to the imine bond, i.e. they are co-planar, supporting the choice of these ligands as 'rigid' where electrons are delocalized across the pyridyl ring and the imine double bond. It is possible that these rotations only occur to lower the overall crystal packing energy and incorporate the metal atoms into the structure, meaning that if the binding sites already have suitable access at the crystal surface, the rotation would not occur during metal-surface binding.

Conformational changes of the imine group and spacer unit within the ligand were characterized by the change in torsion angle between the two, with most having rotations of less than 10° from the unbound form and the **M3** structure showing the largest, 20.7°, change. These small conformational changes are likely the result of including metal atoms within the crystal structure and finding the lowest packing energy, meaning they are likely to be even less significant when a metal is bound only to a crystal surface.

The metal binding models shown here, all form extended structures due to having multiple available binding sites per ligand which are sufficiently separated to attach to different metal centres. The 1-D, 2-D and 3-D structures created here are not the focus of this study, but their extended MOF structures

could potentially be studied by others with the intention of probing their gas absorption, electrical and mechanical properties.

4.4 Experimental Details

All chemicals were purchased from Sigma-Aldrich, Alfa Aesar or Fisher Scientific and were used as received without further purification. Crystal structures were determined by single crystal X-ray diffraction at 150 K using Cu or Mo radiation on an Oxford Diffraction Gemini A Ultra diffractometer. Crystal structures were solved by direct methods and resolved using least squares analysis using the ShelXS and ShelXL packages respectively and Olex 2 (OlexSys Ltd.) as an interface. Graphics of the structures were produced in CrystalMaker (CrystalMaker Software Ltd.).

Synthesis of the silver complexes in this chapter was conducted by Glenn Lamming, a supervised MChem student in the Houlton group.

$[Cu(en)_2(NO_3)_2]$ (M1)

X-ray diffraction quality crystals were produced by dissolving **8** (95.3 mg, 0.4 mmol) in water (3 mL) and mixing with $Cu(NO_3)_2 \cdot 2.5H_2O$ (46.5 mg, 0.2 mmol), also dissolved in water (3 mL). The mixture was lightly stirred for 1 hour before being left to crystalize. Greenish blue, plate shaped crystals grew after 2 weeks.

Sum formula	$C_4H_{16}CuN_6O_6$	
Formula weight	307.78	
Temperature	150.01(10) K	
Radiation, wavelength	MoKα, λ = 0.71073 Å	
Crystal system, space group	Monoclinic, $P2_1/c$	
Unit cell parameters	a = 8.2271(8) Å	α = 90°
	b = 9.9877(6) Å	β = 111.951(10)°
	c = 7.8223(6) Å	γ = 90°
Cell volume	596.16(9) $Å^3$	
Z	2	
Crystal colour and size	Green/blue, 0.28 x 0.24 x 0.05 mm^3	
Final *R* indices [$F^2>2\sigma$]	R_1 = 0.0298	
R indices (all data)	wR_2 = 0.0712	
Large diff. peak and hole	0.41/-0.37 e $Å^{-3}$	

$[Zn(8)(H_2O)_4]_2NO_3 \cdot 2H_2O$ (M2)

X-ray diffraction quality crystals were produced by dissolving **8** (95.3 mg, 0.4 mmol) in water (3 mL) and mixing with $Zn(NO_3)_2 \cdot 6H_2O$ (59.5 mg, 0.2 mmol), also dissolved in water (3 mL). The mixture was lightly stirred for 1 hour before being left to crystalize. Blue, needle shaped crystals grew after 4 weeks.

Sum formula	$C_{14}H_{26}N_6O_{12}Zn$
Formula weight	535.78
Temperature	150.01(10) K
Radiation, wavelength	CuKα, λ = 1.54184 Å
Crystal system, space group	Monoclinic, *C2/c*
Unit cell parameters	a = 17.3189(4) Å α = 90°
	b = 6.68084(14) Å β = 112.785(3)°
	c = 20.4178(4) Å γ = 90°
Cell volume	2178.08(9) Å^3
Z	4
Crystal colour and shape	Light blue, needle
Final *R* indices [$F^2>2\sigma$]	R_1 = 0.0281
R indices (all data)	wR_2 = 0.0780
Large diff. peak and hole	0.62/-0.38 e Å^{-3}

[Ag(10)(tos)] (M3)

X-ray diffraction quality crystals were produced by layering solutions of ligand and metal in a 1:1 ratio. A cold solution of silver p-toluenesulfonate (55.8 mg, 0.2 mmol) in MeCN (10mL) was carefully layered onto a cold solution of **10** (58.5 mg, 0.2 mmol) in DCM (10mL) before being left to crystallize in the freezer (-20°) allowing for a slow diffusion. Small colourless crystals with undefined edges grew after about a month.

Sum formula	$C_{16}H_{17}AgN_2O_3S$
Formula weight	425.25
Temperature	150.0(2) K
Radiation, wavelength	CuKα, λ = 1.54184 Å
Crystal system, space group	Monoclinic, $P2_1/c$
Unit cell parameters	a = 11.5000(5) Å α = 90°
	b = 9.1978(3) Å β = 95.622(3)°
	c = 15.3517(4) Å γ = 90°
Cell volume	1616.02(10) Å^3
Z	4
Crystal colour and size	Colourless, 0.19 × 0.11 × 0.03 mm^3
Final *R* indices [$F^2>2\sigma$]	R_1 = 0.0287
R indices (all data)	wR_2 = 0.0653
Large diff. peak and hole	0.44/-0.39 e Å^{-3}

$[Ag(10)_3]NO_3$ (M4)

X-ray diffraction quality crystals were produced by layering solutions of ligand and metal in a 3:1 (L:M) ratio. A cold solution of silver nitrate (33.9 mg, 0.2 mmol) in MeCN (10mL) was carefully layered onto a cold solution of **10** (175.4 mg, 0.6 mmol) in DCM (10mL) before being left to crystallize in the freezer (-20º) allowing for a slow diffusion. Small colourless crystals with undefined edges grew after about a month.

Sum formula	$C_{54}H_{60}AgN_{13}O_2$
Formula weight	1031.02
Temperature	150.01(10) K
Radiation, wavelength	MoKα, λ = 0.71073 Å
Crystal system, space group	Trigonal, *R* -3
Unit cell parameters	a = 18.9544(16) Å α = 90º
	b = 18.9544(16) Å β = 90º
	c = 11.8873(11) Å γ = 120º
Cell volume	3698.6(7) Å^3
Z	3
Crystal colour and size	Colourless, 0.21 × 0.21 × 0.04 mm^3
Final *R* indices [$F^2>2\sigma$]	R_1 = 0.0450
R indices (all data)	wR_2 = 0.1052
Large diff. peak and hole	0.89/-0.30 e Å^{-3}

$[Ag(9)(NO_3)]$ (M5)

X-ray diffraction quality crystals were produced by layering solutions of ligand and metal in a 1:1 ratio. A cold solution of silver nitrate (33.9 mg, 0.2 mmol) in MeCN (10mL) was carefully layered onto a flash frozen (using liquid nitrogen) solution of **9** (57.3 mg, 0.2 mmol) in DCM (10mL) before being cooled again left to crystallize in the freezer (-20º) allowing for slow melting and diffusion. Small yellow crystals grew after about a month.

Sum formula	$C_{18}H_{14}AgN_5O_3$
Formula weight	456.21
Temperature	150.00(10) K
Radiation, wavelength	CuKα, λ = 1.54184 Å
Crystal system, space group	Monoclinic, $P2_1/c$
Unit cell parameters	a = 5.1492(11) Å α = 90º
	b = 15.991(5) Å β = 90º
	c = 21.033(5) Å γ = 90º
Cell volume	1731.9(7) Å^3
Z	4
Crystal colour	Yellow

Final *R* indices [$F^2>2\sigma$]	R_1 = 0.0668
R indices (all data)	wR_2 = 0.1860
Large diff. peak and hole	2.48/-1.15 e Å^{-3}

Interpenetrated 2-D $[Ag(9)_3]NO_3$ Framework d 3-D $[Ag(9)_3]NO_3$ MOF (M6)

X-ray diffraction quality crystals were produced by layering solutions of ligand and metal in a 3:1 (L:M) ratio. Cold DMF (5 mL) was layered onto a flash frozen (using liquid nitrogen) solution of **9** (171.8 mg, 0.6 mmol) in DCM (10mL) before a cold solution of silver nitrate (33.9 mg, 0.2 mmol) in MeCN (10mL) was carefully added as the third layer, cooled again and left to crystallize in the freezer (-20º), allowing for slow melting and diffusion. Small pale yellow crystals with undefined edges grew after about a month.

Sum formula	$C_{54}H_{42}AgN_{13}O_3$
Formula weight	1028.88
Temperature	150.0(2) K
Radiation, wavelength	CuKα, λ = 1.54184 Å
Crystal system, space group	Trigonal, *R* -3
Unit cell parameters	a = 18.2534(3) Å α = 90º b = 18.2534(3) Å β = 90º c = 23.4303(5) Å γ = 120º
Cell volume	6760.8(3) Å^3
Z	6
Crystal colour and size	Colourless, 0.20 × 0.15 × 0.09 mm^3
Final *R* indices [$F^2>2\sigma$]	R_1 = 0.0307
R indices (all data)	wR_2 = 0.0827
Large diff. peak and hole	0.35/-1.06 e Å^{-3}

4.5 References

1. S. M. Goldup, D. A. Leigh, P. J. Lusby, R. T. McBurney and A. M. Z. Slawin, *Angew. Chem. Int. Ed.*, 2008, **47**, 6999-7003.
2. M. J. Irwin, J. J. Vittal, G. P. A. Yap and R. J. Puddephatt, *J. Am. Chem. Soc.*, 1996, **118**, 13101-13102.
3. K. Biradha, C. Seward and M. J. Zaworotko, *Angew. Chem. Int. Ed.*, 1999, **38**, 492-495.
4. D. I. Gittins and F. Caruso, *Angew. Chem. Int. Ed.*, 2001, **40**, 3001-3004.
5. C. R. Mayer, E. Dumas and F. Secheresse, *Chem. Commun.*, 2005, 345-347.
6. Y. P. Prananto, D. R. Turner, J. Lu and S. R. Batten, *Aust. J. Chem.*, 2009, **62**, 108-114.
7. S. R. Batten, S. M. Neville and D. R. Turner, *Coodination Polymers: Design, Analysis and Application*, The Royal Society of Chemistry, 2008.

8. J. W. Steed and J. L. Atwood, *Supramolecular Chemistry*, John Wiley & Sons, Ltd., 2009.
9. J. R. Long and O. M. Yaghi, *Chem. Soc. Rev.*, 2009, **38**, 1213-1214.
10. M. Fujita, O. Sasaki, T. Mitsuhashi, T. Fujita, J. Yazaki, K. Yamaguchi and K. Ogura, *Chem. Commun.*, 1996, 1535-1536.
11. B.-H. Qian, W.-X. Ma, L.-D. Lu, X.-J. Yang and X. Wang, *Acta Crystallogr. Sect. Sect. E: Struct. Rep. Online*, 2006, **62**, m2818-m2819.
12. Y.-S. Zhang, G. D. Enright, S. R. Breeze and S. Wang, *New J. Chem.*, 1999, **23**, 625-628.
13. L. Carlucci, G. Ciani, D. M. Proserpio and A. Sironi, *Angew. Chem. Int. Ed. Engl.*, 1995, **34**, 1895-1898.
14. O. M. Yaghi, M. O'Keeffe, N. W. Ockwig, H. K. Chae, M. Eddaoudi and J. Kim, *Nature*, 2003, **423**, 705-714.
15. K. Sumida, D. L. Rogow, J. A. Mason, T. M. McDonald, E. D. Bloch, Z. R. Herm, T.-H. Bae and J. R. Long, *Chem. Rev.*, 2012, **112**, 724-781.
16. N. L. Rosi, J. Eckert, M. Eddaoudi, D. T. Vodak, J. Kim, M. O'Keeffe and O. M. Yaghi, *Science*, 2003, **300**, 1127-1129.
17. M. Eddaoudi, J. Kim, N. Rosi, D. Vodak, J. Wachter, M. O'Keeffe and O. M. Yaghi, *Science*, 2002, **295**, 469-472.
18. A. A. Talin, A. Centrone, A. C. Ford, M. E. Foster, V. Stavila, P. Haney, R. A. Kinney, V. Szalai, F. El Gabaly, H. P. Yoon, F. Léonard and M. D. Allendorf, *Science*, 2014, **343**, 66-69.
19. J. Lee, O. K. Farha, J. Roberts, K. A. Scheidt, S. T. Nguyen and J. T. Hupp, *Chem. Soc. Rev.*, 2009, **38**, 1450-1459.
20. L. E. Kreno, K. Leong, O. K. Farha, M. Allendorf, R. P. Van Duyne and J. T. Hupp, *Chem. Rev.*, 2012, **112**, 1105-1125.
21. J. G. Speight, *Lange's Handbook of Chemistry*, McGraw-Hill, 1956.
22. J. P. Gambino, *Copper interconnect technology for the 22 nm node*, International Symposium on VLSI Technology, Systems and Applications, 2011.
23. Y. Geng, A. C. Pearson, E. P. Gates, B. Uprety, R. C. Davis, J. N. Harb and A. T. Woolley, *Langmuir*, 2013, **29**, 3482-3490.
24. Y. K. Tseng, C. J. Huang, H. M. Cheng, I. N. Lin, K. S. Liu and I. C. Chen, *Adv. Funct. Mater.*, 2003, **13**, 811-814.
25. C. E. Housecroft and A. G. Sharpe, *Inorganic Chemistry*, Pearson Education Limited, 2001.
26. H. Yan, S. H. Park, G. Finkelstein, J. H. Reif and T. H. LaBean, *Science*, 2003, **301**, 1882-1884.
27. Cambridge Structural Database, http://www.ccdc.cam.ac.uk/.
28. Y.-H. Liu, Q. Xu and Z.-Y. Han, *Acta Crystallogr. Sect. Sect. E: Struct. Rep. Online*, 2010, **66**, m903.
29. S. R. Batten, *CrystEngComm*, 2001, **3**, 67-72.
30. S. R. Batten and R. Robson, *Angew. Chem. Int. Ed.*, 1998, **37**, 1460-1494.

Chapter 5

Surface Characterization of Molecular Crystal Substrates

Table of Contents

5.1 Introduction

As the feature resolution of electronic semiconductor devices shifts into the nanometer and angstrom scale, 'bottom-up' techniques have emerged as viable methods for continuing the Moore's law trend[1] and may soon lead to functional nanoelectronics.[2, 3] 10 nm node process technologies are to be used this year (2015) with the DRAM half pitch size (half the distance between two identical features of an array on a dynamic random access memory chip) expected to reach 10 nm by 2025.[4] This shift in scale means that molecules and atoms can provide the building blocks for such features in an approach.[5]

One component that plays a key role in both 'top-down' and 'bottom-up' fabrication is the substrate, a platform on which to etch details or grow architectures. Silicon wafers are typically used as substrates on which to perform photolithographic techniques for use in the semiconductor industry. This is primarily due to its conductive properties, but also because of its high abundance and the ability in industry, to produce very pure, very flat wafers, ideal as a blank slate for printing processes or deposition of a resist for etching.

The substrate plays a more intelligent role in the design of certain 'bottom-up' systems. Substrates can provide particular chemistries present at the surface ideal for directed deposition or self-organized growth of material.

Self assembled monolayers (SAMs) of organic material attached to metal based single crystal substrates have been well studied[6] for their surface engineering capabilities, most notably alkanethiolates, which when formed on a Au (111) surface produce an ordered array as a result of directed growth.[7]

Cu and Ag nanostructures have been shown to grow on Pd (110) and Pt (111)[8] surfaces respectively, as well as Ge quantum dots grown on Si (100)[9] and a boron nitride nanomesh grown on Rh (111)[10]. Nanostructures of organic compounds have also been grown on surfaces of metallic based single crystals such as Ag (111).[11]

The disadvantages of these metal-based substrates are the limited number of options for chemical interaction and influence on the adopted architectures of deposited material (number of patterns provided by substrate are fairly limited

as there is a lack of controllable spacing of surface binding sites), as well as the cost of procuring and purifying the precious metals used on a large scale. Molecular based substrates provide the advantage of consisting of building blocks themselves, giving a much wider range of possible substrate functionalities and tunable surface architectures.[12] These substrates are pre-organized for material deposition. Molecular substrates are also cheaper to manufacture, the raw materials (small organic molecules or polymers) are typically cheaper than purified metal substrates and substrate production can be performed at low cost atmospheric temperatures and pressures via supramolecular self assembly processes. Examples of such molecular based substrates include the use of Di-block poly(styrene)-*b*-poly(methyl methacrylate) (PS-*b*-PMMA) polymers as pre-organized substrates for directed metal binding. [13-15]

The characteristics of molecular based crystals show promise as functional substrates for directed metal binding. Crystals provide an inherent order and rigid architecture of functional groups that can extend to the crystal face surface, offering a spatially well defined array of binding sites pre-organized for material binding. This use of information embedded in the substrate itself to direct deposition or growth of material on its surface is very efficient and crystal substrates have the added advantage and again efficiency of being prepared by crystallization, a self assembly process. The variety in possible crystal structures is enormous, with the Cambridge Structural Database (CSD) containing over 750,000 known crystal structures and over 40,000 new structures added each year (as of 16th February 2015)[16] giving a wide range of surface functionalities and available architectures. Fine tuning surface architectures may also possible by predicting how new compounds will crystallize using crystal engineering,[17] however, the intermolecular forces governing crystallization are very delicate and at times unpredictable.[18]

Microscopy is a valuable method of characterizing substrate surfaces. AFM (atomic force microscopy) can provide a way of mapping surface topologies with near atomic resolution. The technique was developed Gerd Binnig, Calvin Quate, and Christoph Gerber in 1986,[19] and is based around the principle of a tip or probe (at the end of a cantilever) tracking across the sample surface and

being subjected to relative long range attractive (van der Waals interactions) forces and short range repulsive (atomic) forces. Maintained at a constant vertical force, the probe and sample are moved relative to each other in a raster pattern with the cantilever deflecting when the probe encounters any surface features. These deflections are monitored by a laser, which reflects from the top surface of the cantilever onto a four-segment photodetector. Changes in the y-position on the photodetector are used to construct a 3D topological representation of the sample surface.

Topologies obtained by AFM typically have a height (z axis) resolution of 0.1 nm, with lateral resolutions (x-y axes) usually being larger (2-10 nm) and are highly dependent on the tip radius, typically 10-20 nm. The use of sharper tips however (1-5 nm radius), can provide greater resolution.

AFM can be performed in a number of imaging modes, most notably contact mode (tip remains in constant contact with the sample at a defined set point value), non-contact mode (tip is held near the surface and is oscillated at a low amplitude, being subjected to long range forces), TappingMode™ (tip oscillates at higher amplitudes than non-contact mode) and PeakForce Tapping™ mode (tip oscillates at frequencies well below the cantilever resonance) mode.

AFM has previously been used to characterize organic crystal surfaces,[20] revealing information on crystal growth and dissolution mechanisms, ledges relating to the crystal structure and in some cases achieving molecular-scale contrast (Figure 1.18a and b), where the crystal's unit cell dimensions for that plane can be visualized.

Spectroscopic characterization of substrate surfaces is commonly performed by XPS (X-ray photoelectron spectroscopy) as it is a highly surface sensitive technique, providing chemical information relating only to the first 0.1-10 nm of sample material. This spectroscopic technique was developed in 1954 by Kai Seigbahn and referred to as ESCA (electron spectroscopy for chemical analysis)[21] before it's commercialization as XPS. The technique capitalizes on the photoelectric effect by bombarding the sample under investigation with X-rays of sufficiently high energy to promote photoemission of core energy level electrons, overcoming their high binding energies. These binding energies can

be accurately calculated from the kinetic energy of the emitted electrons and their known X-ray excitation energies, enabling elemental identification, as core energy level binding energies are highly characteristic of the elements from which they originate.

XPS can also be used to gain information on the chemical environment and oxidation state of atoms. Small 'chemical shifts' can take place based on simple electrostatic forces between the leaving electron and the atomic nucleus, a more positively charged nucleus will have a stronger binding energy. The other main feature of XPS is its surface sensitivity. This sensitivity arises due to the short mean free path of electrons in solids so only electrons from the first few atomic layers of the sample are detected. Electrons emitted from deeper in the sample collide with the surrounding sample material and lose energy to give a disperse range of detected energies. These energies make up the background of the spectrum.

5.2 Results and Discussion

5.2.1 Crystal Substrates of Py-Im-Et (8)

From the molecules synthesized and crystallized earlier in Chapter 2, the first candidate chosen for surface characterization was Py-Im-Et (**8**) in its original crystal form (not the polymorph discovered in Chapter 3, **8P1**). This molecule was chosen because large crystals with well-defined faces could easily be produced, meaning that microscopy analysis (AFM) and spectroscopy (XPS) could be performed at the crystal surfaces. Crystals of Py-Im-Et were grown slowly by evaporation from a concentrated solution. This was done in ethyl acetate at room temperature, and gave typical dimensions of 2-10 mm creating rectangular block-like crystals. Crystal faces were determined by face indexing analysis on small-scale crystals and are denoted by the Miller indices shown in Figure 5.1.

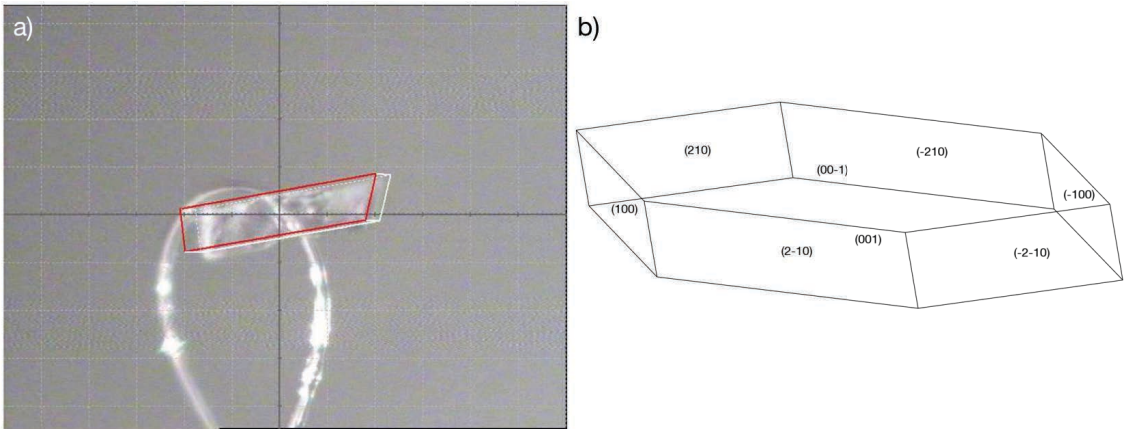

Figure 5.1 a, Face indexing analysis of a Py-Im-Et crystal, red highlighted face determined as the (001) plane. **b**, Full crystal morphology obtained by face indexing with labelled Miller indices.

The crystal face information, along with the crystal structure obtained previously, was used to relate the crystal planes to the crystal faces. Visualization of which atoms, and therefore binding sites, are likely to be present at each face could then be obtained.

It can be seen that the pyridyl binding sites are relatively inaccessible to interaction at the (-210), (100) and (210) faces (Figure 5.2), as well as the parallel lattice planes of (2-10), (-100) and (-2-10) due to the molecule's centrosymmetry. The pyridyl groups are not perpendicular to any of these planes. However, in the case of the (001) face, and therefore (00-1) also, the pyridyl binding groups are perpendicular to that plane, making it more accessible and more well disposed to direct binding of deposited material. The distance between the binding sites (pyridyl nitrogen atoms of adjacent molecules) at the (001) face was measured to be 1.348 nm in the [100] direction and 0.414 nm in the [010] direction. Binding site spacing on this scale offers the potential for any deposited material to form nanostructures with resolutions that may exceed those provided by current conventional lithographic techniques, smaller than 10 nm.

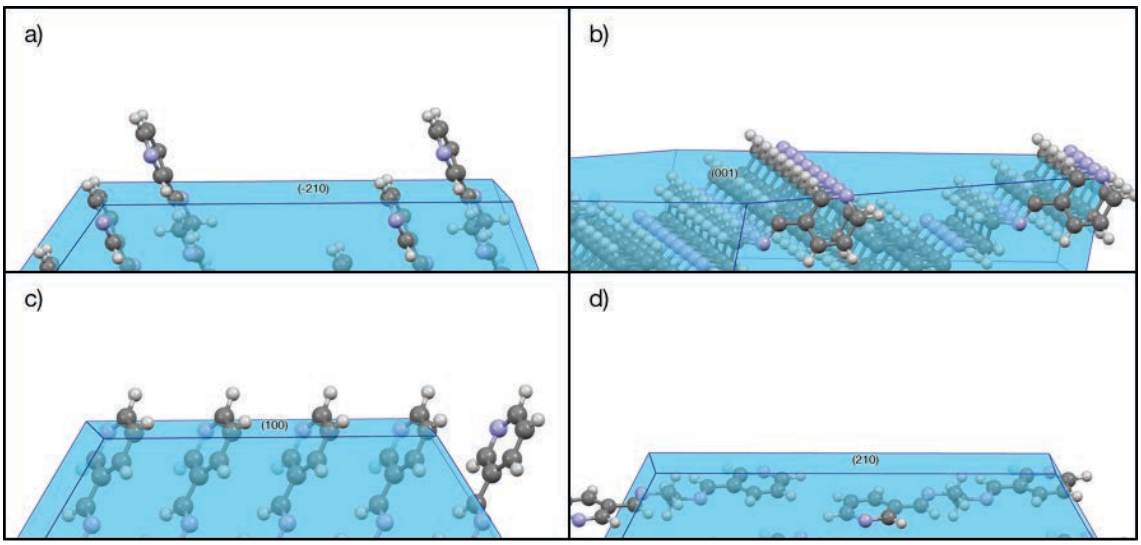

Figure 5.2 Py-Im-Et crystal structure with crystal faces. **a**, molecular orientation at the (-210) face, **b**, molecular orientation at the (001) face, **c**, molecular orientation at the (100) face and **d**, molecular orientation at the (210) face.

Whilst surface imperfections, or a generally rough surface, may be preferable for use in surface catalysis (increasing the surfaces activity and turnover), they are not desired here. Instead, large flat areas of the surface are preferred, enabling the transfer of structural details from the surface to the deposited material with fewer defects.

AFM experiments were performed on the (001) face of the Py-Im-Et crystals (Figure 5.3a). Initial measurements showed very rough regions across the surfaces, roughness analysis over a typical 2x2 μm area gave an rms value of 2.2 nm, roughness is the standard deviation of the Z values (z axis = height) within a set area. Given that any deposited material would be about 2 nm or smaller, flatter regions needed to be produced in order to retain patterning on the sub 2 nm scale.

Taking advantage of the layered structure of the Py-Im-Et crystal, a method of cleavage was employed in which adhesive tape was used to remove single or multiple molecular crystal layers to reveal large flat regions (Figure 5.3b), rms of 0.11 nm over a typical 2x2 μm region. These flatter regions are more suited for material deposition.

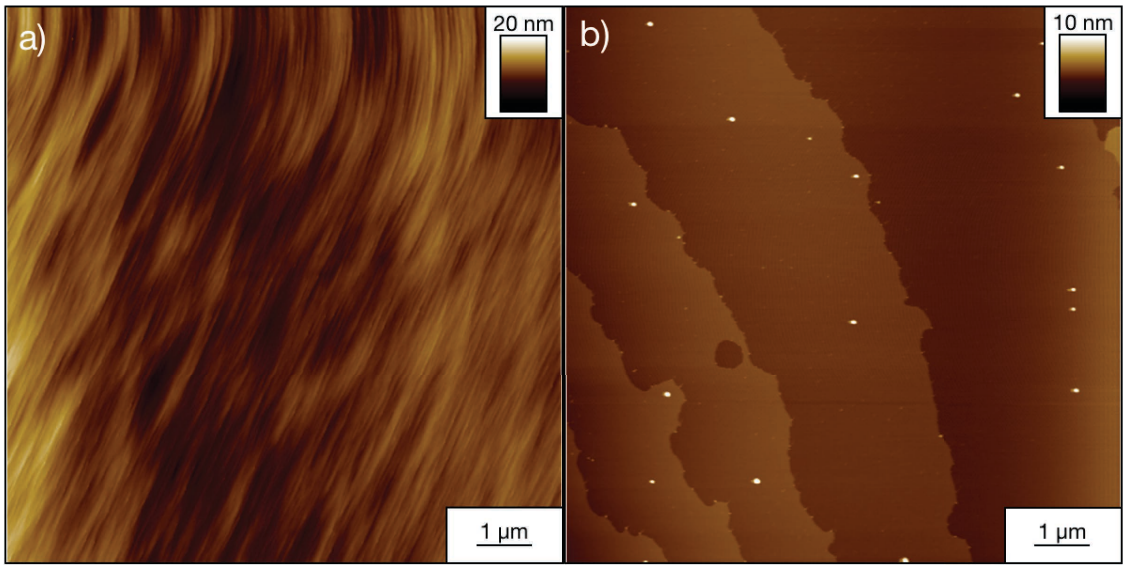

Figure 5.3 AFM height images of the Py-Im-Et (001) crystal face on an untreated sample (**a**) and the same sample after surface cleavage using adhesive tape (**b**).

Microscopy characterization of the Py-Im-Et (001) face by AFM revealed large flat regions, 10x10 μm in some cases, well-suited for binding and imaging of deposited material at a later stage. Ideally, features corresponding to the crystal structure unit cell of the (001) plane would be seen, such as with the molecular contrast work performed by Ward et al.[20] The lateral resolution was unfortunately not high enough to make out these features, possibly due to tip sharpness. However, higher vertical resolution meant that molecular layers of the crystal structure could be compared to step heights across the surface.

Figure 5.4 shows a typical line section across a step edge giving a height value of 0.985 nm compared to the distance observed for two layers of molecules in the crystal structure, 0.949 nm. These measurements show good correlation to the layer distances obtained from single crystal diffraction, with only a minor deviation which could be attributed to the resolution limits of the imaging process.

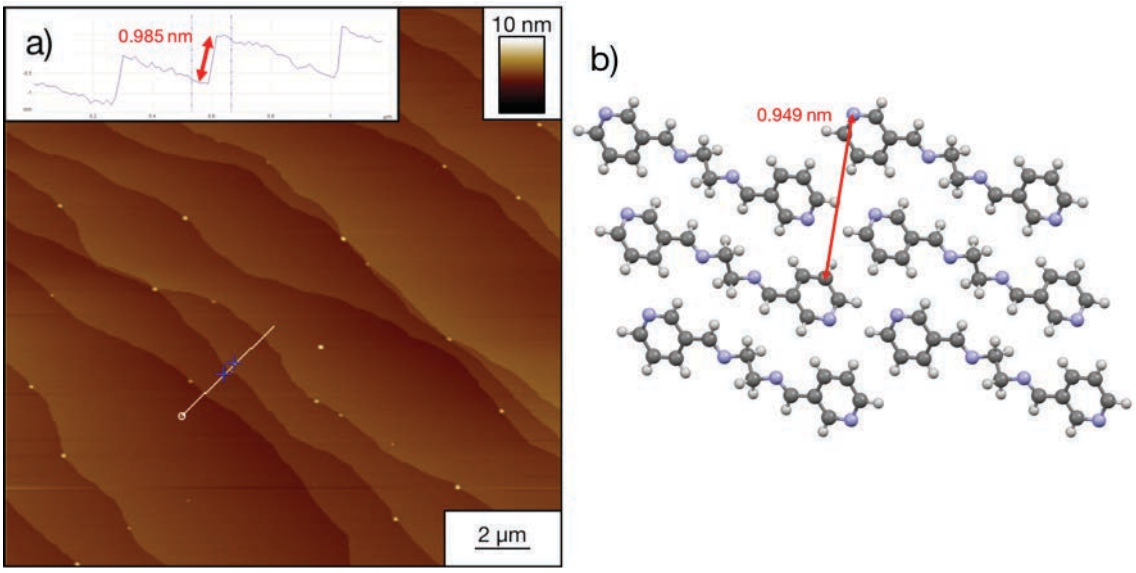

Figure 5.4 a, AFM height image of the Py-Im-Et (001) crystal face with an insert image showing measured step heights across the surface. **b**, Py-Im-Et crystal structure viewed down the [010] axis with the (001) plane horizontal, showing possible molecular steps.

Initial characterization of these Py-Im-Et crystals showed promise as substrates on which to perform directed binding, large, very flat regions can be produced with metal binding sites present at the surface. However, after further studies it was noted that the substrate surface was transforming during imaging. This observation was attributed to the solubility of the Py-Im-Et molecule in moist air (water), which is present in small amounts as it collects on the AFM tip unless performed under environmental control. Figure 5.5 shows how the surface dissolves over time during imaging and possibly occurs via a screw dislocation process,[22] but has not been studied here. These findings also meant that the Py-Im-Et crystals could not be taken to the next stage of investigation, where binding of water-soluble metal complexes would require the crystal to be stable in water.

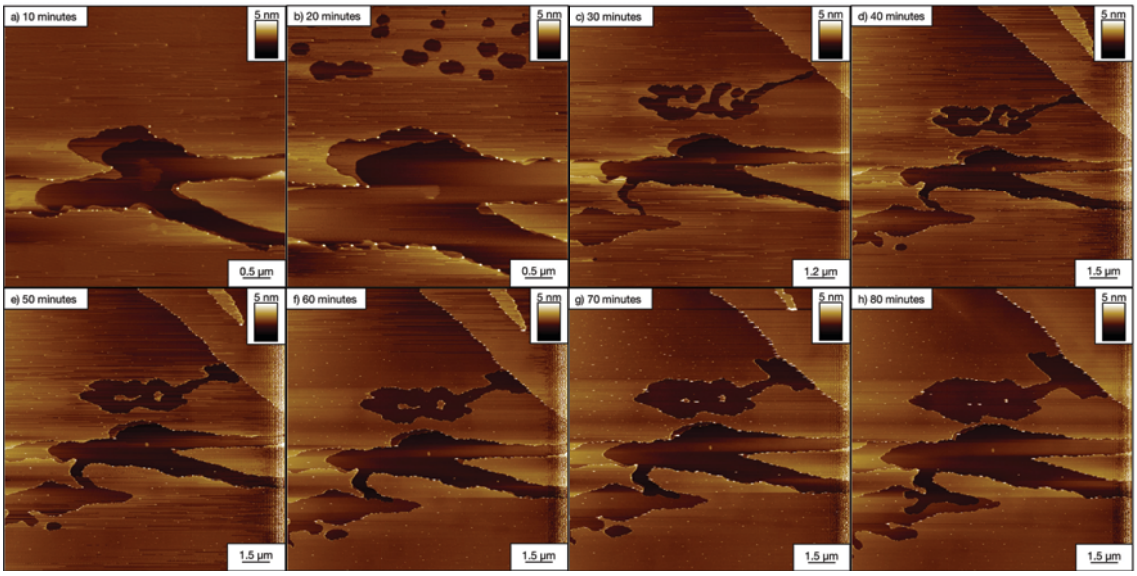

Figure 5.5 a-h, AFM height images of the Py-Im-Et (001) crystal face dissolving over a period of 80 minutes, 10 minutes between each image.

5.2.2 Phosphines as crystal substrates

Of the remaining compounds synthesized in Chapter 2, one other molecule (py-im-cyclo) was ruled out of the metal binding stage for the same reason of water solubility. All of the other synthesized compounds were also ruled out for the reasons of not being able to grow big enough crystals, if any, and not having the pyridyl binding site in the correct orientation for the metal binding process.

In order to continue, and investigate the directed metal binding using crystal substrates concept, it was therefore prudent to choose a set of molecules that posses the desired crystal qualities. These are, the ability to grow large flat surfaces with well defined faces, the possibility for selective binding at these faces (looking at the crystal structure) and water insolubility for both the metal binding stage, and during the imaging process.

The set of molecules chosen were triphenylphosphine (PPh_3), triphenylphosphine sulfide (PPh_3S) and triphenylphosphine oxide (PPh_3O), where the metal binding sites are P, S and O respectively (Figure 5.6). These molecules fulfil all the above criteria as well as being commercially available and low cost.

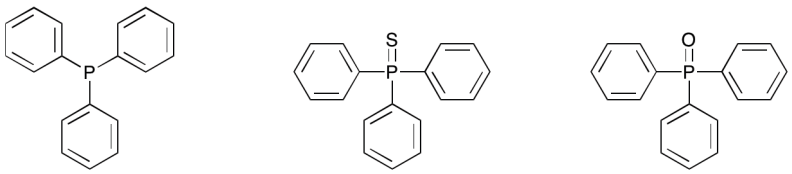

Figure 5.6 Molecular diagrams of **a**, triphenylphosphine, **b**, triphenylphosphine sulfide and **c**, triphenylphosphine oxide.

5.2.3 Crystal Substrates of Triphenylphosphine (PPh_3)

Crystals of triphenylphosphine (PPh_3) were grown by dissolving in toluene at 60°C and cooling slowly in a thermally insulated vessel over the course of 72 hours. The unit cell data collected confirmed the structure to be the same as the structure published previously.[23, 24] Crystals produced had typical face dimensions of 5-20 mm and were indexed in the same manner as for the Py-Im-Et crystals. Figure 5.7 shows the indexed faces as (01-1), (100) and (011) as well as the parallel lattice planes (0-11), (-100) and (0-1-1).

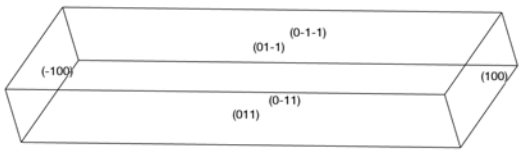

Figure 5.7 Full crystal morphology of PPh_3 obtained by face indexing with labelled Miller indices.

From relation of crystal planes to crystal faces, it can be seen that the phosphorus binding sites are most easily accessible on the (100) and (-100) faces (Figure 5.8). Access to binding sites on the other faces seems to be more sterically hindered by the phenyl groups which are present in a bulky umbrella conformation. The spacing between binding sites on the (100) face is 1.492 nm in the [010] direction and 0.844 nm in the [001] direction, as with the Py-Im-Et crystals, this small spacing of the surface binding sites provides the opportunity to create nanoscale architectures with very small feature size.

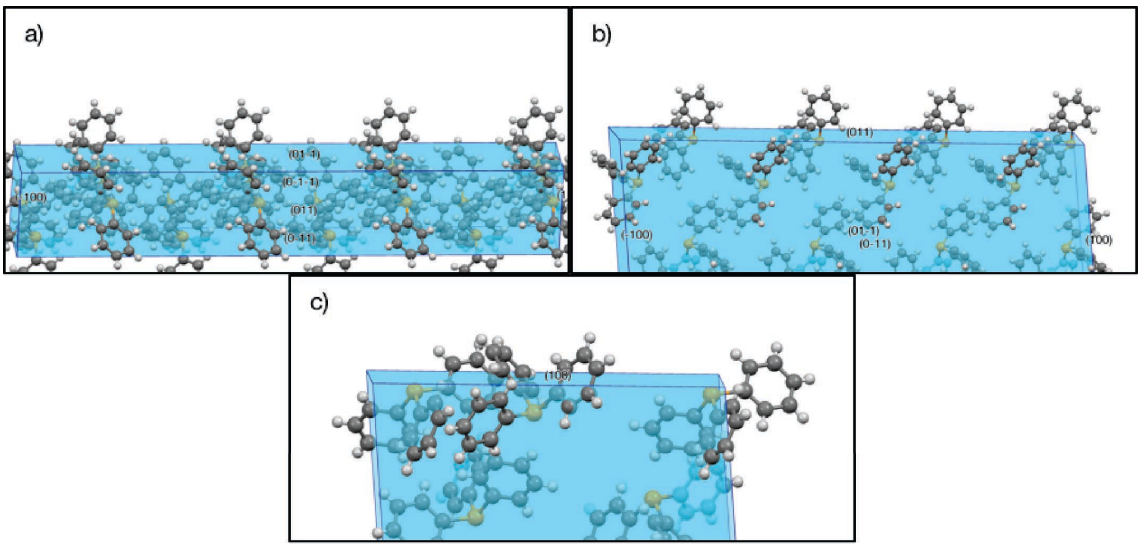

Figure 5.8 PPh_3 crystal structure with crystal faces. **a**, molecular orientation at the (01-1) face, **b**, molecular orientation at the (011) face and **c**, molecular orientation at the (100) face.

Crystals of PPh_3 could be produced with large with well-defined faces, meaning that imaging of all faces could be achieved by AFM. Imaging of the (01-1) face (largest face) shows step heights corresponding to two molecular layers in the crystal structure (1 unit cell in [001] direction, 0.844 nm), Figure 5.9, and roughness rms of 0.14 nm over a 500x500 nm area. This is a low roughness value meaning that this surface provides a flat enough platform for material deposition with binding sites present in a patterned array.

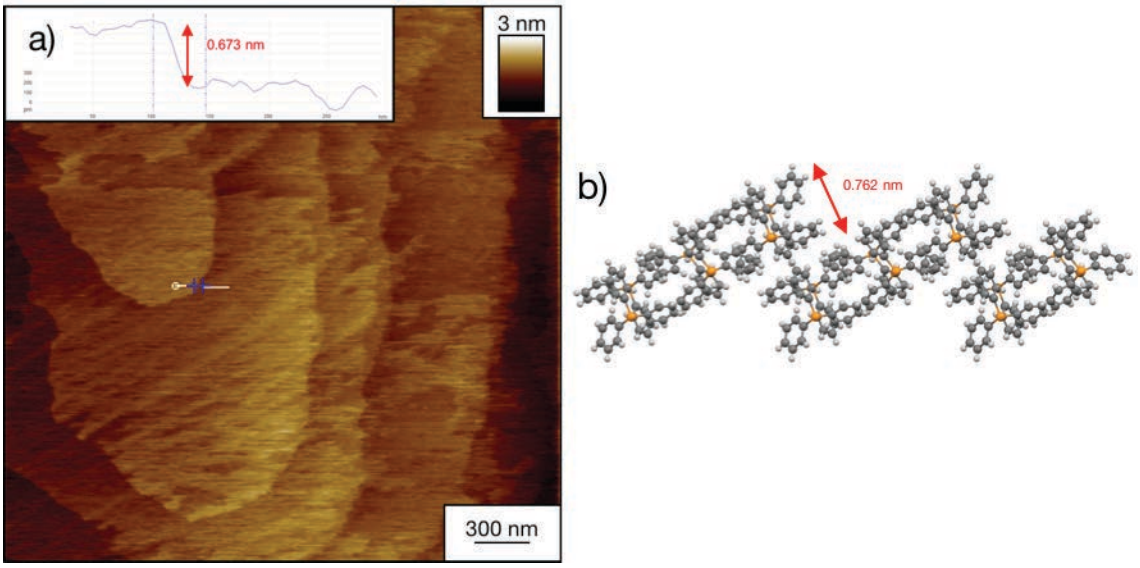

Figure 5.9 a, AFM height image of the PPh_3 (01-1) crystal face with an insert image showing measured step heights across the surface. **b**, PPh_3 crystal structure viewed down the [100] axis with the (01-1) plane horizontal, showing possible molecular steps.

No steps were visible when looking at the (011) face however (Figure 5.10) and a roughness rms of 0.25 nm was calculated over a typical 500x500 nm area. This is just slightly rougher than for the (01-1) face.

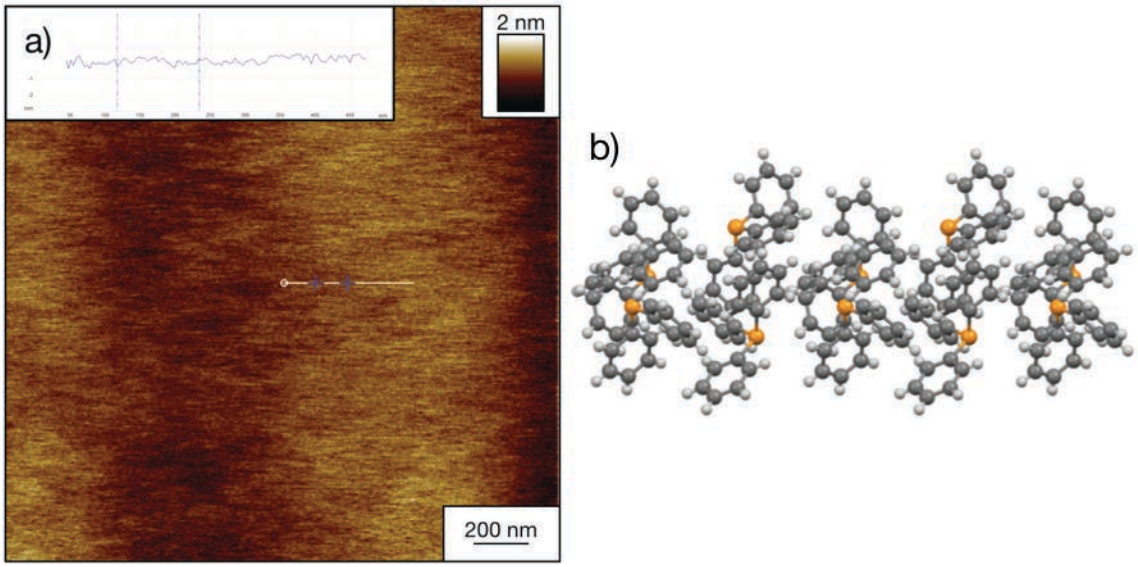

Figure 5.10 a, AFM height image of the PPh_3 (011) crystal face with an insert image showing measured step heights across the surface. **b**, PPh_3 crystal structure viewed down the [03-1] axis with the (011) plane horizontal, showing possible molecular steps.

Imaging and analysis of the (100) face (Figure 5.11a) gave typical step heights of 1 nm, possibly corresponding to a two molecule layer in the crystal structure (half of one unit-cell in the [0-10] direction), however the match dos not seem to be as good here (Figure 5.11b). Roughness analysis for this surface gave an average rms value of 0.50 nm over a 500x500 nm area. This value is higher than for the other faces of the PPh_3 crystal and is attributed to the many small steps present at the surface.

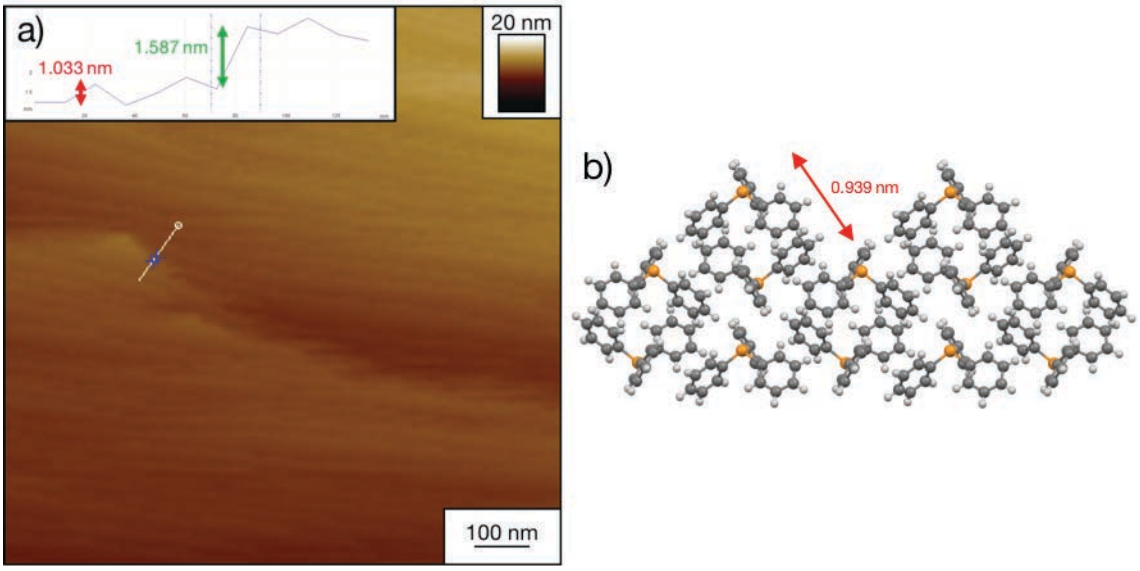

Figure 5.11 a, AFM height image of the PPh_3 (100) crystal face with an insert image showing measured step heights across the surface. **b**, PPh_3 crystal structure viewed down the [001] axis with the (100) plane horizontal, showing possible molecular steps.

The large, well-defined faces of the PPh_3 crystals enabled XPS characterization to be performed.

As a surface sensitive technique, differences in molecular orientation relative to each crystal face may also be obtained by observing the relative intensities of carbon and phosphorus species present at the surface.

XPS survey scans of the (01-1) face of the PPh_3 crystals show trace amounts of silicon (Si 2p), oxygen (O 1s) and fluorine (F 1s), these elements are not present in the crystal substrates and are accounted for as contaminants. Omitting the contaminants, carbon (C 1s) accounts for 91.75% of the surface composition with phosphorus (P 2p) making up the remaining 8.25% (Figure 5.12a), O KLL and F KLL relate to secondary emissions due to an Auger emission or X-ray fluorescence. Survey scans of the (100) face show carbon and phosphorus account for 91.59% and 8.41% of the surface composition respectively (Figure 5.12b). These values show minimal differences from the (01-1) face which may not be significant, meaning crystal faces can not be identified using this technique.

Differences in relative carbon and phosphorus intensities are observed to be very small, this may be due to the surface sensitivity of the XPS experiments. XPS is a surface sensitive technique when compared to many other analytical techniques used in chemistry, however, the escape depth of ejected electrons

can reach ~10 nm, meaning that the majority of the signal here is due to the bulk crystal structure where molecular orientation is irrelevant.

High resolution scans for carbon and phosphorus were performed. For the carbon C 1s region (Figure 5.12 c and d), no significant differences could be observed between the (01-1) and (100) faces. The main C 1s peaks corresponding to the phenyl rings were charge referenced to 284.80 ev, as is standard for adventitious carbon, both spectra show π-π* satellite peaks centred at 291.30 ev for (01-1) and 291.53 ev for (100), which are in agreement with literature data for aromatic carbon (sp^2) 291.27 ev.[25]

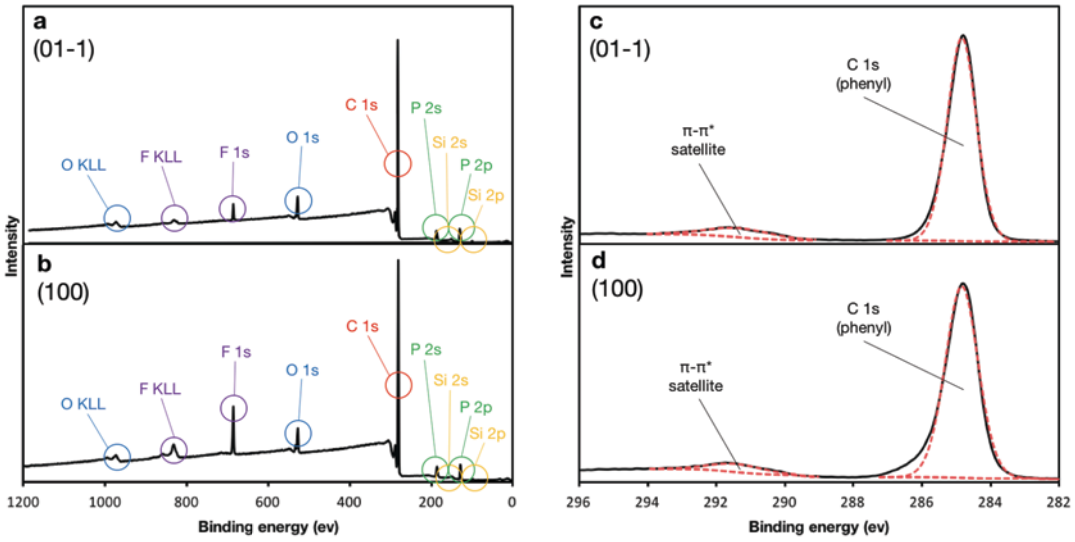

Figure 5.12 XPS survey scans of **a**, the PPh_3 (01-1) crystal face and **b**, the PPh_3 (100) crystal face with major peaks highlighted. High resolution scans of the carbon C 1s region for **c**, the PPh_3 (01-1) crystal face and **d**, the PPh_3 (100) crystal face showing peaks for the aromatic rings and the accompanying π-π* satellite.

For the phosphorus P 2p region, Figure 5.13a and b, again no significant differences could be observed between the (01-1) and (100) faces. However, multiple species of phosphorus seem to present. Both spectra show two sets of peaks for the P 2p binding energies, with the lowest energy P $2p_{3/2}$ component centred at 130.44 ev and 130.52 ev for the (01-1) and (100) faces respectively, with the spin-orbit components being separated by 0.86 ev in both cases. These values are in agreement with literature data obtained for PPh_3, 130.6 ev,[26] and with XPS obtained of PPh_3 in powder form, 130.64 ev, and as a result can be assigned to phosphorus in the (III) oxidation state. The higher energy set of peaks, with the P $2p_{3/2}$ component centred at 132.27 ev and 132.34 ev for the (01-1) and (100) faces respectively, and spin orbit

components separated by 0.86 ev in each case, suggesting higher oxidation state (probably due to oxidation of the phosphorus) due to a stronger electron attraction to the nucleus (higher proton count) and are in closer agreement to literature values for phosphorus(V) (PPh_3O) 132.78 ev.[27] This is also the major component in each case, suggesting that the surface has oxidized and using a surface sensitive technique such as XPS means phosphorus(V) contributes more to the data collection. O 1s spectral data show the presence of two oxygen species (two components within the O 1s peak), Figure 5.13c and d. The first components centre at 532.77 ev and 532.26 ev for the (01-1) and (100) faces respectively and are attributed to trace oxygen contamination which is present on all samples. The second components centre at 530.33 ev and 530.48 ev for the (01-1) and (100) faces, making them closer in energy to the O 1s values obtained for PPh_3O, 531.07 ev.[27] This observation further backs the conclusion that PPh_3 has oxidized to PPh_3O.

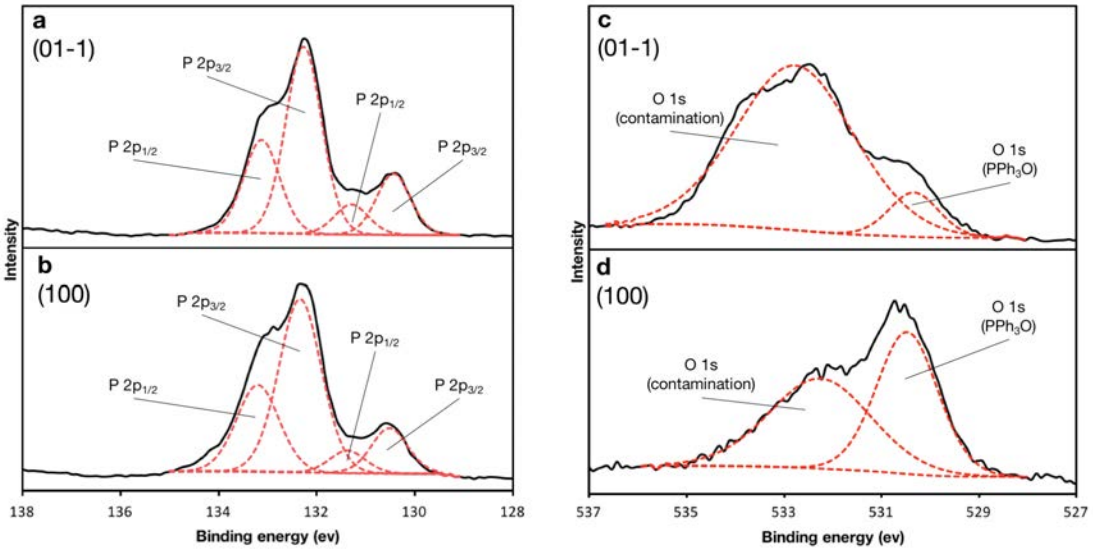

Figure 5.13 High resolution XPS scans of the phosphorus P 2p region of **a**, the PPh_3 (01-1) crystal face and **b**, the PPh_3 (100) crystal face both showing two distinct sets of two peaks. High resolution XPS scans of the oxygen O 1s region of **c**, the PPh_3 (01-1) crystal face and **d**, the PPh_3 (100) crystal face showing two types of oxygen environments.

5.2.4 Crystal Substrates of Triphenylphosphine Sulfide (PPh_3S)

Crystals of triphenylphosphine sulfide (PPh_3S) were grown in the same manner as for PPh_3 crystals, by dissolving in toluene at 60°C and cooling slowly in a thermally insulated vessel over the course of 72 hours. The unit cell confirms the structure to be the same as that shown previously shown.[28-30] Crystals

produced this time were slightly smaller giving typical face dimensions of 3-10 mm. Face indexing analysis identified the crystal faces as (100), the largest face, (001), the side face, (01-1), the small end face and (011), the larger end face. The parallel lattice planes are also indexed as (-100), (00-1), (0-11) and (0-1-1), Figure 5.14.

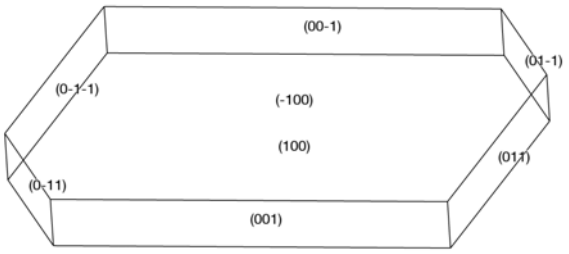

Figure 5.14 Full crystal morphology of PPh_3S obtained by face indexing with labelled Miller indices.

The planes in the crystal structure of PPh_3S were related to the crystal faces after face indexing. For these crystals it is the sulfur atoms that are expected to be the likely binding site for any deposited metal. Figure 5.15 shows the morphologies and it can be seen that the (011) face (Figure 5.15, d) has the potential to present the most accessible sulfur atoms. Molecules in the [011] direction are arranged in layers with one of the layers presenting sulfur to the surface and the other layer facing sulfur inwards. The natural termination site (molecular orientation) for this face may be determined in the metal binding experiments if face selectivity is shown. This is also true for the opposing (0-1-1) face, these sulfur binding sites are separated by a distance of 2.043 nm in the [001] direction and 1.831 nm in the [010] direction. This is some of the larger binding site spacing seen of the crystals tested, giving a good chance of resolving deposited features by AFM. The (001) face also shows some potential for binding, with sulfur atoms possibly accessible (Figure 5.15b, second layer of molecules). As with the PPh_3 crystals, binding sites at the other faces seem to be sterically hindered by the phenyl groups.

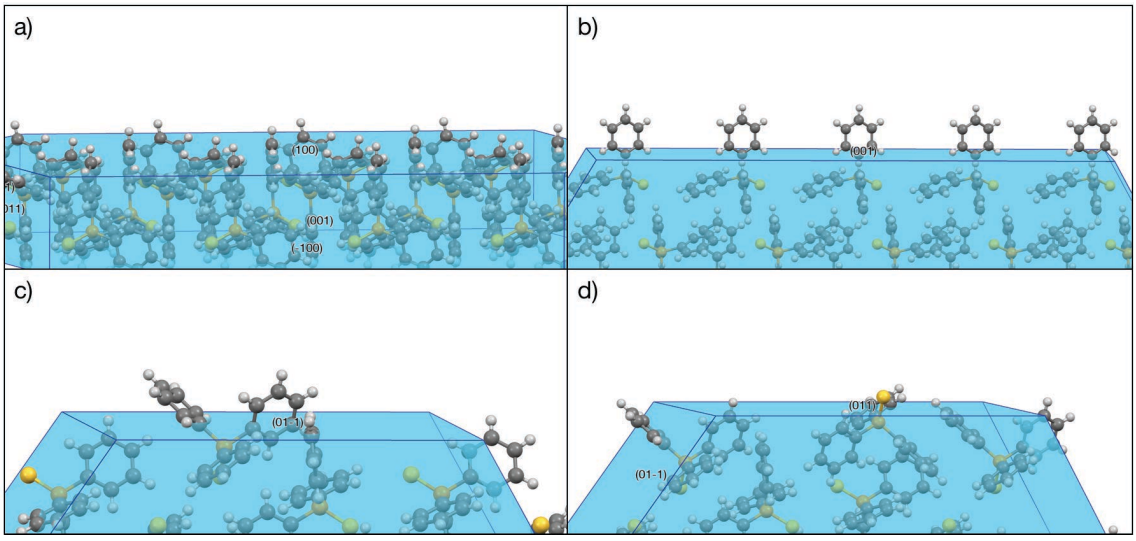

Figure 5.15 PPh_3S crystal structure with crystal faces. **a**, molecular orientation at the (100) face, **b**, molecular orientation at the (001) face, **c**, molecular orientation at the (01-1) face and **d**, molecular orientation at the (011) face.

AFM imaging of the biggest (100) face showed that the surface has steps of 1.2 nm (Figure 5.16a) corresponding to one molecular layer in the crystal structure (Figure 5.16b) and a roughness rms value of 0.14 nm over a 500x500 nm area. The presence of large flat regions means this surface is suitable for binding of material to form nanostructures.

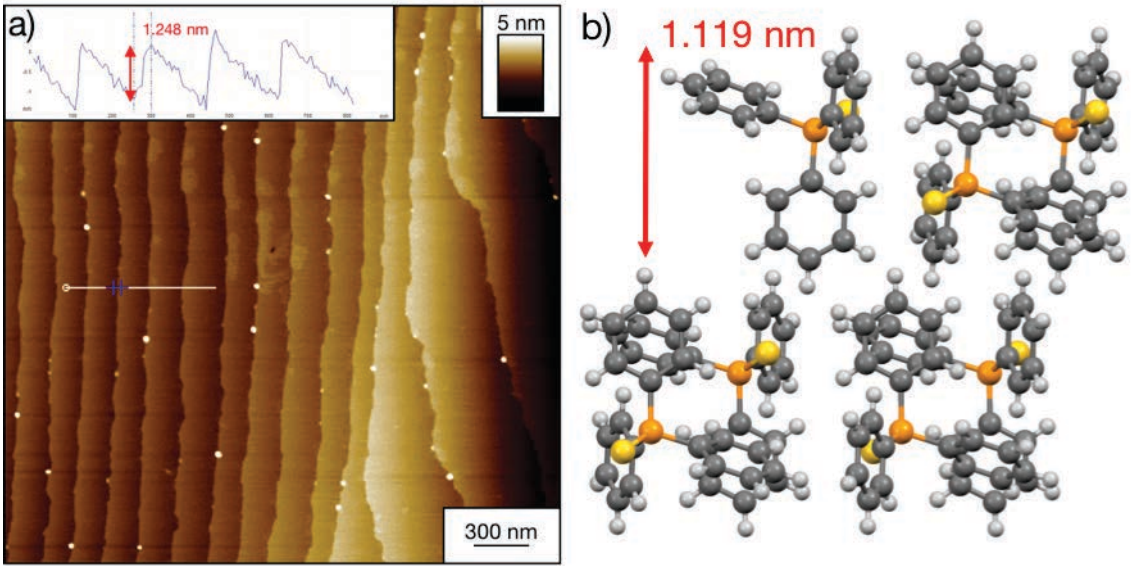

Figure 5.16 a, AFM height image of the PPh_3S (100) crystal face with an insert image showing measured step heights across the surface. **b**, PPh_3S crystal structure viewed down the [010] axis with the (100) plane horizontal, showing possible molecular steps.

Images obtained of the (011) face (larger end face of crystal) revealed surface steps with an average height of 1.2 nm at the surface (Figure 5.17a), however, they are much less well defined. This height corresponds with two molecular

layers in this [011] direction (Figure 5.17b). Some large flat regions can still be seen here, suitable for material binding. Surface roughness analysis gave an rms value of 0.53 nm over a 500x500 nm area showing that the surface is generally more rough than the (100) face.

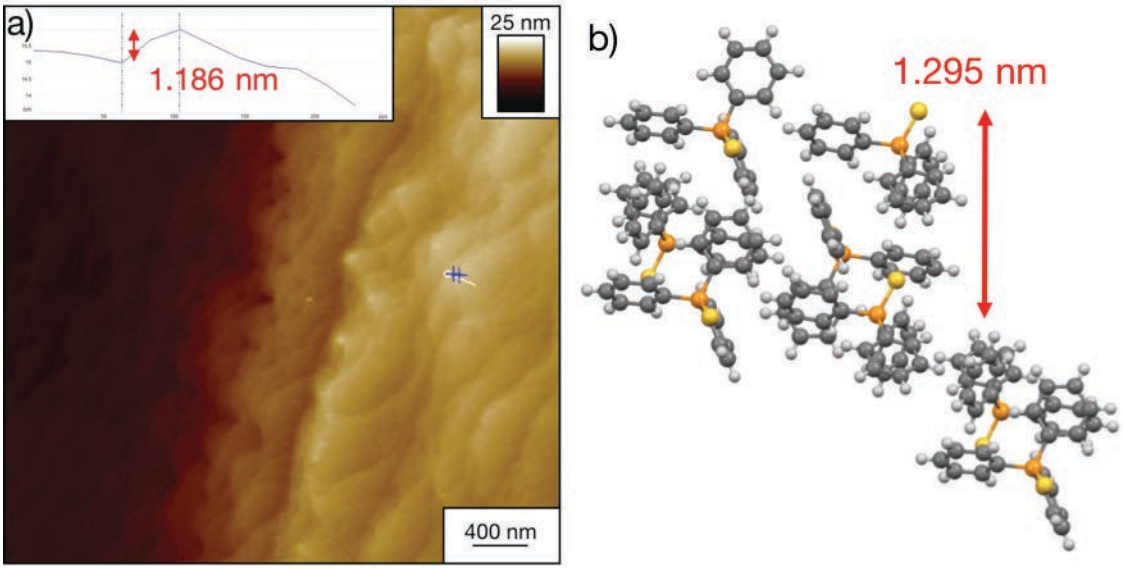

Figure 5.17 a, AFM height image of the PPh_3S (011) crystal face with an insert image showing measured step heights across the surface. **b**, PPh_3S crystal structure viewed down the [01-3] axis with the (011) plane horizontal, showing possible molecular steps.

Imaging of the (001) face (side face of crystal) showed steps of 0.9 nm height (Figure 5.18a) which correspond to one molecular layer in the [001] direction in the crystal structure (Figure 5.18b). Roughness analysis gave an rms value of 0.30 nm over a typical 500x500 nm region showing this surface to be less rough than the (011) face but more rough than the (100) face, and again shows large flat regions between steps, suited for surface binding of material.

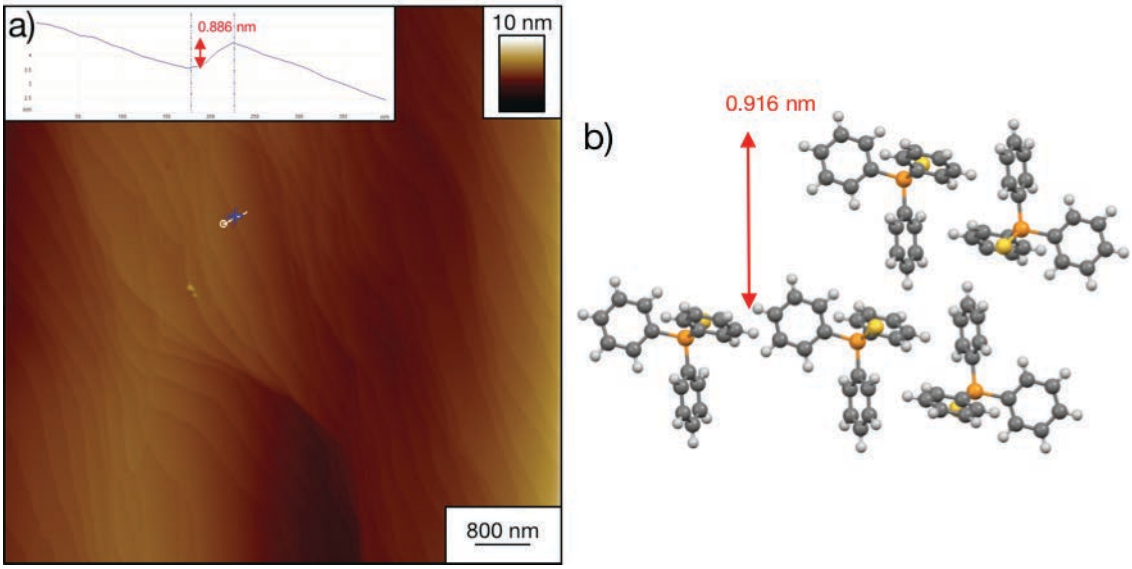

Figure 5.18 a, AFM height image of the PPh_3S (001) crystal face with an insert image showing measured step heights across the surface. **b**, PPh_3S crystal structure viewed down the [010] axis with the (001) plane horizontal, showing possible molecular steps.

Unfortunately, the (01-1) face could not be imaged, as it was too difficult to access and keep intact when cutting and mounting as the face tends to be too small.

XPS survey scans of the (100) face of the PPh_3S crystals (Figure 5.19a) show the same trace elements of silicon, oxygen and fluorine, as for the PPh_3 crystals. Excluding the contaminants, carbon accounts for 88.88% of the surface composition with phosphorus accounting for 6.31% and sulfur making up the remaining 4.81% (Figure 5.10). Survey scans of the (011) face (Figure 5.19b) show carbon, phosphorus and sulfur account for 87.67% and 6.40% and 5.93% of the surface composition respectively. These relative element percentage values are in agreement with the crystal structure where phosphorus is closer to the surface of the (011) face than the (100) face and sulfur is more available at the (011) face.

High resolution scans for carbon, phosphorus and sulfur were performed. For the carbon C 1s region, Figure 5.19a and b, no significant differences could be observed between the (100) and (011) faces. As with the PPh_3 crystals, the main C 1s peaks corresponding to the phenyl rings were charge referenced to 284.80 ev, both spectra again show π-π* satellite peaks centred at 291.29 ev for (100) and 291.27 ev for (011), again agreeing with literature values for aromatic carbon (sp^2), 291.27 ev.[25]

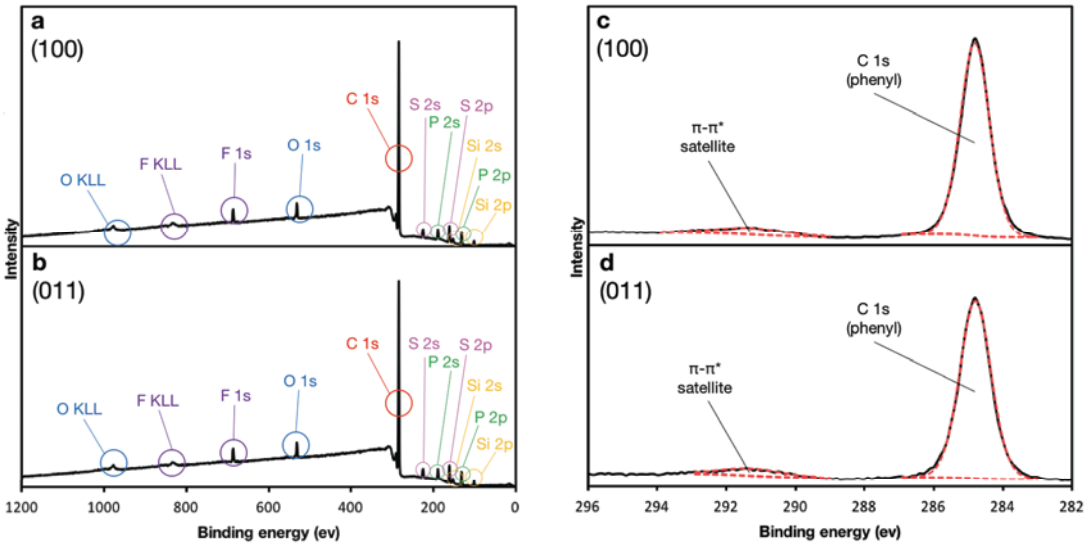

Figure 5.19 XPS survey scans of **a**, the PPh_3S (100) crystal face and **b**, the PPh_3S (011) crystal face with major peaks highlighted. High resolution scans of the carbon C 1s region for **c**, the PPh_3S (100) crystal face and **d**, the PPh_3S (011) crystal face showing peaks for the phenyl rings and the aromatic π-π* satellite.

For the phosphorus P 2p region (Figure 5.20a), again no significant differences could be observed between the (100) and (011) faces with the P $2p_{3/2}$ components centred at 132.14 ev and 132.15 ev for the (100) and (011) faces respectively, with the spin-orbit components being separated by 0.88 ev for the (100) face and 0.90 ev for the (011) face. These values are slightly lower than the literature values for PPh_3S of 132.60-133.10 ev.[27, 31]

Looking at the sulfur S 2p region (Figure 5.20c and d), again no significant differences could be observed between the (100) and (011) faces. The S $2p_{3/2}$ components centred at 162.08 ev and 161.81 ev for the (100) and (011) faces respectively, with the spin-orbit components being separated by 1.22 and 1.18 ev. These values are in agreement with the literature values for PPh_3S of 162.01-163.00 ev.[27, 31]

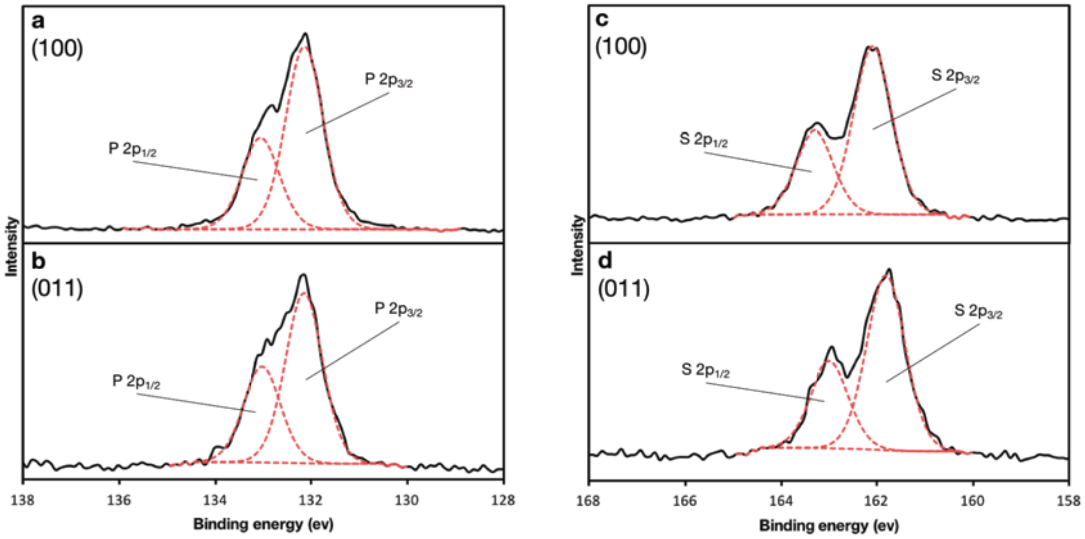

Figure 5.20 High resolution XPS scans of the phosphorus P 2p region of **a**, the PPh_3S (100) crystal face and **b**, the PPh_3S (011) crystal face both showing one peak with two components. High resolution XPS scans of the sulfur S 2p region of **c**, the PPh_3S (100) crystal face and **d**, the PPh_3S (011) crystal face both showing one peak with two components.

5.2.5 Crystal Substrates of Triphenylphosphine Oxide (PPh_3O)

Large crystals of triphenylphosphine oxide (PPh_3O) were grown using the same method as for PPh_3 and PPh_3S crystals, that is by dissolving in toluene at 60°C and cooling slowly over 72 hours. The unit cell was determined and shown to be the same as previously produced.[32, 33] PPh_3O produced the largest crystals in our studies, with typical face dimensions in the order of 5-30 mm, with one face being distinctly larger than the others giving the crystals a very flat plate-like morphology. Face indexing analysis identified the crystal faces as (100), the largest face, (010), the side face, (01-1), the small end face and (011), the larger end face. The parallel lattice planes are indexed as (-100), (0-10), (0-11) and (0-1-1) (Figure 5.21).

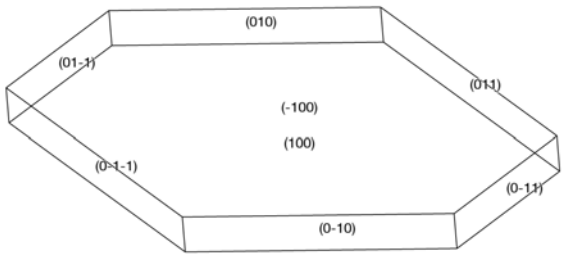

Figure 5.21 Full crystal morphology of PPh_3O obtained by face indexing with labelled Miller indices.

Face indexing analysis of the PPh_3O crystals shows potential access to the oxygen binding sites is greatest at the (01-1) and (011) faces (as well as their

opposites) (Figure 5.22c and d) and shows a similar layered arrangement as the PPh_3S (011) face, where molecular orientation alternates with each layer. The termination orientation may be elucidated by metal binding experiments showing face selectivity or not. The O···O binding sites on the (01-1) face are separated by distances of 2.884 nm in the [100] direction and 1.434 nm in the [011] direction, and binding sites on the (011) face are also separated by 2.884 nm in the [100] direction and 1.434 nm in the [01-1] direction. The large spacing between binding sites provides a good chance of resolving deposited material by AFM. Access to the (100) and (010) faces is again sterically hindered by the phenyl groups.

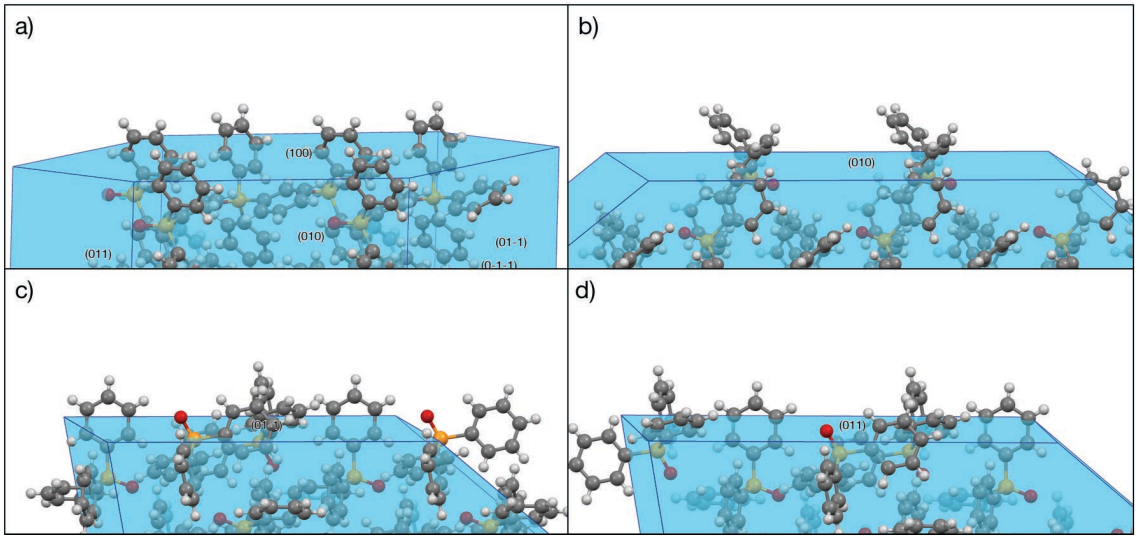

Figure 5.22 PPh_3O crystal structure with crystal faces. **a**, molecular orientation at the (100) face, **b**, molecular orientation at the (010) face, **c**, molecular orientation at the (01-1) face and **d**, molecular orientation at the (011) face

Images obtained from AFM of the (100) face (largest face) showed large atomically flat terraces, several μm^2 in area. The surface has steps of 1.3 nm (Figure 5.23a) indicating to two molecular layers, half the unit cell in this direction (Figure 5.23b). And roughness analysis with an rms value of 0.09 nm over a 2x2 µm area. This is a very low roughness over such a large area and may be due to the large spacing from one step to the next.

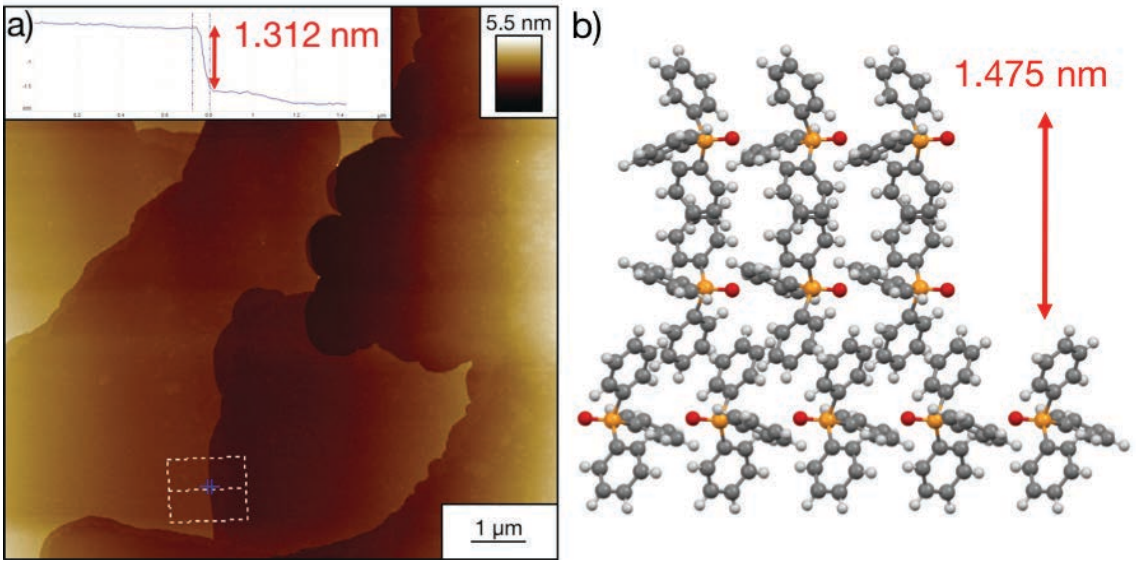

Figure 5.23 a, AFM height image of the PPh_3O (100) crystal face with an insert image showing measured step heights across the surface. **b**, PPh_3O crystal structure viewed down the [010] axis with the (100) plane horizontal, showing possible molecular steps.

Imaging of the (010) face (side face) revealed step heights of 0.5-0.6 nm (Figure 5.24a) corresponding to half a molecular layer in the crystal structure (Figure 5.24b), and a roughness analysis gave an rms value of 0.10 nm over a 200x200 nm area. Low roughness, but the flat areas are smaller than for previous crystals/faces.

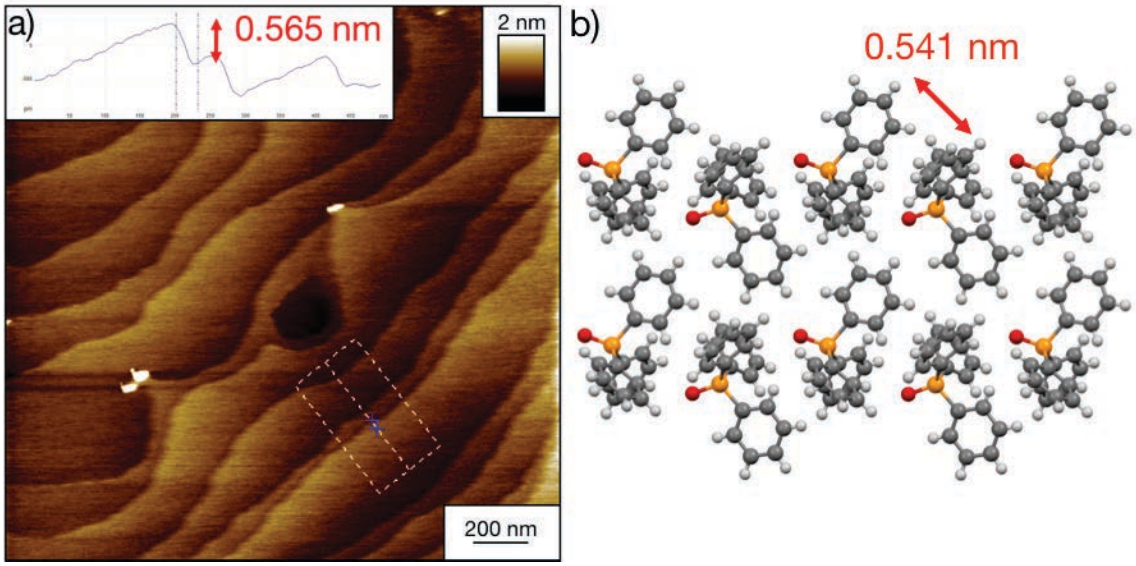

Figure 5.24 a, AFM height image of the PPh_3O (010) crystal face with an insert image showing measured step heights across the surface. **b**, PPh_3O crystal structure viewed down the [100] axis with the (010) plane horizontal, showing possible molecular steps.

AFM data for the (011) face showed step heights of 0.6-0.7 nm (Figure 5.25a) which again relate to half a molecular layer in the crystal structure (Figure

5.25b). Roughness analysis gives this surface an rms value of 0.08 nm across a 500x500 nm region, this is again, a very low roughness measurement over large, flat areas, making this surface suitable for material binding.

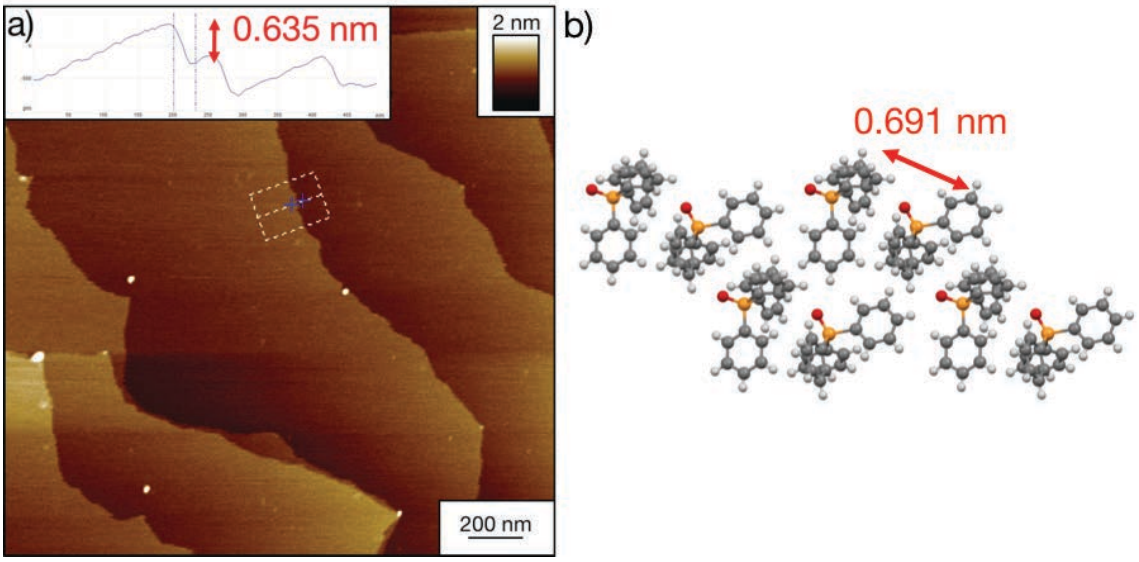

Figure 5.25 a, AFM height image of the PPh_3O (011) crystal face with an insert image showing measured step heights across the surface. **b**, PPh_3O crystal structure viewed down the [100] axis with the (011) plane horizontal, showing possible molecular steps.

Unfortunately, as with the PPh_3S crystals, the (01-1) face of the PPh_3O crystals could not be imaged due to difficulty accessing this small face.

XPS was performed on the PPh_3O crystals. Survey scans of the (100) face (Figure 5.26a) showed only the presence of silicon and fluorine as contaminants as this time the amount of oxygen would be evaluated. Excluding the contaminants, carbon accounted for 86.64% of the surface composition, phosphorus accounted for 5.90% and oxygen accounted for 7.46%. Survey scans of the (011) face (Figure 5.26b) revealed carbon accounted for 84.28% of the surface composition with phosphorus and oxygen calculated at 5.90% and 10.50% respectively. These relative elemental percentage values match well with the crystal structure for PPh_3O, where oxygen atoms can be present at the surface of the (011) face but not the (100) face.

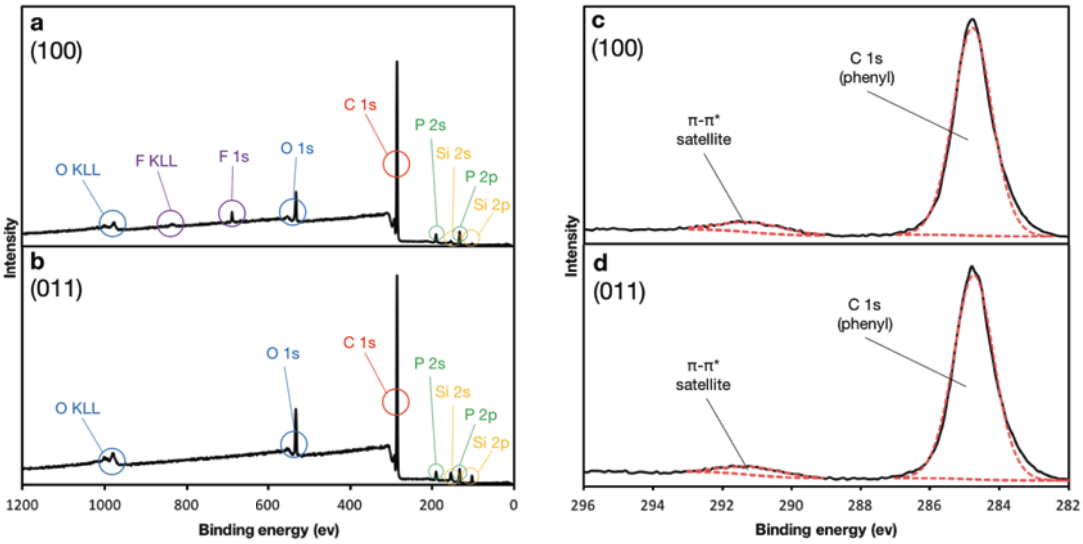

Figure 5.26 XPS survey scans of **a**, the PPh_3O (100) crystal face and **b**, the PPh_3O (011) crystal face with major peaks highlighted. High resolution scans of the carbon C 1s region for **c**, the PPh_3O (100) crystal face and **d**, the PPh_3O (011) crystal face showing peaks for the phenyl rings and the aromatic π-π* satellite.

High resolution scans of the C 1s region showed no significant differences between the (100) and (011) faces (Figure 5.26c and d). The main C 1s peaks (for the phenyl rings) were again charge referenced to 284.80 ev, leading to the π-π* satellite peaks being centred at 291.15 ev and 291.12 ev for the (100) and (011) faces respectively. These energies are again consistent with the literature values for aromatic carbon, 291.27 ev.[25]

Scans of the phosphorus P 2p (Figure 5.27a and b) region did not reveal any substantial differences between the (100) and (011) faces, with the P $2p_{3/2}$ components centred at 132.16 ev and 132.15 ev for the (100) and (011) faces respectively putting the values in close agreement with previously reported data for PPh_3O (not as a single crystal) 132.6-133.0 ev.[27, 31] The P 2p spin-orbit components were separated by 0.87 ev and 0.80 ev, giving P $2p_{1/2}$ values of 133.03 ev for the (100) face and 132.95 ev for the (011) face.

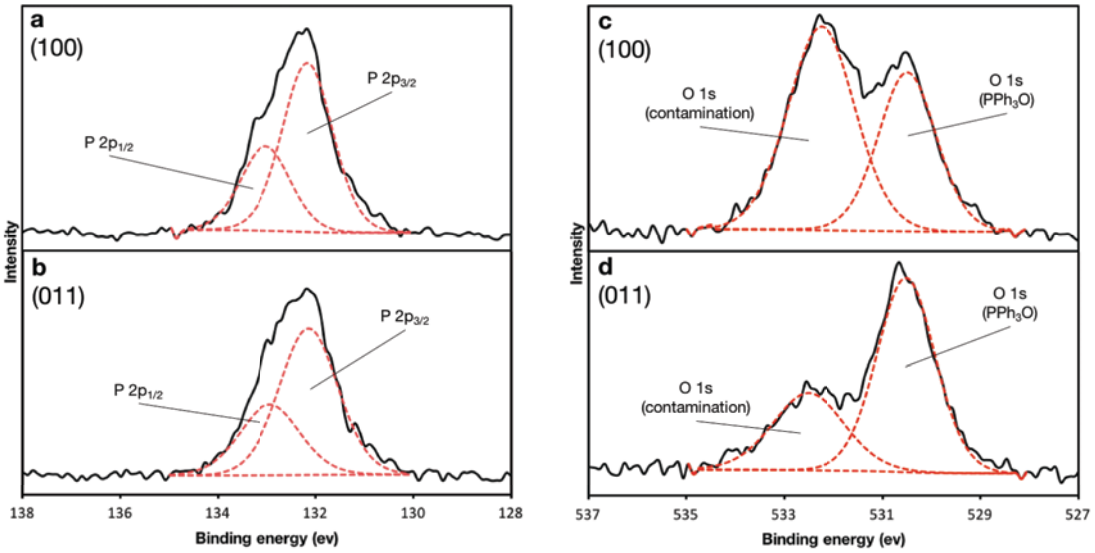

Figure 5.27 High resolution XPS scans of the phosphorus P 2p region of **a**, the PPh_3O (100) crystal face and **b**, the PPh_3O (011) crystal face both showing one peak with two components. High resolution XPS scans of the oxygen O 1s region of **c**, the PPh_3O (100) crystal face and **d**, the PPh_3O (011) crystal face showing two oxygen components present in different amounts.

High resolution scans of the O 1s region were performed and show two components present in the O 1s region (Figure 5.27c and d). The lower energy O 1s components present centre at 530.52 ev for the (100) face and 530.49 ev for the (011) face putting them just lower than the PPh_3O literature vales of 530.70-531.90 ev.[27, 31] The higher energy components centre at 532.51 ev and 532.25 ev and are attributed to a contamination source of oxygen as peaks close to this value are present on all samples. There is more oxygen present due to contamination on the (100) face 59.90% than the (011) face 32.81%, these values agree with the previous survey scan results and the crystal structure for PPh_3O where more oxygen can be present at the (011) face.

5.3 Conclusions

We have utilized single crystal X-ray crystallography and face indexing analysis to determine the functional groups present at each face of the Py-Im-Et (**8**) crystal substrate, as well as crystals of triphenylphosphine (PPh_3), triphenylphosphine sulphide (PPh_3S) and triphenylphosphine oxide (PPh_3O). We have demonstrated the use of AFM to compare surface feature heights to molecular layers in the crystal structure, and showed by roughness analysis that these surfaces are generally flat enough to potentially facilitate the discrete binding of deposited material and provide a substrate base where deposited

material would easily be visible by contrast. The surface binding sites seen by X-ray crystallography exhibit spacing on the angstrom scale offering the potential for any deposited material to form nanostructures with resolutions that may exceed those provided by current conventional lithographic techniques, i.e. sub 10 nm pitch size. It was also observed from the face indexing of all the crystals under investigation in this Chapter, that binding sites were only clearly accessible on some crystal faces, meaning that face selectivity may be observed during metal binding experiments. We have shown here that it is possible to characterize molecular crystal surfaces by XPS however, it was not possible to distinguish between crystal faces using this technique, this is attributed to the large penetration depth of the X-rays meaning the surface atoms only account for a small percentage of analysed material.

It was seen that despite the delicate nature of such small organic compounds (the dissolution of Py-Im-Et crystals due to the imaging processes and the surface oxidation of PPh_3), some of the crystals (PPh_3S and PPh_3O) survived the characterization processes without damage. This shows that these organic crystal substrates are still in contention to be used functional surfaces for material deposition, and will be carried through to the next stage, metal adsorption studies.

5.4 Experimental Details

All chemicals were purchased from Sigma-Aldrich, Alfa Aesar or Fisher Scientific and were used as received without further purification. Unit cell parameters of crystals were determined by single crystal X-ray diffraction at 150 K copper radiation on an Oxford Diffraction Gemini A Ultra diffractometer. Face indexing analysis was performed using CrysAlisPro (Oxford Diffraction Ltd.) and crystal structures were visualized in Mercury CSD (CCDC).

AFM was performed on either a Veeco Dimension V microscope with Nanoscope V controller using TappingMode™ or a Bruker Multimode 8 microscope with a Nanoscope V controller using TappingMode™ or PeakForce Tapping™ with ScanAsyst. Tips used were either Budget Sensors Tap300Al-G silicon tips with resonant frequency = 300 kHz and force constant = 40 N/m or

Bruker SCANASYST-FLUID+ silicon nitride tips with resonant frequency = 150 kHz and force constant = 0.7 N/m. AFM analysis was conducted using NanoScope Analysis (Bruker Corporation).

XPS was performed using a Thermo Scientific K-Alpha system with a microfocused, monochromated Al Kα X-ray source. Data analysis was performed using CasaXPS (Casa Software Ltd.).

Crystals were cut using a scalpel and re-oriented for specific face analysis. Samples were mounted using carbon tape on silicon wafers (for AFM) or copper clips (for XPS).

Py-Im-Et crystals (**8**)

Py-Im-Et crystals (**8**) were prepared and crystallized in the same manner as in Chapter 2, producing large crystals suitable for AFM and XPS analysis. Pyridine-3-carboxaldehyde (5.00 mL, 53.26 mmol) was mixed with ethanol (50 mL) 1,2-diaminoethane (1.78 mL, 26.63 mmol) and dichloromethane (50 mL) before formic acid (two drops) was added. The mixture was stirred at room temperature overnight. The solvent was reduced to dryness and the yellow solid was washed with hexane, dried, and collected giving a yield of 90%.
5 mL of a solution of (**8**) (2.00 g, 8.39 mmol) in ethyl acetate (5 mL) was placed in a glass vial and left to crystallize by evaporation for 10 days. Large well defined block crystals were then retrieved from the vial. Unit cell determination was performed on crystals smaller in size but of the same morphology giving a monoclinic crystal system and a space group of $P2_1/c$. Unit cell parameters were a = 13.4568(19) Å, b = 4.1390(6) Å, c = 11.1975(18) Å, β = 102.282°. Cell volume = 609.40(16) $Å^3$.

Triphenylphosphine crystals (**PPh_3**)
0.5 mL of a solution of triphenylphosphine (4.00 g, 15.25 mmol) in toluene (5 mL) was cooled slowly (3 days) in a glass vial from 80 °C to room temperature (22 °C) to produce small well defined crystals. These crystals were too small for AFM and XPS analysis so were used as seeds in a saturated solution of triphenylphosphine in toluene (1.12 $moldm^{-3}$) at room temperature (22 °C) to

give much larger well defined crystals. Unit cell determination was performed on crystals smaller in size but of the same morphology giving a monoclinic crystal system and a space group of $P2_1/c$. Unit cell parameters were a = 8.489(1) Å, b = 15.000(30) Å, c = 11.404(2) Å, β = 92.83°. Cell volume = 1450.35(7)

Triphenylphosphine sulfide crystals (**PPh_3S**)

3 mL of a solution of triphenylphosphine sulfide (0.40 g, 1.36 mmol) in toluene (5 mL) was cooled slowly (3 days) in a glass vial from 80 °C to room temperature (22 °C) to produce large well defined crystals suitable for AFM and XPS analysis.

Unit cell determination was performed on crystals smaller in size but of the same morphology giving a monoclinic crystal system and a space group of $P2_1/c$. Unit cell parameters were a = 18.314 Å, b = 9.640 Å, c = 18.013 Å, β = 105.99°. Cell volume = 3057.10

Triphenylphosphine oxide crystals (**PPh_3O**)

3 mL of a solution of triphenylphosphine sulfide (0.50 g, 1.80 mmol) in toluene (5 mL) was cooled slowly (3 days) in a glass vial from 80 °C to room temperature (22 °C) to produce large well defined crystals suitable for AFM and XPS analysis.

Unit cell determination was performed on crystals smaller in size but of the same morphology giving a monoclinic crystal system and a space group of $P2_1/a$. Unit cell parameters were a = 11.089 Å, b = 16.302 Å, c = 8.739 Å, β = 107.95°. Cell volume = 1502.88

5.5 References

1. G. E. Moore, *Proc. IEEE*, 1998, **86**, 82-85.
2. Y. Cui and C. M. Lieber, *Science*, 2001, **291**, 851-853.
3. W. Lu and C. M. Lieber, *Nat. Mater.*, 2007, **6**, 841-850.
4. ITRS Roadmap, http://www.itrs.net/).
5. R. P. Feynman, *Eng. Sci.*, 1960, 22-36.
6. A. Ulman, *Chem. Rev.*, 1996, **96**, 1533-1554.
7. C. A. Alves, E. L. Smith and M. D. Porter, *J. Am. Chem. Soc.*, 1992, **114**, 1222-1227.

8. H. Roder, E. Hahn, H. Brune, J.-P. Bucher and K. Kern, *Nature*, 1993, **366**, 141-143.
9. F. M. Ross, R. M. Tromp and M. C. Reuter, *Science*, 1999, **286**, 1931-1934.
10. M. Corso, W. Auwärter, M. Muntwiler, A. Tamai, T. Greber and J. Osterwalder, *Science*, 2004, **303**, 217-220.
11. J. V. Barth, J. Weckesser, C. Cai, P. Günter, L. Bürgi, O. Jeandupeux and K. Kern, *Angew. Chem. Int. Ed.*, 2000, **39**, 1230-1234.
12. G. Whitesides, J. Mathias and C. Seto, *Science*, 1991, **254**, 1312-1319.
13. M. J. Fasolka and A. M. Mayes, *Annu. Rev. Mater. Res.*, 2001, **31**, 323-355.
14. T. Thurn-Albrecht, J. Schotter, G. A. Kästle, N. Emley, T. Shibauchi, L. Krusin-Elbaum, K. Guarini, C. T. Black, M. T. Tuominen and T. P. Russell, *Science*, 2000, **290**, 2126-2129.
15. W. A. Lopes and H. M. Jaeger, *Nature*, 2001, **414**, 735-738.
16. Cambridge Structural Database, http://www.ccdc.cam.ac.uk/).
17. G. R. Desiraju, *Crystal engineering: the design of organic solids*, Elsevier, 1989.
18. A. Gavezzotti, *Acc. Chem. Res.*, 1994, **27**, 309-314.
19. G. Binnig, C. F. Quate and C. Gerber, *Phys. Rev. Lett.*, 1986, **56**, 930-933.
20. M. D. Ward, *Chem. Rev.*, 2001, **101**, 1697-1726.
21. K. Siegbahn, *Philos. Trans. R. Soc., A*, 1970, **268**, 33-57.
22. J. V. Macpherson, P. R. Unwin, A. C. Hillier and A. J. Bard, *J. Am. Chem. Soc.*, 1996, **118**, 6445-6452.
23. J. J. Daly, *J. Chem. Soc.*, 1964, 3799-3810.
24. B. J. Dunne and A. G. Orpen, *Acta Crystallogr. Sect. C: Cryst. Struct. Chem.*, 1991, **47**, 345-347.
25. C. Girardeaux and J.-J. Pireaux, *Surf. Sci. Spectra*, 1996, **4**, 130-133.
26. M. Pelavin, D. N. Hendrickson, J. M. Hollander and W. L. Jolly, *J. Phys. Chem.*, 1970, **74**, 1116-1121.
27. S. Hoste, D. F. Van De Vondel and G. P. Van Der Kelen, *J. Electron. Spectrosc. Relat. Phenom.*, 1979, **17**, 191-195.
28. P. W. Codding and K. A. Kerr, *Acta Crystallogr., Sect. B: Struct. Crystallogr. Cryst. Chem.*, 1978, **34**, 3785-3787.
29. C. Foces-Foces and A. L. Llamas-Saiz, *Acta Crystallogr. Sect. C: Cryst. Struct. Chem.*, 1998, **54**.
30. W. Gao, J. Liu, B. Åkermark and L. Sun, *J. Organomet. Chem.*, 2007, **692**, 1579-1583.
31. W. E. Morgan, W. J. Stec, R. G. Albridge and J. R. Van Wazer, *Inorg. Chem.*, 1971, **10**, 926-930.
32. C. P. Brock and W. B. Schweizer, *J. Am. Chem. Soc.*, 1985, **107**, 6964-6970.
33. A. Spek, *Acta Crystallogr. Sect. C: Cryst. Struct. Chem.*, 1987, **43**, 1233-1235.

Chapter 6

Controlled Metal-Binding to Crystal Surfaces

Table of Contents

6.1 Introduction

The fabrication of nanostructures on surfaces by self-assembly and growth processes is seen as a promising route to the continued miniaturization of electronics.[1] Our proposed system to grow nanostructures from a molecular single crystal surface uses a system where the structural information is embedded in the substrate. Crystals can grow to have well defined faces, each potentially offering different surface chemistries because of the functional groups or atoms presented at them. This provides the opportunity for face selectivity with respect to metal binding, such as that seen on L-cistine,[2] where gold nanoparticles selectively deposit on the (001) face, α-cyclodextrin inclusion complexes[3] where metal nanoparticles selectively deposit onto the (001) face, or naphthalene diimide,[4] where metal complex nanocrystals selectively deposit onto the (01-1) face. For our substrates, it was observed from the crystal structures and face indexing analysis (chapter 5) of all the crystals under investigation in this chapter, that binding sites would be more easily accessed on certain crystal faces, the (011) faces for both PPh_3S and PPh_3O crystals.

It is also noted that the molecules present at these (011) faces can have one of two orientations (with inward or outward facing binding sites) as the crystal forms with alternating layers. The presence or absence of surface bound material may indicate which layer is the natural termination point for that face of the crystal structure.

Gold was selected as the binding material here. Both nanoparticles and ions are used because microscopy of the crystal substrates in Chapter 5 revealed difficulty in obtaining high resolution images. Crystal structure unit cells were not visible by AFM, however, large nanoparticles are more readily imaged and may still show ordering due to the substrate crystal structure. Gold nanoparticles have been shown to have many potential uses, such as in catalysis[5] and nanomedicine.[6] Whilst possibly forming our desired nanostructured conductors, deposition of gold nanoparticles in an ordered array on surfaces is also highly desirable, with potential applications in optical devices,[7] biomedical sensors[8] and for the characterization of trace chemical species by surface-enhanced Raman scattering (SERS).[9]

The reduction of already surface-bound gold ions to elemental gold (Au(0)) may also create ordered nanostructures or discrete nanoparticles through aggregation.[10] Conductivity of potential nanostructures is useful if they are to be used in the semiconductor industry, gold is the 3rd most electrically conductive element[11] and is generally preferred over silver when used as an electrical connector because of its inert nature, being unlikely to react or corrode as quickly.[12]

In Chapter 5, it was discovered that oxide is present at the surface of our triphenylphosphine (PPh_3) crystals, meaning the surface chemistry available is now ambiguous and possibly no different to that of our control surface, triphenylphosphine oxide (PPh_3O). As a result, this chapter will focus on the comparison between triphenylphosphine sulfide (PPh_3S) and the PPh_3O control sample as binding substrates for gold deposition. Gold is known to interact strongly with sulfur in nanoscale systems such as in monolayer or cluster formation,[13] as well as in metal complexes, with PPh_3S specifically,[14, 15] where the sulfur binding site has a bent geometry with P-S-Au angles of around ~106° or ~96°,[16] giving a wide range of possible surface binding angles. Au-O complexes are generally lower in stability (weaker soft acid to hard base interaction)[17] meaning PPh_3O can be used to compare binding selectivity of the crystal surfaces. Au-O bonding is possible, showing P-O-Au bond angles with a bent geometry with ranging from 121°-129°.[18-20]

As in Chapter 5, atomic force microscopy (AFM) and X-ray photoelectron spectroscopy (XPS) are used here for microscopy and chemical identification of different crystal surfaces. The use of AFM for characterization of nanostructures on surfaces is common[21] and can provide accurate information regarding their size and shape, with feature height resolution greater than 0.1 nm.

Here, we plan to monitor gold nanoparticle and gold ion surface binding to crystals of PPh_3S and PPh_3O by AFM and XPS. XPS has the capability to distinguish between oxidation states and chemical environments, making it a useful technique to follow the reduction of surface bound material, or to determine if a material has bound (change in chemical environment). These features make XPS a very useful technique here for studying surface-metal binding where samples go from Au(I) to Au(0), meaning it should be possible to

monitor the reduction of Au on the surface. XPS can also provide quantitative data, which is related to the peak intensities, making it possible to determine the extent of surface coverage of deposited material compared to other surfaces.

6.2 Results and Discussion

6.2.1 Treatment of Crystals with Gold Nanoparticles

The first adsorbed material looked at was gold nanoparticles with a quoted diameter of ~2.2 nm. These citrate stabilized particles are expected to bind at surfaces where the ligands can be displaced by the sulfur or oxygen groups of the crystals. These particles should also be more easily imaged than single atoms, however, the particles themselves are larger than most of the binding site spacing of all the crystal faces studied here but may still attach in an ordered array if the particles were to bind to two or more binding sites or if steric hindrance forces binding to alternating sites in an array.

The experiments took place by immersing the crystal in a 7.7 nM aqueous solution of gold nanoparticles, before washing with water and drying.

6.2.2 Gold Nanoparticles on Triphenylphosphine Sulfide Crystals

Looking at triphenylphosphine sulphide crystals, the crystal structure shows little potential for binding at the (100) face, however, AFM shows a reasonably high surface coverage of discrete particles (Figure 6.1a) with a surface roughness of 0.62 nm compared to the bare crystal (0.14 nm) over a 500x500 nm area as well as some very large clusters of particles. The discrete particles correspond to the dimensions of the gold nanoparticles (~2.2 nm) or multiples of them (Figure 6.1b) indicating that these are indeed gold nanoparticles (also backed up by presence of gold in XPS spectrum, Figure 6.5a). The particles are typically well separated across the surface but, as expected show no indication of an ordered array due to the lack of binding sites present at this surface. Where binding is not expected particles may still be physisorbed onto the surface or bound at step edges or imperfections in the crystal surface.

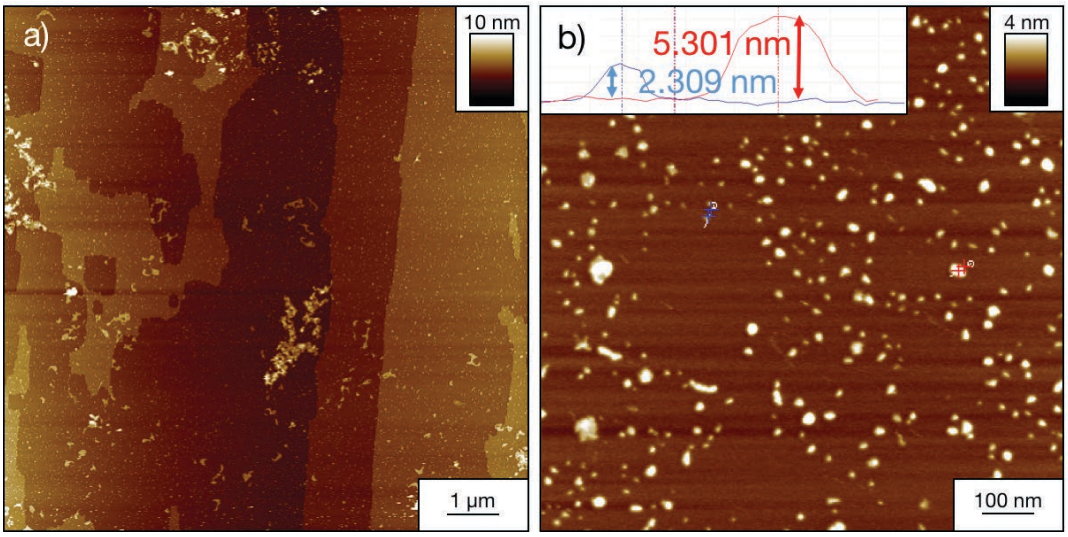

Figure 6.1 **a**, 10 x 10 µm AFM image of the (100) face of a PPh_3S crystal after gold nanoparticle treatment, **b**, expanded view of 1 x 1 µm showing measured particle heights.

The PPh_3S crystal structure also indicates very little chemical binding potential at the (001) face. This is reflected in the very low number of surface features, in the form of adsorbed material seen by AFM (Figure 6.2a). The surface roughness here is 0.15 nm over a 500x500 nm area, lower than for the bare crystal (0.30 nm). In areas where features can be seen, the feature dimensions seem to correspond to that of the gold nanoparticles used ~2.2 nm heights, showing a much lower coverage with well-separated particles (Figure 6.2b).

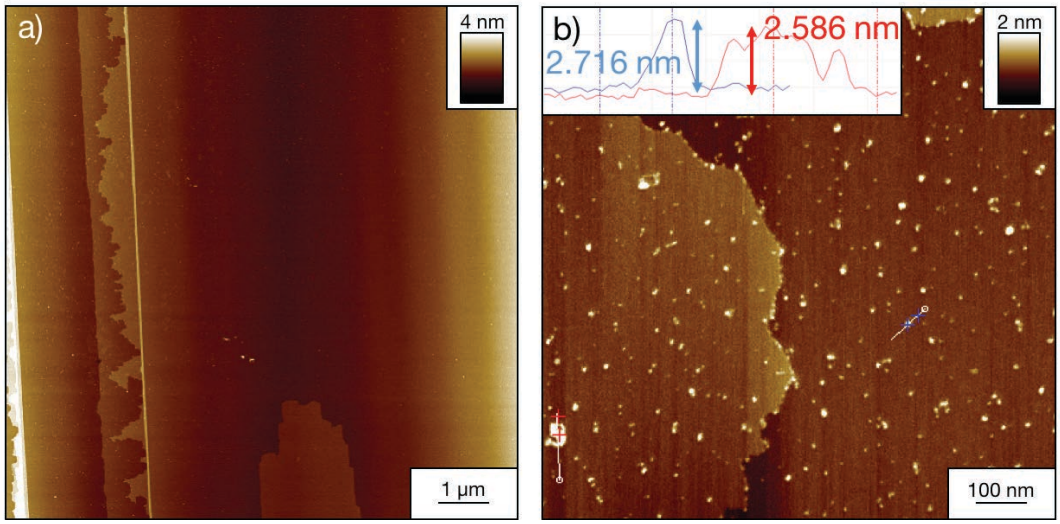

Figure 6.2 **a**, 10 x 10 µm AFM image of the (001) face of a PPh_3S crystal after gold nanoparticle treatment, **b**, expanded view of 1 x 1 µm showing measured particle heights.

The (011) face of the PPh_3S crystals is where stronger binding is expected to take place, as the sulphur atoms are most easily accessible at this crystal face (Chapter 5) with the potential to interact strongly with gold. AFM shows quite a

low coverage of discrete particles on this surface (Figure 6.3a) with a surface roughness of 0.32 nm over a 500x500 nm area, this is also lower than for the bare crystal (0.53 nm). However, much larger clusters of particles can be seen here compared with the other surfaces, which could mean that strong binding has occurred in some areas acting as a seed for cluster formation of particles. The clusters seem to form in layers (Figure 6.3b) with layer heights representing two nanoparticles (~5 nm), the individual nanoparticles in these clusters cannot be resolved by AFM so it is unclear whether they posses any structural order.

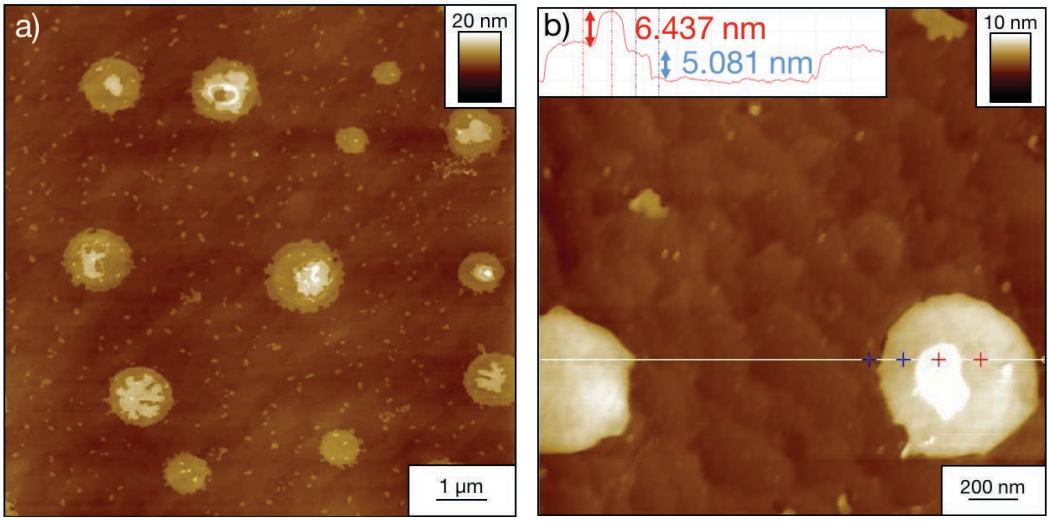

Figure 6.3 **a**, 10 x 10 µm AFM image of the (011) face of a PPh_3S crystal after gold nanoparticle treatment, **b**, expanded view of 2 x 2 µm showing measured particle heights.

XPS data for the same gold nanoparticles deposited on a silicon wafer was obtained as a reference for the oxidation state of our particles. All XPS data here was charge referenced to the adventitious C 1s peak at 284.80 eV as in Chapter 5. The Au 4f region comprises of two components, a 5/2 peak and a 7/2 peak, the latter of which is usually taken as a reference point for gold when using. This Au $4f_{7/2}$ peak was found to be centred at 84.05 eV for the gold nanoparticles on a silicon surface (Figure 6.4).

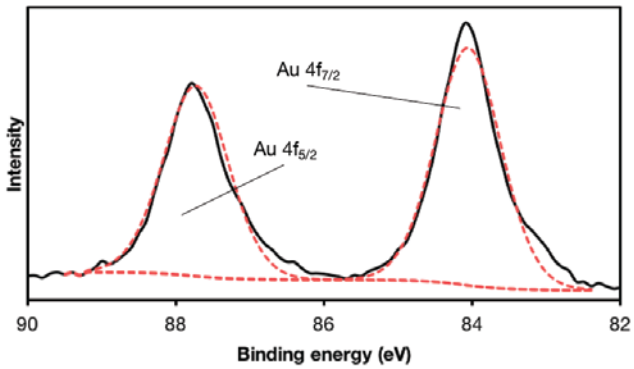

Figure 6.4 High resolution XPS scan of the Au 4f region for the gold nanoparticle reference sample on a silicon substrate.

XPS was performed on the (100) and (011) faces of our PPh_3S crystals surfaces after gold nanoparticle treatment. An overlay of spectra for the Au 4f region (Figure 6.5a) shows peaks for both faces corresponding to that of the control on silicon wafer, with the Au $4f_{7/2}$ peaks for the (100) and (011) faces centred at 84.09 eV and 84.01 eV respectively. The overlay also shows the intensity of the peaks is more than three times higher on the (100) face than on the (011) face, suggesting a higher amount of gold is present on this face. This complements the AFM data where the (100) face appears to have a higher overall coverage of gold.

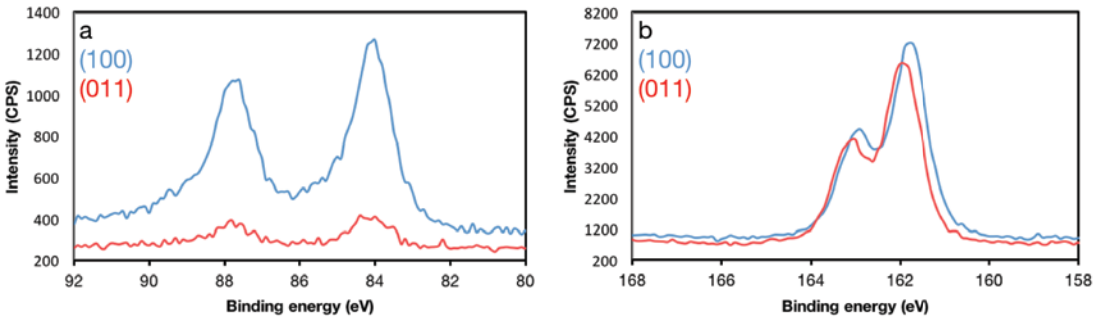

Figure 6.5 High resolution XPS scans of the (100) and (011) faces of PPh_3S crystal after gold nanoparticle treatment, showing **a**, the gold Au 4f region, and **b**, the sulfur S 2p region.

Binding energy shifts in XPS can be used to indicate a change in chemical environment of the observed element and binding energies for sulfur decrease as the environment changes from thiol (R-SH ~164.0 eV) to a gold bound thiol (Au-S ~162.5 eV) to a metal sulphide (~161.5 eV). As gold binds to the sulfur of our surfaces, a decrease in S 2p binding energy may too be seen.

XPS data for the S 2p region of these samples shows a slight binding energy difference between the (100) and (011) faces (Figure 6.5b), with the S $2p_{3/2}$ components centred at 161.76 eV and 161.79 eV for the (100) and (011) faces respectively. Both exhibit lower binding energies than the bare crystal (162.08 eV for the (100) face and 161.81 eV for the (011) face) indicating these particles may be chemisorbed onto the surface rather than physisorbed.

6.2.3 Gold Nanoparticles on Triphenylphosphine Oxide Crystals

Looking at triphenylphosphine oxide crystals now, the crystal structure suggests that the oxygen binding sites are absent from the (100) face, AFM images however, show discrete particles present on this crystal surface (Figure 6.6a), with a roughness value of 0.46 nm over a 500x500 nm area, a significant increase from the 0.09 nm seen for the bare crystal face. These discrete particles measure at ~2.5 or ~5 nm in height (Figure 6.6b), corresponding with the nanoparticles used, however the XPS data for this face (Figure 6.9a) indicates no gold is present. These features may still be nanoparticles, however the low concentration may not have provided a strong enough signal to be detected by XPS.

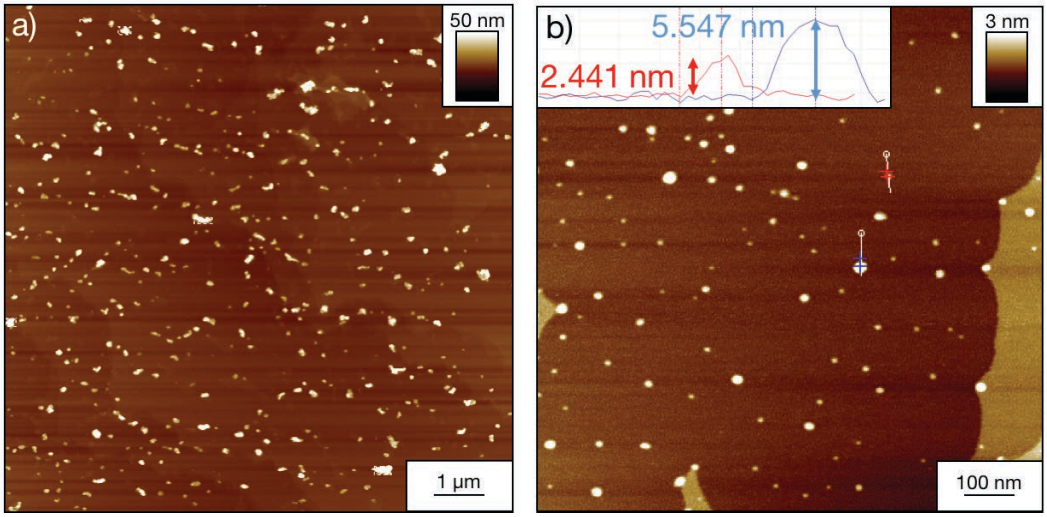

Figure 6.6 a, 10 x 10 µm AFM image of the (100) face of a PPh_3O crystal after gold nanoparticle treatment, **b**, expanded view of 1 x 1 µm showing measured particle heights.

The (010) face of the PPh_3O crystals also shows low potential for surface binding with a lack of binding sites available. AFM images reflect this assumption, showing only very large features present and no discrete

nanoparticles visible (Figure 6.7 a and b), with a surface roughness of 0.23 nm over a 500x500 nm area, similar to the bare crystal (0.10 nm).

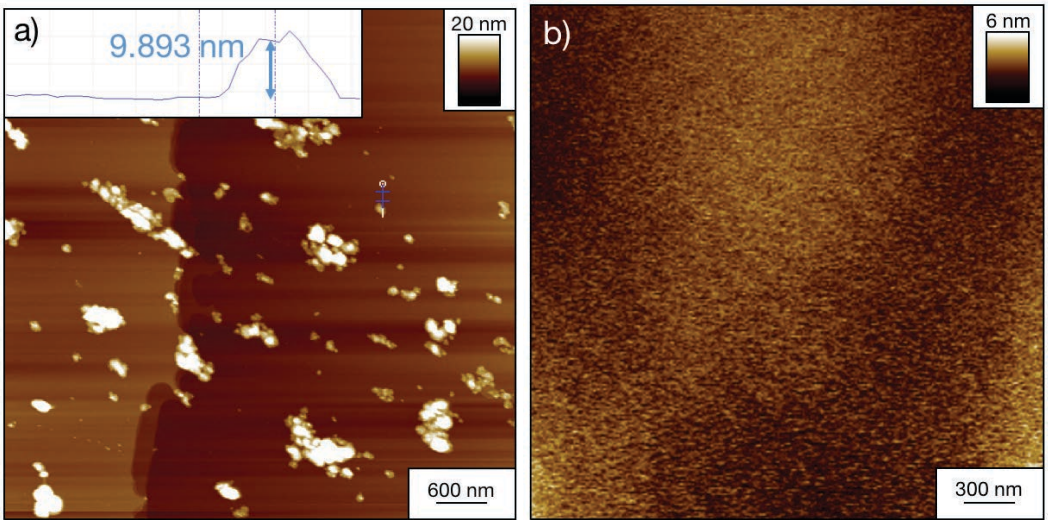

Figure 6.7 a, 6 x 6 µm AFM image of the (010) face of a PPh_3O crystal after gold nanoparticle treatment, **b**, expanded view of 3 x 3 µm showing large areas of the surface with no material present.

If gold particle binding to oxygen was to occur, it would be most likely to happen at the (011) face, as this is where the oxygen is most accessible. AFM again shows only very large features or nothing at all (Figure 6.8 a and b), with a surface roughness of 0.42 nm over a 500x500 nm area. This is a higher roughness than for the bare crystal (0.08 nm) but as no particles can be seen this must be due to variations in the substrate surface itself, possibly a slight rearrangement or dissolution of the crystal during the experimental procedure.

XPS also shows no gold present at this face (Figure 6.9a) suggesting that oxygen is a poor binding site for the gold nanoparticles. A positive note that can be taken from this is that this means the PPh_3O crystals can be used in an attempt to observe binding selectivity when compared to PPh_3S crystals

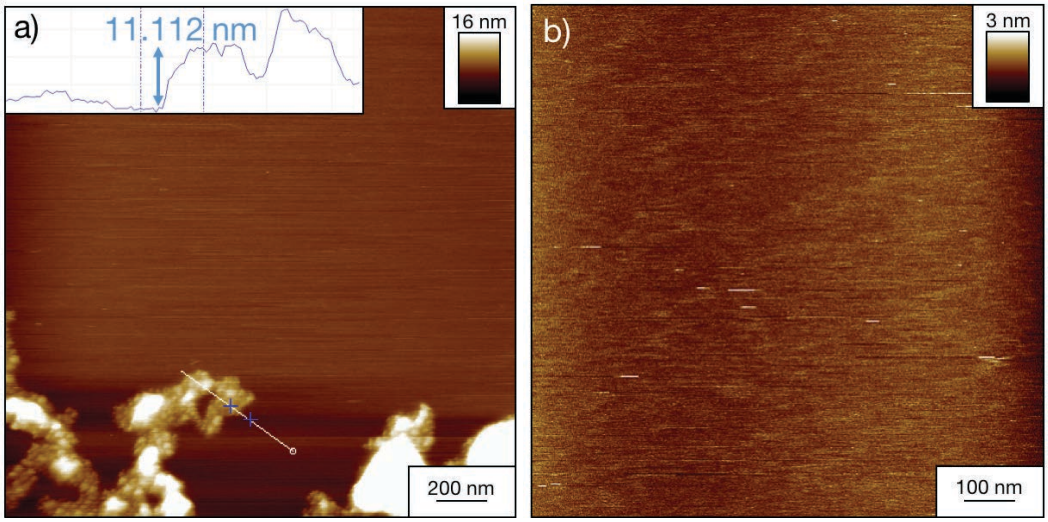

Figure 6.8 **a**, 2 x 2 µm AFM image of the (011) face of a PPh_3O crystal after gold nanoparticle treatment, **b**, expanded view of 1 x 1 µm showing large areas of the surface with no material present.

XPS spectra for the Au 4f region of these samples show no gold present on the surfaces. If gold is present, its concentration is simply not high enough to appear in the spectra (Figure 6.9a). The O 1s region the XPS spectra show the substrate peaks centred at 530.51 eV and 530.50 eV for the (100) and (011) faces respectively (Figure 6.9b). These values have hardly changed from the bare substrate peaks of 530.52 eV and 530.49 eV for the (100) and (011) faces respectively, suggesting no chemisorption has taken place.

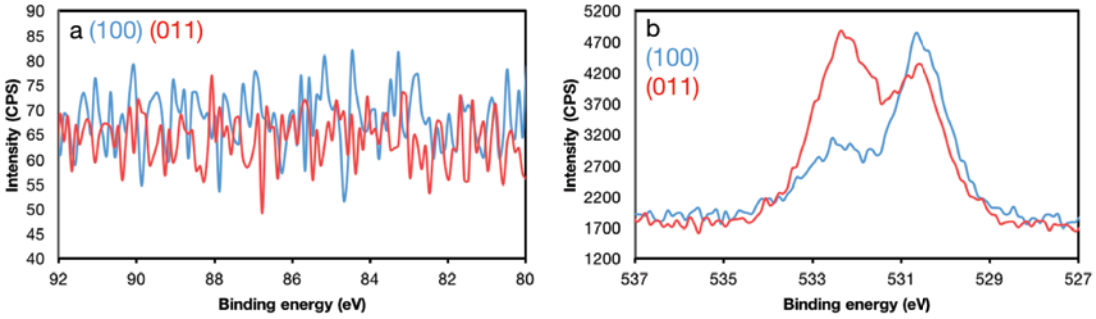

Figure 6.9 High resolution XPS scans of the (100) and (011) faces of PPh_3O crystal after gold nanoparticle treatment, showing **a**, the gold Au 4f region, and **b**, the oxygen O 1s region.

6.2.4 Treatment of Crystals with Au(I) Ions

The next set of experiments were performed using gold ions in place of the nanoparticles. The purpose of using gold ions was to encourage gold binding to every binding site (or as many as possible) forming near monolayer coverage, before a vapour-phase reduction to elemental gold (Au(0)), as a first

step towards potentially creating nanostructures influenced by the order of the crystal structure beneath.

The samples were characterized after the initial Au(I) treatment and again after reduction to Au(0). The Au(I) surface binding experiments took place by immersing the crystal substrates in an aqueous solution of Au(I) created in situ using $HAuCl_4.3H_2O$ and 2,2'-thiodiethanol.

The current resolution limits of commercial AFM instruments do not allow us to directly image individual gold atoms. However, other features may be distinguished and surface roughness may give an indication as to the extent of coverage.

6.2.5 Gold Ions on Triphenylphosphine Sulfide Crystals

Looking at the triphenylphosphine sulfide crystals, the (100) face shows the previously observed steps as well as some particles present at the surface (Figure 6.10a). The surface roughness was measured at 0.56 nm over a 500x500 nm area, suggesting some adsorbed material is present. The particles seen appear in two varieties, with smaller features of up to 10 nm in height and much larger features, potentially contamination, of around 40-50 nm in height (Figure 6.10b). XPS data for this face does show the presence of gold (Figure 6.14a), meaning that these particles are potentially gold which has somehow reduced and formed aggregates.

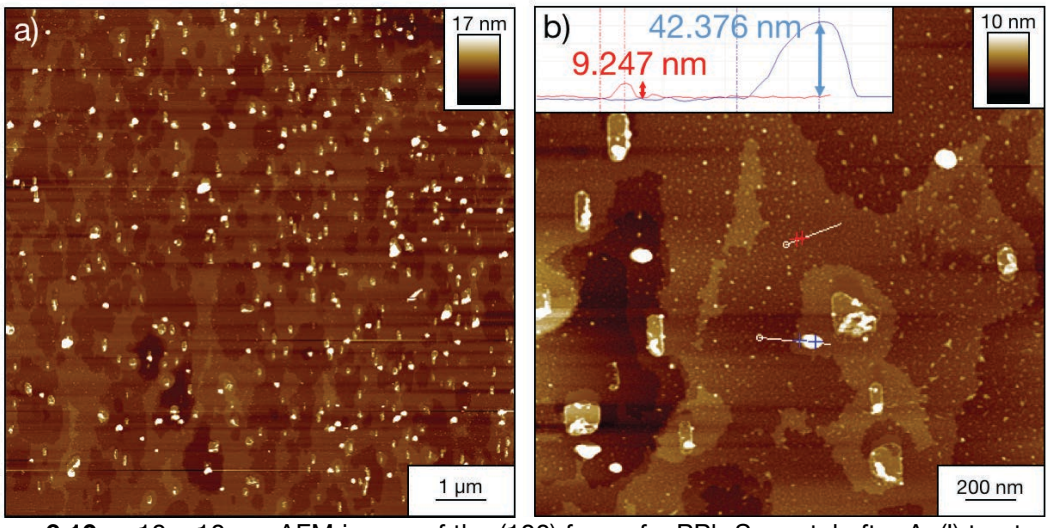

Figure 6.10 a, 10 x 10 µm AFM image of the (100) face of a PPh_3S crystal after Au(I) treatment, **b**, expanded view of 2 x 2 µm showing measured feature heights.

AFM images of the (001) face of this crystal show a much higher and regular coverage of surface features (Figure 6.11a). The surface roughness of 1.36 nm over a 500x500 nm area is also higher. The features here seem to be mostly ~5 nm in height with the occasional large particle possibly due to contamination (Figure 6.11b).

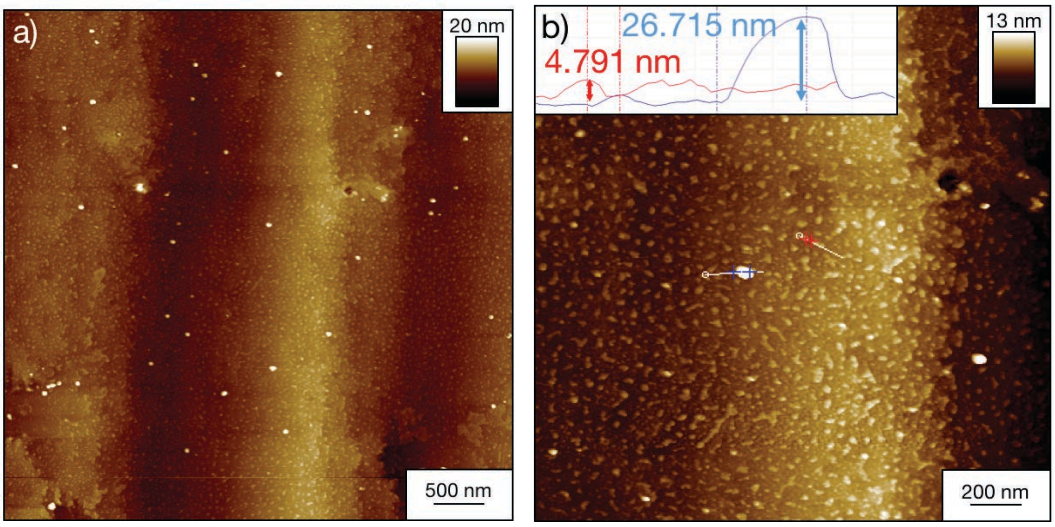

Figure 6.11 **a**, 5 x 5 μm AFM image of the (001) face of a PPh_3S crystal after Au(I) treatment, **b**, expanded view of 2 x 2 μm showing measured feature heights.

The (011) face again shows a high coverage of surface features (Figure 6.12a), with a very high roughness measurement of 1.68 nm over a 500x500 nm area. This is the highest coverage of the three faces and is to be expected as this face presents the most easily accessible binding sites. Features this time seem to be consistently on the 5-10 nm scale in height (Figure 6.12b), this consistency and the presence of gold in the XPS spectrum, suggests that these features are due to our deposited gold which in some areas may have formed aggregates.

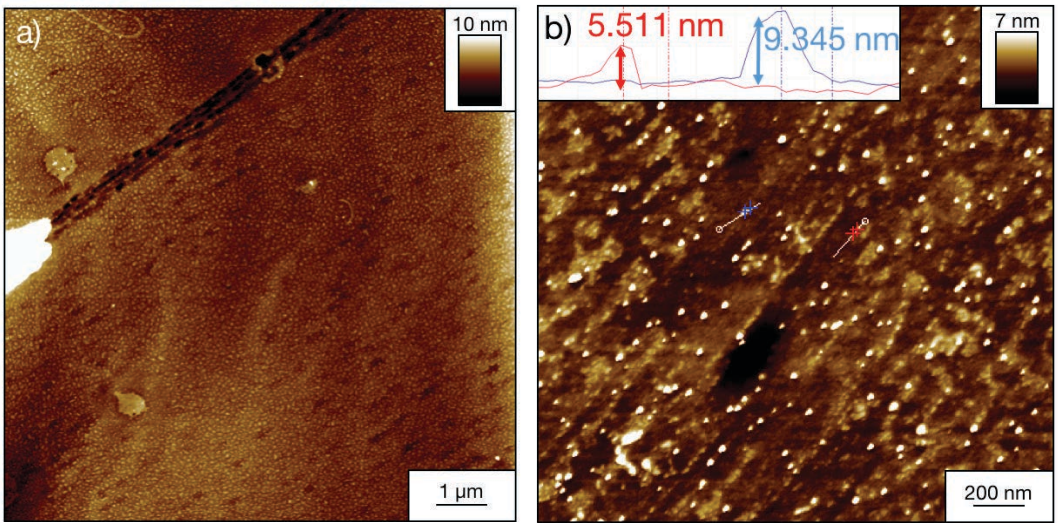

Figure 6.12 a, 10 x 10 µm AFM image of the (011) face of a PPh_3S crystal after Au(I) treatment, **b**, expanded view of 2 x 2 µm showing measured particle heights.

A sample of the Au(I) solution was deposited onto a silicon wafer, creating a reference sample for Au(I). All XPS data here was again charge referenced to the adventitious C 1s peak at 284.80 eV as in chapter 5 and the Au 4f region of the spectrum again shows the two components of Au $4f_{5/2}$ and Au $4f_{7/2}$ with the latter centred at 84.16 eV (Figure 6.13), slightly higher than for the nanoparticles, suggesting gold in this form has a higher oxidation state.

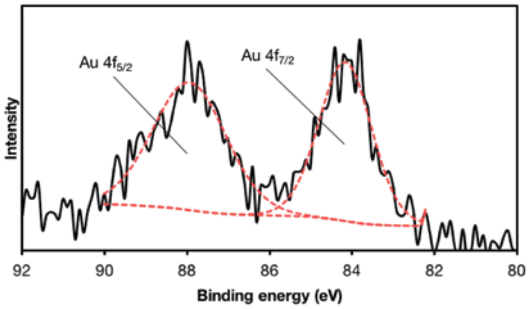

Figure 6.13 High resolution XPS scan of the Au 4f region for the Au(I) reference sample on a silicon substrate.

After treatment with Au(I), XPS was then performed on the (100) and (011) faces of the PPh_3S crystals surfaces. An overlay of spectra for the Au 4f region (Figure 6.14a) shows the Au $4f_{7/2}$ peaks for the (100) and (011) faces centred at 84.83 eV and 84.19 eV respectively. These are also higher than for the nanoparticles, especially for the (100) face showing a similar trend to that of the reference gold sample. The overlay this time shows the intensity of the peaks is higher for the (011) face than for the (100) face, suggesting a higher

amount of gold is present on this face and complementing the AFM data where the (011) face shows the highest concentration of surface particles.

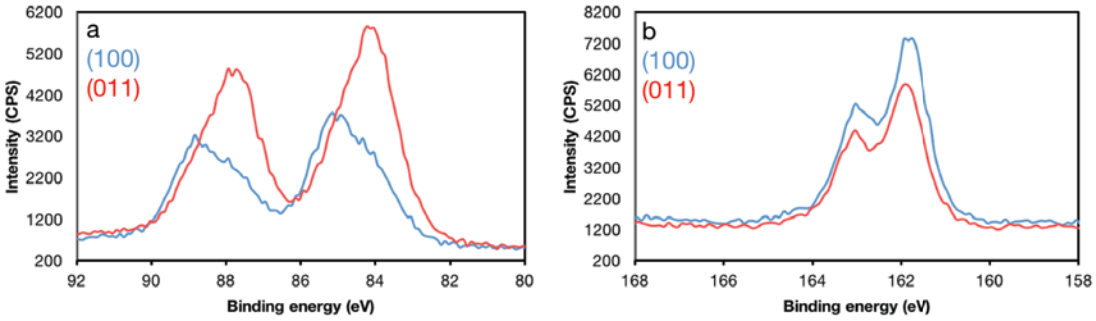

Figure 6.14. High resolution XPS scans of the (100) and (011) faces of PPh_3S crystal after Au(I) treatment, showing **a**, the gold Au 4f region, and **b**, the sulfur S 2p region.

Changes in the S 2p binding energies from the bare crystals seem to be smaller for these samples, where the S $2p_{3/2}$ components are centred at 161.78 eV and 161.83 eV for the (100) and (011) faces respectively (Figure 6.14b). Binding energy for the (100) face is still lower, suggesting chemisorption, but for (011) is slightly higher, possibly suggesting only physisorption here.

6.2.6 Gold Ions on Triphenylphosphine Oxide Crystals

Looking at the triphenylphosphine oxide crystal, the (100) face seems to have quite a low number of new surface features (Figure 6.15a), and has a roughness value of 0.67 nm over a 500x500 nm area. AFM images show very few large features with most measuring on the sub nanometre scale (Figure 6.15b). XPS data however, does indicate the presence of gold at this surface.

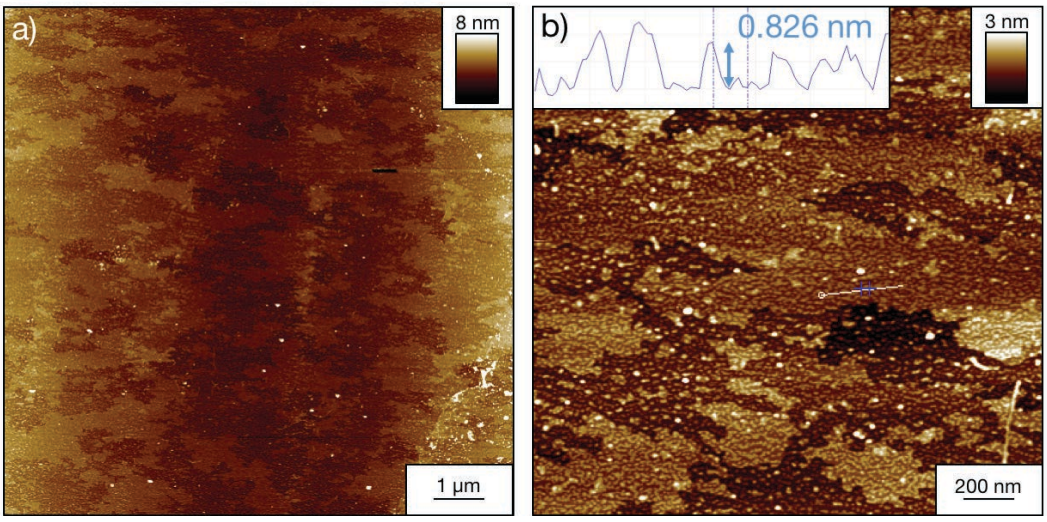

Figure 6.15 a, 10 x 10 µm AFM image of the (100) face of a PPh_3O crystal after Au(I) treatment, **b**, expanded view of 2 x 2 µm showing measured feature heights.

Showing very similar features to that of the (100) face, the (010) face of PPh_3O also shows a low concentration of surface features (Figure 6.16a), with a roughness value of 0.46 nm over a 500x500 nm area. This surface also shows most features at around or below 1 nm (Figure 6.16b), with the occasional large particle clusters possibly due to contamination.

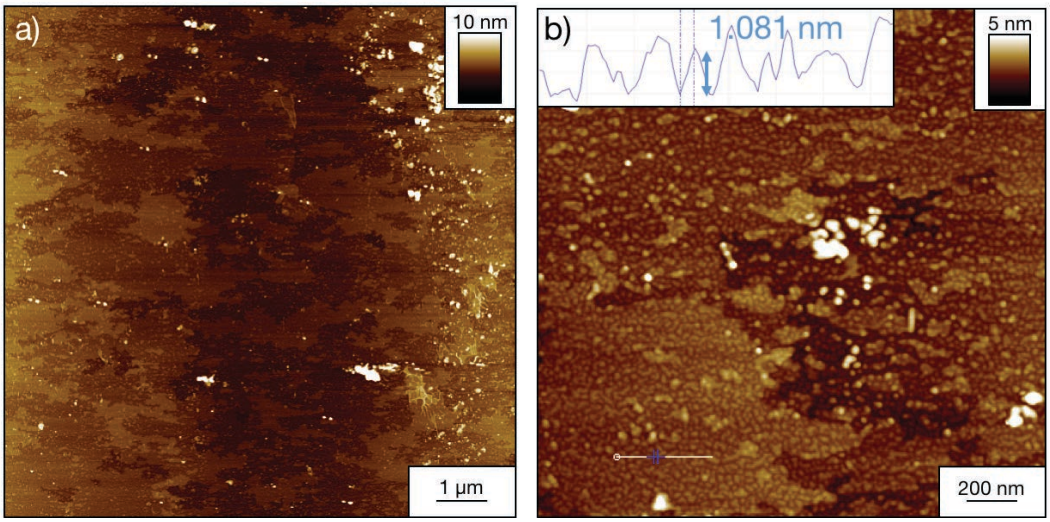

Figure 6.16 a, 10 x 10 µm AFM image of the (010) face of a PPh_3O crystal after Au(I) treatment, **b**, expanded view of 2 x 2 µm showing measured feature heights.

AFM images of the (011) face show an essentially smooth, featureless surface with the only notable features being ~30 and above (Figure 6.17a and b). The surface roughness is also very low (0.16 nm over a 500x500 nm area) and the gold signal in XPS is absent, suggesting little to no gold adsorption. Binding is not expected across any of these faces, but this surface seems to be avoided more so than the others.

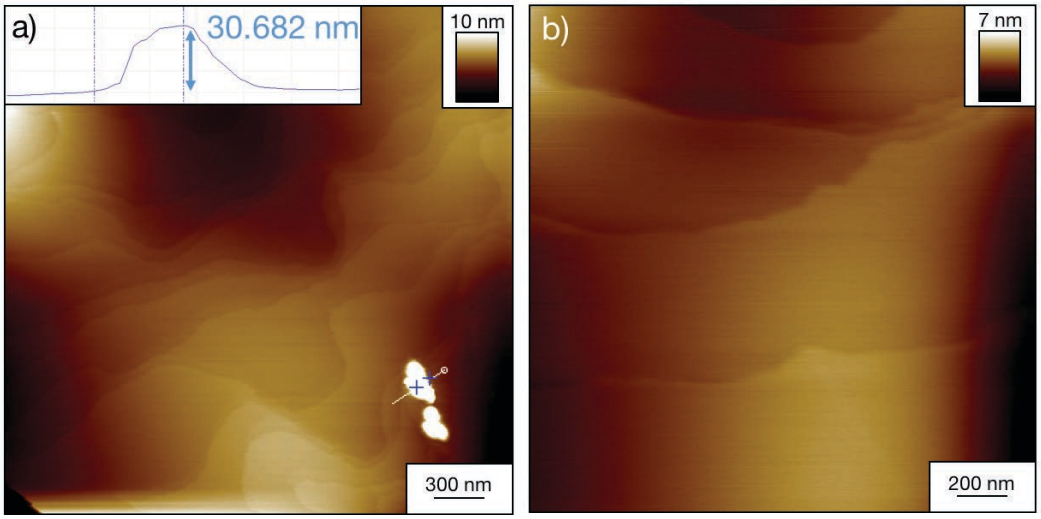

Figure 6.17 a, 3 x 3 µm AFM image of the (011) face of a PPh_3O crystal after Au(I) treatment, **b**, expanded view of 2 x 2 µm showing large areas of the surface with no material present.

XPS for the Au 4f region of these samples show a small amount of gold present on the (100) face and no gold present on the (011) surface (Figure 6.18a), the Au $4f_{7/2}$ peak centres at 84.23 eV for the (100) face, similar in energy to that of the Au(I) reference sample. The O 1s region the XPS spectra show peaks centred at 530.42 eV and 530.38 eV for the (100) and (011) faces respectively (Figure 6.18b). These values are slightly lower than the bare substrate with peaks of 530.52 eV and 530.49 eV for the (100) and (011) faces respectively, but the shifts are too small to confirm binding at the (100) face.

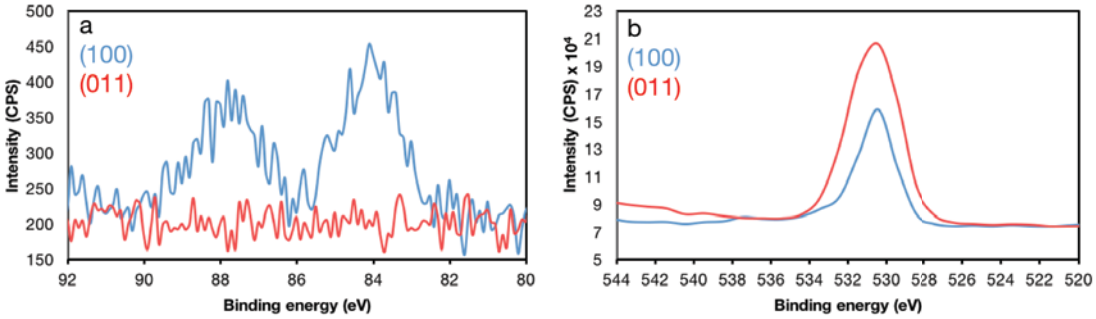

Figure 6.18 High resolution XPS scans of the (100) and (011) faces of PPh_3O crystal after Au(I) treatment, showing **a**, the gold Au 4f region, and **b**, the oxygen O 1s region.

6.2.7 Attempted Reduction of Surface-Bound Gold Ions

After characterization of the crystal surfaces containing Au(I), the samples were then treated with dimethylamino borane (DMAB) vapour in a sealed system in an effort to form aggregated gold species which may form nanostructures. A vapour phase reducing agent was used so as to not disturb the already present Au(I) ions on crystal surfaces, which may detach from the surface when in solution.

6.2.8 Attempted Reduction of Au(I) on Triphenylphosphine Sulfide

Looking at the triphenylphosphine sulfide crystals, on the (100) face, nanoparticles do seem to have formed in a variety of sizes (Figure 6.19a and b) but present no ordered arrangement, this is expected as the sulfur binding sites are not present at this surface to influence an ordered arrangement. The background surface roughness was measured at 0.74 nm over a 500x500 nm area, and the discrete nanoparticles formed give average heights of 5-10 nm (Figure 6.19b) and occasional large particles of ~20-30 nm in height (Fig,

6.19a). XPS data for this face shows a strong gold presence, indicating that these features are gold nanoparticles.

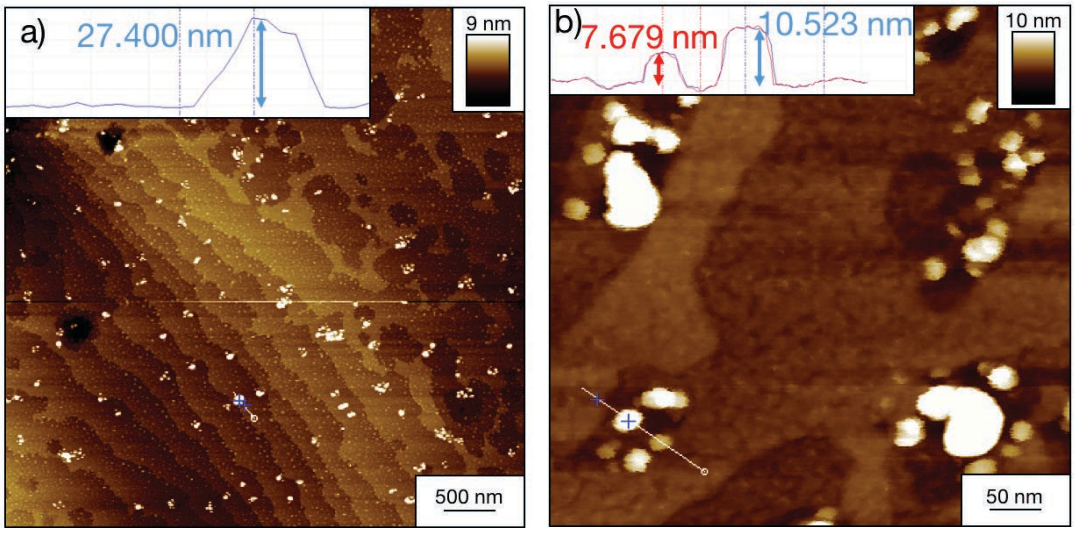

Figure 6.19 a, 5 x 5 µm AFM image of the (100) face of a PPh_3S crystal after reduction to Au(0), **b**, expanded view of 0.5 x 0.5 µm, both showing measured particle heights.

AFM images of the (001) face of this crystal after treatment with DMAB show a much lower number of particles formed (Figure 6.20a) and give a surface roughness of 0.57 nm over a 500x500 nm area. Some large features can be seen on the surface (Figure 6.20b) but the lack of any smaller particles as seen on the previous (100) sample would suggest that these are most likely due to contamination.

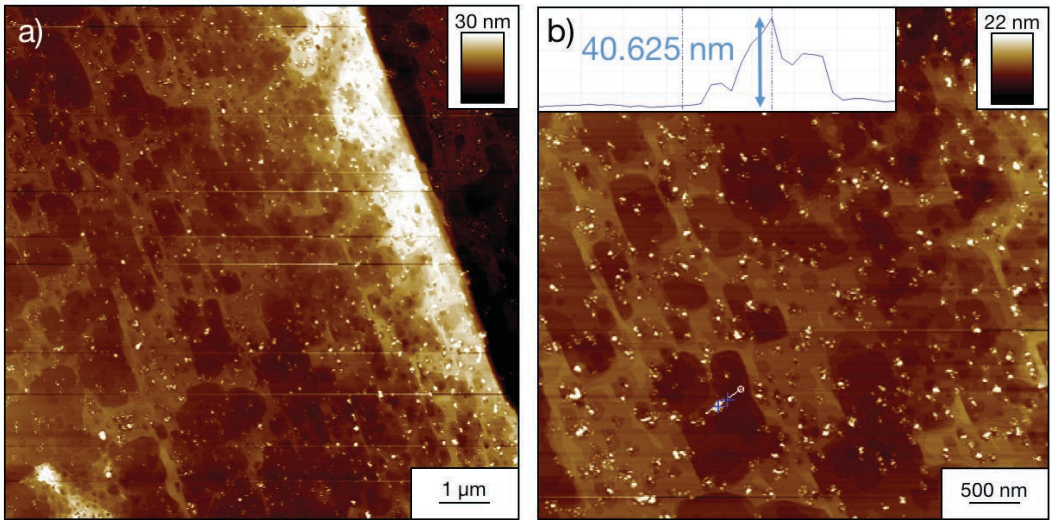

Figure 6.20 a, 10 x 10 µm AFM image of the (001) face of a PPh_3S crystal after reduction to Au(0), **b**, expanded view of 5 x 5 µm showing measured particle heights.

With the sulfur binding sites potentially best presented at the (011) face of this crystal, this surface provides the best chance of both forming gold nanoparticles, and presenting some ordering arrangement. A high density of

particles can be seen by AFM on this substrate (Figure 6.21a) giving a large roughness of 1.92 nm over a 500 x 500 nm area. With XPS confirming the presence of gold on this surface (Figure 6.23a), these features are most likely gold nanoparticles. The feature heights of these particles is very uniform, with most particles measured between 3 and 4 nm (Figure 6.21b). The spacing between particles was measured at ~20-80 nm, much larger than that of the crystal structure, and showing no ordered arrangement provided by the surface.

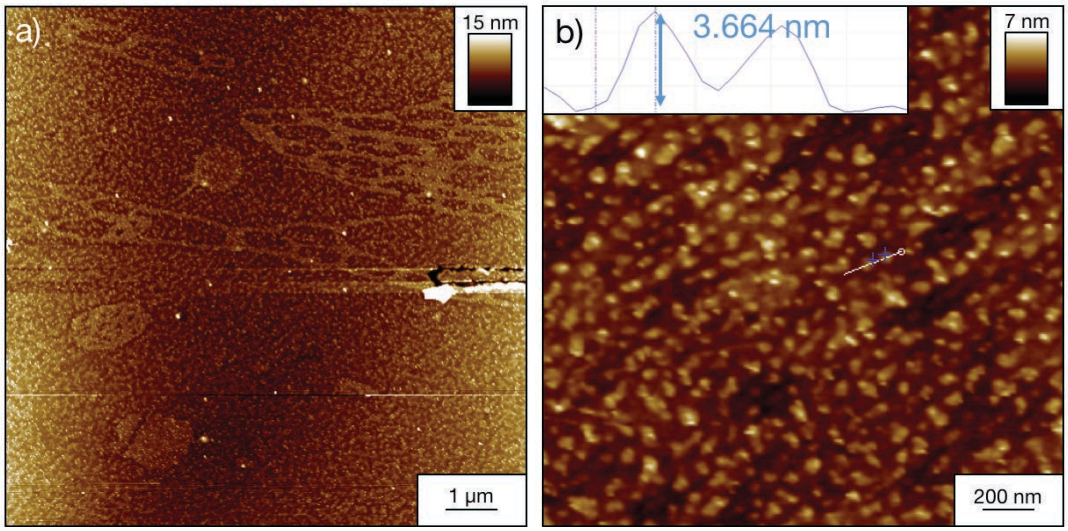

Figure 6.21 a, 10 x 10 µm AFM image of the (011) face of a PPh_3S crystal after reduction to Au(0), **b**, expanded view of 2 x 2 µm showing measured particle heights.

An XPS reference sample for Au(0) was prepared using the same procedure as used to form Au(0) on the crystal surfaces, vapour phase reduction of the previous Au(I) reference sample using DMAB. The data presented here was again all charge referenced to the adventitious C 1s peak at 284.80 eV as in chapter 5. The Au 4f region of this reference sample again showed the two components expected for gold, Au $4f_{5/2}$ and Au $4f_{7/2}$ with the latter centred at 83.89 eV (Figure 6.22). This lowering in binding energy from the Au(I) sample is evidence that a reduction of the gold oxidation state has taken place, producing Au(0).

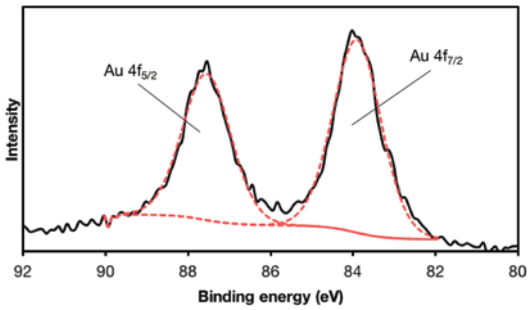

Figure 6.22 High resolution XPS scan of the Au 4f region for the Au(0) reference sample on a silicon substrate.

Now looking at the (100) and (011) faces of the PPh_3S crystals after this vapour phase reducing agent has been used, a lowering in binding energies of the Au $4f_{7/2}$ components is observed (Figure 6.23a), 84.10 eV for the (100) face and 83.97 eV for the (011) face, indicating the gold has indeed been reduced to Au(0). The overlay of spectra shows only a marginal difference in peak intensities with the higher of the two on the (100) face.

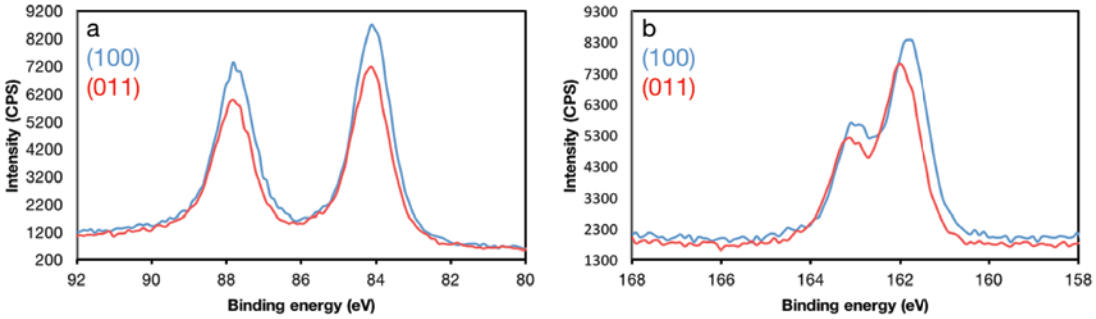

Figure 6.23 High resolution XPS scans of the (100) and (011) faces of PPh_3S crystal after reduction to Au(0), showing **a**, the gold Au 4f region, and **b**, the sulfur S 2p region.

An overlay of spectra for the S 2p region (Figure 6.23b) shows the S $2p_{3/2}$ components centre at 161.81 eV for the (100) face and 161.77 eV for the (011) face, these values are both slightly lower than for the bare crystals, indicating that the gold is chemisorbed onto these surfaces.

6.2.9 Attempted Reduction of Au(I) on Triphenylphosphine Oxide

Looking at the triphenylphosphine oxide crystals now, the (100) face gives a roughness value of 0.49 nm over a 500x500 nm area and shows surface features present of many different heights (Figure 6.24a) with larger particles between 10-15 nm and the more frequent smaller particles ~5 nm in height

(Figure 6.24b). XPS indicates the presence of gold at this surface (Figure 6.27a) which suggests the features observed may well be gold nanoparticles.

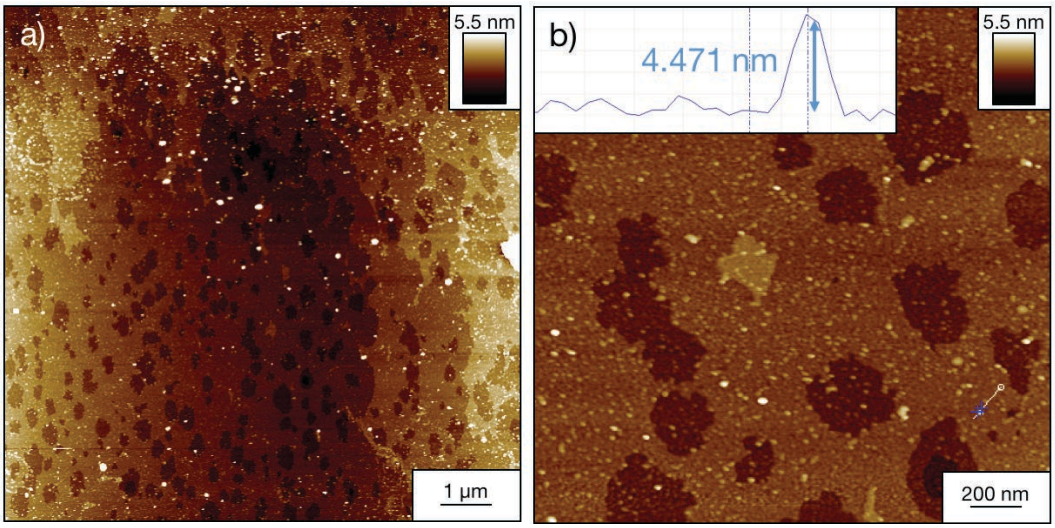

Figure 6.24 a, 10 x 10 µm AFM image of the (100) face of a PPh_3O crystal after reduction to Au(0), **b**, expanded view of 2 x 2 µm showing measured particle heights.

AFM images of the (010) face of this crystal show very little change from that of the Au(I) sample, with a similar roughness value of 0.66 nm over a 500x500 nm area, and few particles found on the surface (Figure 6.25a). This time however there are some larger particles in the range of 4-10 nm in height suggesting some gold particles may have formed as well as some longer nanostructures seen in Figure 6.25b, measuring at ~4 nm in height.

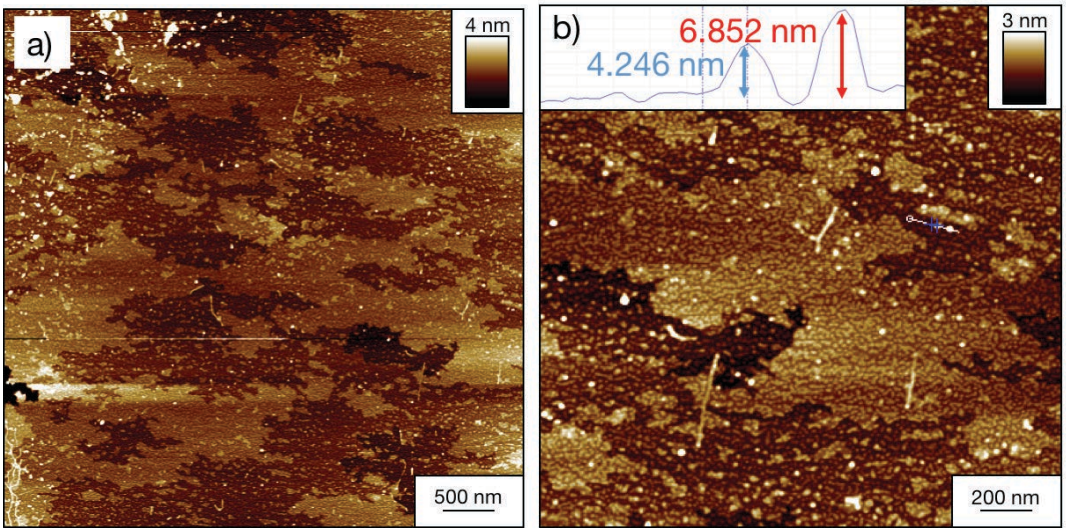

Figure 6.25 a, 5 x 5 µm AFM image of the (010) face of a PPh_3O crystal after reduction to Au(0), **b**, expanded view of 2 x 2 µm showing measured particle heights.

The (011) face of this crystal seemed to deter binding earlier, and this trend has continued through the process as AFM shows some but few surface features (Figure 6.26a). This surface has quite a high roughness value, 1.96 nm over a

500x500 nm area, but looking at the images, this seems to be due to the underlying surface roughness and not a consequence of particle formation. The surface shows fluctuations of less than 1 nm in height (Figure 6.26b).

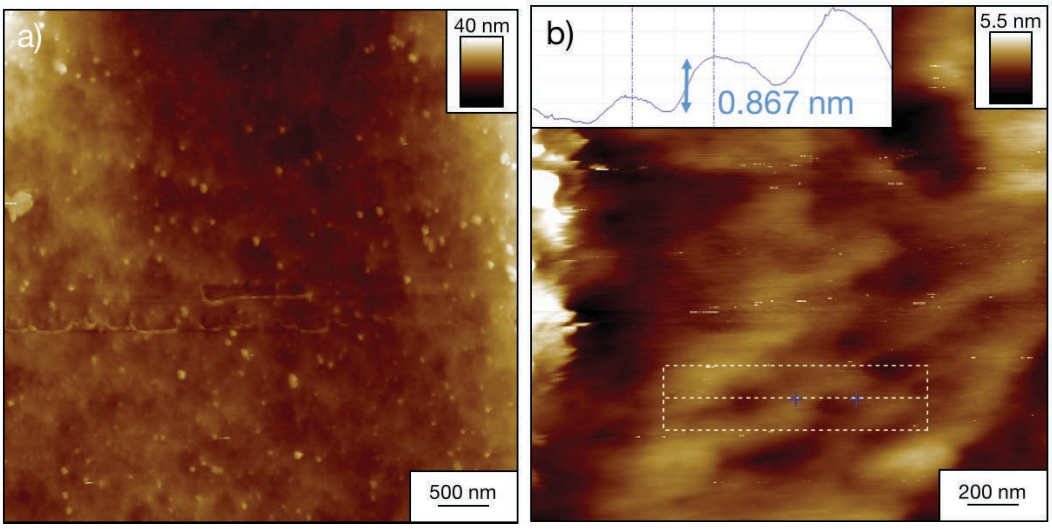

Figure 6.26 **a**, 5 x 5 μm AFM image of the (011) face of a PPh_3O crystal after reduction to Au(0), **b**, expanded view of 2 x 2 μm showing measured feature heights.

The XPS Au 4f region of these samples show a very small amount of gold present on the (100) face and only trace amounts gold present on the (011) surface (Figure 6.27a). The Au $4f_{7/2}$ peaks centre at 84.10 eV for the (100) face, and 84.12 eV for the (011) face, slightly higher than that of the Au(0) reference sample.

The peaks in the O 1s region of the spectra centre at 530.39 eV and 530.29 eV for the (100) and (011) faces respectively (Figure 6.27b). These values are similar to that of the Au(0) samples, where peaks are shifted to a lower binding energy than the bare crystals, indicating something is bound to oxygen, possibly gold.

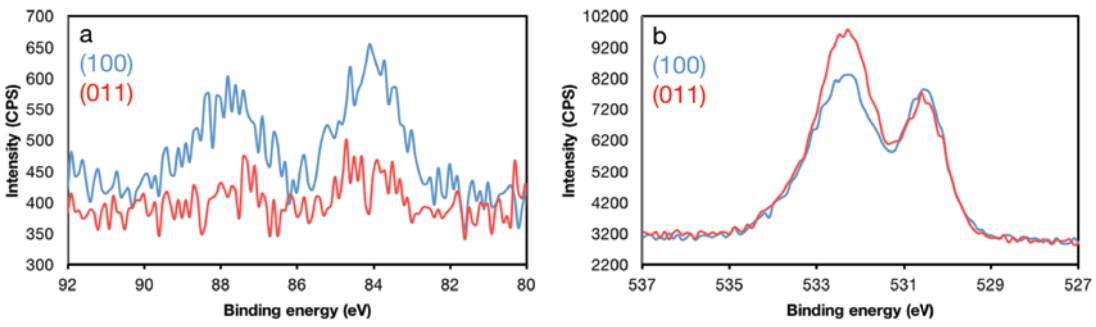

Figure 6.27 High resolution XPS scans of the (100) and (011) faces of PPh_3O crystal after reduction to Au(0), showing **a**, the gold Au 4f region, and **b**, the oxygen O 1s region.

6.3 Conclusions

Firstly, we have shown by AFM and XPS that there is a general preference for gold nanoparticle and gold ion adsorption, onto surfaces of PPh_3S crystals over PPh_3O crystals. These results maybe partly due to the stronger Au-S bonds which may be formed, allowing species to be chemisorbed onto the surface.

AFM and XPS data also suggests face selectivity where binding sites are present or absent at certain faces. The preference for gold ion binding to the (011) face of the PPh_3S crystal, suggests this face is indeed terminated with sulfur atoms. The fact that nanostructures seem to form more easily on this face and pre-formed nanoparticles seem to grow from a seeded position also back this conclusion. Similarly, the preference for gold ions to not bind to the (011) face of the PPh_3O crystal is an indication that this face is not terminated with oxygen binding sites. These experiments show that AFM and XPS coupled with material binding could be used for other systems to determine the natural termination point at crystal faces where alternating layers are present and an absolute answer cannot be determined by other techniques.

Ordered arrays of nanoparticles or nanostructures were not observed here, however nanoscale features of deposited material were observed by AFM, showing nanoparticle island growths on the PPh_3S (011) face after addition of gold nanoparticles, and regularly sized, although randomly scattered particles across the PPh_3S faces.

We have also shown it is possible to reduce crystal surface-bound gold ions to the elemental state using a vapour phase reduction process with DMAB, so as to not disturb any arrangement information passed on by the crystal structure beneath. This reduction process can produce uniform gold nanoparticles on the ~3 nm scale, as seen on the PPh_3S (011) face with Au(0).

6.4 Experimental Details

All chemicals were purchased from Sigma-Aldrich, Alfa Aesar, Fisher Scientific and Nanopartz and were used as received without further purification. AFM was performed on either a Veeco Dimension V microscope with Nanoscope V controller using TappingMode™ or a Bruker Multimode 8 microscope with a Nanoscope V controller using TappingMode™ or PeakForce Tapping™ with

ScanAsyst. Tips used were either Budget Sensors Tap300Al-G silicon tips with resonant frequency = 300 kHz and force constant = 40 N/m or Bruker SCANASYST-FLUID+ silicon nitride tips with resonant frequency = 150 kHz and force constant = 0.7 N/m. AFM analysis was conducted using NanoScope Analysis (Bruker Corporation).

XPS was performed using a Thermo Scientific K-Alpha system with a microfocused, monochromated Al Kα X-ray source. Data analysis was performed using CasaXPS (Casa Software Ltd.).

Crystals were cut using a scalpel and re-oriented for specific face analysis. Samples were mounted using carbon tape on silicon wafers (for AFM) or copper clips (for XPS).

Crystal formation

Crystals of triphenylphosphine sulphide (PPh_3S) and triphenylphosphine oxide (PPh_3O) were produced in the same manner as in Chapter 5, by growing from a concentrated solution in toluene over 3 days.

Gold nanoparticle treatment

Citrate stabilized gold nanoparticles (~2.2 nm, 0.77 μM) were purchased from Nanopartz and were diluted by a factor of 100, i.e. final concentration of 7.7 nM in water. Crystals were then submerged in the solution for 5-10 minutes before being removed, washed with nanopure water for a few seconds and then dried under a flow of nitrogen gas.

Au(I) treatment

Gold thiodiethanol chloride (Au(I)) was formed and used in situ by dissolving $HAuCl_4.3H_2O$ (3.94 mg, 10 μmol) in nanopure water (998 μL) before the addition of 2,2'-thiodiethanol (2 μL, 20 μmol). The yellow solution turned colourless after about one minute, indicating the formation of Au(I). This solution was then diluted by a factor of 100 giving a 0.1 mM solution of AuCl(2,2'-thiodiethanol). Crystals were then submerged in the solution for 5-10 minutes before being washed with nanopure water for a few seconds and finally dried under a flow of nitrogen gas.

Au(0) treatment

Crystal samples which had already undergone the Au(0) deposition were placed in a sealed glass chamber along with solid dimethylamino borane complex (500 mg, 8.49 mmol) in a vial with a perforated lid. The dimethylamino borane vapour was allowed to pass over the sample for ~12 hours before the sample was removed from the chamber ready for analysis.

6.5 References

1. J. V. Barth, G. Costantini and K. Kern, *Nature*, 2005, **437**, 671-679.
2. Y. Fujiki, N. Tokunaga, S. Shinkai and K. Sada, *Angew. Chem. Int. Ed.*, 2006, **45**, 4764-4767.
3. L. Barrientos, P. Allende, C. Orellana and P. Jara, *Inorg. Chim. Acta*, 2012, **380**, 372-377.
4. Y. Fujiki, S. Shinkai and K. Sada, *Cryst. Growth Des.*, 2009, **9**, 2751-2755.
5. M. Haruta and M. Daté, *Appl. Catal., A*, 2001, **222**, 427-437.
6. E. Boisselier and D. Astruc, *Chem. Soc. Rev.*, 2009, **38**, 1759-1782.
7. S. A. Maier, M. L. Brongersma, P. G. Kik, S. Meltzer, A. A. G. Requicha and H. A. Atwater, *Adv. Mater.*, 2001, **13**, 1501-1505.
8. N. Nath and A. Chilkoti, *Anal. Chem.*, 2002, **74**, 504-509.
9. H. Wang, C. S. Levin and N. J. Halas, *J. Am. Chem. Soc.*, 2005, **127**, 14992-14993.
10. A. D. Pomogailo and G. I. Dzhardimalieva, *Nanostructured Materials Preparation via Condensation Ways*, Springer Netherlands, 2014.
11. J. G. Speight, *Lange's Handbook of Chemistry*, McGraw-Hill, 1956.
12. R. Holliday and P. Goodman, *IEE Review*, 2002, **48**, 15-19.
13. H. Hakkinen, *Nat Chem*, 2012, **4**, 443-455.
14. M. S. Hussain and E. O. Schlemper, *Acta Crystallogr. Sect. C: Cryst. Struct. Commun.*, 1987, **43**, 450-453.
15. P. Jones and E. Bembenek, *J. Crystallogr. Spectrosc. Res.*, 1992, **22**, 397-401.
16. Q.-S. Li, C.-Q. Wan, R.-Y. Zou, F.-B. Xu, H.-B. Song, X.-J. Wan and Z.-Z. Zhang, *Inorg. Chem.*, 2006, **45**, 1888-1890.
17. C. E. Housecroft and A. G. Sharpe, *Inorganic Chemistry*, Pearson Education Limited, 2001.
18. K. Aikawa, M. Kojima and K. Mikami, *Angew. Chem. Int. Ed.*, 2009, **48**, 6073-6077.
19. M. Raducan, M. Moreno, C. Bour and A. M. Echavarren, *Chem. Commun.*, 2012, **48**, 52-54.
20. S. M. Kim, J. H. Park and Y. K. Chung, *Chem. Commun.*, 2011, **47**, 6719-6721.
21. L. C. Palmer and S. I. Stupp, *Acc. Chem. Res.*, 2008, **41**, 1674-1684.

Appendix

Unit Cell Dimensions for Single Crystals of 8

Formed from cooling in acetone

Radiation, wavelength	MoKα, λ = 0.71073 Å	
Crystal system, Pearson symbol	Monoclinic, mP	
Unit cell parameters	a = 11.243(16) Å	α = 90°
	b = 4.164(16) Å	β = 102.04(17)°
	c = 13.46(3) Å	γ = 90°
Cell volume	616(3) Å^3	

Formed from cooling in acetonitrile

Radiation, wavelength	MoKα, λ = 0.71073 Å	
Crystal system, Pearson symbol	Monoclinic, mP	
Unit cell parameters	a = 11.213(11) Å	α = 90°
	b = 4.147(5) Å	β = 102.28(7)°
	c = 13.508(9) Å	γ = 90°
Cell volume	614(1) Å^3	

Formed from cooling in toluene

Radiation, wavelength	MoKα, λ = 0.71073 Å	
Crystal system, Pearson symbol	Monoclinic, mP	
Unit cell parameters	a = 11.156(17) Å	α = 90°
	b = 4.144(8) Å	β = 102.51(14)°
	c = 13.54(2) Å	γ = 90°
Cell volume	611(2) Å^3	

Formed from cooling in ethanol

Radiation, wavelength	MoKα, λ = 0.71073 Å	
Crystal system, Pearson symbol	Monoclinic, mP	
Unit cell parameters	a = 11.198(12) Å	α = 90°
	b = 4.143(7) Å	β = 102.45(12)°
	c = 13.51(2) Å	γ = 90°
Cell volume	612(2) Å^3	

Formed from cooling in water

Radiation, wavelength	MoKα, λ = 0.71073 Å	
Crystal system, Pearson symbol	Monoclinic, mP	
Unit cell parameters	a = 11.191(4) Å	α = 90°
	b = 4.233(5) Å	β = 102.918(6)°
	c = 13.634(5) Å	γ = 90°
Cell volume	614(4) Å^3	

Formed from evaporation of toluene (forms polymorph)

Radiation, wavelength	MoKα, λ = 0.71073 Å	
Crystal system, Pearson symbol	Monoclinic, mP	
Unit cell parameters	a = 5.8191(4) Å	α = 90°
	b = 7.2333(5) Å	β = 95.918(6)°
	c = 7.6349(5) Å	γ = 90°
Cell volume	308.87(4) Å^3	

Formed from cooling of a melt

Radiation, wavelength	MoKα, λ = 0.71073 Å	
Crystal system, Pearson symbol	Monoclinic, mP	
Unit cell parameters	a = 11.12(5) Å	α = 90°
	b = 4.163(9) Å	β = 102.4(3)°
	c = 13.51(3) Å	γ = 90°
Cell volume	611(3) Å^3	

Unit Cell Dimensions for Single Crystals of 9

Formed from cooling in acetone

Radiation, wavelength	MoKα, λ = 0.71073 Å	
Crystal system, Pearson symbol	Monoclinic, mP	
Unit cell parameters	a = 11.466 (19) Å	α = 90°
	b = 4.737(13) Å	β = 92.65(17)°
	c = 12.77(3) Å	γ = 90°
Cell volume	693(3) Å^3	

Formed from cooling in acetonitrile

Radiation, wavelength	MoKα, λ = 0.71073 Å	
Crystal system, Pearson symbol	Monoclinic, mP	
Unit cell parameters	a = 7.043(10) Å	α = 90°
	b = 6.107(9) Å	β = 95.86(6)°
	c = 16.51(2) Å	γ = 90°
Cell volume	706(2) Å^3	

Formed from cooling in toluene

Radiation, wavelength	MoKα, λ = 0.71073 Å	
Crystal system, Pearson symbol	Monoclinic, mP	
Unit cell parameters	a = 7.074(8) Å	α = 90°
	b = 6.082(12) Å	β = 96.03(9)°
	c = 16.56(5) Å	γ = 90°
Cell volume	709(3) Å^3	

Formed from cooling in ethanol

Radiation, wavelength	MoKα, λ = 0.71073 Å

Crystal system, Pearson symbol	Monoclinic, mP	
Unit cell parameters	a = 7.047(10) Å	α = 90°
	b = 6.112(8) Å	β = 95.48(10)°
	c = 16.516(16) Å	γ = 90°
Cell volume	786.7(8) Å^3	

Formed from cooling in ethyl acetate

Radiation, wavelength	MoKα, λ = 0.71073 Å	
Crystal system, Pearson symbol	Monoclinic, mP	
Unit cell parameters	a = 7.063(8) Å	α = 90°
	b = 6.126(8) Å	β = 95.81(5)°
	c = 16.54(3) Å	γ = 90°
Cell volume	712(2) Å^3	

Formed from evaporation of acetone

Radiation, wavelength	MoKα, λ = 0.71073 Å	
Crystal system, Pearson symbol	Monoclinic, mP	
Unit cell parameters	a = 11.438(15) Å	α = 90°
	b = 4.703(12) Å	β = 92.54(13)°
	c = 12.83(3) Å	γ = 90°
Cell volume	689(2) Å^3	

Formed from evaporation of toluene

Radiation, wavelength	MoKα, λ = 0.71073 Å	
Crystal system, Pearson symbol	Monoclinic, mP	
Unit cell parameters	a = 11.45(2) Å	α = 90°
	b = 4.712(10) Å	β = 92.55(14)°
	c = 12.83(2) Å	γ = 90°
Cell volume	691(2) Å^3	

Formed from evaporation of ethyl acetate

Radiation, wavelength	MoKα, λ = 0.71073 Å	
Crystal system, Pearson symbol	Monoclinic, mP	
Unit cell parameters	a = 7.082(5) Å	α = 90°
	b = 6.087(16) Å	β = 95.71(7)°
	c = 16.54(2) Å	γ = 90°
Cell volume	709(2) Å^3	

Formed from cooling of a melt

Radiation, wavelength	MoKα, λ = 0.71073 Å	
Crystal system, Pearson symbol	Monoclinic, mP	

Unit cell parameters	a = 7.054(12) Å	α = 90°
	b = 6.110(4) Å	β = 95.96(14)°
	c = 16.50(3) Å	γ = 90°
Cell volume	707(2) Å^3	

Unit Cell Dimensions for Single Crystals of 10

Formed from cooling in acetonitrile

Radiation, wavelength	MoKα, λ = 0.71073 Å	
Crystal system, Pearson symbol	Monoclinic, mP	
Unit cell parameters	a = 6.057(8) Å	α = 90°
	b = 5.588(7) Å	β = 93.61(10)°
	c = 23.26(3) Å	γ = 90°
Cell volume	786(2) Å^3	

Formed from cooling in toluene

Radiation, wavelength	MoKα, λ = 0.71073 Å	
Crystal system, Pearson symbol	Monoclinic, mP	
Unit cell parameters	a = 6.074(5) Å	α = 90°
	b = 5.596(4) Å	β = 93.68(6)°
	c = 23.275(16) Å	γ = 90°
Cell volume	789(1) Å^3	

Formed from cooling in ethyl acetate

Radiation, wavelength	MoKα, λ = 0.71073 Å	
Crystal system, Pearson symbol	Monoclinic, mP	
Unit cell parameters	a = 6.064(7) Å	α = 90°
	b = 5.578(6) Å	β = 93.74(9)°
	c = 23.29(2) Å	γ = 90°
Cell volume	786(4) Å^3	

Formed from cooling in methanol

Radiation, wavelength	MoKα, λ = 0.71073 Å	
Crystal system, Pearson symbol	Monoclinic, mP	
Unit cell parameters	a = 6.061(4) Å	α = 90°
	b = 5.586(3) Å	β = 93.80(5)°
	c = 23.286(12) Å	γ = 90°
Cell volume	786.7(8) Å^3	

Formed from evaporation of acetone

Radiation, wavelength	MoKα, λ = 0.71073 Å	
Crystal system, Pearson symbol	Monoclinic, mP	
Unit cell parameters	a = 6.062(5) Å	α = 90°
	b = 5.603(6) Å	β = 93.75(5)°
	c = 23.268(11) Å	γ = 90°

Cell volume	789(1) Å^3

Formed from evaporation of toluene

Radiation, wavelength	MoKα, λ = 0.71073 Å	
Crystal system, Pearson symbol	Monoclinic, mP	
Unit cell parameters	a = 6.069(4) Å	α = 90°
	b = 5.591(3) Å	β = 93.54(6)°
	c = 23.268(17) Å	γ = 90°
Cell volume	787.9(9) Å^3	

Formed from evaporation of ethyl acetate

Radiation, wavelength	MoKα, λ = 0.71073 Å	
Crystal system, Pearson symbol	Monoclinic, mP	
Unit cell parameters	a = 6.066(8) Å	α = 90°
	b = 5.586(7) Å	β = 93.71(11)°
	c = 23.35(3) Å	γ = 90°
Cell volume	789(2) Å^3	

Formed from evaporation of methanol

Radiation, wavelength	MoKα, λ = 0.71073 Å	
Crystal system, Pearson symbol	Monoclinic, mP	
Unit cell parameters	a = 6.080(5) Å	α = 90°
	b = 5.594(5) Å	β = 93.72(6)°
	c = 23.297(12) Å	γ = 90°
Cell volume	791(1) Å^3	

Formed from addition of water anti-solvent in methanol

Radiation, wavelength	MoKα, λ = 0.71073 Å	
Crystal system, Pearson symbol	Monoclinic, mP	
Unit cell parameters	a = 6.063(5) Å	α = 90°
	b = 5.585(3) Å	β = 93.65(5)°
	c = 23.306(14) Å	γ = 90°
Cell volume	787(9) Å^3	

Formed from cooling of a melt

Radiation, wavelength	MoKα, λ = 0.71073 Å	
Crystal system, Pearson symbol	Monoclinic, mP	
Unit cell parameters	a = 6.076(6) Å	α = 90°
	b = 5.589(4) Å	β = 93.67(7)°
	c = 23.265(18) Å	γ = 90°
Cell volume	788(1) Å^3	

X-ray Powder Diffraction Patterns for Microcrystalline/Powders of 8

Formed from evaporation of acetone

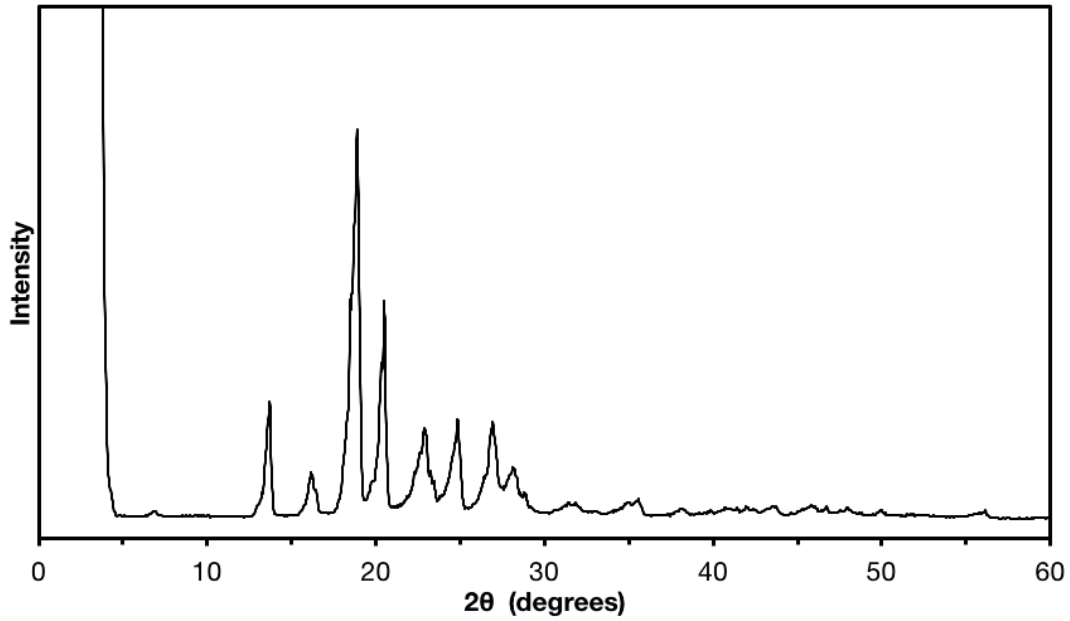

Formed from evaporation of acetonitrile

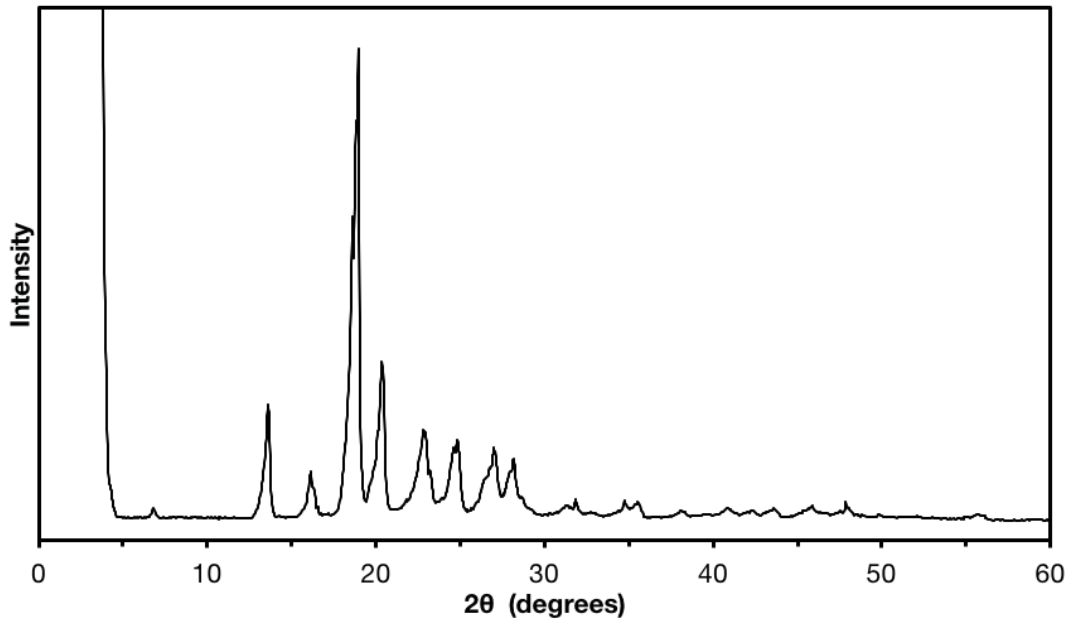

Formed from evaporation of ethanol

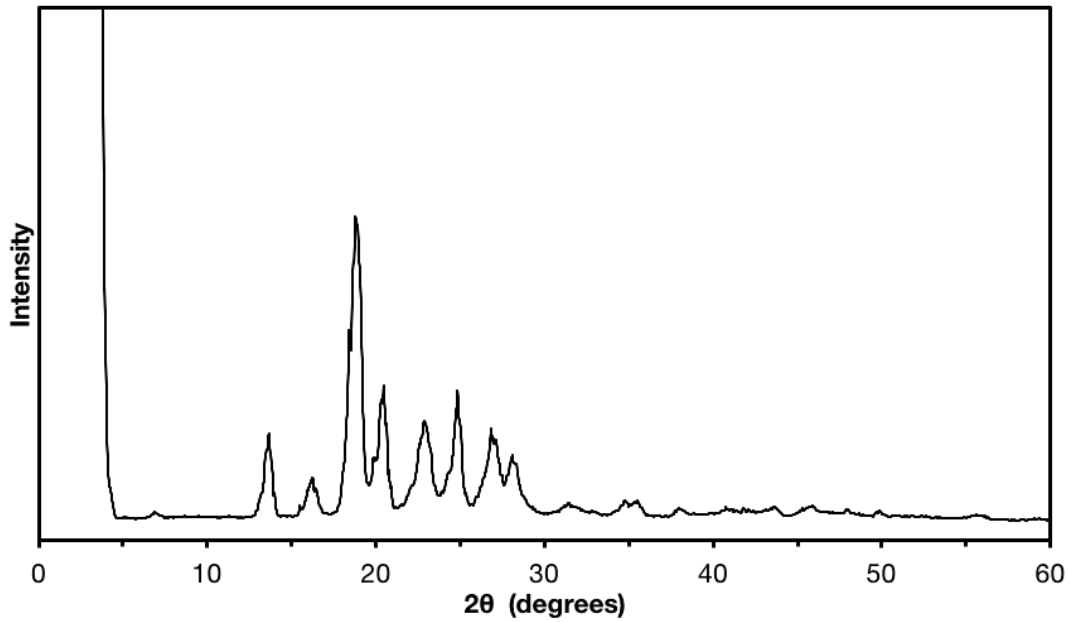

Formed from evaporation of water

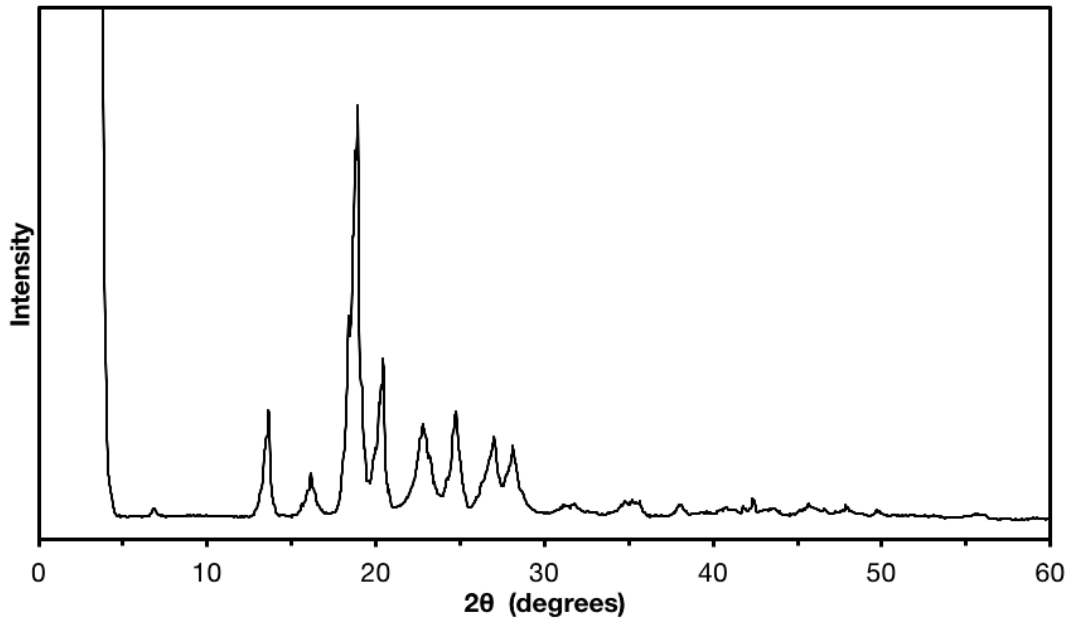

Formed from addition of diethyl ether anti-solvent in acetone

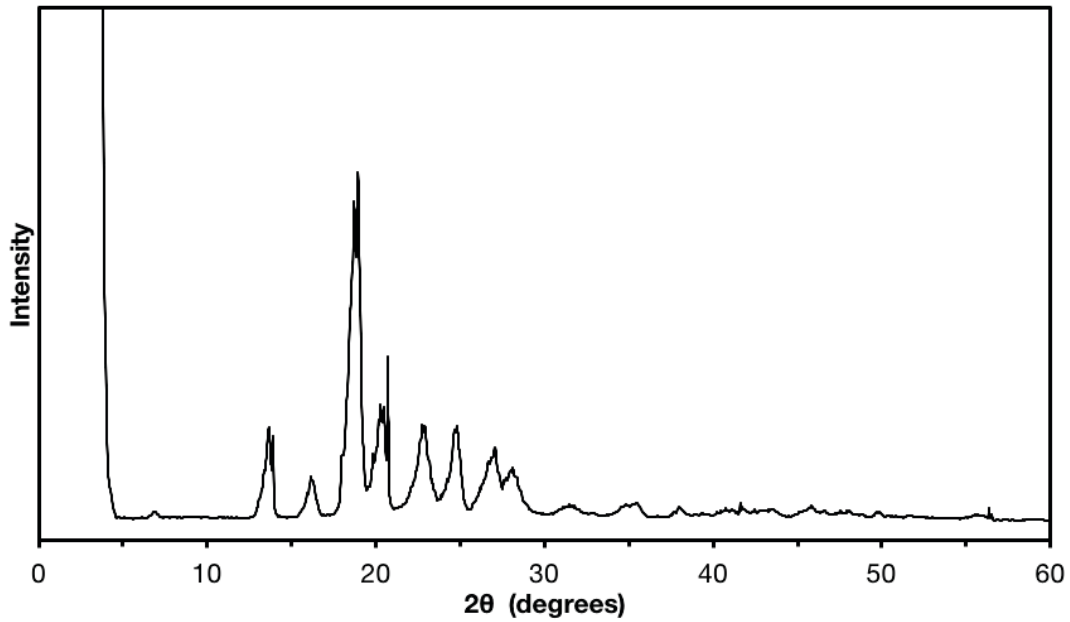

Formed from addition of diethyl ether anti-solvent in acetonitrile

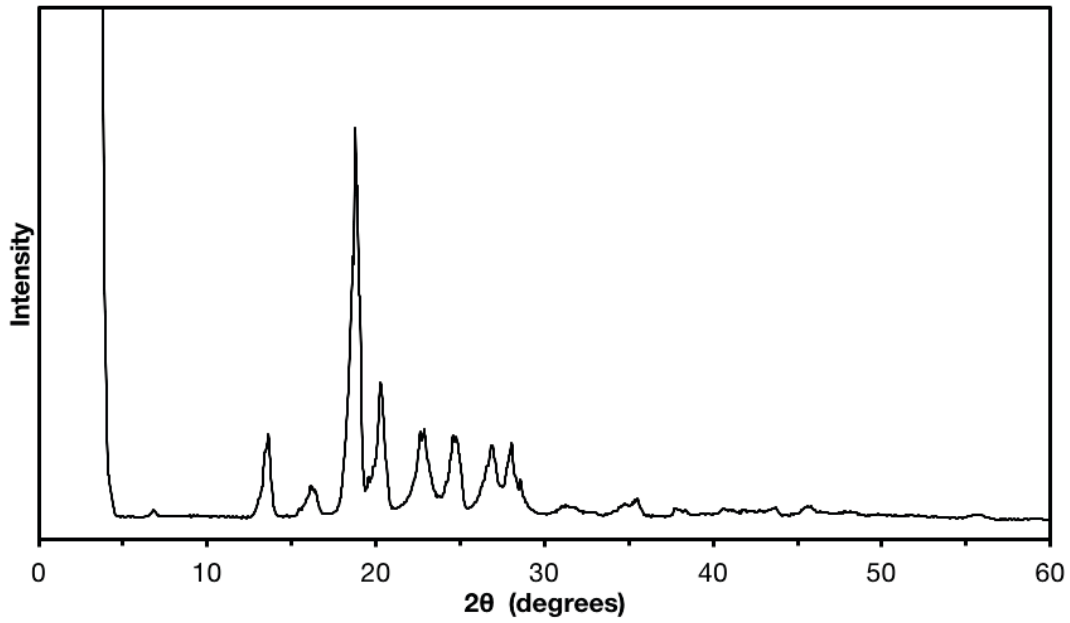

Formed from addition of diethyl ether anti-solvent in toluene

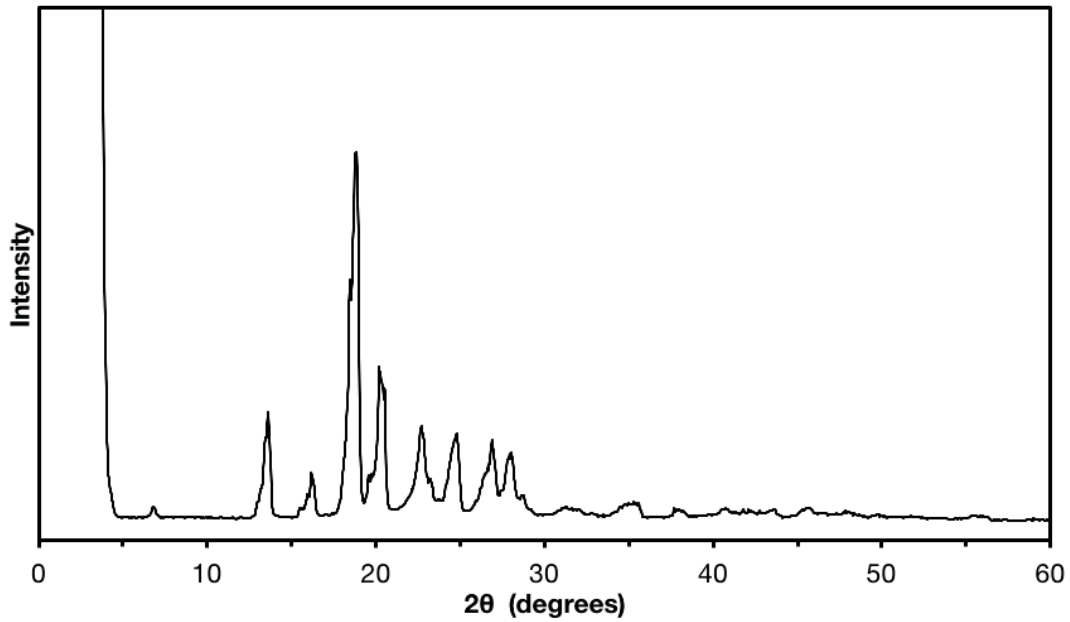

Formed from addition of diethyl ether anti-solvent in ethanol

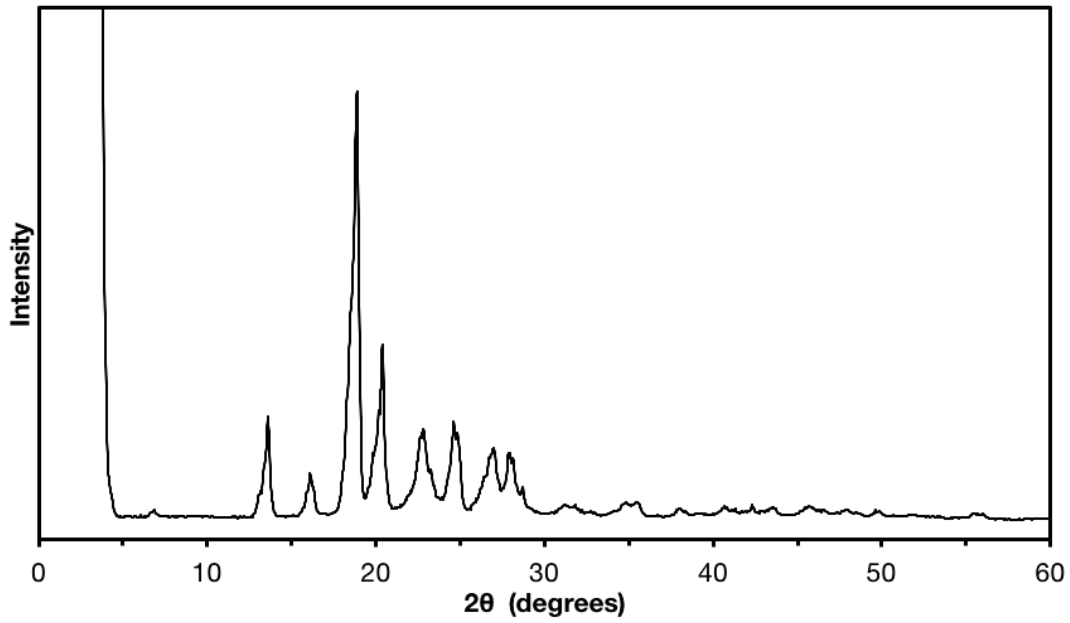

Formed from addition of THF anti-solvent in water

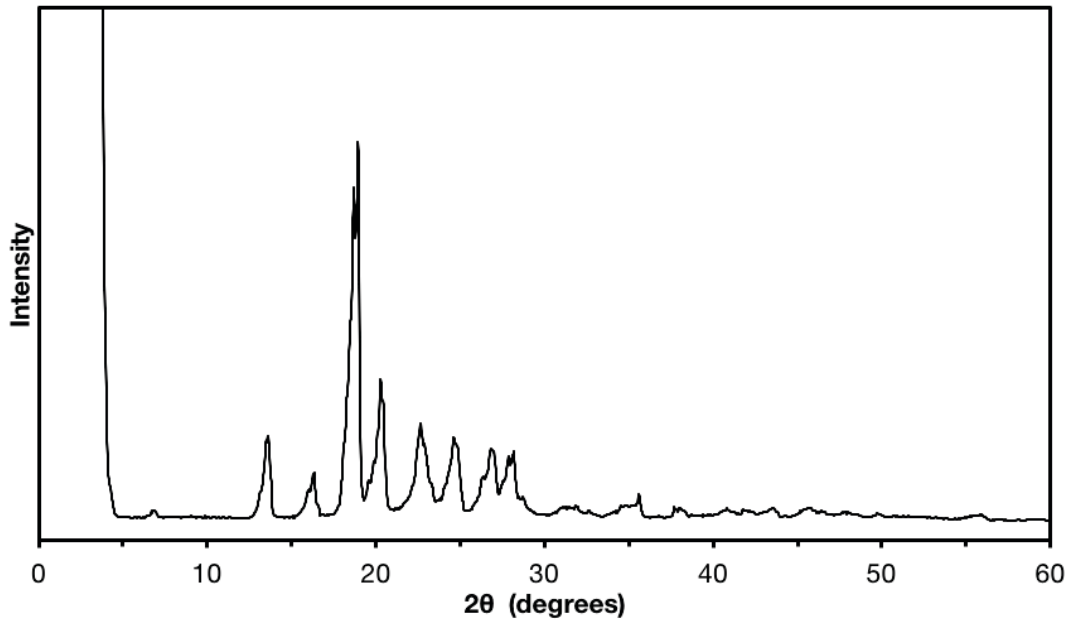

X-ray Powder Diffraction Patterns for Microcrystalline/Powders of 9

Formed from evaporation of acetonitrile

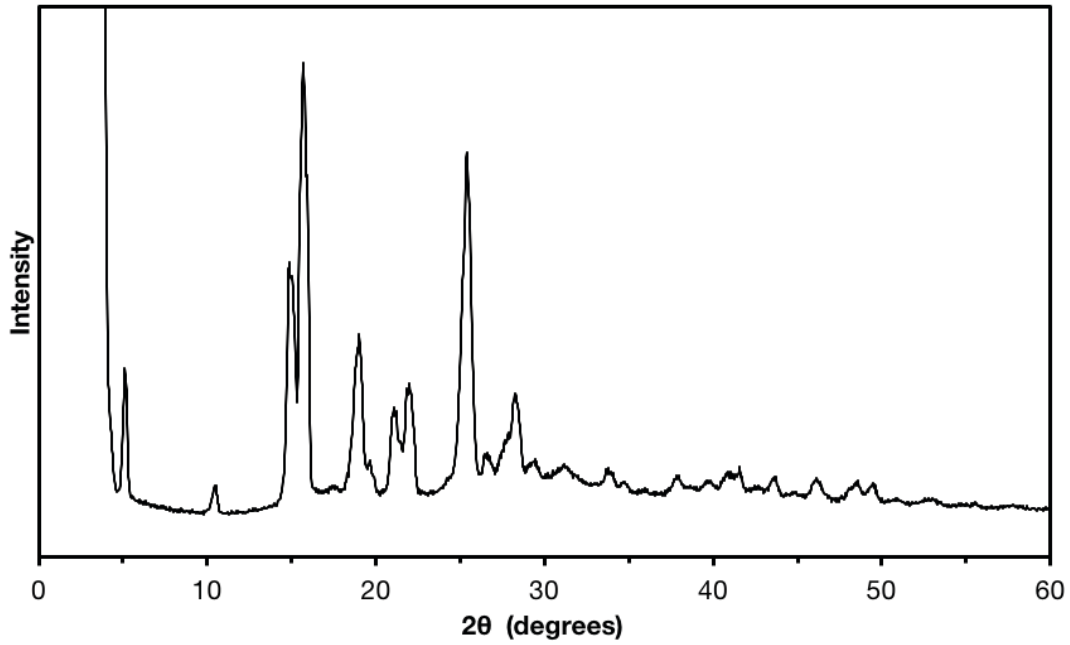

Formed from addition of water anti-solvent in acetone

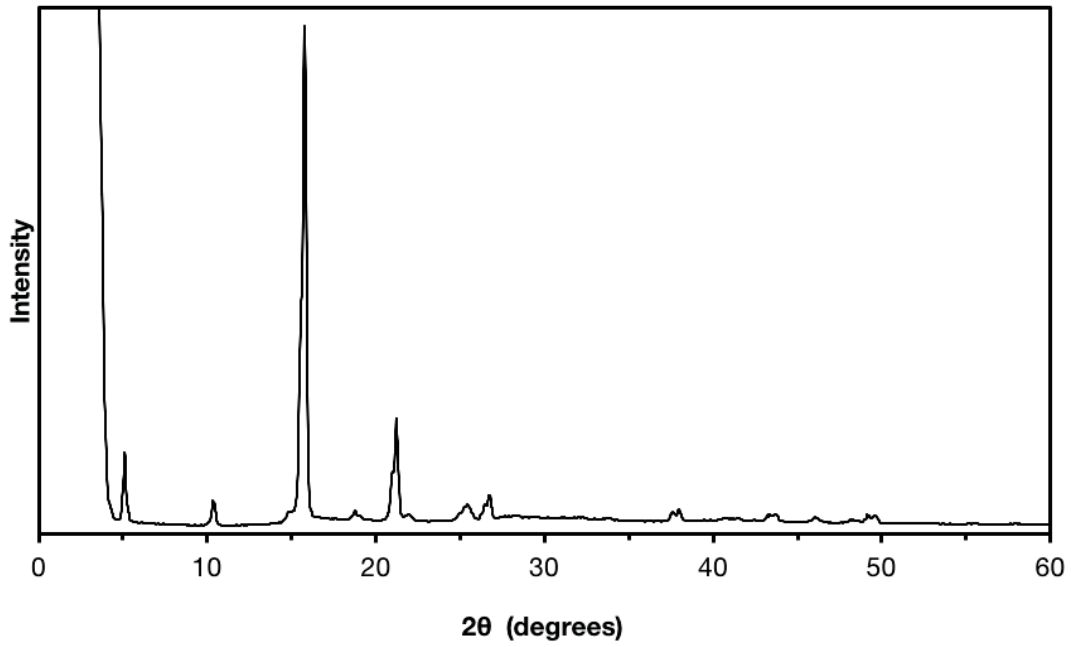

Formed from addition of water anti-solvent in acetonitrile

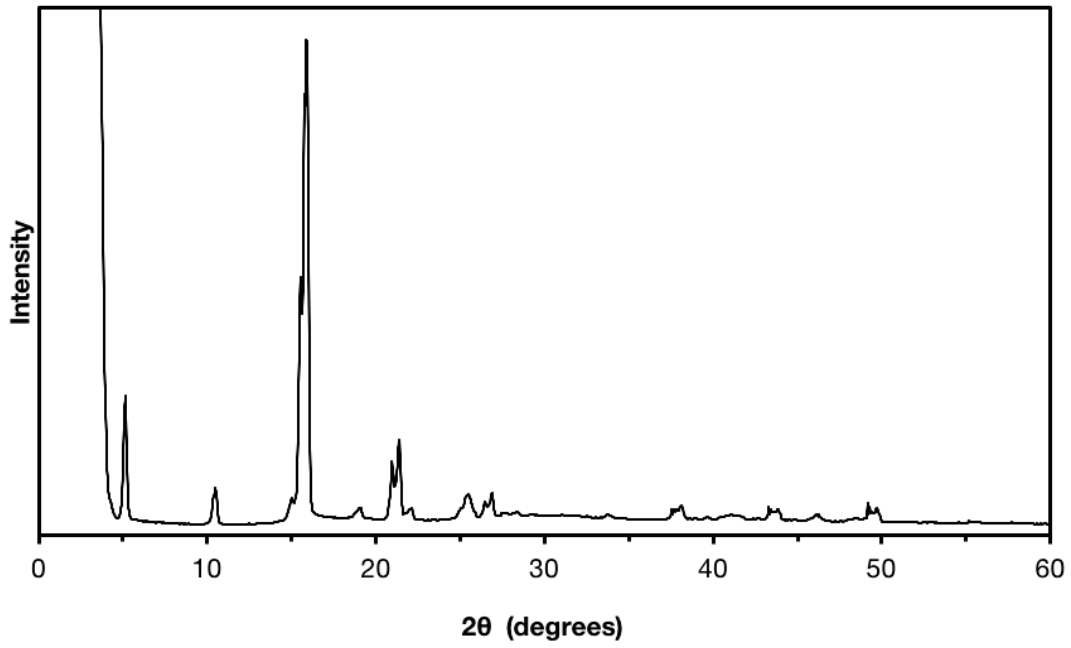

Formed from addition of THF anti-solvent in toluene

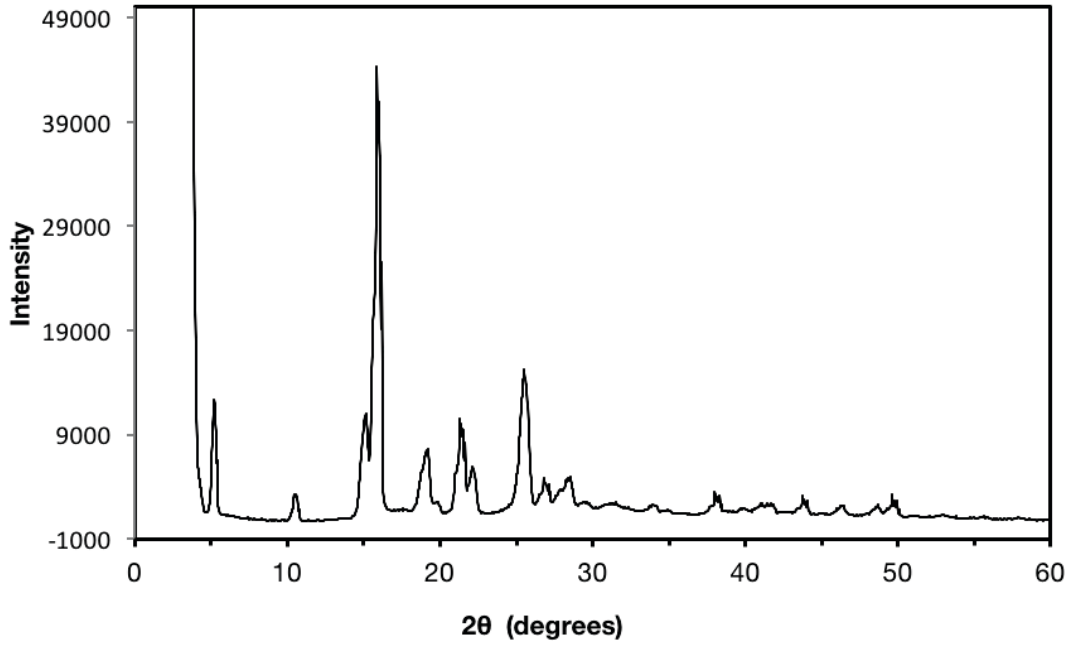

Formed from addition of water anti-solvent in ethanol

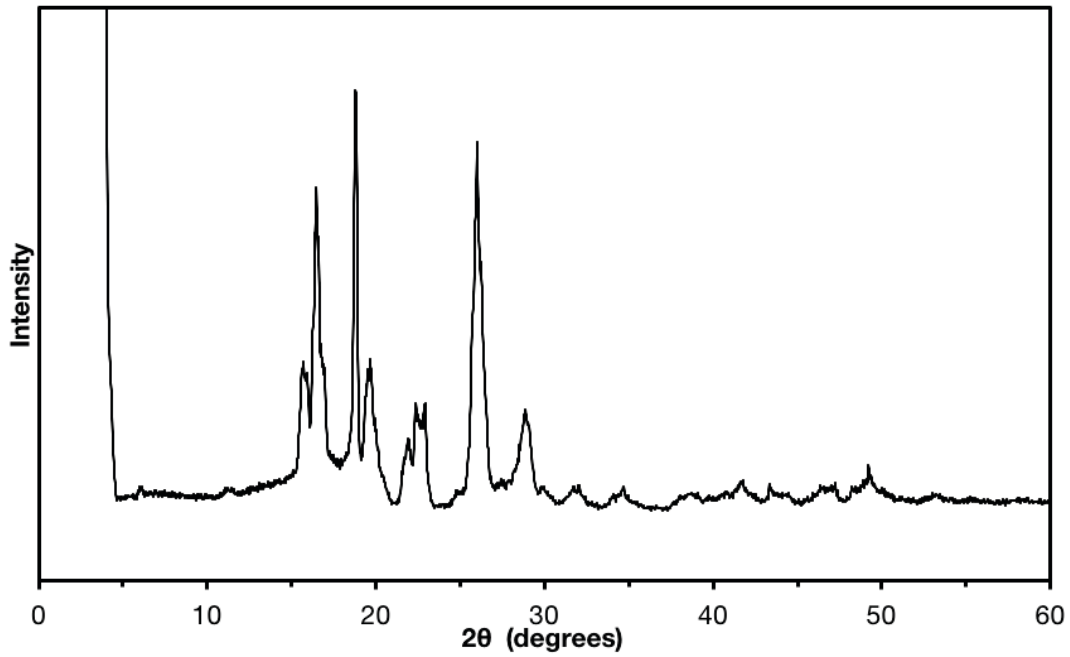

Formed from addition of THF anti-solvent in ethyl acetate

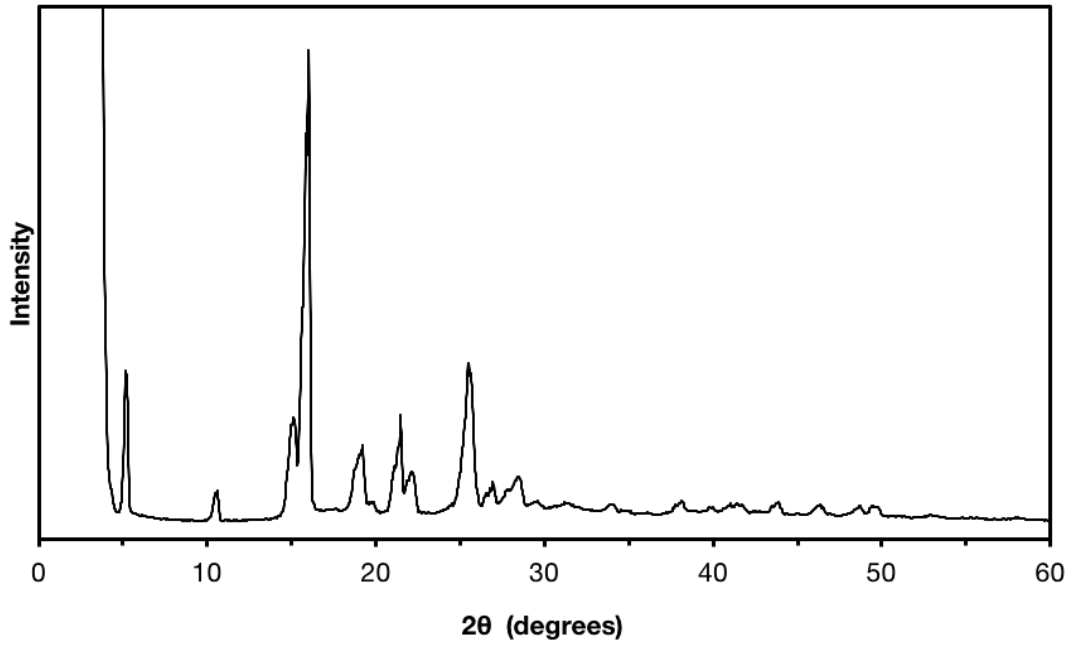

X-ray Powder Diffraction Patterns for Microcrystalline/Powders of 10

Formed from evaporation of acetonitrile

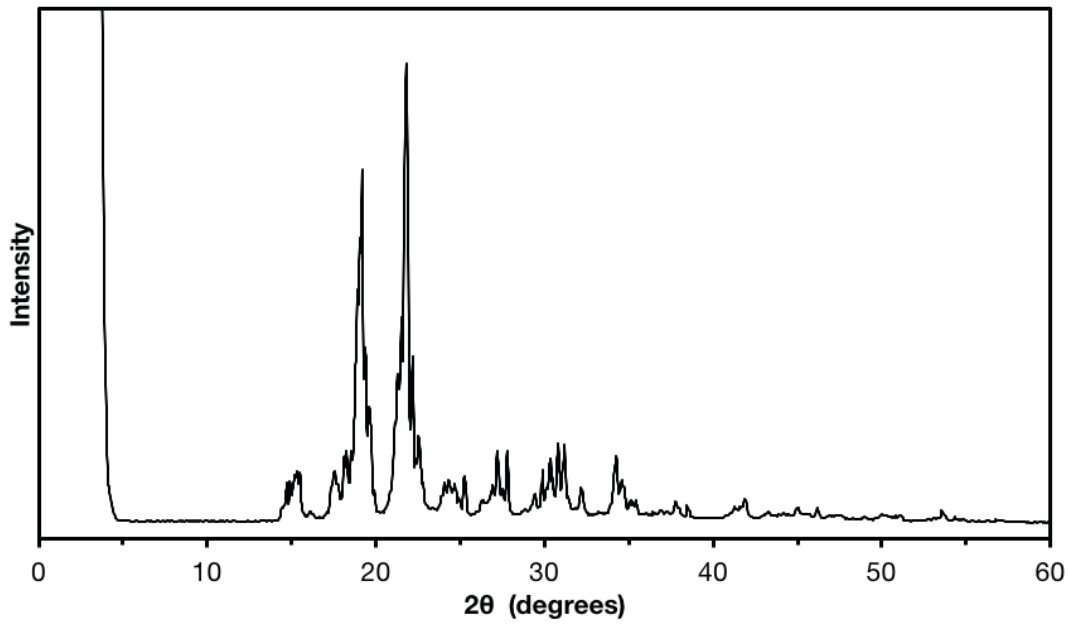

Formed from addition of water anti-solvent in acetone

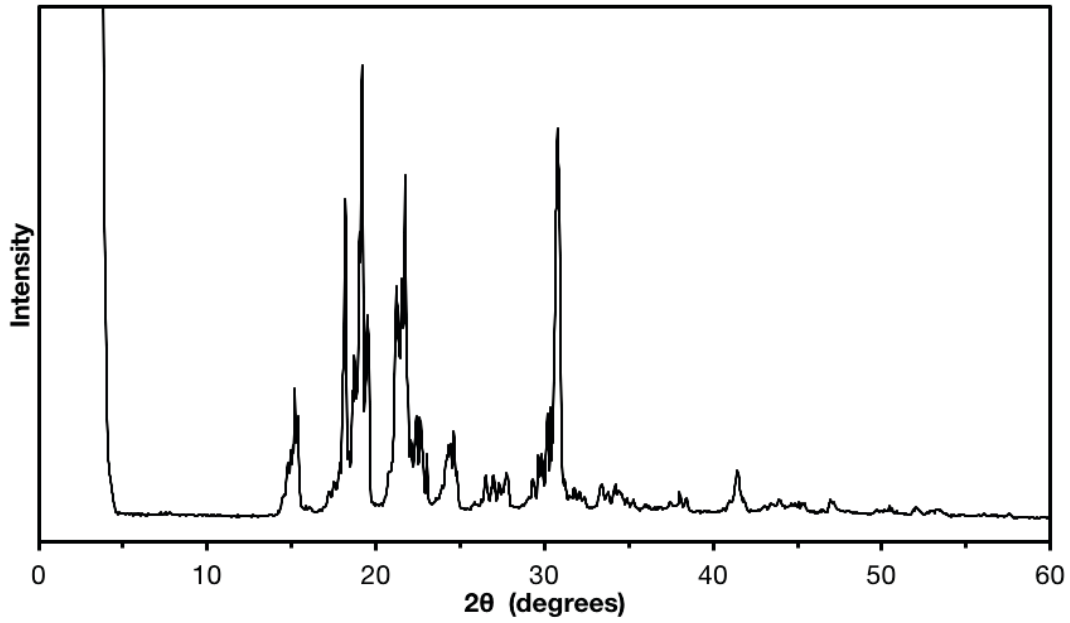

Formed from addition of water anti-solvent in acetonitrile

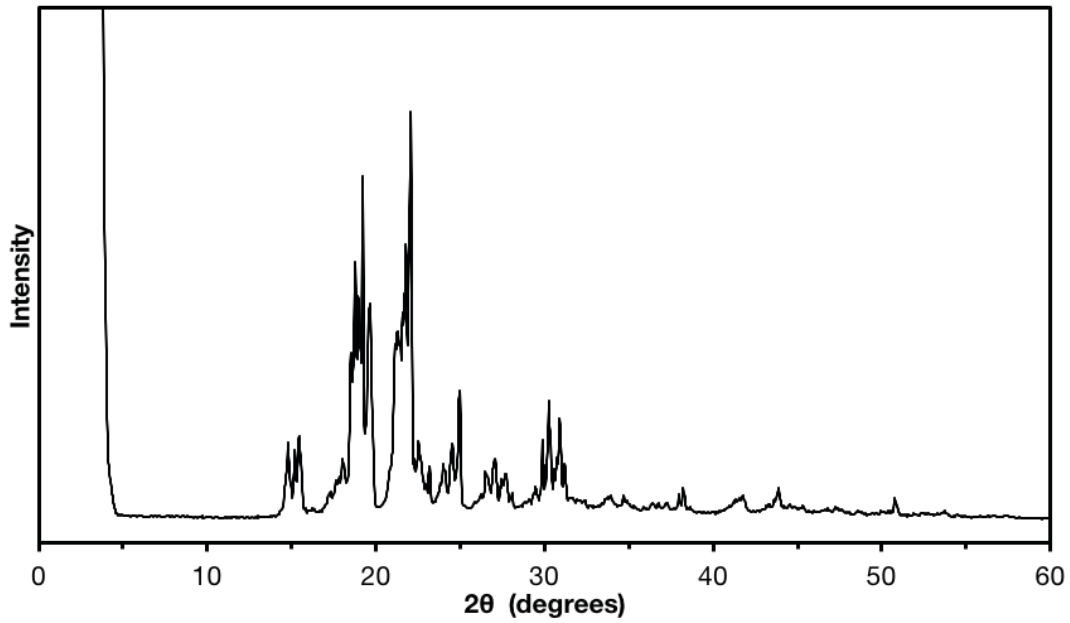

Formed from addition of THF anti-solvent in toluene

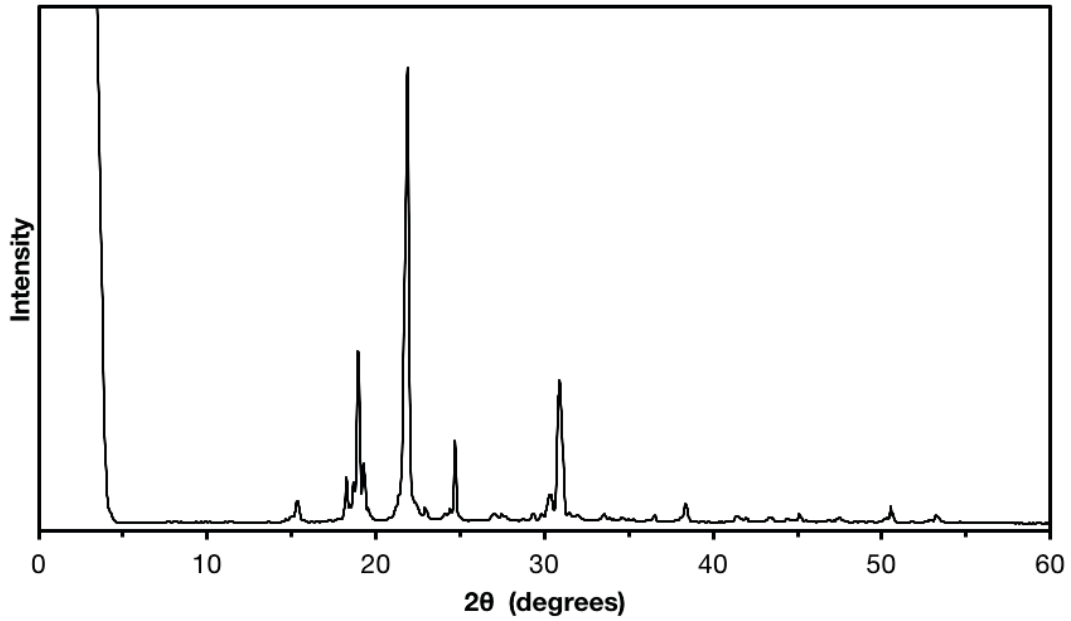

Formed from addition of THF anti-solvent in ethyl acetate